



UNIVERSITY OF  
BIRMINGHAM

# **Assessment of High-Cr Alloys for Cathode Air Pre-heaters in Solid Oxide Fuel Cells**

by

**Kun Zhang**

A Thesis submitted to The University of Birmingham for  
the Degree of

**Doctor of Philosophy**

Supervisor:

Centre for Hydrogen and Fuel Cell Research

Prof. Robert Steinberger-Wilckens

School of Chemical Engineering

Co-supervisor:

College of Engineering and Physical Sciences

Dr. Ahmad El-Kharouf

The University of Birmingham

May 2020

UNIVERSITY OF  
BIRMINGHAM

**University of Birmingham Research Archive**

**e-theses repository**

This unpublished thesis/dissertation is copyright of the author and/or third parties. The intellectual property rights of the author or third parties in respect of this work are as defined by The Copyright Designs and Patents Act 1988 or as modified by any successor legislation.

Any use made of information contained in this thesis/dissertation must be in accordance with that legislation and must be properly acknowledged. Further distribution or reproduction in any format is prohibited without the permission of the copyright holder.

## Acknowledgements

I would like to express my deepest appreciation to my supervisors, Prof. Robert Steinberger-Wilckens and Dr. Ahmad El-kharouf for their insightful suggestion throughout my PhD and for their support and guidance during writing this thesis. I would like to thank Dr. Jong-Eun Hong for offering me the opportunity to do PhD in this Fuel Cell Group and for his guidance during the initial stage of my PhD.

I am thankful to Prof. Jan Froitzheim and Dr. Falk-Windisch from Chalmers University of Technology, Sweden for their assistance in establishing the denuder test rig for my work.

I would like to thank our project manager, John Hooper and everyone in the Chen Eng PG administration office for always being there to help me solve many difficulties outside of my research works. I would like to thank the technical staff at University of Birmingham namely Bob Sharpe, Chynthol Kanhimbe, Theresa Morris, Prof. Ted Forgan, Elaine Mitchell, Dr. Artur Majewski, Christopher Stark, Stephen Brookes, Stephen Williams for their help in using various equipment for this work.

I also wish to express my gratitude to the European Union's H2020 Programme for providing scholarship for my PhD study. I would like to gratefully acknowledge the support of all our collaborators in the HEATSTACK project.

I am thankful to all my friends especially Sathish Pandiyan, Melissa Oum, Oujen Hodjati-Pugh, Daniel Escalera Lopez, Vikrant Venkataraman, Bernardo Sarruf, Carolina Branco, Miguel Angel Molina Garcia, Yaxiang Lu, Andrea Masi, Peter Mardle, Alan Stephen, Zeyu Jiang, Bhargav Pandya, Christopher Harrison, Nasser Khan, Liam Cooper, Abby Snowdon,

Ahmed Ibrahim, Irving Annan for their suggestions, support and encouragement during the 7 years of my student life in University of Birmingham.

Finally, I would like to deeply thank my family, my father, my mother, my brother and my sisters for supporting me spiritually throughout writing this thesis and my life in general. Without their constant support and encouragement, I would never been able to complete this PhD.

## Abstract

Efficient heat recovery and management is critical for the economic and environmental performance of a micro-CHP system. The cathode air pre-heater (CAPH) plays a pivotal role in the operation of Solid Oxide Fuel Cell micro-CHP systems as it heats up the inlet air close to the operating temperature (e.g. 750°C) of the SOFC by utilising the recovered thermal energy from the high temperature exhaust gas of the SOFC system. The current CAPH stacks, which are made from high Cr-containing alloys, are still vulnerable to high temperature corrosion and chromium evaporation, which can have a serious detrimental effect on the lifetime of the SOFC stack. For this reason, the aim of this study was to perform extensive corrosion and chromium evaporation measurements on various high temperature alloys and to implement a material progression for CAPH from chromia-forming alloys to alumina-forming alloys.

The effect of exposure temperature and water content on the oxidation and Cr evaporation behaviour of Inconel 625, SS309 and AluChrom 318 was analysed. The findings of this study showed that Cr evaporation and oxidation rates of Inconel 625 and SS309 were dramatically reduced when the temperature was reduced from 850 to 650°C. AluChrom 318 also exhibited a decreased oxidation rate with decreasing temperature but it also demonstrated a reverse trend in Cr evaporation temperature dependence. The main effect of water vapour on the alloys exposed to high temperature was to accelerate Cr evaporation.

The corrosion behaviour and Cr retention capability of an aluminised alloy (aluminised SS309) and an alumina-forming alloy (AluChrom 318) were compared with a conventional chromia-forming alloy (SS309) in simulated SOFC cathode atmosphere. The SS309 samples failed the specifications for application as cathode air preheater (CAPH) material due to a

high Cr evaporation rate and massive scale spallation. The surface aluminisation dramatically decreased the Cr evaporation rate of SS309, but not in the long-term due to breakaway oxidation induced alumina scale spallation. The AluChrom 318 formed a  $\gamma\text{-Al}_2\text{O}_3/\alpha\text{-Al}_2\text{O}_3$  layer scale and demonstrated the highest Cr retention ability and oxidation resistance among the tested alloy samples.

Microstructural analysis was conducted on an AluChrom 318 CAPH stack after 25,000 hours of industrial operation in simulated SOFC CAPH environment. The results showed a large amount of  $\text{Cr}_2\text{O}_3$  formation around the exhaust outlet (cold zone) and a high Al oxidation rate around the exhaust inlet (hot zone). This implied that the as-received AluChrom 318 CAPH plates did not have sufficient corrosion protection and a good barrier layer to stop Cr evaporation formed at high temperatures. For material optimisation, pre-treatment of AluChrom 318 in a high temperature oxidising atmosphere was then prescribed to achieve a better oxidation resistance and Cr retention capability of CAPH stacks in service. It was found that pre-treatment applied on the AluChrom 318 developed an  $\alpha\text{-Al}_2\text{O}_3$  surface scale that reduced the Al oxidation rate and reduced the tendency towards formation of a  $\text{Cr}_2\text{O}_3$  layer.

## List of Publications

1. **K. Zhang**, A. El-kharouf, J.E. Hong, R. Steinberger-Wilckens. The effect of aluminium addition on the high-temperature oxidation behaviour and Cr evaporation of aluminised and alumina-forming alloys for SOFC cathode air pre-heaters, *Corrosion Science*. 169 (2020) 108612.
2. **K. Zhang**, A. El-kharouf, R. Steinberger-Wilckens. Effect of temperature and water content on the oxidation behaviour and Cr evaporation of high-Cr steels for SOFC cathode air pre-heater, *Corrosion Science*. Manuscript submitted.
3. **K. Zhang**, A. El-kharouf, R. Steinberger-Wilckens. The effect of pre-treatment of AluChrom 318 on the corrosion behaviour and Cr evaporation in SOFC cathode air pre-heater, *ACS Applied Material & Interfaces*. Manuscript submitted.
4. **K. Zhang**, A. El-kharouf, R. Steinberger-Wilckens. The effect of pre-heat treatment of AluChrom 318 on the corrosion behaviour and Cr evaporation in SOFC cathode air pre-heater, *ECS Transactions* 91 (2019) 2253-2260.
5. **K. Zhang**, J.E. Hong, R. Steinberger-Wilckens. Effect of alloy composition on the oxidation behaviour and Cr vapourisation of high-Cr steels for SOFC cathode air pre-heater, *ECS Transactions* 78 (2017) 1641-1651.

Publication No. 2 contains work from chapter 4. Publication No. 1 and No. 5 contain work from chapter 5. Publication No. 3 and No. 4 contain work from chapter 6 and chapter 7. I declare that the work presented in this thesis is my own work. The co-authors listed in these publications are my supervisors.

## Table of Contents

<b>Acknowledgements</b> .....	<b>i</b>
<b>Abstract</b> .....	<b>iii</b>
<b>List of Publications</b> .....	<b>v</b>
<b>List of Figures</b> .....	<b>xi</b>
<b>List of Tables</b> .....	<b>xx</b>
<b>List of Abbreviations</b> .....	<b>xxi</b>
<b>Chapter 1 – Introduction</b> .....	<b>1</b>
1.1 Background of the research .....	1
1.2 Micro-combined heat and power generation .....	3
1.2.1 PEFC-based micro-CHP .....	6
1.2.2 SOFC based micro-CHP .....	7
1.3 Cathode air pre-heater.....	9
1.3.1 Ceramic materials .....	10
1.3.2 Metallic materials.....	11
1.4 Thesis objective and outline.....	12
<b>Chapter 2 – Literature Review</b> .....	<b>15</b>
2.1 Principle of Oxidation.....	16
2.1.1 Oxide formation .....	16
2.1.2 Defects and diffusion .....	21

2.1.3 Oxidation kinetics .....	24
2.1.4 Selective oxidation.....	26
2.2 Oxidation of chromia-forming alloys .....	29
2.2.1 Effect of Cr content.....	29
2.2.2 Effect of Mn content .....	31
2.2.3 Effect of Si content .....	36
2.3 Oxidation of alumina-forming alloys.....	38
2.3.1 Fe-Cr-Al based alloys .....	38
2.3.2 Different phases of the alumina .....	42
2.3.3 Oxidation of alumina forming alloys .....	44
2.4 Volatilisation of Cr(VI)-containing species.....	49
2.4.1 Formation of Cr(VI)-containing gases.....	49
2.4.2 Effect of Cr(VI) species on SOFC cathode material .....	54
2.4.3 Determination of chromium evaporation.....	57
2.4.4 Chromium evaporation from alloys .....	59
2.5 Summary .....	64
<b>Chapter 3 – Experimental.....</b>	<b>65</b>
3.1 Materials .....	66
3.2 Pre-heat treatment on AluChrom 318 .....	66

3.3 Exposure tests .....	67
3.3.1 Cr <sub>2</sub> O <sub>3</sub> evaporation tests .....	67
3.3.2 Long-term oxidation tests .....	73
3.4 Physical characterisation.....	74
3.4.1 Mass measurements .....	74
3.4.2 Scanning electron microscope (SEM) .....	75
3.4.3 Focused ion beam-scanning electron microscope (FIB-SEM).....	75
3.4.4 X-ray diffraction (XRD) .....	76
3.4.5 TEM and Scanning transmission electron microscopy (STEM) .....	77
<b>Chapter 4 – Effect of Temperature and Water Content on the Oxidation Behaviour and Cr Evaporation of High-Cr Steels for SOFC Cathode Air Preheater .....</b>	<b>78</b>
4.1 Results.....	79
4.1.1 Gravimetric measurements .....	79
4.1.2 Cr <sub>2</sub> O <sub>3</sub> evaporation measurements .....	80
4.1.3 Microstructural analysis.....	84
4.2 Discussion.....	90
4.2.1 Cr <sub>2</sub> O <sub>3</sub> evaporation corrected mass gain .....	90
4.2.2 Influence of temperature .....	92
4.2.3 Influence of water content .....	98

4.3 Conclusions.....	102
<b>Chapter 5 – The effect of aluminium addition on the high temperature oxidation behaviour and Cr evaporation of aluminised and alumina-forming alloys for SOFC cathode air pre-heaters.....</b>	<b>104</b>
5.1 Results.....	105
5.1.1 Mass measurements .....	105
5.1.2 Cr <sub>2</sub> O <sub>3</sub> evaporation .....	105
5.1.3 Microstructural investigation .....	107
5.2. Discussion.....	118
5.2.1 Corrosion and Cr <sub>2</sub> O <sub>3</sub> evaporation of SS309 .....	118
5.2.2 Corrosion and Cr <sub>2</sub> O <sub>3</sub> evaporation of alumina formers .....	119
5.3 Conclusions.....	123
<b>Chapter 6 – Microstructural analysis of an AluChrom 318 Cathode Air Pre-heater for an SOFC system .....</b>	<b>125</b>
6.1 Results.....	126
6.1.1 AluChrom 318 CAPH stack.....	126
6.1.2 Hot zone .....	128
6.1.3 Cold zone .....	131
6.2 Discussion.....	133
6.2.1 Hot zone .....	133
6.2.2 Cold zone .....	135

6.3 Conclusions.....	136
<b>Chapter 7 – The Effect of Pre-treatment of AluChrom 318 on the Corrosion Behaviour and Cr Evaporation in SOFC Cathode Air Pre-heaters .....</b>	<b>137</b>
7.1 Results.....	139
7.1.1 Pre-Treatment .....	139
7.1.2 Exposure Test.....	147
7.2 Discussion.....	150
7.2.1 Pre-heat Treatment.....	150
7.2.2 Exposure Test.....	153
7.3 Conclusions.....	156
<b>Chapter 8 – Summary .....</b>	<b>158</b>
8.1 Conclusions.....	158
8.2 Future work.....	160
<b>References.....</b>	<b>162</b>

## List of Figures

<b>Figure 1.1</b> (a) UK emissions across different sectors in 2016; (b) Primary energy consumption by sector in the UK in 2017 [1].....	1
<b>Figure 1.2</b> Energy savings through employment of a CHP unit as compared to traditional sources of heat and power generation (displayed in units of energy) [6].....	2
<b>Figure 1.3</b> General flow chart of a PEFC-based micro-CHP unit [5].....	6
<b>Figure 1.4</b> General flow chart of an SOFC-based micro-CHP system [5]. ....	7
<b>Figure 2.1</b> Ellingham/Richardson diagram illustrating the formation of stable oxide for a given metal at a given temperature and oxygen partial pressure, taken from [65,66].....	18
<b>Figure 2.2</b> Diffusion mechanism and interfacial reactions for high temperature alloy oxidation: (a) cation migration and (b) anion migration.....	20
<b>Figure 2.3</b> A schematic showing an individual vacancy and interstitial defect in a single component crystal lattice. ....	20
<b>Figure 2.4</b> Schematic of oxidation controlled by diffusion. Metal excess or vacancy leads to oxide growth at the oxide/gas interface. Oxygen excess or vacancies results in oxide growth at the metal/oxide interface [68]. ....	22
<b>Figure 2.5</b> The oxidation kinetics of three common growth mechanisms.....	24
<b>Figure 2.6</b> The influence of oxide scale on the temperature increase across a heated tube wall for different power ratings [90].....	31
<b>Figure 2.7</b> SEM cross-section and EDX line scan of Crofer 22 APU after oxidation in air for 1200 hours at 800°C [96].....	33
<b>Figure 2.8</b> Schematic of oxide structures formed on Ni-based alloys oxidised in humid environment [89].....	33
<b>Figure 2.9</b> SEM cross-section of (a) Crofer 22 APU, (b) Corfer 22 H, (c) Sanergy HT, (d) ZMG232 and (e) E-Brite after oxidation in 3% H <sub>2</sub> O humidified air at 850°C for 1000 hours.	

In the figure: (i) Ni coating; (ii) (Cr,Mn) <sub>3</sub> O <sub>4</sub> spinel; (iii) Cr <sub>2</sub> O <sub>3</sub> , (iv) internal Ti-oxide and (v) Laves phase [99].	34
<b>Figure 2.10</b> SEM cross-section images of the Fe-Cr-xMn alloys: (a) 0.0 Mn, (b) 0.5 Mn, (c) 1.0 Mn and (d) 3.0 Mn oxidised in air for 100 hours at 750°C [100].	36
<b>Figure 2.11</b> (a) Cross-section SEM image of the thin oxide scale for the B445JIM steel oxidised at 1200°C for 2 hours in air with the EDS element map of Si [110]; (b) BF-STEM cross-section of the oxide scale formed on Type 310 after exposure in 0.1 MPa air + 10% H <sub>2</sub> O at 800°C for 500 hours with the STEM-EDS element map of Si [111].	38
<b>Figure 2.12</b> Oxide map for Fe-Cr-Al ternaries at temperature greater than 1000°C [44].	39
<b>Figure 2.13</b> Arrhenius plot of K <sub>p</sub> for the oxidation of pure NiAl [72].	43
<b>Figure 2.14</b> Approximate Al <sub>2</sub> O <sub>3</sub> transformation temperature observed on bulk material [42].	43
<b>Figure 2.15</b> STEM/EDX images of the oxide scale formed on Kanthal AF after oxidation in dry oxygen at 900°C for 1 hour [136].	46
<b>Figure 2.16</b> Equilibrium vapour pressure of Cr-O-H gases at (a) 1000°C and (b) 800°C with water partial pressure of 3 kPa based on thermodynamic data from Ebbinghaus [41,160].	50
<b>Figure 2.17</b> Partial pressure of volatile chromium species (a) at 1223K in air (p(O <sub>2</sub> ) = 2.13×10 <sup>4</sup> Pa) with different partial pressure of water vapour, (b) in humidified air (p(O <sub>2</sub> ) = 2.13×10 <sup>4</sup> Pa and p(H <sub>2</sub> O = 2×10 <sup>3</sup> Pa)) at different temperatures, (c) in air (p(O <sub>2</sub> ) = 2.13×10 <sup>4</sup> Pa) without water at different temperatures, and (d) at 1223K and different O <sub>2</sub> partial pressure [26].	51
<b>Figure 2.18</b> (a) Oxygen dependence and (b) water vapour dependence for Cr <sub>2</sub> O <sub>3</sub> volatility at 837K [80].	52
<b>Figure 2.19</b> Partial pressure of CrO <sub>3</sub> in dry air and CrO <sub>2</sub> (OH) <sub>2</sub> in humid air (3% water) over Cr <sub>2</sub> O <sub>3</sub> at various temperatures [162].	52

<b>Figure 2.20</b> Arrhenius plot showing the influence of temperature on both oxide growth (squares) and Cr evaporation rate (triangles) for Sanergy HT (black) and Crofer 22 H (grey) in 6.0 L/min air with 3% H <sub>2</sub> O [163].	54
<b>Figure 2.21</b> Schematic of volatile chromium species deposition at the TPB (cathode/electrolyte interface) based on electrochemical deposition mechanism [27].	55
<b>Figure 2.22</b> Activation energy graphs of electrode conductivity of high- and low- frequency arcs for oxygen reduction on LSM electrodes in the presence and absence of chromium-containing alloy in air [166].	56
<b>Figure 2.23</b> Schematic of an experimental apparatus of transpiration method [168].	57
<b>Figure 2.24</b> The mass of evaporated chromium per area as a function of time for selective alloys at 850°C in air + 3% H <sub>2</sub> O [99].	61
<b>Figure 2.25</b> The mass of evaporated chromium per unit area as a function of time for different alloys at 800°C in air with p(H <sub>2</sub> O)=1.88×10 <sup>-3</sup> pa [48].	62
<b>Figure 2.26</b> Visual appearance of crucible and alloys after high temperature treatment at (a)1100°C and (b) 1200°C for 1000 hours [176].	63
<b>Figure 3.1</b> The schematic diagram of denuder technique.	67
<b>Figure 3.2</b> The process flow chart for the denuder technique equipped with Bronkhorst liquid-gas delivery system.	69
<b>Figure 3.3</b> The effect of air flow rate on the Cr evaporation rate of uncoated Sanergy HT. Each test lasted 72 hours [94].	70
<b>Figure 3.4</b> The UV-vis spectra of sodium chromate solution with different concentrations; (b) Extraction and analysis of the peak values of UV-vis spectra.	71
<b>Figure 3.5</b> The process flow chart for the long-term exposure set-up equipped with Bronkhorst liquid-gas delivery system.	73

**Figure 4.1** Mass gain of (a) Inconel 625, (b) SS309 and (c) AluChrom 318 isothermally exposed at 650, 750 and 850°C in air with 3% H<sub>2</sub>O for 168 hours; Mass gain of (d) Inconel 625, (e) SS309 and (f) AluChrom 318 isothermally exposed at 850°C in dry air and air containing 1%, 3% and 9% H<sub>2</sub>O for 168 hours. ....79

**Figure 4.2** Accumulated Cr<sub>2</sub>O<sub>3</sub> evaporation as a function of time for (a) Inconel 625, (b) SS309 and (c) AluChrom 318 isothermally exposed at 650, 750 and 850°C in air with 3% H<sub>2</sub>O for 168 hours; Rate of Cr<sub>2</sub>O<sub>3</sub> evaporation as a function of time for (d) Inconel 625, (e) SS309 and (f) AluChrom 318 isothermally exposed at 650, 750 and 850°C in air with 3% H<sub>2</sub>O for 168 hours. ....81

**Figure 4.3** Accumulated Cr<sub>2</sub>O<sub>3</sub> evaporation as a function of time for (a) Inconel 625, (b) SS309 and (c) AluChrom 318 isothermally exposed at 850°C in air containing 1%, 3% and 9% H<sub>2</sub>O for 168 hours; Rate of Cr<sub>2</sub>O<sub>3</sub> evaporation as a function of time for (d) Inconel 625, (e) SS309 and (f) AluChrom 318 isothermally exposed at 850°C in air containing 1%, 3% and 9% H<sub>2</sub>O for 168 hours. ....82

**Figure 4.4** XRD patterns for (a) Inconel 625, (b) SS309 and (c) AluChrom 318 isothermally exposed at 650, 750 and 850°C in air containing 3% H<sub>2</sub>O for 168 hours. ....83

**Figure 4.5** Surface SEM images of Inconel 625 exposed in air with 3% H<sub>2</sub>O for 168 hours at (a) 650°C, (b) 750°C and (c) 850°C; EDX line scan along the line in indicated Figure 4.5c. 84

**Figure 4.6** Surface SEM images and EDX element maps of SS309 exposed in air + 3% H<sub>2</sub>O for 168 hours at (a) 650°C, (b) 750°C and (c) 850°C. ....85

**Figure 4.7** Surface SEM images of AluChrom 318 exposed in air with 3% H<sub>2</sub>O for 168 hours at (a) 650°C, (b) 750°C and (c) 850°C with corresponded EDX line scan analysis. ....86

**Figure 4.8** XRD patterns for (a) Inconel 625, (b) SS309 and (c) AluChrom 318 isothermally exposed at 850°C in air containing 1%, 3% and 9% H<sub>2</sub>O for 168 hours. ....87

<b>Figure 4.9</b> Surface SEM images of Inconel 625 exposed at 850°C in air with (a) 1% H <sub>2</sub> O, (b) 3% H <sub>2</sub> O and (c) 9% H <sub>2</sub> O for 168 hours, SS309 exposed at 850°C in air with (d) 1% H <sub>2</sub> O, (e) 3% H <sub>2</sub> O and (f) 9% H <sub>2</sub> O for 168 hours, and AluChrom 318 exposed at 850°C in air with (g) 1% H <sub>2</sub> O, (h) 3% H <sub>2</sub> O and (i) 9% H <sub>2</sub> O for 168 hours. ....	87
<b>Figure 4.10</b> Cross-sectional SEM of Inconel 625 exposed in (a) 1% and (b) 9% H <sub>2</sub> O at 850°C for 168 hours; EDX maps of Inconel 625 exposed in 1% at 850°C for 168 hours. ....	88
<b>Figure 4.11</b> Cross-sectional SEM of SS309 exposed in (a) 1% and (b) 9% H <sub>2</sub> O at 850°C for 168 hours; EDX maps and linescans of SS309 exposed in 1% at 850°C for 168 hours. ....	89
<b>Figure 4.12</b> Gross mass gain and net mass gain for (a) Inconel 625, (b) SS309 and (c) AluChrom 318 isothermally exposed at 650, 750 and 850°C in air + 3% H <sub>2</sub> O for 168 hours; Gross mass gain and net mass gain for (d) Inconel 625, (e) SS309 and (f) AluChrom 318 isothermally exposed at 850°C in air containing 1%, 3% and 9% H <sub>2</sub> O for 168 hours.....	92
<b>Figure 4.13</b> Arrhenius plot showing the influence of temperature on the Cr <sub>2</sub> O <sub>3</sub> evaporation rate from Figure 4.2 for SS309 and Inconel 625 in 6.0 L/min air with 3% H <sub>2</sub> O.....	95
<b>Figure 4.14</b> Mass gain curves of (a) Kanthal APMT exposed in 5% O <sub>2</sub> + 95% N <sub>2</sub> and 5% O <sub>2</sub> + 55% N <sub>2</sub> + 40% H <sub>2</sub> O at 900-1100°C for 72 hours [158] and (b) Kanthal AF oxidised in O <sub>2</sub> and O <sub>2</sub> + 40% H <sub>2</sub> O at 900°C for 168 hours [152]. ....	101
<b>Figure 5.1</b> (a) Discontinuous mass measurements and (b) mass gain rates as a function of time for SS309, aluminised SS309 and AluChrom 318 in 3% H <sub>2</sub> O humidified air at 850°C for 2500 hours; (c) Accumulated Cr <sub>2</sub> O <sub>3</sub> evaporation and (d) Cr <sub>2</sub> O <sub>3</sub> evaporation rates as a function of time for SS309, aluminised SS309 and AluChrom 318 exposed to 3% H <sub>2</sub> O humidified air at 850°C for 168 hours. ....	106
<b>Figure 5.2</b> SEM top view and EDX mapping of SS309 exposed at 850°C in air + 3% H <sub>2</sub> O for (a) 100 and (b) 1000 hours.....	107

<b>Figure 5.3</b> XRD patterns of SS309 after oxidation at 850°C in air with 3% H <sub>2</sub> O (6.0 L/min) for 0, 100, 500, 1000 and 2000 hours. ....	108
<b>Figure 5.4</b> SEM cross-sectional images of SS309 after exposure to humidified air at 850°C for 1000 hours with the corresponded EDX maps.....	109
<b>Figure 5.5</b> SEM top view of aluminised SS309 exposed at 850°C in air + 3% H <sub>2</sub> O for (a) 100 and (b) 1000 hours. EDX mapping showing the element distribution on Figure 5.5b. ....	110
<b>Figure 5.6</b> XRD patterns of aluminised SS309 after oxidation at 850°C in air with 3% H <sub>2</sub> O (6.0 L/min) for 0, 100, 500, 1000 and 2000 hours.....	111
<b>Figure 5.7</b> SEM cross-sectional images and EDX mapping of aluminised SS309 after exposure to humidified air at 850°C for 1000 hours. ....	112
<b>Figure 5.8</b> Cross-sectional SEM image and EDX mapping of aluminised SS309 after 100 hours exposure at 850°C in air with 3% H <sub>2</sub> O environment. ....	113
<b>Figure 5.9</b> SEM top view of AluChrom 318 exposed at 850°C in air + 3% H <sub>2</sub> O for (a) 100 and (b) 1000 hours. EDX linescan along the line indicated in Figure 5.9b. EDX mapping showing element distribution on Figure 5.9b. ....	113
<b>Figure 5.10</b> XRD patterns of AluChrom 318 after oxidation at 850°C in air with 3% H <sub>2</sub> O (6.0 L/min) for 0, 100, 500, 1000 and 2000 hours. ....	114
<b>Figure 5.11</b> (a) STEM cross-sectional image and EDX mapping of AluChrom 318 exposed at 850°C in air + 3% H <sub>2</sub> O for 1000 hours; (b) EDX linescan along the line indicated in Figure 5.11a.....	115
<b>Figure 5.12</b> TEM bright field cross-sectional images of the duplex alumina scales on the AluChrom 318 exposed at 850°C in air + 3% H <sub>2</sub> O for 1000 hours.....	117
<b>Figure 6.1</b> (a-b) Picture of CAPH stack made of AluChrom 318 developed at Senior Flexonics Ltd.; (c-d) picture of CAPH stack made of multiple cells, showing the inlet and outlet for exhaust gas and fresh air. ....	127

**Figure 6.2** (a) Schematic of heat distribution on a single CAPH cell during operation; (b) photograph of a single CAPH cell, showing different oxidation states in different temperature regions..... 128

**Figure 6.3** Photos of the outer (a) and inner (b) surfaces of a single CAPH cell exposed to the hot zone. The sample was selected at location 1 in Figure 6.2b..... 128

**Figure 6.4** Top view SEM images of (a) region 1 on outer surface, (b) region 2 on outer surface and (c) inner surface of the single cell exposed to the hot zone with corresponding EDX line scan analysis. .... 129

**Figure 6.5** XRD patterns of the outer (a) and inner (b) surfaces of a single CAPH cell exposed in the hot zone..... 130

**Figure 6.6** Cross-sectional SEM images of the outer (a) and inner (c) surfaces of a single CAPH cell exposed in the hot zone. EDX linescan profiles across the oxide film on the outer (b) and inner (d) surface of a single CAPH cell exposed in the hot zone..... 130

**Figure 6.7** Pictures of the outer (a) and inner (b) surfaces of a single CAPH cell exposed in the cold zone. The sample was selected at location 2 in Figure 6.2b. .... 131

**Figure 6.8** Top view SEM images and EDX linescan profiles of (a,c) outer and (b,d) inner surfaces of a single cell exposed in the cold zone for 25,000 hours..... 132

**Figure 6.9** XRD patterns of outer (a) and inner (b) surface of a single CAPH cell exposed in the cold zone for 25,000 hours..... 132

**Figure 6.10** Cross sectional images of outer (a) and inner (c) surface of a single CAPH cell exposed in the cold zone. EDX line scan profiles across the oxide film on the outer (b) and inner (d) surface of a single CAPH cell exposed in the cold zone. .... 133

**Figure 7.1** (a) Mass gain of AluChrom 318 pre-treated at 800°C for 1, 2 and 4 hours, 900°C for 1, 2 and 4 hours, 1000°C for 1, 2 and 4 hours and 1100°C for 0.5, 1 and 2 hours; (b) Mass

gain of the AluChrom pre-treated at 800°C, 900°C, 1000°C and 1100°C for 1 and 2 hours. .....	139
<b>Figure 7.2</b> Photographs of the non-treated AluChrom 318 and the AluChrom 318 pre-treated at 800, 900, 1000 and 1100°C in dry air for 1 hour. ....	140
<b>Figure 7.3</b> EDX elemental concentration of AluChrom 318 surface pre-heated at (a) 800°C for 1, 2 and 4 hours, (b) 900°C for 1, 2 and 4 hours, (c) 1000°C for 1, 2 and 4 hours and (d) 1100°C for 0.5, 1 and 2 hours. ....	140
<b>Figure 7.4</b> XRD patterns of the AluChrom 318 pre-treated at 800, 900, 1000 and 1100°C for 1 hour. ....	142
<b>Figure 7.5</b> Backscattered electron images of the oxide scale formed after being pre-treated at 800°C for 1 (a), 2 (b) and 4 (c) hours, at 900°C for 1 (d), 2 (e) and 4 (f) hours, at 1000°C for 1 (g), 2 (h) and 4 (i) hours and at 1100°C for 0.5 (j), 1 (k) and 2 (l) hours. ....	142
<b>Figure 7.6</b> EDX line scan of Al (a) and Cr (b) for the AluChrom 318 pre-heated at 800, 900, 1000 and 1100°C for 1 hour along the line indicated in Figure 7.5. ....	143
<b>Figure 7.7</b> (a) TEM bright field cross-sectional images of the oxide scale formed on the AluChrom 318 pre-treated at 900°C for 1 hour; (b) Magnified TEM image of Figure (a), showing a two-layered structure. ....	144
<b>Figure 7.8</b> (a) TEM bright field cross-sectional images of the oxide scale formed on the AluChrom 318 pre-treated at 900°C for 1 hour; (b) Magnification of location 1 in Figure 7.8a, showing the platelet-like alumina grown above a pit; (c) Magnification of location 2 in Figure 7.8a, showing a two-layered structure. ....	145
<b>Figure 7.9</b> STEM bright field image and EDX maps of the AluChrom 318 pre-treated at 1100°C for 1 hour; (b) EDX linescan along the line indicated in Figure 7.9a. ....	146
<b>Figure 7.10</b> Discontinuous mass measurements of the non-treated and pre-treated AluChrom 318 exposed to 3% humidified air (6.0 L/min) at 850°C for 500 hours. ....	147

**Figure 7.11** Accumulated  $\text{Cr}_2\text{O}_3$  evaporation as function of time for the non-treated and pre-heated AluChrom 318 exposed at 850°C in 3% humidified air for 168 hours..... 148

**Figure 7.12** Surface SEM images of the non-treated AluChrom 318 and the AluChrom 318 pre-treated for 1 hour at 800, 900, 1000 and 1100°C before and after being exposed at 850°C in 3% humidified air for 500 hours..... 149

## List of Tables

<b>Table 1.1</b> Technical data of four main micro-CHP system designs [8]. Fuel cell systems include the polymer electrolyte (PEFC) and the solid oxide (SOFC) fuel cell.....	3
<b>Table 2.1</b> A summary of different analytic techniques employed to quantify chromium vapours [168]......	58
<b>Table 3.1</b> The chemical compositions of the stainless steel materials investigated in this study. ....	66
<b>Table 3.2</b> The matrix for pre-heat treatment conditions of AluChrom 318. ....	67
<b>Table 4.1</b> Type of the outer oxide scales formed on Inconel 625, SS309 and AluChrom 318 at respective temperatures in air containing 3% H <sub>2</sub> O for 168 hours.....	83
<b>Table 5.1</b> EDX point analysis on the indicated spots in Figure 5.2. ....	109
<b>Table 5.2</b> EDX point analysis on the indicated spots Figure 5.11a. ....	116
<b>Table 6.1</b> Thermal specifications of the AluChrom 318 made CAPH during operation. Data supplied by Vaillant GmbH. ....	127

## List of Abbreviations

A (cm <sup>2</sup> )	The area of the steel coupon
BOP	Balance of plant
BSE	Back scatter electron
CAPH	Cathode air pre-heater
CBED	Convergent beam electron diffraction
CEM	Controlled evaporation and mixture
CHP	Combined heat and power
Cr(IV)	Cr <sup>6+</sup>
EDX	Energy dispersive X-ray analysis
FIB-SEM	Focused ion beam-scanning electron microscope
GDC	Gadolinium doped ceria
GFC	Gas flow controller
GHG	Greenhouse gas

GI-XRD	Grazing incidence X-ray diffraction
HT-WGS	High temperature water gas shift
IC	Internal combustion
ICP-AES	Inductively coupled plasma-atomic emission
ICP-MS	Inductively coupled plasma-mass spectrometry
ICP-OES	Inductively coupled plasma-optical emission spectrometry
LSM	Lanthanum strontium manganite
$m_{\text{before}}$ (mg)	The mass of the steel coupon before exposure
$m_{\text{after}}$ (mg)	The mass of the steel coupon after exposure
$\Delta m$ (mg/cm <sup>2</sup> )	The mass gain of the steel coupon after each exposure test
PBR	Pilling-Bedworth ratio
PEFC	Polymer electrode fuel cell
PEM-FC	Proton exchange membrane fuel cell
PROX	Preferential oxidiser

PVD	Physical vapour deposition
RE	Reactive element
SE	Secondary electron
SEM	Scanning electron microscope
SOFC	Solid oxide fuel cell
SR	Steam reforming
STEM	Scanning
TEM	Transmission electron microscope
TPB	Triple phase boundary
UV-vis	Ultraviolet-visible
WGS	Water gas shift
XRD	X-ray diffraction
YSZ	Yttria-stabilised zirconia

# Chapter 1 – Introduction

## 1.1 Background of the research

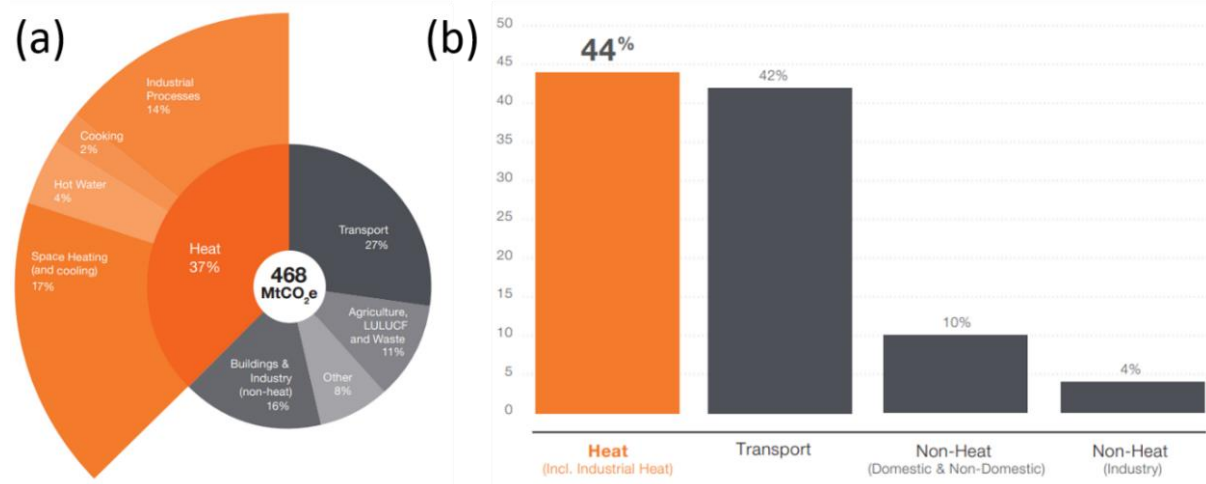


**Figure 1.1** (a) UK emissions across different sectors in 2016; (b) Primary energy consumption by sector in the UK in 2017 [1].

Globally, the supply of heat contributes to almost half of the overall CO<sub>2</sub> emissions and energy consumption, but decarbonisation of heat has gained little attention compared to transport and electricity [2]. In the UK, heat accounted for 37% of the emissions in 2016 and 44% of the energy consumed in 2017 [1], as shown in Figure 1.1. Since 1990, domestic gas consumption has been growing steadily, primarily owing to the proliferation of installed gas-fired boilers [3]. The UK government has set a target of 80% reduction in greenhouse gas (GHG) emissions by 2050, compared with 1990 levels [4]. Cities being the largest source of GHG emissions, they provide the greatest potential for mitigation of global warming. Thus, decarbonisation of heat supply to buildings is considered as a fundamental step in achieving the 2050 target [4]. The challenge in meeting the decarbonisation target is that over 80% of domestic buildings in the UK would be required to upgrade their heating system by 2050. This has led the industry and the research community into an increasing desire and interest in developing more efficient and cleaner heat and power generators. Micro-cogeneration or

micro-combined heat and power (micro-CHP), simultaneously offering heat and power, has been suggested as a possible alternative to gas-fired boilers for households since the 1990s [5]. Figure 1.2 compares the energy cost of a packaged combined heat and power (CHP) unit with the separate means of conventional generation via a power station and boiler. To generate an equivalent amount of electricity and heat, the traditional boiler and power station would require 139 units of fuel, while the packaged CHP would yield 28% (39/139) of primary energy saving [6]. CHPs have been recognised as a proven and well-established technology that can considerably reduce CO<sub>2</sub> emissions and meet energy demand for larger-scale industrial and commercial applications [7]. Thus, the possibility of developing smaller-scale micro-CHP could be a promising solution to reduce GHG emissions in the residential building sector [5].

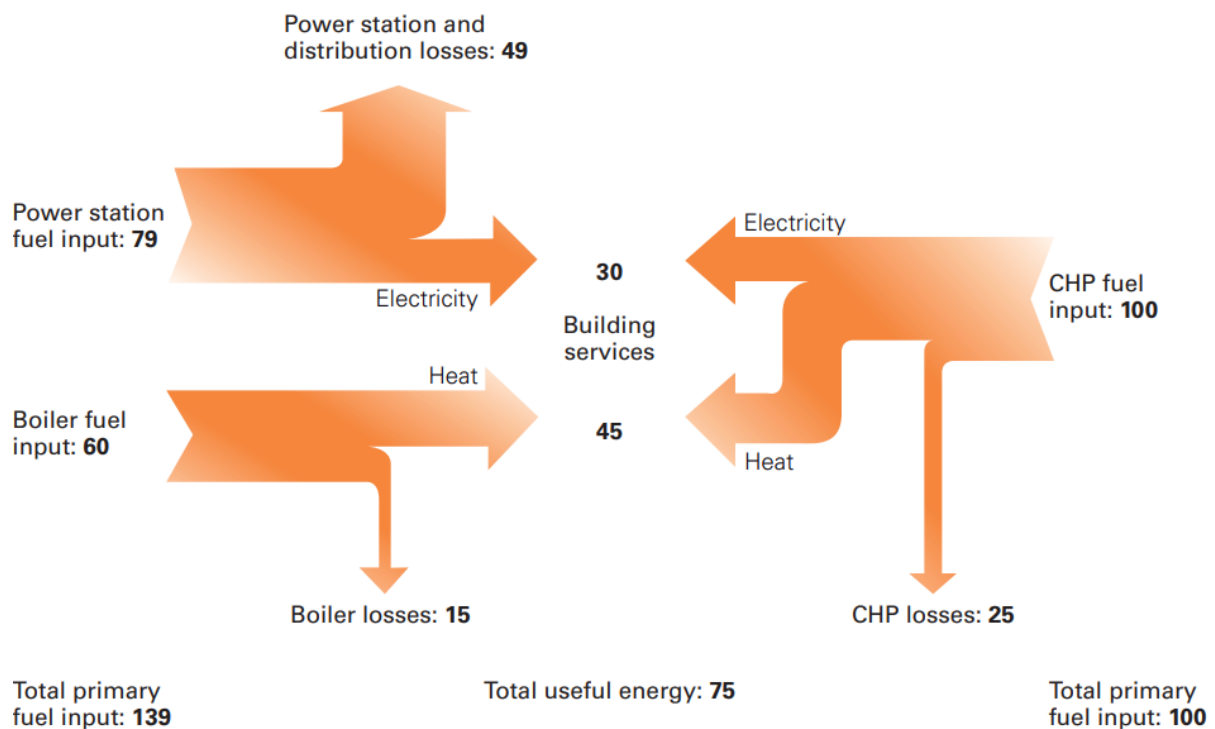


**Figure 1.2** Energy savings through employment of a CHP unit as compared to traditional sources of heat and power generation (displayed in units of energy) [6].

## 1.2 Micro-combined heat and power generation

**Table 1.1** Technical data of four main micro-CHP system designs [8]. Fuel cell systems include the polymer electrolyte (PEFC) and the solid oxide (SOFC) fuel cell.

	Internal combustion engine	PEFC	SOFC	Stirling engine
Electrical efficiency (part load, full load)	10%, 25%	30%, 26%	45%, 40%	5%, 10%
Overall efficiency (part load, full load)	80%, 85%	80%, 85%	85%, 90%	80%, 90%
Supplementary thermal system efficiency	86%	86%	86%	86%
Minimum operating set point (% of rated power)	20%	20%	20%	20%
Minimum up-time (min)	10	60	60	10
Maximum ramp rate ( $\text{kW}_e \text{ min}^{-1}$ )	0.2	0.2	0.05	0.2
Start-up energy consumption ( $\text{kW}_e, \text{kW}_{th}$ )	0.008, 0.5	0.017, 1.6	0.017, 2.0	0.008, 0.5

Micro-CHP systems have been developed using different technologies, including Stirling engines, internal combustion (IC) engines and fuel cells [8], as shown in Table 1.1. A CHP unit integrated with an IC engine works in a similar way to the vehicle engine. It burns the fuel (normally compression-ignition diesel or natural gas) which produces motive power [9]. This power is then converted into electricity by an alternator. The waste heat from the combustion process is captured to produce hot water for domestic use. The electrical efficiency of an IC-CHP unit is 10 to 25% with a total efficiency of 80 to 85%. The Stirling engine CHP is also known as external combustion engine where the combustion process is separated from the working gas. The fuel combustion heats up the fully enclosed working fluid (normally helium) within the Stirling engine, causing it to expand. As the working fluid expands, it forces a piston to move up and down between a copper coil, producing electricity. Since the combustion process is used for providing a continuous heat input to the working fluid, it is potentially more efficient, quieter and cleaner than IC engines [10]. The overall efficiency of the Stirling engine based CHP is slightly higher than for the IC based

micro-CHP. However, system electrical efficiency of the Stirling engine based CHP in field trials has been found to range from 5 to 10%. Fuel cells based CHPs are a new technology introduced to the residential markets offering simultaneous power and heat generation. A fuel cell is an electrochemical energy conversion device that directly converts the chemical energy stored in fuels into heat and electricity via an oxidation – reduction reaction without the process of combustion. Compared to the heat engine based CHPs, the fuel cell based CHP unit provides much higher electrical efficiency (Table 1.1). This is because fuel cell based CHPs are able to convert chemical energy directly to electric energy, maximising their efficiency. It has been reported that the net electrical efficiency for a fuel cell based system ranges from 30 to 45% , instead of 10 to 25% as in the case of heat engine-based system [11–14]. Furthermore, as fuel cell based CHP is able to operate at lower heat-to-power ratios, excess generation of heat is avoided [11]. Staffell compared the carbon intensity of heat generated from different CHP technologies: Stirling engines 155 to 200 g/kWh; internal combustion engines: 70 to 120 g/kWh; and fuel cells: average -110 to 85 g/kWh [2]. It can be seen that the fuel cell based systems provide the most reduction in CO<sub>2</sub> emissions compared to the heat engine-based CHPs. Thus, there is a strong opportunity for fuel cells to contribute to low-carbon heat, and reduce air pollution and primary energy consumption [15]. Japan is recognised as the leading country in the development of fuel cell based micro-CHPs, with the Ene-Farm project, launched in 2009: the total sales hit the 10,000 mark in April 2012 and 292,654 in December 2018 [14,16]. After Japan, Germany is the second leading country in fuel cell based micro-CHP area, with the Callux project launched in 2008 [17]. A total 350 fuel cell-based micro-CHP installations were installed between 2008 and 2012 [18]. The experiences from Callux were shared within a European-wide micro-CHP demonstration programme called Ene.field, launched in October 2012 [19]. The Ene.field project deployed

more than 1,000 residential fuel cell based micro-CHP installations, across 10 European countries [14].

There are different kinds of fuel cell technologies available with very different designs, each suitable for different applications. Therefore, depending on the fuel cell type, the fuel and the application, the configuration of a fuel cell based micro-CHP system may vary. Of the technologies currently employed, the most promising fuel cell types for the application in micro-CHP are the low temperature polymer electrolyte fuel cell (PEFC) and the high temperature solid oxide fuel cell (SOFC) [11]. The fuel cell stack, which is the most important and expensive component of the entire micro-CHP system, consists of a multitude of individual cells (with anode, electrolyte and cathode) electrically interconnected using metallic plates (bipolar plates for PEFC and interconnects for SOFC) that also distribute fuel and air to the electrodes. Balance-of-plant (BOP) components and auxiliary equipment (i.e. inverters, heat exchanger, control unit, power conditioners, sensors, etc.) are also necessary for the operation of a fuel cell based CHP system. In terms of fuels, hydrogen is considered as the best fuel for all the fuel cell based micro-CHPs in terms of durability and electrochemical performance. Nevertheless, due to the difficulties in hydrogen storage and lack of hydrogen supply infrastructure, natural gas is also recognised as a suitable fuel. By using the existing natural gas supply network, the fuel cell based micro-CHPs offer an easy replacement of the installed gas-fired boilers. In the case of natural gas used as fuel, natural gas must be converted to hydrogen via a fuel processor especially if a PEFC fuel cell stack is employed.

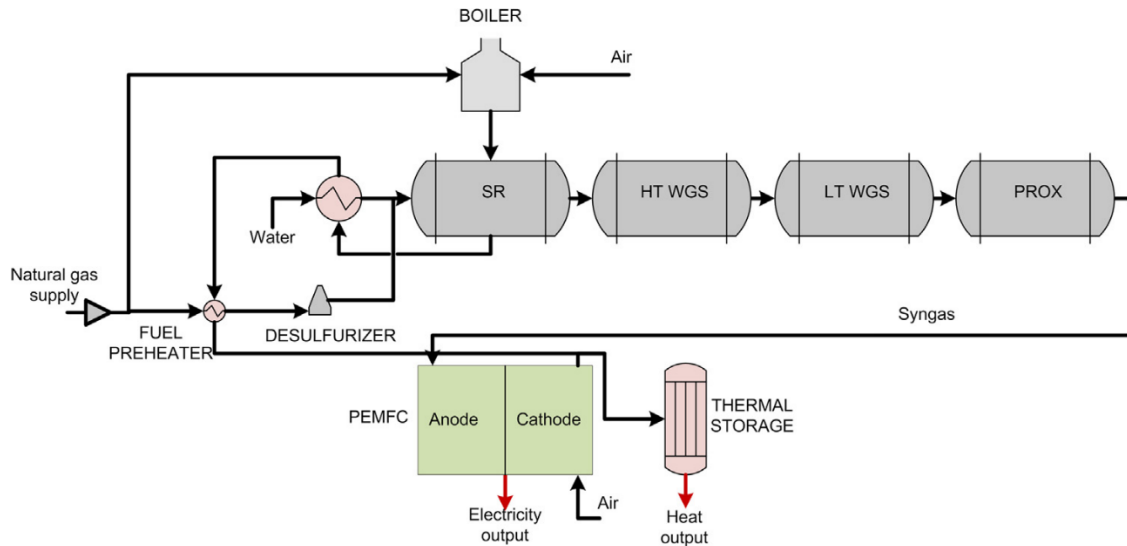


**Figure 1.3** General flow chart of a PEFC-based micro-CHP unit [5].

### 1.2.1 PEFC-based micro-CHP

PEFCs are recognised as a very promising technology for adoption as a prime mover in micro-CHP systems due to various advantages, such as high power density, rapid start-up (due to low temperature operation) and low pollutant emissions [20]. Real home field trials by EneFarm of a 0.7 kWe PEFC micro-CHP in Japanese households have illustrated that annual CO<sub>2</sub> emission reductions of up to 750 to 1250 kg per annum are achievable [16]. A typical PEFC based micro-CHP system generally consists of the PEFC stack, the fuel processing system, pre-heating sections, the heat recovery loop, and all other auxiliary BOP components [21]. A general component arrangement of a PEFC based micro-CHP is presented in Figure 1.3. The fuel cell stack is used to generate electrical power for the micro-CHP system. Thermal energy is recovered from the fuel cell stack itself, from the reformat fuel entering the stack and from the burner exhaust before being transferred to heating up water in a secondary circuit (water loop) connected to the heating system in the building [14,21]. The operation of PEFC based systems requires high purity hydrogen in order to avoid the poisoning of electro-catalysts (Pt) by CO generated from the natural gas reforming process. Therefore, a large reformer is strictly required for the PEFC based micro-CHP. A

traditional fuel processor within a PEFC based system usually consists of three stages: steam reforming (SR), water gas shift (WGS) processor, and preferential oxidiser (PROX) [12]. The SR reactor within a PEFC based micro-CHP has the target to convert the natural gas entering the micro-CHP into hydrogen-rich steam [8]. The integration of the fuel processing subsystem, including high temperature water gas shift (HT-WGS), low temperature water gas shift (LT-WGS), and PROX, is required to reduce the CO content to less than 10 ppm [5,8]. Therefore, the entire fuel processing unit for a PEFC based micro-CHP is relatively large and complicated with each step requiring precise temperature control and thermal integration [8].

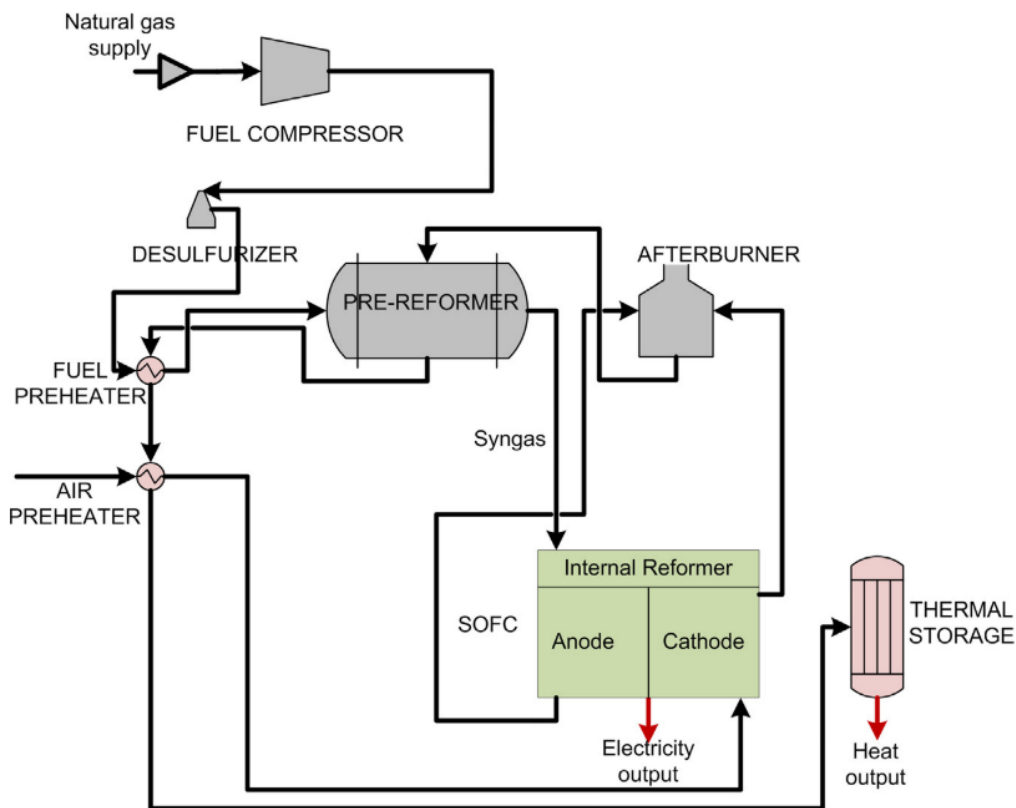


**Figure 1.4** General flow chart of an SOFC-based micro-CHP system [5].

### 1.2.2 SOFC based micro-CHP

In comparison to PEFCs, SOFCs generally run at much higher temperature of around 500 to 950°C. Because of the high operating temperature, SOFC based CHPs have the highest electrical efficiency and also provide high-grade heat that can be used within the household

[2,13]. The slow start-up and shut-down of a SOFC-based system is however problematic, especially in the case of large scale SOFC operated in the high temperature region (850 to 1000°C) [22]. Thus, the transition from the high temperature operation used in early large-scale systems into the intermediate temperature (IT) range of 500 to 700°C currently attracts the most attention for micro-CHP applications [23]. SOFCs are also recognised as a versatile fuel cell due to the flexibility in fuels. The capability of SOFCs to maintain high efficiency with hydrocarbon fuels is a main advantage over PEFCs, specifically for micro-CHP applications [8]. Field trials of a BlueGen 1.5 kW SOFC micro-CHP were carried out by Elmer et al. [24] at the University of Nottingham to evaluate its economic and emission performance. The annual assessment results exhibited that the SOFC micro-CHP can provide cost reductions of 177% and annual CO<sub>2</sub> emissions reductions of up to 56% compared to the base case scenario [24]. Figure 1.4 shows the typical configuration of an SOFC based micro-CHP. A complete SOFC based micro-CHP system is typically composed of a fuel cell stack, fuel processing unit, a control system, heat exchange system, and power-conditioning units [13]. It can be seen that the major difference between SOFC and PEFC system is in the configuration of the fuel processor. The fuel processor used for SOFC based micro-CHP usually consists of a desulfuriser and an external pre-reformer and an internal reforming process. The SOFC based micro-CHPs operated at high temperature are capable of reforming hydrocarbon fuels internally [8]. However, in order to avoid possible carbon deposition and excessive thermal stress on the anode materials, an external reformer is required to further improve the efficiency of the reforming process [13]. Since the by-product CO from the main reformer can also be used as a fuel in the SOFC system, the cost and size of the fuel processing subsystem is dramatically reduced in an SOFC based micro-CHP system [5,8]. Thus, it is clear that SOFCs demonstrate an obvious advantage over PEFCs in terms of fuel processing.

### 1.3 Cathode air pre-heater

Thermal management plays a pivotal role in the successful application of the fuel cell based micro-CHP system in terms of practicality, efficiency, and operational flexibility [25]. Appropriate thermal management must be implemented, since some streams require cooling, while others require heating [5]. Due to the large difference in the operating temperature between PEFC and SOFC-based systems, the thermal management requirement for each case is remarkably different. For PEFC, the hydrogen stream leaving the fuel processing unit requires cooling before entering the fuel cell stack while air enters the cathode at room temperature [21]. In contrast, pre-heating of air and fuel is necessary for an SOFC stack due to the requirement for high temperature operation [8]. Thus, both air and fuel pre-heaters are required for an SOFC based micro-CHP system, as the pre-reformer and the SOFC stack cannot tolerate the gas supply at low temperatures [5,8,13]. The temperatures of incoming fuel and air must be raised until they are close to the reaction temperature of the SOFC stack. To achieve this, counter-current heat exchangers are generally employed to recover the thermal energy from the afterburner of the SOFC exhaust gases to heat the air flowing to the cathode and the fuel before pre-forming. According to the actual performance of other metallic components in the SOFC systems, the operating environment within the cathode air pre-heater (CAPH) is more corrosive than that in the anode fuel pre-heater due to the high oxygen partial pressure on the cathode side [26,27]. Therefore, the CAPH, a critical component in BOP, has stringent material criteria to ensure long-term SOFC operation. It is common sense that the thermal conductivity of the material from which heat exchange elements are fabricated must be as high as possible to maximise the heat exchanger performance [28]. Whilst this is generally true, thermal conductivity cannot be the sole criterion for the practical material selection of CAPH, as the CAPH stack will be exposed to an extremely oxidising environment on the cathode side at elevated temperatures for many

years. Due to the high operating temperature and severe environment within the CAPHs (oxidant and humidity), the materials selected for this application must be robust enough to ensure reliable, safe and continuous operation of the SOFC based micro-CHP. Suitable materials researched to date, including ceramic materials and high temperature alloys, capable of withstanding high operating temperature and thermal cycling. Considering the operating environment, the CAPH material has to satisfy the following requirements [28–30]:

- Excellent thermal conductivity;
- Low pressure drop;
- Superior high temperature corrosion resistance (metallic material only);
- Low or zero Cr release (metallic material only);
- Sufficient creep resistance at elevated temperature;
- Machinability;
- Weldability (metallic material only);
- Cost effectiveness.

### **1.3.1 Ceramic materials**

Ceramic materials such as silicon nitride, silicon carbide or even hybrid cermet materials have been considered as candidates for applications like high temperature heat exchangers, owing to their excellent mechanical and thermal properties [31]. However, each of these materials requires unique fabrication techniques that could dramatically increase the manufacturing cost [28]. For this reason, materials like alumina silicate or alumina with less thermal conductivity but high machinability have been considered as alternative ceramic materials for the fabrication of the pre-heater. Córdova et al. recently fabricated a novel ceramic heat exchanger using alumina-silicate as a CAPH for SOFC application [28]. The

current design of heat exchangers developed by Córdova et al. has walls of approximately 5 mm thickness [28], which may result in bulky heat exchanger stacks. In addition, due to their particular crystalline structure, ceramic materials suffer from poor mechanical resistance and are difficult to machine, which has inhibited wide spread application. Thus, the (relatively brittle and expensive to machine) ceramic materials have less advantage compared to the metal-based CAPH.

### 1.3.2 Metallic materials

Remarkable progress has been achieved in the reduction of the operating temperature of SOFCs to 500 to 700°C because of the development of novel electrode materials and the decrease of the electrolyte thickness [23,32–36]. Furthermore, by lowering the operating temperature, a wider range of cheap materials can be used, especially in relation to BOPs and interconnects [8,23]. CAPHs made from metallic materials have received substantial attention because of their high thermal conductivity, formability, manufacturability and superior mechanical properties for use in fuel cell technology. Metallic materials permit the design of ultra-thin CAPH plates decreasing the bulk size and weight of the CAPH stacks while decreasing the manufacturing cost. Potential high temperature alloys normally contain a high concentration of Cr to offer oxidation resistance under SOFC environment by producing a continuous layer of chromia ( $\text{Cr}_2\text{O}_3$ ) [37]. However, chromia-forming alloys have two main limitations, namely, a rapid growth rate of  $\text{Cr}_2\text{O}_3$  scale at elevated temperatures, which decreases the material lifetime, and evaporation and migration of volatile Cr (VI) species (i.e.  $\text{CrO}_3$  or  $\text{CrO}_2(\text{OH})_2$ ), which impacts on the lifetime of the SOFC cells by poisoning of the cathode [27,38–40]. Alloys forming a silica scale with slow growth rate are also able to offer superior oxidation resistance at elevated temperatures [41]. Nevertheless, the use of Si as alloying element is usually restrained by the metallurgical properties of alloys. As the

toughness and weldability of the Fe- and Ni-based alloys can be reduced by Si addition, the content of Si in the alloy is normally limited to relatively low levels so that formation of a continuous silica outer layer cannot be achieved [42]. Alumina-forming alloys are promising candidates for BOP applications include piping, pumps and heat exchangers, as well as for other high temperature components without current-conducting function [43]. Alumina-forming alloys containing a small amount of aluminium (3 to 5 wt.%) exhibit superior high-temperature oxidation resistance and Cr retention capability by forming an alumina scale with a low defect concentration. Due to their high stability and oxidation resistance alumina formers are utilised for a number of high temperature applications such as furnace components for temperatures up to 1300°C [43]. Alumina grows at a rate slower than chromia due to its extremely low defect concentration [44]. Furthermore, alumina offers a significantly higher degree protection than chromia in the presence of steam at high temperatures. It has been proven that alumina volatility by  $\text{Al}(\text{OH})_3$  formation is not expected to be an issue below 1300°C for long-term applications [45]. Thus, the utilisation of high-temperature alloys with alumina as protective layer presents a significant opportunity to allow compact designs of CAPHs while extending their lifetime and alleviating the SOFC degradation caused by volatile Cr (VI) species.

#### **1.4 Thesis objective and outline**

As the metallic components such as interconnects and BOP play a key role in SOFC systems, the oxidation and Cr evaporation characteristics of chromia- and alumina-forming alloys have been extensively studied [29,30,51–54,37,41,43,46–50]. However, the majority of studies carried out within this field were directed towards the evaluation and optimisation of the Cr evaporation issue of interconnects, by exploring suitable alloys or by applying coatings. Limited research was been conducted on the chromia- and alumina-forming alloys for

minimising the high temperature Cr evaporation and scaling specifically in SOFC CAPHs. The project HEATSTACK looked into issues of CAPH in SOFC systems, including manufacturability, structural integrity, and chromium release [55]. As this work was funded by the HEATSTACK project, the focus of this work was therefore on the selection of high-Cr alloys that possess a slow oxidation rate and extremely low levels of Cr evaporation, suitable for the SOFC CAPH application. The aim was to conduct extensive material testing to achieve a better understanding of the corrosion and Cr evaporation behaviours of various high-Cr alloys supplied by the HEATSTACK project. Based on the experimental results, the HEATSTACK project implemented a material transformation for CAPH from chromia-forming alloys to alumina-forming alloys so as to reduce the chromium leakage. The following objectives were identified for this study:

- I. To establish a denuder test rig for quantitative analysis of the volatile Cr (VI) species evaporated from the high-Cr alloys supplied by the HEATSTACK project.
- II. To develop a better understanding of the influence of temperature (650, 750 and 850°C) and humidity level (1%, 3% and 9%) on the oxidation behaviour and Cr evaporation in the available high-Cr alloys;
- III. To develop a better understanding of the relationship between the alloying elements and the oxidation behaviour and Cr evaporation in high-Cr alloys exposed to simulated SOFC environment (850°C, 6.0 L/min air with 3% H<sub>2</sub>O);
- IV. To optimise the AluChrom 318 by a pre-treatment to obtain a better performance in simulated SOFC environment and to have a CAPH material ready for production for the HEATSTACK project.

Chapter 2 of this thesis reviews the studies that have been carried out on the corrosion behaviour and Cr evaporation of various high-Cr alloys exposed to high temperatures.

Chapter 3 presents the experimental methods employed in this study. Chapter 4 investigates the influence of temperature and water vapour on the corrosion behaviour and Cr evaporation of various high-Cr alloys. Chapter 5 compares the corrosion resistance and Cr retention capability of aluminised and alumina-forming alloys in simulated SOFC environment. Chapter 6 conducts microstructural analysis on the AluChrom 318 CAPH operated for 25,000 hours. Chapter 7 looks at the effect of pre-treatment on the performance of AluChrom 318. Finally, chapter 8 summarises the findings and conclusions from this work and presents suggestions for future work.

## **Chapter 2 – Literature Review**

This chapter provides an introduction to the fundamental principles of metal/alloy oxidation. Following this, the focus will be shifted to the high temperature oxidation of various chromia-forming alloys. The role of alloying elements such as Cr, Mn and Si on oxidation of the chromia-forming alloys is discussed. After that, this chapter elaborates the mechanisms for the oxidation of alumina-forming alloys from the following four aspects: 1) Al content, 2) alumina phases, 3) oxidation conditions (temperature and water content), and 4) reactive elements. Finally, this chapter highlights the formation mechanism of the volatile Cr(VI) species and their deleterious effect on SOFC cathode materials. Moreover, this chapter summarizes the different techniques used to quantify volatile Cr(VI) species evaporated from various alloys. Recent studies on quantifying Cr evaporation from various alloys are also outlined.

## 2.1 Principle of Oxidation

### 2.1.1 Oxide formation

Alloys are considered to be thermodynamically unstable in most environments. Various products can be formed on the alloy surface such as oxides [44], carbides [56], chlorides [57] and sulphides [58] depending on the exposure conditions [59]. One of the key factors dominating the oxide formation is temperature, as the reaction rate increases with temperature [60]. For the metallic material used for SOFC cathode air preheater applications, the corrosion process is generally related to high temperature corrosion in humidified air which can easily cause material failure. It is well-known that the oxidation resistance of an alloy strongly depends on the protective and well-adherent oxide scale formed on the surface of the alloy. The oxidation reaction between a metal (Mt) and oxygen (O<sub>2</sub>) can be presented as shown in equation 2.1 [61,62]. The feasibility of the chemical reaction at constant temperature and pressure can be determined based on the second law of the chemical reaction at constant temperature and pressure can be determined based on the second law of thermodynamics using Gibbs energy as expressed in equation 2.2.



$$\Delta G = \Delta H - T\Delta S \quad \text{Equation 2.2}$$

Where  $\Delta H$  is the change in enthalpy and  $\Delta S$  is the change in entropy. The  $\Delta G$  of a reaction is a measure of the thermodynamic force that makes a reaction occur. If the  $\Delta G = 0$  the reaction is in equilibrium,  $\Delta G > 0$  the reaction is non-spontaneous and if  $\Delta G < 0$  the reaction is spontaneous. Thus, the change in Gibb's free energy for reaction 2.1 is given by equation

$$\Delta G = \Delta G^\circ + RT \ln \left( \frac{a(Mt_xO_y)}{a(Mt)^x a(O_2)^{\frac{y}{2}}} \right) \quad \text{Equation 2.3}$$

Where  $\Delta G^\circ$  represent the change in free energy for all the species in their standard state (i.e., at standard temperature and pressure),  $T$  is the temperature,  $R$  is the universal gas constant, and  $a$  is the thermodynamic activity of a specific species. The activity of pure solids, in this case the metal and its oxide, can be approximated as unity. At equilibrium,  $\Delta G = 0$  and equation 2.3 can be written as

$$\Delta G^\circ = -RT \ln \left( \frac{1}{a(O_2)^{\frac{y}{2}}} \right) \quad \text{Equation 2.4}$$

And if the oxygen activity is approximated as oxygen partial pressure this becomes

$$pO_2 = \exp \left( \frac{2\Delta G^\circ}{yRT} \right) \quad \text{Equation 2.5}$$

Thus, knowing the Gibbs standard free energy of oxidation at a given temperature, it is easy to calculate the oxygen partial pressure needed for oxidation reaction to occur. Ellingham and Richardson constructed a diagram to represent the correlation between standard free energies of formation of oxides and temperature, as shown in Figure 2.1. These diagrams are usually known as Ellingham/Richardson diagrams and allow the oxygen pressure for oxide formation at any required temperature to be determined directly. This can be done by aligning the point  $O$  at the upper left of the diagram with the reaction and temperature of interest, and reading off the pressure on the scale on the right of the diagram. The Ellingham diagram defines the oxidation process using basic thermodynamic criterion. It simply tells whether a metal can be oxidized or not at a particular temperature and at a given pressure of oxygen [63]. In considering the oxidation of an alloy it is also useful to decide which components oxidise preferentially. This may be determined by comparing the free energies of oxide formation; the oxide with the most negative free energy of formation forms preferentially [64]. The Ellingham/Richardson diagram can also be used for comparison between the stability of different metals and oxides. The lower line is in the diagram the more stable is the oxide and consequently a metal is more stable the higher its line is in the diagram. It is clear from the

diagram that elements like aluminium, silicon and chromium that are near the bottom for unit activity of the metal, the oxides of these metals are more stable than the oxides of the elements above.

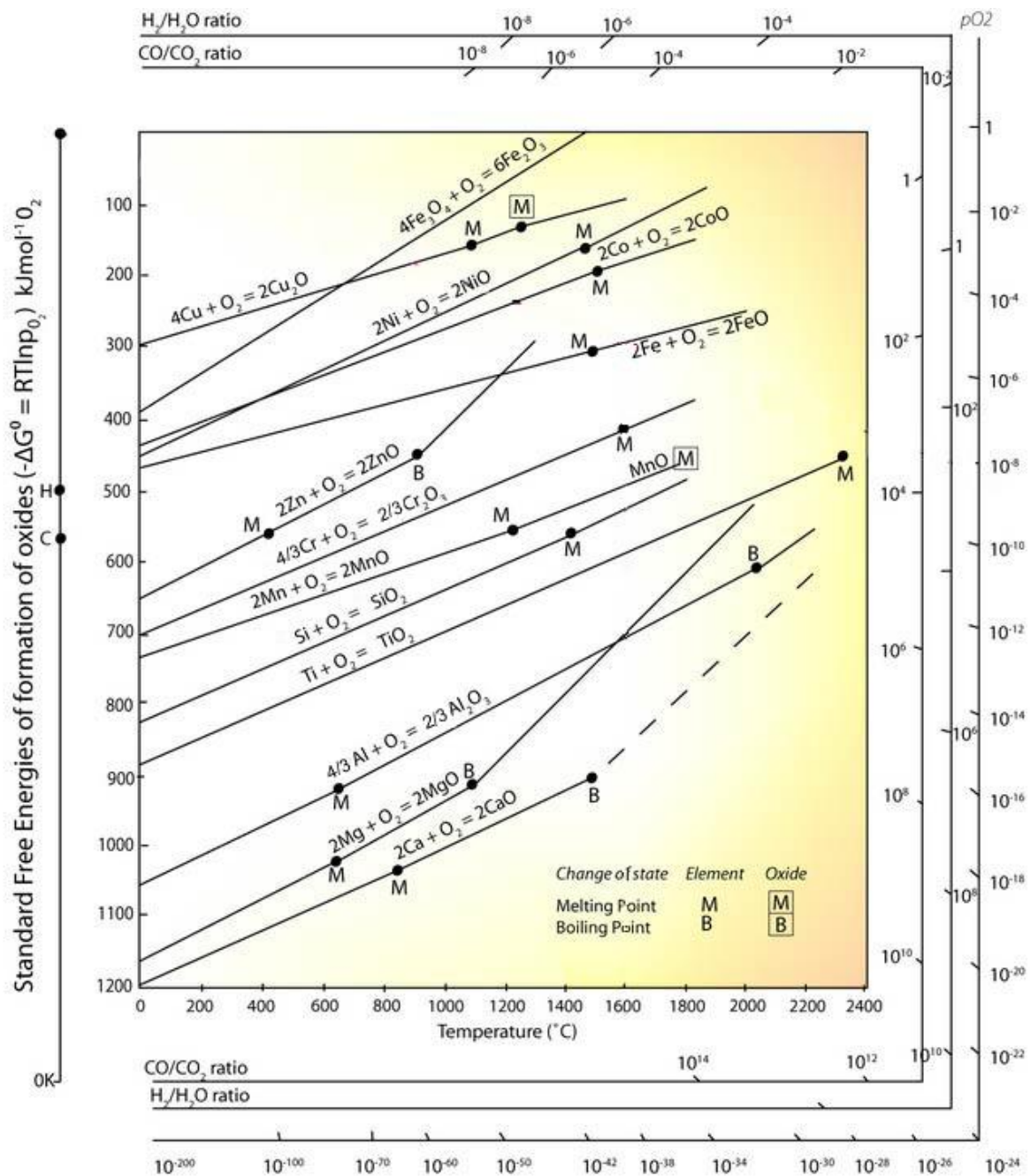


**Figure 2.1** Ellingham/Richardson diagram illustrating the formation of stable oxide for a given metal at a given temperature and oxygen partial pressure, taken from [65,66].

The oxidation process of a metal involves two steps. In the first step, the clean metal surface is exposed to an oxidising and high temperature environment with gas molecules such as  $\text{H}_2\text{O}$  or  $\text{O}_2$ . The oxygen molecule ( $\text{O}_2$ ) dissociates into oxygen atoms (O) and then adsorbs on the metal surface. During the second step, the adsorbed oxygen atoms start to reduce and attract electrons to form oxide nuclei on the surface of the metal. The individual oxide nuclei on the metal surface continuously grow and connect to each other until the entire metal surface is covered with an oxide film [67]. The oxygen adsorption and the initial oxide formation are determined by several factors such as crystal defects, temperature and surface preparation. The oxide film established in the second step serves as a diffusion barrier and separates the metal from the oxidising environment. For further oxidation of the metal in prolonged exposure, the oxygen or metal ions have to diffuse through the oxide layer by solid-state diffusion. Either the oxygen ions have to be transported through the oxide film to the metal/oxide interface or the metal ions have to diffuse through the oxide layer to the oxide/gas interface, depending on which ions (metal or oxygen ions) dominate the solid-state diffusion process through the oxide layer. Birks et al. [61] distinguished the growth of an oxide scale by anion migration and cation migration (Figure 2.2). Anion migration results in the oxide formation at the metal-oxide interface whereas cation migration results in the oxide formation at the oxide-gas interface as exhibited in Figure 2.2. In a thin oxide scale, the driving force for ion diffusion is the electric field across the oxide, while the gradient in the chemical potential is the driving force for ion transport in compact and thick oxide layers. Oxidation of alloys involves the same steps as described above for pure metals. For pure metals, for example when iron oxidises in air at a temperature above  $570^\circ\text{C}$ , it develops an oxide scale consisting of layers of  $\text{FeO}$  (Wustite),  $\text{Fe}_3\text{O}_4$  (magnetite), and  $\text{Fe}_2\text{O}_3$  (hematite) and, thus, offers a good example of the formation of multi-layered scales. Under a wide range of temperatures, nickel produces only one oxide,  $\text{NiO}$ , by the outward diffusion of electrons

and cations forming a single phase scale. Chromium also forms one oxide,  $\text{Cr}_2\text{O}_3$ , by outward diffusion of  $\text{Cr}^{3+}$  and therefore a single-layered scale with single phase is expected when pure chromium is oxidised. However, volatile species such as  $\text{CrO}_3$  can form at elevated temperatures, causing scale thinning. For aluminium, the only thermodynamically stable oxide is  $\alpha\text{-Al}_2\text{O}_3$  where scale growth is controlled by inward anion transport. However, a number of metastable aluminas such as  $\gamma\text{-Al}_2\text{O}_3$ ,  $\delta\text{-Al}_2\text{O}_3$ , and  $\theta\text{-Al}_2\text{O}_3$  sometimes form by cation outward diffusion on high-temperature alloys before the stable  $\alpha\text{-Al}_2\text{O}_3$  forms.

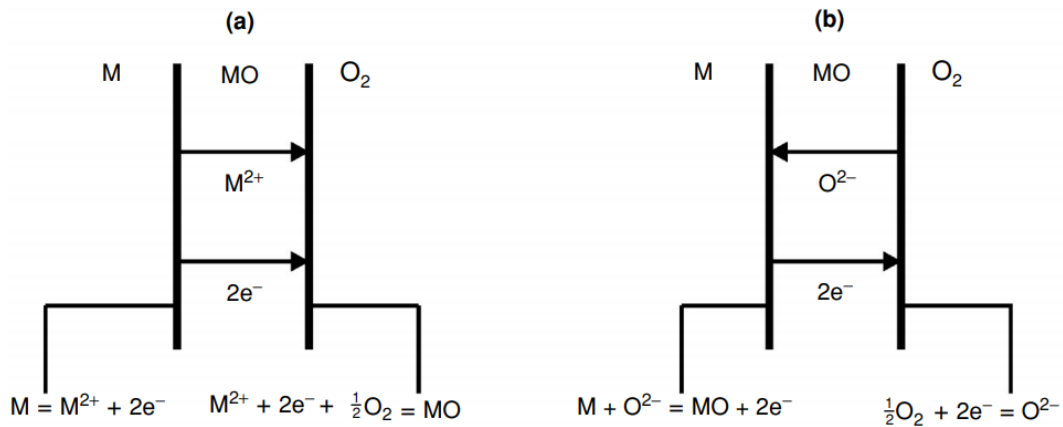


**Figure 2.2** Diffusion mechanism and interfacial reactions for high temperature alloy oxidation: (a) cation migration and (b) anion migration.

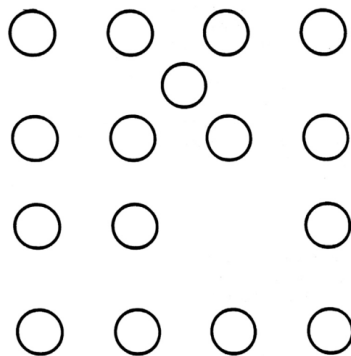


**Figure 2.3** A schematic showing an individual vacancy and interstitial defect in a single component crystal lattice.

### 2.1.2 Defects and diffusion

Considering the schematic of the inward and outward oxide growth processes exhibited in Figure 2.2, the inward or outward diffusion of neutral atoms or electrons and ions through the oxide film is the only way to continue the oxidation reaction since the oxide scale formed on the metal surface separates the metal from the oxidising environment. Solid-state diffusion involves the movement of individual particles (atoms or ions) that constitute the material. These particles are capable of movement because they vibrate around their mean positions, and due to the existence of defects in the solid crystal an occasional vibration could extend into a transmission to an available nearby lattice. Two common defects are illustrated in Figure 2.3 for the case of a pure, single component solid: a vacancy, or unoccupied lattice site, and an interstitial atom, i.e., one located between normal lattice sites. To understand why cation or anion transfer is predominant one must consider the type of defects existing in the oxide crystals. The oxide crystals consist of ordered arrays of oxygen anions and metal cations. Nevertheless, because of entropic forces, crystals have different types of defects depending on the properties of the elements they are made of. The defect structure of an oxide crystal strongly depends on oxygen partial pressure, temperature, and the energy of formation for a specific defect in the lattice. The defect type decides which type of diffusion mechanism will be predominant. Like semiconductors, oxides are divided into p- or n-type depending on the transport mechanism of electrical charge, as shown in Figure 2.4. n-type oxides carry electrical charges by electrons in the conduction band and p-type oxides by electron holes in the valence band.

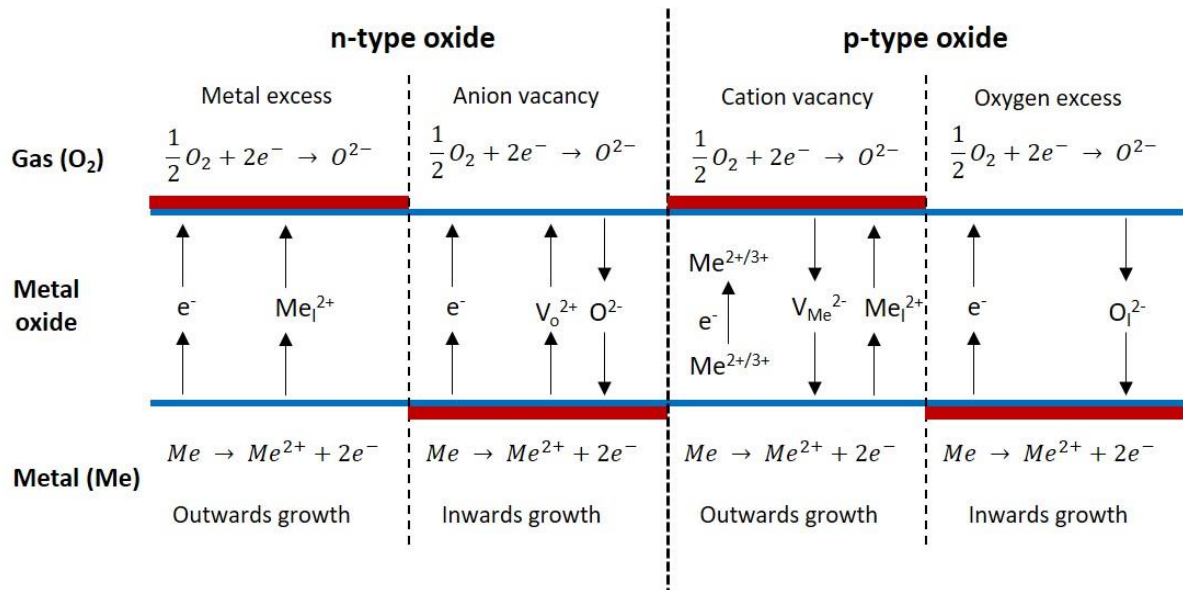


**Figure 2.4** Schematic of oxidation controlled by diffusion. Metal excess or vacancy leads to oxide growth at the oxide/gas interface. Oxygen excess or vacancies results in oxide growth at the metal/oxide interface [68].

n-type oxide semiconductors can be classified into two categories, i.e. oxygen deficient or excess metal but can also be a combination of both. Metal excess oxides have interstitial cations in the lattice that are compensated for by an equal charge of electrons in the conduction band. Cations can therefore be conducted via the lattice by changing interstitial sites. n-type oxides can also exist as oxygen vacancies leading to positive charges, that also are compensated for by electrons in the conduction band. ZnO is a typical n-type cation-excess semiconductor, i.e., having interstitial Zn ions and electrons within the conduction band. p-type oxide semiconductors can have excess oxygen or metal deficit resulting in negative charges that are compensated for by electron holes in the valence band. Excess ions, i.e. interstitial ions, can transport through the oxide by changing interstitial sites. Ion vacancies can also diffuse in the lattice resulting in conduction of the vacant ion species. NiO has been concluded to be a metal deficient p-type semiconductor, with nickel vacancies as the predominating defects [69].

The high-temperature oxidation of Ni at temperatures above 1100°C follows a parabolic rate law. The oxidation rate is governed by outward lattice diffusion of Ni via singly or doubly charged Ni vacancies [69]. However, at intermediate temperature, the growth rate predicted from lattice diffusion and the Wagner theory is usually several orders of magnitude slower than is actually observed (e.g. NiO, Fe<sub>3</sub>O<sub>4</sub>, Cr<sub>2</sub>O<sub>3</sub>, and Al<sub>2</sub>O<sub>3</sub>). This can be explained by short-circuit diffusion. The term ‘short-circuit diffusion’ always embraces diffusion of metal or oxygen ions via extended defects in the oxide scale rather than through the crystal lattice in the bulk scale, so that it includes diffusion along dislocations, grain boundaries, cracks and other features such as interconnected porosity [70]. Previously, the rates of growth of NiO, ZrO<sub>2</sub>, Cr<sub>2</sub>O<sub>3</sub> and Al<sub>2</sub>O<sub>3</sub> scales were all believed to be influenced by short-circuit diffusion of some kind or other. The evidence for the participation of the short-circuit process was, however, of qualitative nature. For example, the rate of growth of the scale is observed to be much faster than expected from measured bulk diffusion coefficients.

Grain boundary diffusion is often more important than lattice diffusion at low temperature (500 to 1000°C) [70]. A principal reason for this is the lower activation energy of the boundary process, corresponding to the more disordered structure in the boundaries. The experiments performed by Atkinson et al. have shown that the oxidation of nickel is controlled by the diffusion of nickel along grain boundaries for temperatures below about 1100°C [70]. The measurement of transport in a growing Cr<sub>2</sub>O<sub>3</sub> scale, using <sup>16</sup>O/<sup>18</sup>O-exchange measurements, indicated that growth was primarily by Cr ions moving outward along grain boundaries [71]. Extensive studies of Al<sub>2</sub>O<sub>3</sub> reviewed that the metastable aluminas grow primarily by outward diffusion of cations, while  $\alpha$ -Al<sub>2</sub>O<sub>3</sub> grows mainly by inward migration of oxygen ions along oxide grain boundaries [72]. The protection afforded by the Al<sub>2</sub>O<sub>3</sub> scales arises from the sluggish diffusion kinetics of both O and Al; lattice

diffusion is so slow that scale formation kinetics are dominated by grain boundary diffusion [73]. Heuer et al. [74] stated that the growth of  $\text{Al}_2\text{O}_3$  scales occurs entirely by grain boundary diffusion, and is particularly interesting for NiCrAl and FeCrAl alloys lacking reactive element addition, where simultaneous inward diffusion of O and outward diffusion of Al is known to occur [74]. Because  $\alpha\text{-Al}_2\text{O}_3$  does not measurably deviate from stoichiometry, its native defect concentration is extremely low and self-diffusion is very slow [44].

### 2.1.3 Oxidation kinetics

The mass change measurement is the most common method to investigate the oxidation rate and predict lifetime of an alloy. Based on the experimental data, the oxidation rate can be presented in three common growth mechanisms, namely, linear law, parabolic law and logarithmic law [61], as shown in Figure 2.5:

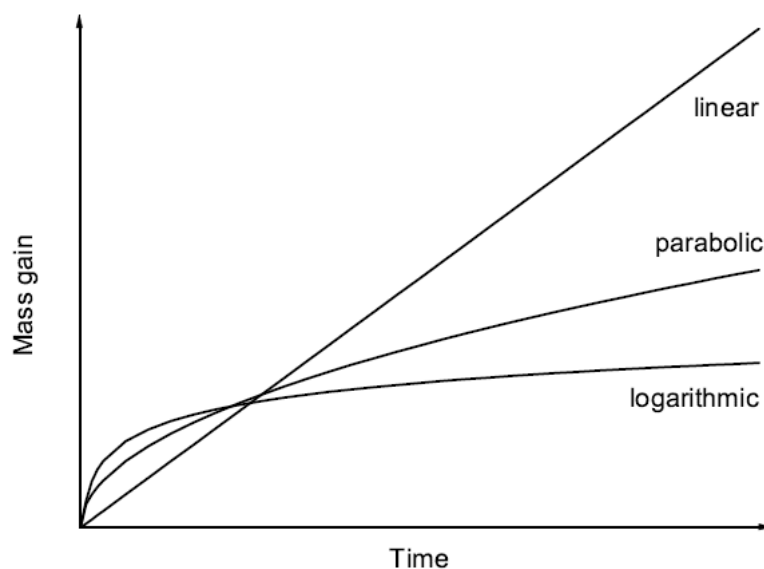


**Figure 2.5** The oxidation kinetics of three common growth mechanisms.

The reaction rate of the linear mechanism stays constant in time and is independent of metal consumption and oxygen intake. The linear oxidation mechanism is generally detected under the condition where a phase boundary process (oxygen atom absorption) is the rate-determining step for the reaction [61]. This always occurs during the initial stage of the oxidation process when the clean metal surface is directly exposed to an oxidising environment. Under this condition, the diffusion through the scale is very fast and cannot be the rate controlling step because the initial scale formed is very thin. The oxide scale shows no barrier effect when the linear law is dominant in the mass gain curve. The linear kinetics can be described as in equation 2.6:

$$x = k_1 t \quad \text{Equation 2.6}$$

where  $k_1$  is the linear rate constant (cm/s),  $x$  is the thickness of the oxide scale in cm, and  $t$  is the exposure time in s.

It was mentioned above that constant rate kinetics are usually detected with thin scales. However, when the oxidation of a metal or alloy proceeds at a constant rate the scale thickness increases. Therefore, the oxidation reaction rate must be equivalent to the diffusion rate of ions across the scale. However, with a further increase in the scale thickness, the migration of ions across the oxide layer eventually becomes slower than the constant phase boundary reaction rate and turns into the rate-controlling process [61]. The oxidation rate then decreases with time according to a parabolic rate law. It is, therefore, possible for the growth of a scale to be controlled by a phase boundary reaction in the early stage and by solid state diffusion in the later. The basic assumption of parabolic oxidation behaviour is that the diffusion of metal ions, oxygen ions or electrons through the oxide layer is the rate-determining process [61]. The parabolic mechanism displays a reaction rate which is inversely proportional to the square root of time, and can be described as in equation 2.7:

$$x^2 = 2k't \quad \text{Equation 2.7}$$

where  $k'$  with the unit of  $\text{cm}^2 \text{s}^{-1}$  represents the scaling constant, and the square of oxide scale thickness  $x$  is proportional to the exposure time  $t$ . The detected kinetics of this rate decreases with time according to a parabolic rate law due to the increased diffusion path (scale thickness). The parabolic law is the optimal oxidation behaviour for alloys since the surface oxide scale growth is slow and so is unlikely to spall.

The logarithmic mechanism represents a typical oxidation behaviour of a number of alloys exposed at low temperatures (normally below 300 to 400°C) [61] and the oxide scale formed usually has an extremely low thickness [75]. As can be seen in Figure 2.5, the reaction rate is fast initially and then dramatically drops down to a very low level. The rate-determining step of the oxidation process following the logarithmic law can be potentially explained by the ions or electrons diffusing due to an electric field across the oxide scale [61]. The logarithmic kinetics can be described as in equations 2.8 and 2.9:

$$\text{Direct log law: } x = k_{\log} \log(t + t_0) + A \quad \text{Equation 2.8}$$

$$\text{Inverse log law: } \frac{1}{x} = B - k_{il} \log(t) \quad \text{Equation 2.9}$$

where  $k$ ,  $k_{il}$ ,  $A$ ,  $B$  and  $t$  are constant in isothermal condition.

#### 2.1.4 Selective oxidation

The oxidation process of an alloy is more complicated than that for the pure metals due to the multiple elements present in alloys. It is worth noting that the type of oxide formed on the surface depends on the relative proportion among the alloying elements, their affinity to oxygen and their potential to diffuse [76,77]. Different metal oxides possess different growth rates in the same oxidising environment, meaning that the element with the most negative

free energy always overgrows the others. An alloy needs to produce a continuous oxide scale to cover the entire surface via external oxidation in order to obtain effective oxidation resistance. However, the internal oxidation of alloys, which has a detrimental effect on the oxidation protection, generally occurs by the inward oxygen diffusion into an alloy to form the sub-surface precipitates [78]. Therefore, the formation of a compact oxide scale with a low diffusion rate is necessary for the alloys to acquire effective oxidation resistance.

The protective property of an alloy is offered by the selective oxidation of high concentration alloy elements presented in the alloy such as Al, Cr, or Si which preferentially oxidise to the parent element and produce a continuous scale on the alloy surface [79]. From a thermodynamics perspective, a higher oxygen affinity is necessary for the desired oxides in comparison with other elements in the alloy. From kinetics perspective, a relatively slow growth rate is expected from the desired oxide scale. Selective oxidation can be affected by various factors, such as the oxygen partial pressure, temperature and concentration of active element in the alloy. Selective oxidation allows the design of a high temperature alloy to have more than one alloying element so as to improve the resistance to high temperature corrosion. Based on thermodynamic theory, the order of Fe-Cr-Al-Si-Mn alloy oxidation products is:  $\text{Al}_2\text{O}_3 > \text{SiO}_2 > \text{MnO} > \text{Cr}_2\text{O}_3 > \text{Fe}_3\text{O}_4 > \text{Fe}_2\text{O}_3$ , indicating the affinity between oxygen and the elements. However, the final oxidation behaviour is also related to the content of alloy elements and kinetics [79]. During the initial stage of the oxidation process, all the elements presented in the alloy will oxidise and the elemental composition of the formed oxide scale during the initial phase will be same as that present in the alloy. The formation of these transient oxides during the initial stage will lead to a decrease in the oxygen activity at the metal/oxide interface, thereby allowing the continuous growth of the more stable oxide. The ability of the alloy to maintain this stable oxide scale in the long-term relies on its element

reservoir and its ionic diffusion rate for further oxidation. However, certain alloying elements such as aluminium, that improve the oxidation resistance, always show a negative effect on other alloy properties, especially mechanical strength, if the concentration exceeds a critical limit [72]. Thus, in this case, the concentration of the added elements should be controlled within the appropriate range in order to achieve the optimum performance for the alloy.

As mentioned before, aluminium, chromium and silicon are three common additive elements that form protective layers on the surface of an alloy because their oxides (alumina, chromia and silica) show the lowest diffusion rate of ions [60]. It is well known that iron-, nickel-, and cobalt-based alloys are the most commercial heat resistant alloys. High temperature alloys usually form two or more oxides on the surface, and the oxides exhibit a great difference in their stability. Elements such as nickel, iron or cobalt present in the alloy can produce a moderately stable oxide, while elements such as aluminium, chromium and silicon can form a highly stable oxide in high temperature environment. Many high-temperature alloys are designed to form a protective  $\text{Cr}_2\text{O}_3$  scale. However, the volatility of chromia in a humidified environment at high temperature has restrained the use of chromia-forming alloys in SOFC. The alumina scale usually offers effective protection to the alloy due to its chemical inertness, great adherence and much slower growth rate compared to other oxides. Opila *et al.* [80] has proven that alumina volatility by  $\text{Al}(\text{OH})_3$  formation is not expected to be an issue below  $1300^\circ\text{C}$  for long-term applications. Generally, silica is not employed as protective scale for structural alloys since Si tends to embrittle most alloys.

## 2.2 Oxidation of chromia-forming alloys

### 2.2.1 Effect of Cr content

High-Cr alloys usually provide corrosion resistance by producing a continuous  $\text{Cr}_2\text{O}_3$  layer. Concerning Fe- and Ni-based alloy, it was suggested that the critical minimum Cr content to ensure the formation of a protective, continuous  $\text{Cr}_2\text{O}_3$  scale is approximately 20-25 wt.% chromium. A model binary alloy of Fe-28Cr formed an external scale of  $\text{Cr}_2\text{O}_3$  alone when reacted with oxygen at  $900^\circ\text{C}$  [42]. However, when the alloy chromium content was too low, this protective layer did not form. A model alloy of Fe-7.5Cr reacted with oxygen at  $850^\circ\text{C}$  to form a fast growing, iron-rich scale [42]. It should be noted that alloys with low Cr content have also been tested as interconnects in SOFC applications. However, the corrosion resistance was dramatically reduced under high temperatures when the Cr content was low in the alloy [81]. Geng et al. [38] studied the corrosion behaviour of a Fe-Co-Ni base alloy, containing 6 wt.% Cr, at  $800^\circ\text{C}$  in air for 12 weeks and found that a double-layered structure with a Cr-free spinel outer layer and a thin  $\text{Cr}_2\text{O}_3$  inner layer was formed on the alloy surface. However, the initial oxidation rate of this low chromium Fe-Co-Ni alloy was found to be much higher than that of Crofer 22 APU with 22 wt.% of Cr. Yang et al. [82] tested the effect of Cr content on the oxidation performance of three commercial Ni-Cr-base alloys (Haynes 230: 22 wt.%Cr, Hastelloy S: 16 wt.%Cr, and Haynes 242: 12 wt.%Cr) in moist air at high temperature. The results they obtained showed that Hastelloy S and Haynes 230 with relatively high concentration of Cr formed a thin scale mainly consisting of  $\text{Cr}_2\text{O}_3$  and  $(\text{Mn,Cr,Ni})_3\text{O}_4$ . This duplex scale offered excellent corrosion resistance. While Hyanes 242 developed a thick duplex scale comprised of a NiO outer layer over a chromia-rich inner layer, indicating limited corrosion resistance in the cathode environment of SOFC. The formation of a NiO top layer over a mixed  $\text{Cr}_2\text{O}_3/(\text{Mn,Cr,Ni})_3\text{O}_4$  inner layer on Haynes 242

was also detected by Liu and Zhu [83] after exposing the sample at 800 °C in air for 1000 hours. Zhu et al. [84] investigated the oxidation behaviour of two low-Cr alloys, namely Thermo-Span (5.5 wt.% Cr) and HRA 929C (2.0 wt.% Cr), and it was observed that a double-layered  $\text{CoFe}_2\text{O}_4/\text{Cr}_2\text{O}_3$  was formed on the Thermo-Span surface after three weeks of thermal exposure at 800°C in air, while only a single  $\text{CoFe}_2\text{O}_4$  spinel layer formed on HRA 929C. Obviously, the corrosion resistance of these two low-Cr alloys was not acceptable for SOFC applications since the weight gains increased linearly with exposure time, which was much higher than the weight gain of Crofer 22 APU as reference sample.

In addition to the formation of a continuous  $\text{Cr}_2\text{O}_3$  scale, this critical quantity of chromium is also necessary to prevent the spallation of the oxide scale and minimise internal oxidation due to the exhaustion of the chromium reservoir at the sub-surface [72]. Cheng et al. [85] studied the isothermal oxidation behaviour of three ferritic stainless steels, 430 (Cr: 16.2 wt.%, Mn: 0.4 wt.%), 443 (Cr: 21 wt.%, Mn: <0.1 wt.%) and 445 (Cr: 21.5 wt.%, Mn: 0.15 wt.%) at 1150°C in humid air. The breakaway oxidation of these three alloys occurred rapidly for 430 and 443 or slowly for 445 during the test duration. For stainless steels, reaching the breakaway oxidation point implied the loss of the protective  $\text{Cr}_2\text{O}_3$  scale with continuous and fast growth of non-protective  $\text{Fe}_2\text{O}_3/\text{Fe}_3\text{O}_4$ . XRD confirmed that the surface oxide of the 430 and 443 steels were primarily  $\text{Fe}_2\text{O}_3$ , while a  $\text{Cr}_2\text{O}_3/(\text{Cr,Mn})_3\text{O}_4$  multi-layer scale was detected on the 445 steel. The authors stated that the chemical failure of 430 was caused by a chromium concentration gradient across the specimen section that was below what was needed to generate a protective chromia layer. Yu et al. [86] investigated the corrosion behaviour of an austenitic stainless steel (Fe-20Ni-14.9Cr-1.54Mn) in  $\text{O}_2+10\% \text{H}_2\text{O}$  at 800°C. The breakaway oxidation took place after only 15 hours exposure. A multi-layer scale of steel/ $(\text{Cr,Fe})_2\text{O}_3/\text{Mn}(\text{Fe,Cr})_2\text{O}_4$  was formed on the steel surface in the initial oxidation, and

then turned into steel/  $\text{Ni}(\text{Fe,Cr})_2\text{O}_4/\text{Fe}_2\text{O}_3$  due to Cr depletion in further oxidation. Continuous transport of Fe into the  $\text{Cr}_2\text{O}_3$  scale can lead to the linear growth of a porous  $\text{Fe}_2\text{O}_3$  external scale that is prone to thickening [85,87,88]. For CAPH application, thickening of the external Fe-rich oxide will have negative influence on the heat transfer across heat exchanger plates and will behave as a thermal barrier coating [89]. The magnitude of the thermal insulating effect of the thick Fe-rich oxide has been studied by Ennis and Quadackers [90]. Figure 2.6 shows the correlation between the oxide scale thicknesses on the inside surface a tube and the increase in the tube temperature resulting from the thermal insulation effect of the oxide. It was found that the thermal insulation effect of a thick oxide scale which decrease the heat transfer across the component can lead to overheating of material. A small increase in the operating temperature of the component will dramatically reduce the stress rupture life [90].

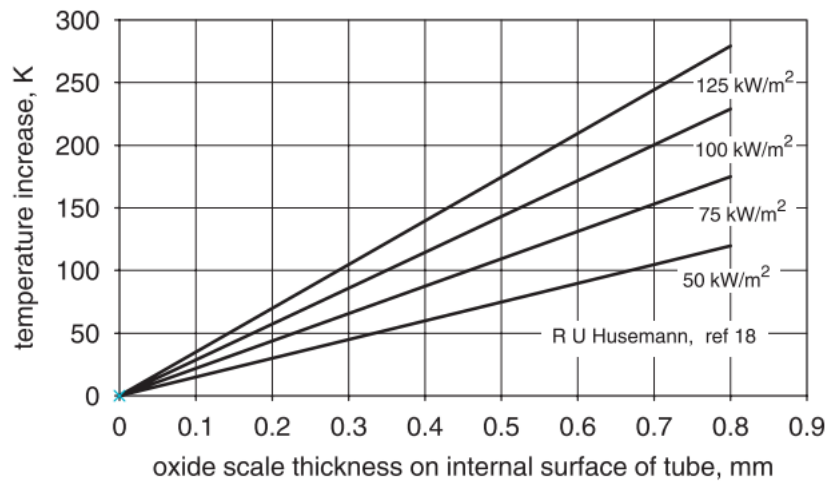


**Figure 2.6** The influence of oxide scale on the temperature increase across a heated tube wall for different power ratings [90].

### 2.2.2 Effect of Mn content

As mentioned before, during the operation of SOFC, the CAPH will face an oxidising environment with the presence of water vapour. The chromia-forming alloy is susceptible to

chromium leakage by reacting with oxygen and/or steam to produce the volatile chromium species ( $\text{CrO}_2(\text{OH})_2$  or  $\text{CrO}_3$ ). An alternative way for reducing Cr evaporation is to develop new alloys by modifying the composition of the conventional Ni- or Fe-based stainless steels. The addition of a small amount of Mn facilitates the formation of a  $(\text{Mn,Cr})_3\text{O}_4$  spinel scale on the top of an inner  $\text{Cr}_2\text{O}_3$  or  $\text{Cr}_2\text{O}_3$ -rich scale. Mn is considered to be soluble in  $\text{Cr}_2\text{O}_3$ , up to a limit of 1.6% of the cation site at  $1000^\circ\text{C}$  [91]. Cox et al. [92] showed that  $\text{Mn}^{2+}$  diffuses faster than  $\text{Cr}^{3+}$  in a  $\text{Cr}_2\text{O}_3$  lattice. This faster diffusion of  $\text{Mn}^{2+}$  led to the rapid growth of a fine, continuous chromia matrix during the early stage of oxidation. The formation of  $\text{MnCr}_2\text{O}_4$  can be understood from the following reactions [44]:



The formation of this  $(\text{Mn,Cr})_3\text{O}_4$  spinel scale is highly desirable and has been widely researched for SOFC application with humid air environment (cathode) as it can dramatically decrease the oxidation and Cr evaporation rates compared to the pure chromia scale. This is due to the lower partial pressure of Cr in  $(\text{Mn,Cr})_3\text{O}_4$  spinel than that for the pure  $\text{Cr}_2\text{O}_3$  [38]. Some new high-temperature alloys such as Sanergy [93], Crofer 22 APU [94] or ZMG232 [95] provide enhanced corrosion resistance due to the formation of a  $(\text{Mn,Cr})_3\text{O}_4$  spinel at elevated temperatures. Yang et al. [96] showed the formation of a layered oxide scale comprised of a  $\text{Cr}_2\text{O}_3$ -rich sublayer and a  $(\text{Mn,Cr})_3\text{O}_4$  spinel top layer on Crofer 22 APU after oxidation at  $800^\circ\text{C}$  for 1200 hours in air, as shown in Figure 2.7. Figure 2.8 schematically shows the morphology of scales formed on Ni-based alloys at high temperature, which usually consist of an outer layer of essentially  $\text{Cr}_2\text{O}_3$ , with some  $\text{MnCr}_2\text{O}_4$  and traces of Ni [89]. England et al. [97,98] studied the oxidation kinetics of thin foils of Haynes 230 in humidified hydrogen and air at temperatures between  $700$  and  $1000^\circ\text{C}$  for up to 10,000 hours.

It was found that  $\text{Cr}_2\text{O}_3$  and  $\text{MnCr}_2\text{O}_4$  were formed in both atmospheres following the parabolic law.

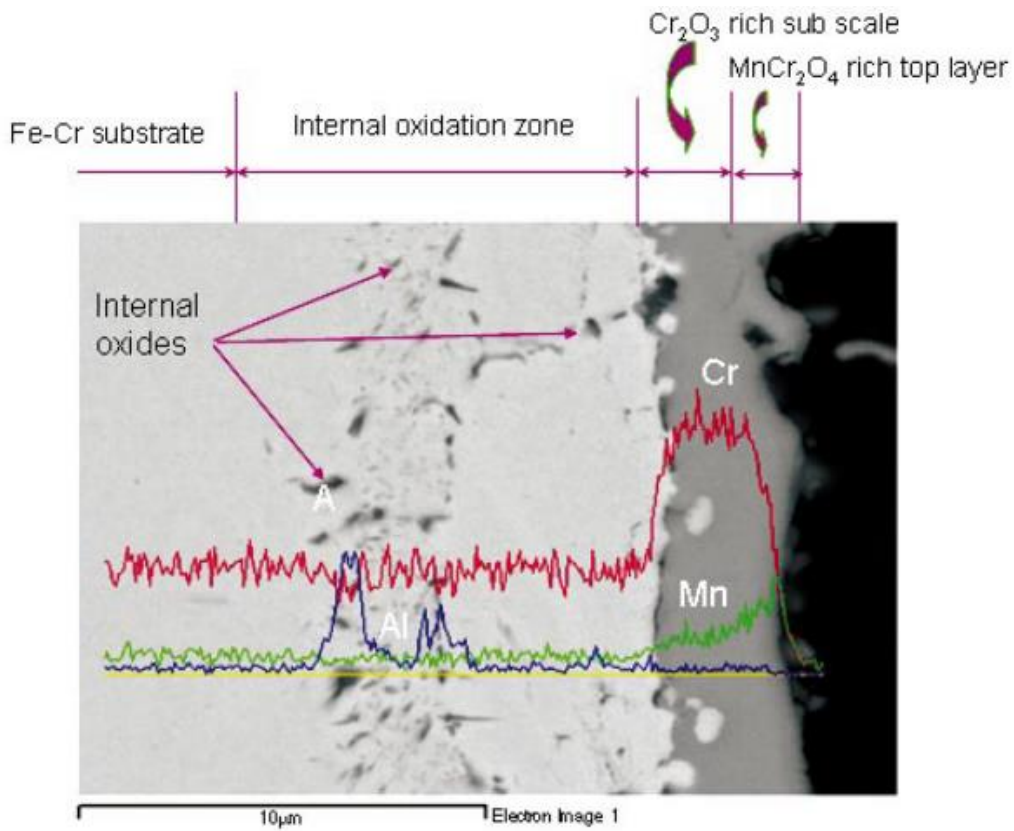


**Figure 2.7** SEM cross-section and EDX line scan of Crofer 22 APU after oxidation in air for 1200 hours at 800°C [96].

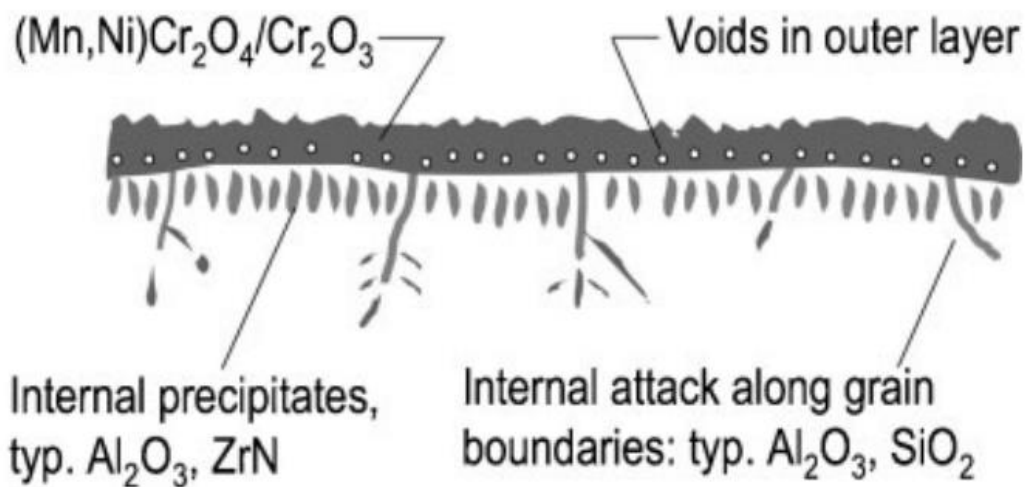


**Figure 2.8** Schematic of oxide structures formed on Ni-based alloys oxidised in humid environment [89].

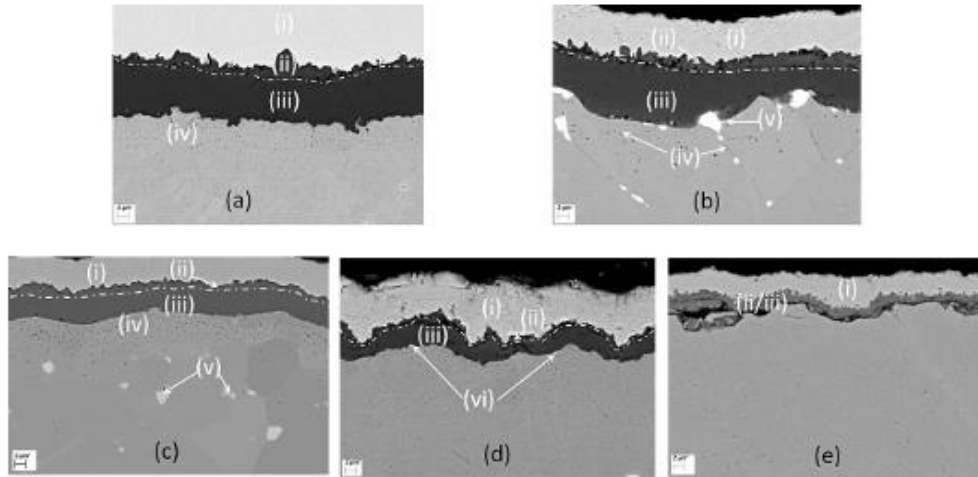


**Figure 2.9** SEM cross-section of (a) Crofer 22 APU, (b) Corfer 22 H, (c) Sanergy HT, (d) ZMG232 and (e) E-Brite after oxidation in 3% H<sub>2</sub>O humidified air at 850°C for 1000 hours. In the figure: (i) Ni coating; (ii) (Cr,Mn)<sub>3</sub>O<sub>4</sub> spinel; (iii) Cr<sub>2</sub>O<sub>3</sub>, (iv) internal Ti-oxide and (v) Laves phase [99].

The content of Mn in the alloy has a remarkable influence on the protective property of the formed spinel scale. Smaller amounts of Mn would result in lower reductions in chromia activity, but would still be beneficial. Too much Mn can be detrimental from an oxidation and physical property point of view. Sachitanand et al. [99] examined the oxide system formed on five Fe-Cr alloys with different Mn content: E-Brite (Mn: 0.08 wt.%), ZMG232 G10 (Mn: 0.28 wt.%), Sanergy HT (Mn: 0.3 wt.%), Crofer 22 H (Mn: 0.42 wt.%), and Crofer 22 APU (Mn: 0.48 wt.%) at 850°C in simulated SOFC cathode conditions (6.0 L/min air + 3 vol% H<sub>2</sub>O). The authors found that all studied alloys developed an inner Cr<sub>2</sub>O<sub>3</sub> scale and an outer (Cr,Mn)<sub>3</sub>O<sub>4</sub> spinel scale, as shown in Figure 2.9. However, the outer spinel scale formed on E-brite was thin and discontinuous due to an insufficient supply of Mn, leading to high Cr evaporation and severe corrosion. They stated that a higher concentration of Mn in the alloy led to a thicker and more Mn-rich spinel scale which could effectively reduce the oxidation and Cr evaporation rate. Hua et al. [100] studied the oxidation behaviour of four Fe-17Cr alloys with Mn concentrations of 0.0, 0.5, 1.0 and 3.0 wt.% at 750°C for 700 hours

in dry air. They found that the corrosion rate and scale thickness of the Fe-17Cr-xMn alloys increased with the content of Mn in the alloy. The oxide scales formed on the alloys with different content of Mn are shown in Figure 2.10. The results indicated that a single pure  $\text{Cr}_2\text{O}_3$  layer formed on the Fe-Cr-0Mn alloy; a double-layered scale comprised of an outer  $(\text{Mn,Cr})_3\text{O}_4$  and an inner  $\text{Cr}_2\text{O}_3$  scale developed on the Fe-Cr-0.5Mn alloy; a triple layered oxide scale with  $(\text{Mn,Cr})_3\text{O}_4$  between the inner  $\text{Cr}_2\text{O}_3$  and outer  $\text{Mn}_2\text{O}_3$  formed on the Fe-Cr-1.0Mn alloy; a duplex oxide scale with  $\text{Mn}_2\text{O}_3$  on top of  $(\text{Mn,Cr})_3\text{O}_4$  formed on the surface of Fe-Cr-3.0Mn alloy. With further increase of Mn content, Mn-rich oxides, such as  $\text{Mn}_2\text{O}_3$  and  $\text{Mn}_3\text{O}_4$ , form on the outermost surface of the Fe–Cr alloys, resulting in a higher oxidation rate and oxide scale spallation, as reported by Stott et al. [101] and Marasco and Young [102]. These results suggest that the oxidation behaviour and scale microstructure were sensitive to the Mn content in the alloys. Cheng et al. [85] stated that alloys containing 0.3 to 0.5 wt.% of Mn form a compact and well-adherent  $(\text{Cr,Mn})_3\text{O}_4$  spinel outer layer on top of the  $\text{Cr}_2\text{O}_3$  layer at 800 and 850°C, and that the Cr evaporation rate was 2 to 3 times lower than with those stainless steels that developed a discontinuous  $(\text{Cr,Mn})_3\text{O}_4$  layer or pure  $\text{Cr}_2\text{O}_3$  scale.

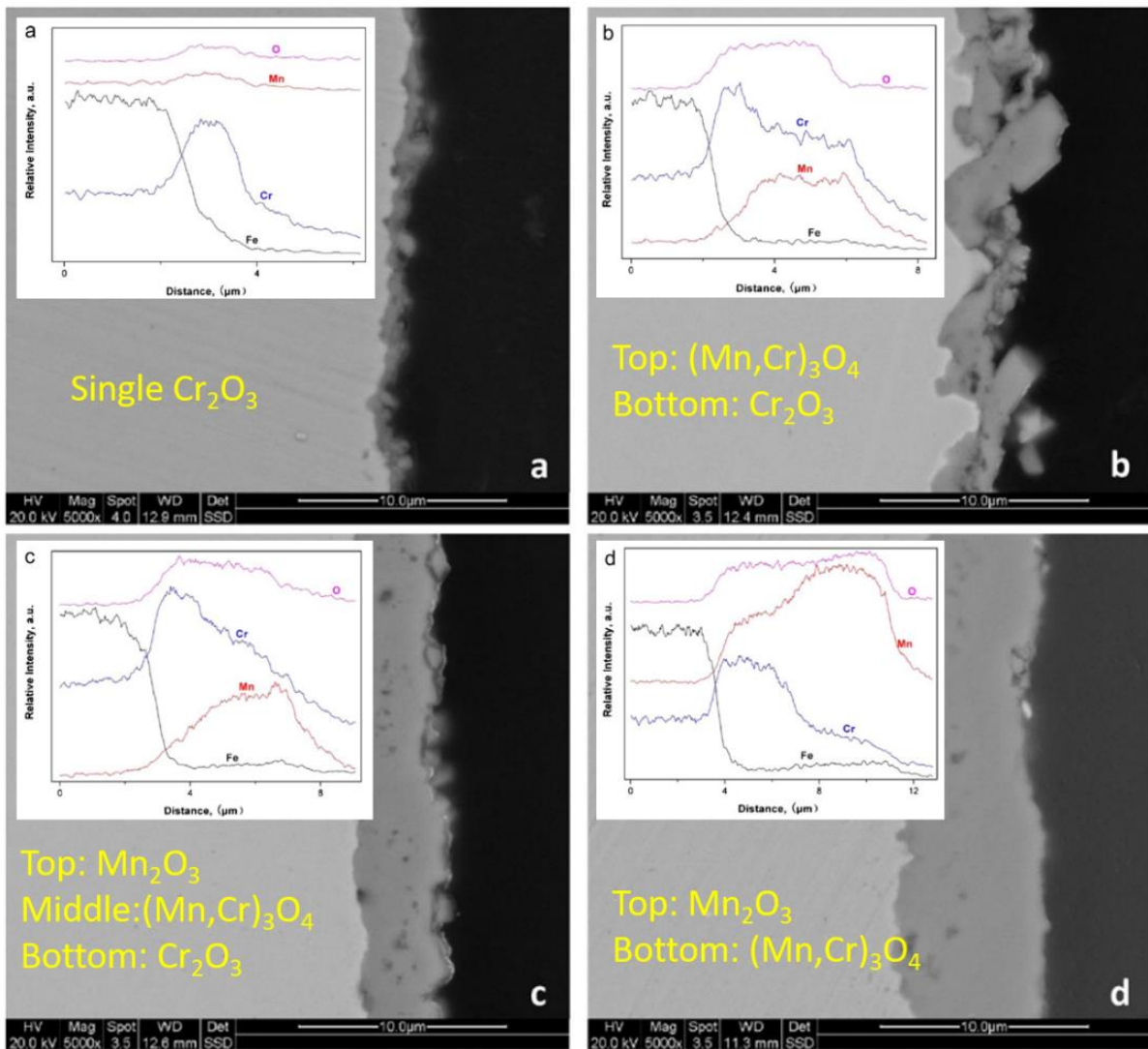


**Figure 2.10** SEM cross-section images of the Fe-Cr-xMn alloys: (a) 0.0 Mn, (b) 0.5 Mn, (c) 1.0 Mn and (d) 3.0 Mn oxidised in air for 100 hours at 750°C [100].

### 2.2.3 Effect of Si content

The majority of Fe-Cr alloys capable of developing a chromia scale as protective scale usually contain a small amount of Si. The SiO<sub>2</sub> layer that forms on the Fe-Cr alloys during high temperature exposure generally has long range atomic disorder and is amorphous [103]. The amorphous SiO<sub>2</sub> precipitates usually lack grain boundaries and have a low density of defects [104]. The combination of these two features contributes significantly to impede the outward diffusion rate of the oxide forming elements via the inner SiO<sub>2</sub> scale, thereby leading to a decrease in the overall corrosion rate. It has been proven that the addition of Si can

effectively reduce the parabolic rate constant during high temperature oxidation as it forms a silica ( $\text{SiO}_2$ ) barrier layer beneath the  $\text{Cr}_2\text{O}_3$  scale [105–109]. Mahboubi et al. [110] studied the oxidation behaviour of Type 319 and Type 310 alloys in a flowing ambient pressure (0.1 MPa) air-10%  $\text{H}_2\text{O}$  mixture at  $800^\circ\text{C}$ . They found that a high Si concentration (5.9 wt.%) in the Type 309 alloy led to a lower mass loss and parabolic rate constant during wet oxidation by producing a continuous  $\text{SiO}_2$  layer at the scale/metal interface compared to the low-Si Type 310 stainless steel.  $\text{SiO}_2$  usually forms at the scale/metal interface by oxygen anion inward diffusion due to the relatively slow diffusion rate of Si in alloys. Depending on the exposure condition and Si content, the  $\text{SiO}_2$  can form as either a continuous layer [110] (Figure 2.11a) or a non-continuous layer (precipitates) [111] (Figure 2.11b) at the scale/metal interface. It has been argued that the microstructure of the  $\text{SiO}_2$  inner scale plays a pivotal role in offering corrosion protection, with a continuous layer serving to decrease the outer diffusion rate of metal cations to a greater extent than a non-continuous  $\text{SiO}_2$  layer [112]. If the steel contains Si in amounts greater than 0.5 wt.%, insulating, continuous, or network-like films of silica also grow under the chromia-rich scale. However, the establishment of a continuous  $\text{SiO}_2$  layer has been considered to be detrimental to corrosion resistance by triggering scale spallation. Proposed reasons include a large Pilling-Bedworth ratio of 2.15 for  $\text{SiO}_2$ , one would expect considerable stresses to be developed which could cause the oxide to crack or spall [106,113]. Furthermore, the thermal expansion coefficient of  $\text{SiO}_2$  is much lower than that of  $\text{Cr}_2\text{O}_3$ , resulting again in a tendency for scale spallation of multi-layered scales exposed to thermal cycling [104]. Sachitanand et al. [99] attributed the poor adhesion of the duplex  $\text{Cr}_2\text{O}_3/(\text{Cr,Mn})_3\text{O}_4$  scale formed on E-Brite surfaces to the formation of a low TEC silica layer after exposure in humidified air at  $850^\circ\text{C}$  for 1000 hours.

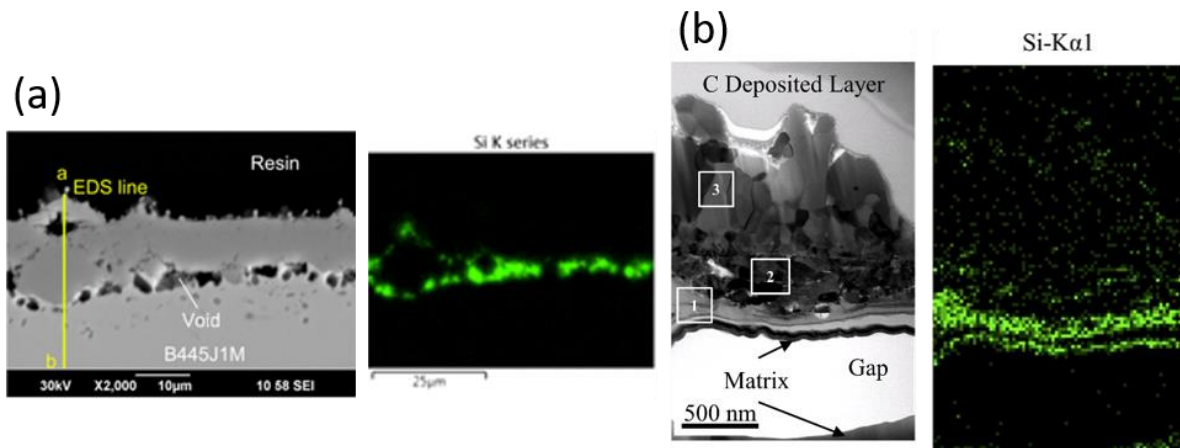


**Figure 2.11** (a) Cross-section SEM image of the thin oxide scale for the B445J1M steel oxidised at 1200°C for 2 hours in air with the EDS element map of Si [110]; (b) BF-STEM cross-section of the oxide scale formed on Type 310 after exposure in 0.1 MPa air + 10% H<sub>2</sub>O at 800°C for 500 hours with the STEM-EDS element map of Si [111].

## 2.3 Oxidation of alumina-forming alloys

### 2.3.1 Fe-Cr-Al based alloys

Alloys with more than 15% of chromium and a critical minimum of 3% aluminium content are defined as alumina formers [37]. The excellent barrier effect from alumina-forming alloys is attributed to the formation of a highly protective and slowly growing  $\alpha$ -Al<sub>2</sub>O<sub>3</sub> outer layer [114,115]. Alumina-forming alloys have been employed to establish interconnect components in SOFC stacks in which the insulating Al<sub>2</sub>O<sub>3</sub> layer does not lie in the current path, such as sealing materials [116]. For the BOP components in SOFC, alumina-forming alloys have been recognised as promising materials for pumps, casting, piping and heat exchangers [29,117–119]. Jönsson et al. [120] concluded that the formation of the adherent alumina layer during exposure offered great resistance to corrosion attack in most aggressive environments and provided advantages in comparison with chromia-forming alloys in terms of maximum working life and temperature. Furthermore, alumina is more stable than chromia and does not suffer from evaporation at higher temperature such as chromia does [45].

Additionally, the alumina-forming alloys possess a stronger intrinsic adherence between the scale and bulk matrix than the chromia formers, and thus demonstrate better spall-off resistance under thermal cycling. The effect of alloying elements in Fe–Cr–Al alloys has been studied by Tomaszewicz and Wallwork [121], who claimed that Al is the most effective alloying element in terms of reduction of oxidation rate. The weight gains were lowest for aluminium contents greater than 3 wt.% due to the formation of an external protective alumina scale. At lower Al content in the alloy, Al<sub>2</sub>O<sub>3</sub> mixed with Fe- and Cr-rich oxide scale were observed [122]. Thus, to provide excellent oxidation resistance by producing an external and continuous alumina scale, the critical minimum level of aluminium in the alloy has to be over 3 wt.% [114,123]. Furthermore, a high Cr content is also required in order to enable the formation of an alumina scale with such low Al content in the alloy. The oxide map in Figure 2.12 demonstrates that alloys containing more than 20 wt.% of Cr need only 2 wt.% to 3 wt.% of Al to develop an  $\alpha$ -Al<sub>2</sub>O<sub>3</sub> coating. In addition, for alloys with sufficient aluminium content, chromium is not crucial to oxidation resistance, but a minimum amount of 15% is still needed to maintain the mechanical properties and inhibit corrosion [37].

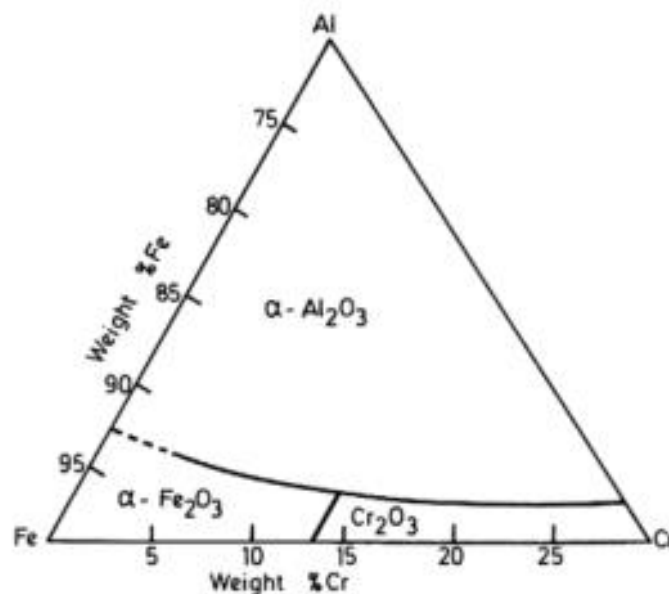


**Figure 2.12** Oxide map for Fe-Cr-Al ternaries at temperature greater than 1000°C [44].

### *2.3.1.1 FeCrAl alloy with low Al content*

Liu et al. [114] compared the oxidation behaviour of six FeCrAl alloys with different Al content ranging from 0 wt.% to 4 wt.% in air at 1050°C. Their results showed that all the 4 wt.% Al alloys with 14 wt.%, 16 wt.% and 18 wt.% of Cr developed a uniform and smooth Al<sub>2</sub>O<sub>3</sub> scale, however, the 2 wt.% Al alloys with 11 wt.% and 16 wt.% of Cr formed a discontinuous Al<sub>2</sub>O<sub>3</sub> scale mixed with some Cr- and Fe-rich oxides in the scale. Therefore, the author concluded that the content of chromium and aluminium had to be greater than 14 wt.% and 2 wt.%, respectively, in order to form a compact Al<sub>2</sub>O<sub>3</sub> scale with good adherence. In another study by Liu et al. [124], the oxidation behaviour of a Fe-14Cr alloy with different Al content of 0, 1.5, 3, and 4.5 wt.% was investigated. The Fe-14Cr-0Al formed a 300 µm Fe-Cr-O complex oxide with severe scale spallation after only 6 hours of oxidation. For Fe-14Cr-1.5Al, the oxide scale was mainly made of a 12 µm Cr<sub>2</sub>O<sub>3</sub> scale with a certain amount of Al and Fe after 6 hours oxidation. With the content of Al increased to 3 wt.%, a uniform and smooth oxide scale of 3 µm comprised of Cr<sub>2</sub>O<sub>3</sub> and Al<sub>2</sub>O<sub>3</sub> was established on the surface after 6 hours oxidation. However, a much thicker scale (8 µm) dominated by Al<sub>2</sub>O<sub>3</sub> formed on the Fe-14Cr-3.0Al alloy surface after the oxidation time increased to 200 hours. A homogeneous Al<sub>2</sub>O<sub>3</sub> scale with a low thickness of 3 µm developed on the Fe-14Cr-4.5Al alloy after only 6 hours oxidation. It is interesting to note that the thickness of this alumina scale on the Fe-14Cr-4.5Al alloy only slightly increased from 3 to 4 µm with the exposure time increasing from 6 to 200 hours. Therefore, the author stated that the content of Al should not be lower than 4.5 wt.% in order to achieve a continuous and compact Al<sub>2</sub>O<sub>3</sub> scale on the Fe-14Cr alloy. Kvernes et al. [125] studied the oxidation behaviour of Fe-13Cr alloys containing up to 4.5 wt.% Al in the temperature range 680 to 980°C. They proposed that the critical Al content required for selective oxidation of Al increases as the exposure

temperature increases. Therefore 4 wt.% Al is necessary for 980°C while 1 wt.% Al provides excellent corrosion resistance at 680°C.

### *2.3.1.2 FeCrAl alloy with high Al content*

Early studies carried out by Turker [126] exhibited that MA956 (4.5 wt.% Al and 20 wt.% Cr), ODM 751 (4.5 wt.% Al and 16.5 wt.% Cr) and PM2000 (5.5 wt.% and 20 wt.% Cr) formed an external adherent scale of  $\alpha$ -Al<sub>2</sub>O<sub>3</sub> with excellent corrosion protection during the exposure to air at 1100 to 1200°C in the long-term. Gomez-Vidal et al. [127] stated that the corrosion resistance of Fe-Cr-Al alloys improved with the increase of aluminium content present in the steel. However, it has been reported by Yang et al. [37] that the upper limit of 5.5 wt.% Al is normally implemented due to processing and forming considerations. Furthermore, a high content of Al alloying element dramatically affected the creep strength of the ferritic matrix, due to the very strong bcc-stabilising effects of Fe and Al [86]. Kimura et al. [128] found the creep strength of Fe-16Cr alloy at 937K was dramatically weakened by adding 4 wt.% Al in the alloy. Commercial nickel-base alloys offering high creep strength and excellent oxidation resistance, based on protective alumina scale formation, are currently available. However, their cost is about 5 to 10 times higher than conventional Fe-base stainless steels, which limits their use to niche applications [129]. In order to maintain the high corrosion resistance without sacrificing the high temperature creep strength, a new series of alumina-forming alloys which form an external Al<sub>2</sub>O<sub>3</sub> scale in dry air oxidation were developed [129–131]. By adding an adequate amount of stabilising elements such as Ni and optimising the manufacturing process, the content of Al in the alloy was successfully decreased to 2.5 wt.% which was still capable of producing a continuous Al<sub>2</sub>O<sub>3</sub> scale while maintaining an acceptable creep strength [86]. The alumina-forming alloy HTUPS-4 (Fe-20Ni-14Cr-2.5Al wt.%) tested by Yamamoto et al. [130] provided superior oxidation

resistance in humidified air at 800°C for 2000 hours via the formed external alumina scale on the alloy surface. Meanwhile, it had a long creep-rupture lifetime at 750°C under 100 MPa due to the formation of nano-NbC precipitates.

### 2.3.2 Different phases of the alumina

Yang et al. reported that the alumina-forming alloys such as Fecralloy demonstrated a much higher oxidation resistance than the chromia-forming alloys, including Crofer22 APU [96]. For high temperature applications, the excellent anti-corrosion property of alumina-forming steels is attributed to the formation of the highly protective and slow growing  $\alpha$ -Al<sub>2</sub>O<sub>3</sub> scale [114,115]. It is widely known that  $\alpha$ -Al<sub>2</sub>O<sub>3</sub> is the only thermodynamically stable oxide of aluminium. Besides,  $\alpha$ -Al<sub>2</sub>O<sub>3</sub> has a rhombohedral structure consisting of a hexagonal packing of oxide anions with cations occupying two-thirds of the octahedral interstitial sites [67]. The excellent corrosion resistance derives from the depressed diffusion kinetics of both aluminium and oxygen ions [73]. It has been evidenced from FeCrAl and NiCrAl alloys that grain boundary diffusion dominates the scale growth of alumina, while lattice diffusion is extremely slow [132,133]. The slow growth rate of  $\alpha$ -Al<sub>2</sub>O<sub>3</sub> is due to its large band gap and highly stoichiometric structure which makes electronic conduction difficult [134]. In addition, the oxidation rate of alumina-forming steels will dramatically reduce once a continuous  $\alpha$ -Al<sub>2</sub>O<sub>3</sub> scale is formed [135,136]. Thus, this particular crystalline structure of  $\alpha$ -Al<sub>2</sub>O<sub>3</sub> makes it a perfect candidate as protective film for many high-temperature alloys. However, when an alumina-forming alloy is exposed at temperatures lower than 1150°C, different forms of transient (metastable) Al<sub>2</sub>O<sub>3</sub> with different crystalline structures will form such as  $\gamma$ -Al<sub>2</sub>O<sub>3</sub>,  $\theta$ -Al<sub>2</sub>O<sub>3</sub> and  $\delta$ -Al<sub>2</sub>O<sub>3</sub> [127]. The transient aluminium oxides contain lattice defects, so they provide no significant protection to further oxidation of the alloy compared with  $\alpha$ -Al<sub>2</sub>O<sub>3</sub> scale [137,138]. The structure of  $\gamma$ -Al<sub>2</sub>O<sub>3</sub> is cubic spinel,  $\theta$ -Al<sub>2</sub>O<sub>3</sub> has a monoclinic type

structure and  $\delta$ - $\text{Al}_2\text{O}_3$  is tetragonal [67]. Figure 2.13 compares the scale thickening rate of  $\theta$ - $\text{Al}_2\text{O}_3$  and  $\alpha$ - $\text{Al}_2\text{O}_3$ . The oxidation behaviour of alumina-formers AluChrom YHf and Kanthal has been reported by Nicholls et al. [139] and Bennett et al. [140]. It was found that the oxide scales developed on the FeCrAl alloys at low temperature contained metastable aluminas and consequently offered poor protection against high temperature corrosion. Furthermore, the different morphologies formed by the alumina phase also lead to the different growth rate: whereas  $\alpha$ - $\text{Al}_2\text{O}_3$  forms a dense layer, the metastable oxides tend to form as whiskers or blade morphologies.

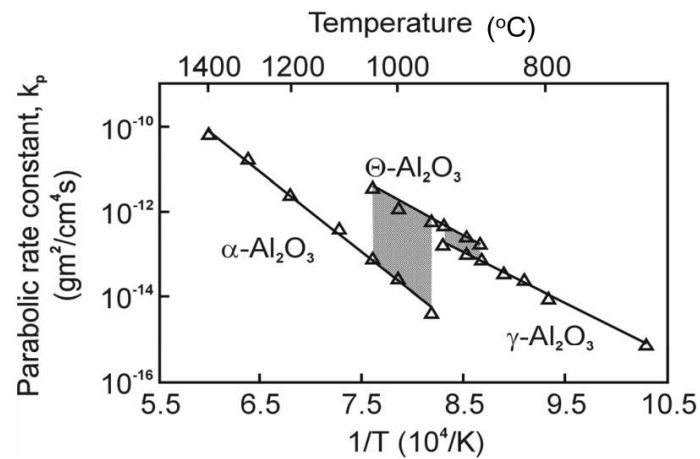


**Figure 2.13** Arrhenius plot of  $K_p$  for the oxidation of pure NiAl [72].

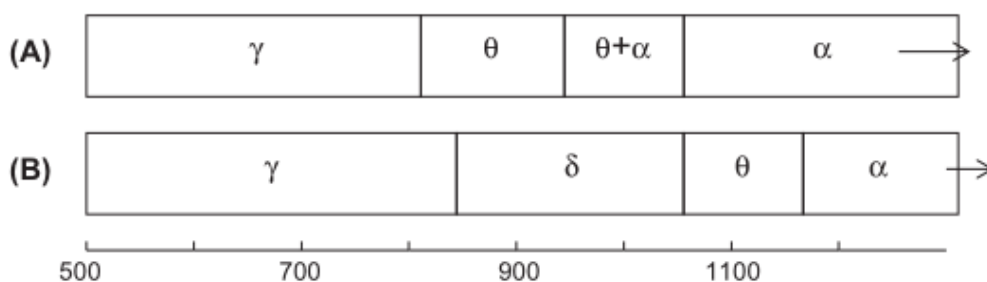


**Figure 2.14** Approximate  $\text{Al}_2\text{O}_3$  transformation temperature observed on bulk material [42].

It is widely known that all the metastable alumina can transform to  $\alpha$ - $\text{Al}_2\text{O}_3$  by further heat treatment [141]. The phase transformation generally takes place at higher temperature or/and extended oxidation time at the expense of the metastable alumina that is formed during the heating process at the lower temperature [134]. The sequences of phase transformation given

in the literature are known to be  $\gamma\text{-Al}_2\text{O}_3 \rightarrow \delta\text{-Al}_2\text{O}_3 \rightarrow \theta\text{-Al}_2\text{O}_3 \rightarrow \alpha\text{-Al}_2\text{O}_3$  or be  $\gamma\text{-Al}_2\text{O}_3 \rightarrow \theta\text{-Al}_2\text{O}_3 \rightarrow \alpha\text{-Al}_2\text{O}_3$ , as exhibited in Figure 2.14 [141]. The transformation is a reconstructive process involving a continuous ordering of cations, with a final restructuring of anions in the hexagonal closed-packed arrangement in the rhombohedral [134]. Due to the lower density of metastable aluminas than the  $\alpha\text{-Al}_2\text{O}_3$ , the phase transformation is accompanied by a 13% reduction in volume [42], leading to tensile stresses and radial cracks detrimental to the adherence of the final  $\alpha\text{-Al}_2\text{O}_3$  scale. Rybicki and Smialek [142] found that the  $\theta\text{-Al}_2\text{O}_3$  scale completely covered Zr-doped NiAl after oxidation at 800°C for 100 hours while it transformed into  $\alpha\text{-Al}_2\text{O}_3$  in about 8 hours at 1000°C. Brumm and Grabke [143] detected the phase transformation of  $\gamma$  to  $\theta$  and  $\theta$  to  $\alpha$  occurring simultaneously on NiAl at 900°C. The transformation from the initially formed  $\gamma\text{-Al}_2\text{O}_3$  to  $\theta\text{-Al}_2\text{O}_3$  took about 10 hours. However, the transformation from  $\theta\text{-Al}_2\text{O}_3$  to  $\alpha\text{-Al}_2\text{O}_3$  occurred at much longer times but accelerated when the exposure temperature was increased. Pint and Hobbs [144] identified only  $\alpha\text{-Al}_2\text{O}_3$  phase formed on undoped NiAl after 160 seconds oxidation at 1500°C.

### 2.3.3 Oxidation of alumina forming alloys

#### 2.3.3.1 Effect of temperature

The formation of alumina on the surface of an alumina forming alloy (FeCrAl or NiCrAl) is completely different from the theory presented in Figure 2.14 as all the elements presented in the FeCrAl alloy will oxidise depending on the exposure conditions. Thus, depending on the exposure conditions and the alloying compositions, the transformation of the alumina phase may differ [136,141]. Temperature has been considered as one of the most important factors in the oxidation of alumina-forming alloys. The temperature has to be high enough to facilitate the phase transformation from metastable alumina to  $\alpha\text{-Al}_2\text{O}_3$  as metastable alumina could be detected during the initial stages of oxidation when the oxidation occurred at higher

temperature [134]. Nakayama and Kaneko [145] reported the formation of spinel type  $\gamma$ - $\text{Al}_2\text{O}_3$  after exposing an iron-based alumina forming steel to a hydrogen-steam mixture at  $700^\circ\text{C}$  for 1 hour. However, the oxide scale consisted of corundum type  $\alpha$ - $\text{Al}_2\text{O}_3$  with trace amounts of iron after exposure to the same atmosphere at  $920^\circ\text{C}$ . Boggs [146] reported the formation of  $\gamma$ - $\text{Al}_2\text{O}_3$  with very small  $\alpha$ - $\text{Al}_2\text{O}_3$  crystals at  $600^\circ\text{C}$  on an iron-aluminium alloy. However, the oxide scale seemed to contain more  $\alpha$ - $\text{Al}_2\text{O}_3$  than the metastable  $\gamma$ - $\text{Al}_2\text{O}_3$  once the temperature was over  $900^\circ\text{C}$ . It has also been pointed out that the transformation of  $\gamma$ - $\text{Al}_2\text{O}_3$  to  $\alpha$ - $\text{Al}_2\text{O}_3$  may involve an intermediate phase,  $\delta$ - $\text{Al}_2\text{O}_3$ . Ramanarayanan et al. reported the existence of  $\delta$ - $\text{Al}_2\text{O}_3$ , mixed with  $\alpha$ - $\text{Al}_2\text{O}_3$  on an iron-based alloy at  $900^\circ\text{C}$  [147]. Mosely et al. [115] reported the presence of whiskers of  $\theta$ - $\text{Al}_2\text{O}_3$  on a FeCrAl alloy at  $1000^\circ\text{C}$ . On heating to  $1200^\circ\text{C}$ , these whiskers were transformed to  $\alpha$ - $\text{Al}_2\text{O}_3$ , with a high degree of crystalline strain. Peters and Grabke [148] found the presence of a fine grained film of  $\theta$ - $\text{Al}_2\text{O}_3$  on an Fe-based alloy during the initial stage of oxidation at  $1000^\circ\text{C}$ . The phase transformation to the stable  $\alpha$ - $\text{Al}_2\text{O}_3$  started at the interface between the alloy base and the  $\theta$ - $\text{Al}_2\text{O}_3$ , and occurred more quickly on ferritic alloys than on austenitic alloys.

However, the formation of  $\alpha$ - $\text{Al}_2\text{O}_3$  is also observed by exposing the FeCrAl alloy at relatively low temperatures. Josefsson et al. [149] proved the formation of  $\alpha$ - $\text{Al}_2\text{O}_3$  on Kanthal AF with XRD analysis after exposing it to dry  $\text{O}_2$  at  $700^\circ\text{C}$  for 168 hours. The authors attributed such low temperature formation of  $\alpha$ - $\text{Al}_2\text{O}_3$  to the few percent of chromium and iron present in the oxide scale. Chen et al. [150] also detected the formation of a large amount of  $\alpha$ - $\text{Al}_2\text{O}_3$  coexisting with  $\gamma$ - $\text{Al}_2\text{O}_3$  at  $650^\circ\text{C}$ . The authors found that the outward diffusion of Al atoms incorporated into the precursor oxide of  $\alpha$ - $\text{Fe}_2\text{O}_3$  and the  $\text{Al}^{3+}$  ions substituted for  $\text{Fe}^{3+}$  in the  $\alpha$ - $\text{Fe}_2\text{O}_3$ , eventually leading to the  $\text{Al}^{3+}$  doped  $\alpha$ - $\text{Fe}_2\text{O}_3$ . Thus, nucleation and growth of  $\alpha$ - $\text{Al}_2\text{O}_3$  on the  $\text{Al}^{3+}$  doped  $\alpha$ - $\text{Fe}_2\text{O}_3$  might be a direct way for the

formation of  $\alpha$ -Al<sub>2</sub>O<sub>3</sub> scale without detection of intermediate alumina at low temperature (650°C). It has been widely reported that the transient oxides ( $\alpha$ -Cr<sub>2</sub>O<sub>3</sub> and  $\alpha$ -Fe<sub>2</sub>O<sub>3</sub>) which are isostructural with  $\alpha$ -Al<sub>2</sub>O<sub>3</sub>, can act as crystallographic template for the nucleation and growth of  $\alpha$ -Al<sub>2</sub>O<sub>3</sub> [114,123,149]. Furthermore, these transient oxides doped with Al<sup>3+</sup> increase the nucleation of  $\alpha$ -Al<sub>2</sub>O<sub>3</sub> and accelerate the growth of the protective layer. The developed protective layer of  $\alpha$ -Al<sub>2</sub>O<sub>3</sub> can subsequently suppress the formation of metastable alumina, resulting in less formation of the non-protective metastable alumina scale. The work performed by the Swedish High Temperature Corrosion Centre [136,151,152] reported in detail that the oxide scale formed on the alumina-forming alloy (Kanthal AF) exposed at 900°C in dry O<sub>2</sub> for 1 hour had a double-layered structure including a bottom layer of  $\alpha$ -Al<sub>2</sub>O<sub>3</sub> and an upper layer of  $\gamma$ -Al<sub>2</sub>O<sub>3</sub> with a Cr-rich band in the middle, indicating the original metal/gas interface, as shown in Figure 2.15. A fast outward growth of  $\gamma$ -Al<sub>2</sub>O<sub>3</sub> by Al outward diffusion resulted in a rapid mass gain while a slow growth of  $\alpha$ -Al<sub>2</sub>O<sub>3</sub> grains nucleated on the isostructural Cr<sub>2</sub>O<sub>3</sub> (native oxide film) eventually formed a dense inner  $\alpha$ -Al<sub>2</sub>O<sub>3</sub> layer by oxygen inward diffusion.

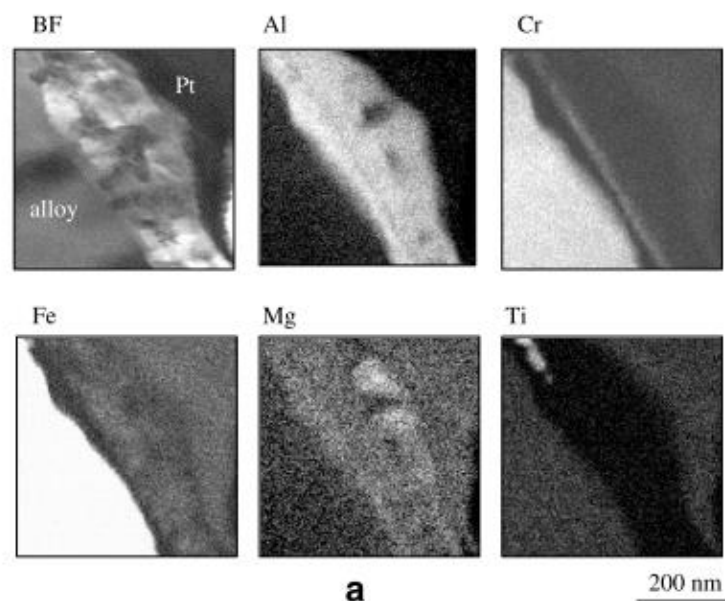


**Figure 2.15** STEM/EDX images of the oxide scale formed on Kanthal AF after oxidation in dry oxygen at 900°C for 1 hour [136].

### 2.3.3.2 Effect of water content

The literature on the effect of water vapour on the growth behaviour of alumina scale in alumina-forming alloys is somewhat contradictory. While some articles report that water vapour slows down the oxidation rate of FeCrAl alloys, others claim that water vapour accelerates alumina growth on the alumina-forming alloys. Further to Kvernes et al.'s study [125], they reported that the oxidation of Fe-13Cr-4.4Al alloys was not significantly dependent on the humidity level of the air once continuous Al<sub>2</sub>O<sub>3</sub> scales were formed at 680°C, 820°C and 920°C. Buscail et al. [153] compared the oxidation behaviour of the Fe-21.5Cr-5.6Al alloy in dry and humidified oxygen at 1000°C. The authors revealed that the formation of hexagonal alumina, which has a similar structure to the protective  $\alpha$ -Al<sub>2</sub>O<sub>3</sub>, slowed the oxidation rate in wet oxygen atmosphere, whereas  $\gamma$ -Al<sub>2</sub>O<sub>3</sub> with a faster growth rate formed in dry oxygen in the initial oxidation. However, it has been confirmed that, during extended exposure, the hexagonal alumina formed in the humidified oxygen contained a high concentration of Cr and Fe, which offered less corrosion resistance compared to the  $\alpha$ -Al<sub>2</sub>O<sub>3</sub> that was established in the steam free environment. Unocic et al. [154] observed thinner layers and slower growth rates of the alumina scales formed on PM2000 (Fe-19Cr-10Al) exposed at 1050°C in air with 10% H<sub>2</sub>O and Ar with 10% H<sub>2</sub>O compared to the scale formed in dry O<sub>2</sub> at 1050°C. The authors attributed the reduction of the oxidation rate in humid atmosphere to the change in the diffusion species (water molecules or hydroxyl group) along the oxide grain boundaries.

The opposite results were reported in early work from Boggs et al. [146]. They found that the oxidation rate of the Fe-based alloy with 5 wt.% Al was remarkably increased during exposure at 800°C when 3% water was added to the oxygen atmosphere. They observed that the initially formed  $\gamma$ -Al<sub>2</sub>O<sub>3</sub> in dry oxygen transformed into  $\alpha$ -Al<sub>2</sub>O<sub>3</sub> with about 1 wt.% Fe-

rich oxides after 16 hours oxidation, whereas in wet oxygen Fe-rich nodular oxides occupied almost 20% of the surface. It was suggested that a hydrated alumina may have developed in the initial stage of oxidation in the humidified environment which was more susceptible to cracking and this resulted in more formation of nodular oxides. Onal et al. [155] reported the detrimental effect of water vapour on the oxidation behaviour of alumina-forming alloys. They found the oxidation of alumina-forming alloys can be influenced by steam in certain ways, namely, more metastable alumina is formed over the  $\alpha$ -Al<sub>2</sub>O<sub>3</sub> compared to the layer formed in dry air. The formation of an adherent and continuous alumina scale was restrained, and spallation and cracking of the  $\alpha$ -Al<sub>2</sub>O<sub>3</sub> scale occurred in steam atmosphere at elevated temperatures. It was proposed that water molecules can affect the  $\alpha$ -Al<sub>2</sub>O<sub>3</sub>/alloy interfacial toughness. Smialek and Morscher [156] proved that water immersion caused additional oxide spallation at metal/oxide interfaces for both yttrium-doped and undoped Rene N5 alloys oxidised at 1150°C for 500 and 1000 hours. This phenomenon can be aggravated by the existence of impurities such as sulphur segregating to the scale/alloy interface and thereby reducing the interfacial bonding strength. The increased oxidation rate of FeCrAl alloy oxidised in H<sub>2</sub>O containing environment was also observed on Kanthal AF studied by Gotlind et al. [152] and on Kanthal APMT studied by Hellstrom et al. [157], and Engkvist et al. [158]. All these three papers found that the oxide scales were composed of a two-layered oxide structure in both dry and humidified oxygen environment. The bottom layer consisted of  $\alpha$ -Al<sub>2</sub>O<sub>3</sub> grown by oxygen inward diffusion while the top layer initially consisted of  $\gamma$ -Al<sub>2</sub>O<sub>3</sub> grown by Al outward diffusion. In dry O<sub>2</sub>, the outer  $\gamma$ -Al<sub>2</sub>O<sub>3</sub> scale was transformed to  $\alpha$ -Al<sub>2</sub>O<sub>3</sub> during the early stage of exposure. However, this phase transformation did not occur in humidified oxygen environment. It was proposed that the formed surface-hydroxylated  $\gamma$ -Al<sub>2</sub>O<sub>3</sub> was considered to be more stable and less reactive than the  $\gamma$ -Al<sub>2</sub>O<sub>3</sub> formed in dry atmosphere, thereby inhibiting the formation of  $\alpha$ -Al<sub>2</sub>O<sub>3</sub> [136,152,157,158]. The higher

oxidation rate in the presence of H<sub>2</sub>O was thus due to an accelerated formation of the metastable oxides.

## **2.4 Volatilisation of Cr(VI)-containing species**

### **2.4.1 Formation of Cr(VI)-containing gases**

As discussed before, high temperature resistant alloys used in BOP components in SOFCs, such as CAPH, typically possess high chromium content to form a protective Cr<sub>2</sub>O<sub>3</sub> scale [29,117,119,159]. Under the cathodic environment, chromia reacts with water vapour and oxygen, forming high valent chromium gases, contaminating the cell by accumulating chromium species around the electrolyte and cathode interface and depleting the chromium reservoir in the alloy. The chromium species in vapour phase can be produced at temperatures ranging from 600 to 800°C [29]. Volatilisation of chromium-containing species is a very common problem for stainless steel components in the SOFC stack, such as interconnects. The evaporation of chromium-containing species strongly depends on the water content and the oxygen partial pressure [26,160]. Ebbinghaus et al. [160] investigated the constituents of fifteen kinds of chromium-containing gases evaporated from Cr<sub>2</sub>O<sub>3</sub> at fixed partial pressure of water (10.0 kPa) and oxygen (1.0 kPa) in the temperature range from 800 to 1600K. The volatilisation of chromium will reach the maximum when the partial pressure of steam and oxygen are about equal, and the pressure of chromium gas will decrease remarkably if either the partial pressure of oxygen or steam reduces.

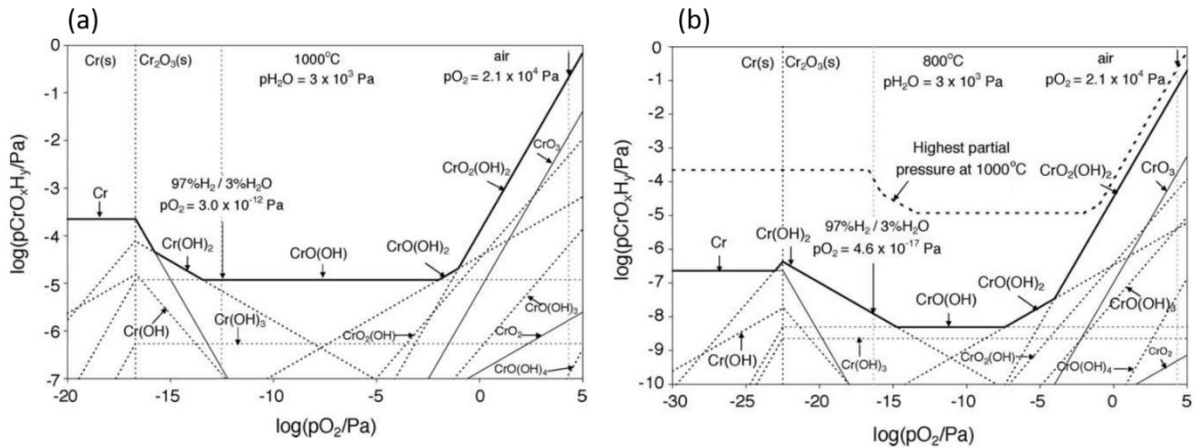


**Figure 2.16** Equilibrium vapour pressure of Cr-O-H gases at (a) 1000°C and (b) 800°C with water partial pressure of 3 kPa based on thermodynamic data from Ebbinghaus [41,160].

Fergus [41] made calculations for the equilibrium gas pressures of the volatile Cr species at 800 and 1000°C based on the thermodynamic data from Ebbinghaus and assuming a maximum water vapour pressure of 3 kPa, as shown in Figure 2.16. The maximum partial pressure of all Cr vapour at 1000°C was plotted as bold dashed line in Figure. 2.16b (800°C) for comparison. At both temperatures, the results indicated that the difference between the highest Cr gas pressure between 800 and 1000°C was much smaller in air environment than in hydrogen environment. The calculation demonstrated that the most abundant Cr vapour on the fuel side would be CrO(OH) or Cr(OH)<sub>2</sub> at 1073K, and that the partial pressures of these chromium gases would be approximately 7 orders of magnitude lower than for the cathode side. Thus, degradation by volatile Cr species in the anode side could be expected to be negligible, and would not likely influence anode performance. At the air/cathode side, the thermodynamic instability of the Cr<sub>2</sub>O<sub>3</sub> scale formed on the steel substrate is the essential reason for chromium volatility at high temperature. Based on the thermodynamic calculations, the most abundant Cr (VI) volatile species are CrO<sub>3</sub>, CrO<sub>2</sub>(OH), and CrO<sub>2</sub>(OH)<sub>2</sub> in high oxygen partial pressure with the presence of water vapour. The involved chemical reactions are shown below [26,161]:

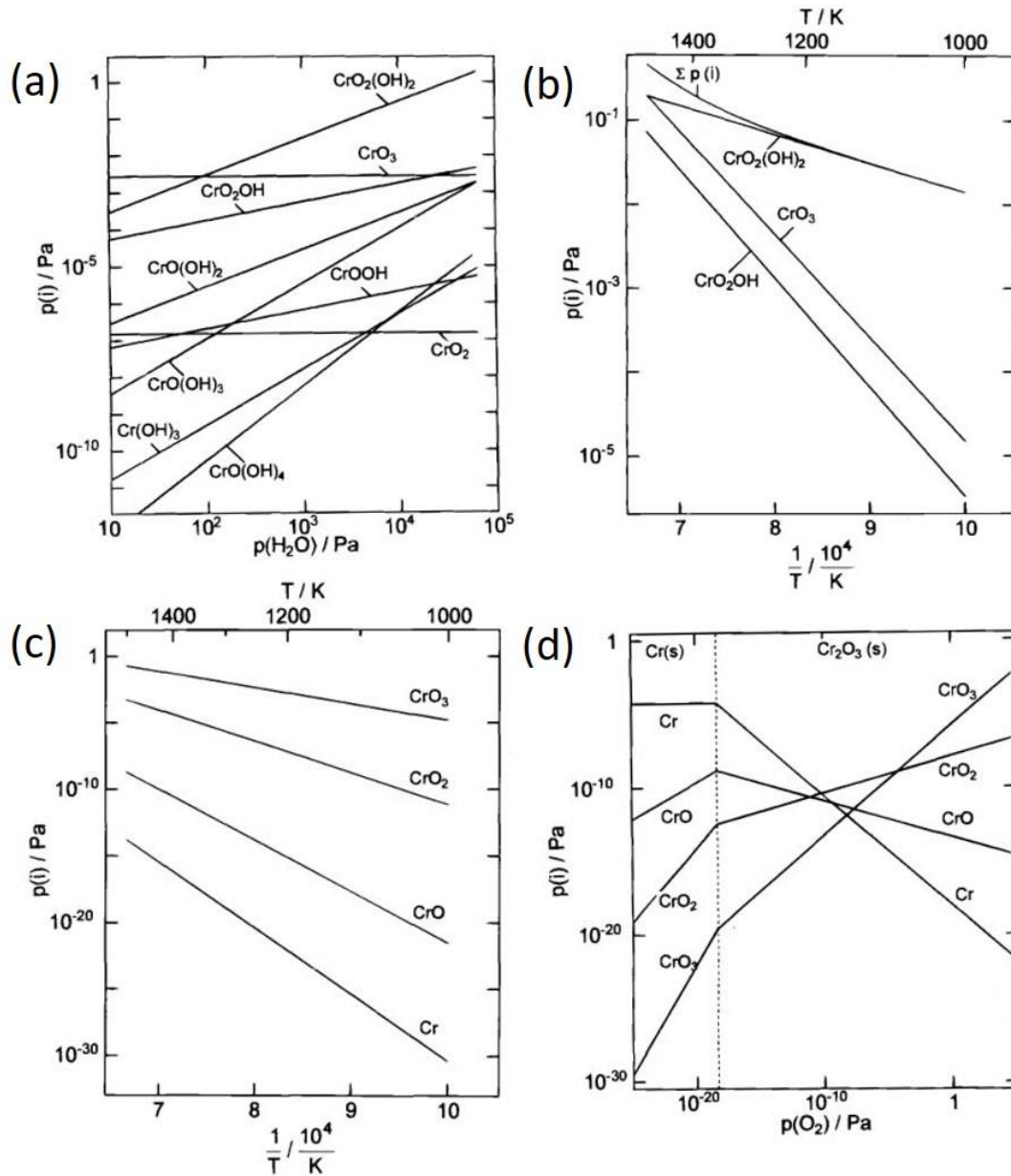
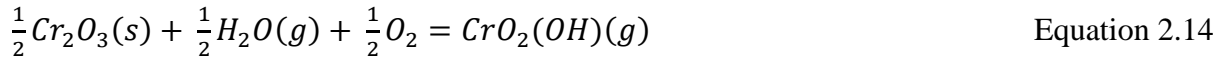
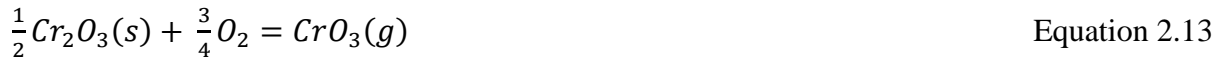
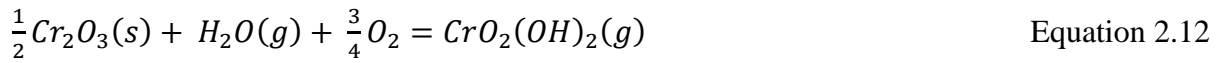


**Figure 2.17** Partial pressure of volatile chromium species (a) at 1223K in air ( $p(O_2) = 2.13 \times 10^4 \text{ Pa}$ ) with different partial pressure of water vapour, (b) in humidified air ( $p(O_2) = 2.13 \times 10^4 \text{ Pa}$  and  $p(H_2O) = 2 \times 10^3 \text{ Pa}$ ) at different temperatures, (c) in air ( $p(O_2) = 2.13 \times 10^4 \text{ Pa}$ ) without water at different temperatures, and (d) at 1223K and different  $O_2$  partial pressure [26].

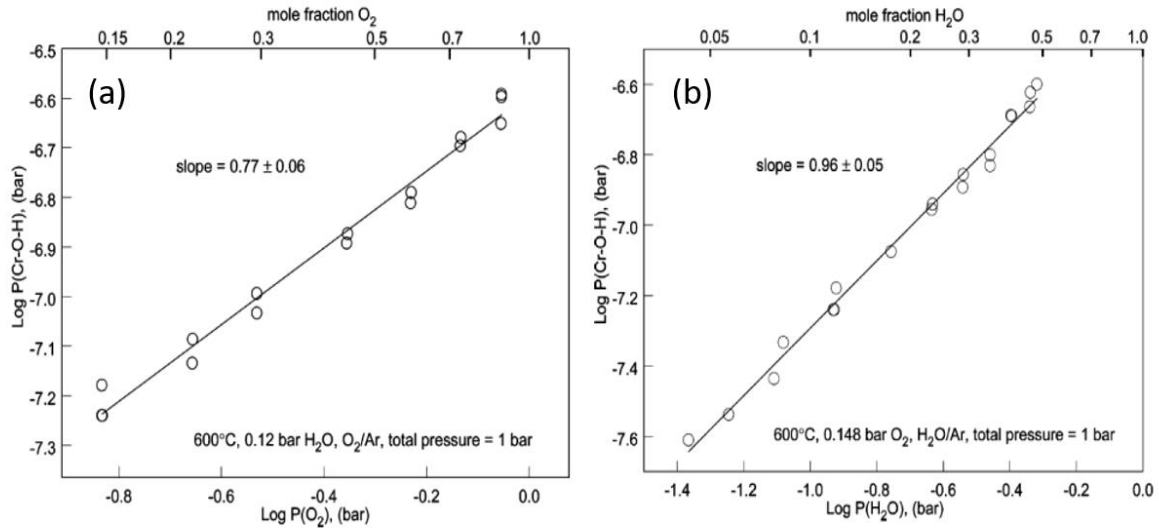


**Figure 2.18** (a) Oxygen dependence and (b) water vapour dependence for  $\text{Cr}_2\text{O}_3$  volatility at  $837\text{K}$  [80].

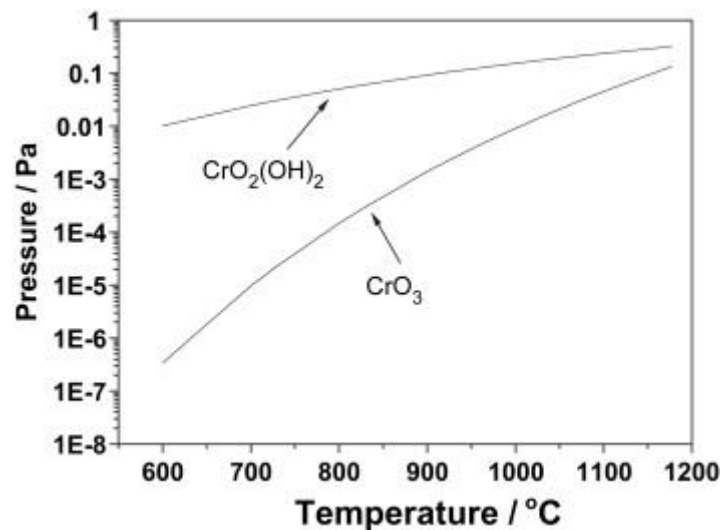


**Figure 2.19** Partial pressure of  $\text{CrO}_3$  in dry air and  $\text{CrO}_2(\text{OH})_2$  in humid air (3% water) over  $\text{Cr}_2\text{O}_3$  at various temperatures [162].

Hilpert et al. [26] investigated the effect of water vapour partial pressure, oxygen partial pressure and temperature on the vaporisation of Cr-containing species from metallic interconnects via thermodynamic modelling. The steam partial pressure dependence on partial pressure of all kinds of volatile chromium species is shown in Figure 2.17a. Results from Figure 2.17 are consistent with Ebbinghaus's finding that  $\text{CrO}_3$ ,  $\text{CrO}_2(\text{OH})$  and

$\text{CrO}_2(\text{OH})_2$  are the most abundant Cr vapour species during high temperature exposure in humid air. Figure 2.17b shows the temperature dependence of partial pressure of the three different volatile chromium species. It can be clearly seen that the chromium oxyhydroxide ( $\text{CrO}_2(\text{OH})_2$ ) is the dominant Cr volatile species in humid air under SOFC operation temperature range of 800 to 1000°C. However,  $\text{CrO}_3$  with six valent chromium is the most abundant volatile species in cathode environment if the SOFC is fed with dry air containing no  $\text{H}_2\text{O}$ , as can be seen in Figure 2.17c & d. Gindorf et al. [161] employed the transpiration technique to study the chromium volatilisation from  $\text{Cr}_2\text{O}_3$  powder at 1223K in air with different humidity levels and discovered that the amount of evaporated chromium species ( $\text{CrO}_2(\text{OH})_2$ ) increased remarkably when the humidity in air increased from 0.07 to 0.3 kPa. Based on Hilpert et al.'s and Gindorf et al.'s data, it can be inferred that the partial pressure of  $\text{CrO}_3$  does not depend on the partial pressure of water vapour. Opila et al. [80] used the same technique to investigate the dependence of  $\text{CrO}_2(\text{OH})_2$  volatility on oxygen and steam partial pressure at 600°C, indicating that volatility exhibits a power law dependency of  $0.77 \pm 0.06$  and  $0.96 \pm 0.05$  for oxygen and steam, respectively, as shown in Figure 2.18. Chen et al. [162] examined the temperature dependence of partial pressure of  $\text{CrO}_3$  and  $\text{CrO}_2(\text{OH})_2$  evaporated from  $\text{Cr}_2\text{O}_3$  in dry and wet air, respectively, as shown in Figure 2.19. Similar to Fergus's observation, they found that the partial pressure of  $\text{CrO}_3$  gas in dry air increased promptly with the increase of temperature whereas the variation in the partial pressure of  $\text{CrO}_2(\text{OH})_2$  in wet air within the same temperature range was limited.

The partial pressure of gaseous chromium species has an Arrhenius relationship with temperature. Falk-Windisch et al. [163] investigated the influence of exposure temperatures (650, 750 and 850°C) on oxidation and Cr evaporation behaviour for Crofer 22 H and Sanergy HT which formed  $(\text{Cr},\text{Mn})_3\text{O}_4$  spinel as protective layer for both alloys. They

employed the Arrhenius equation to conduct the activation energy calculations on Sanergy HT and Crofer 22 H for both oxide scale growth and Cr evaporation reactions. For both alloys, it was found that the obtained activation energies were approximately 90 kJ/mol for Cr evaporation and 270 kJ/mol for oxide scale growth. The Arrhenius plot (Figure 2.20) showed that the temperature had a greater effect on oxide scale growth than Cr evaporation due to the much higher activation energy of oxide scale growth than Cr evaporation.

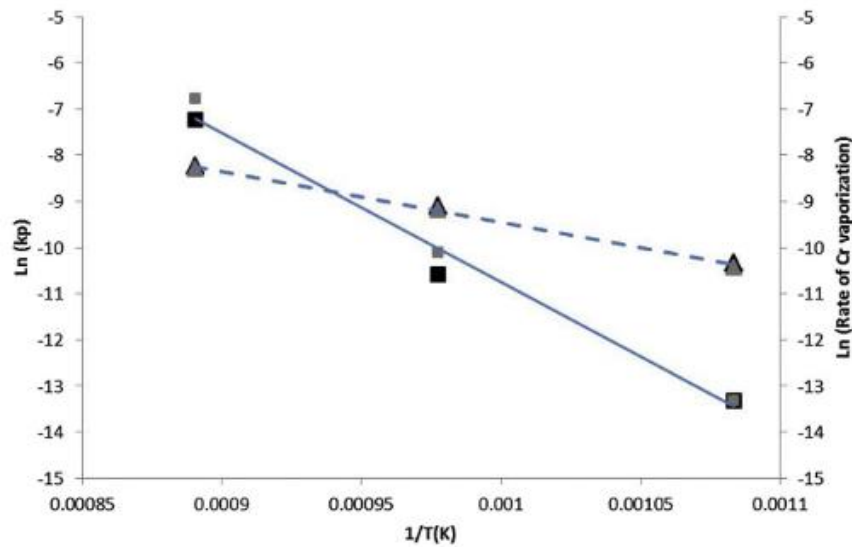


**Figure 2.20** Arrhenius plot showing the influence of temperature on both oxide growth (squares) and Cr evaporation rate (triangles) for Sanergy HT (black) and Crofer 22 H (grey) in 6.0 L/min air with 3% H<sub>2</sub>O [163].

#### 2.4.2 Effect of Cr(VI) species on SOFC cathode material

The volatilization of Cr species from the oxide scale not only weakens the corrosion resistance of the substrate, but it also leads to the degradation of SOFC. The deposition of Cr-containing gases is associated with the oxygen activity at the electrolyte/electrode interface. The electrochemical reduction of volatile Cr(VI) species such as CrO<sub>3</sub> and CrO<sub>2</sub>(OH)<sub>2</sub> has been suggested as the primary mechanism for the Cr(VI) deposition at the LSM/YSZ electrode system. Figure 2.21 shows a schematic of the electrochemical reduction of the volatile hexavalent chromium at the triple phase boundary (TPB) of the SOFC

cathode/electrolyte/oxidant interface [27]. As a result, the active sites in the cathode are blocked by the deposited chromium species, leading to fuel cell performance degradation [41]. However, some authors also reported that the distribution of deposited Cr-containing species did not necessarily locate at the TPB. Deposition of Cr(VI)-containing species was also found on the whole LSM electrode at 1100°C [164] and on the YSZ electrolyte surface after anodic polarisation of an LSM electrode at 900°C [165]. Therefore, it can be inferred that the deposition of Cr volatile species can also take place by the chemical reduction reaction of the Cr(VI)-containing gases, promoted by the nucleation reaction between the Cr(VI)-containing gases and  $Mn^{2+}$  ions produced under cathode polarisation conditions [27].

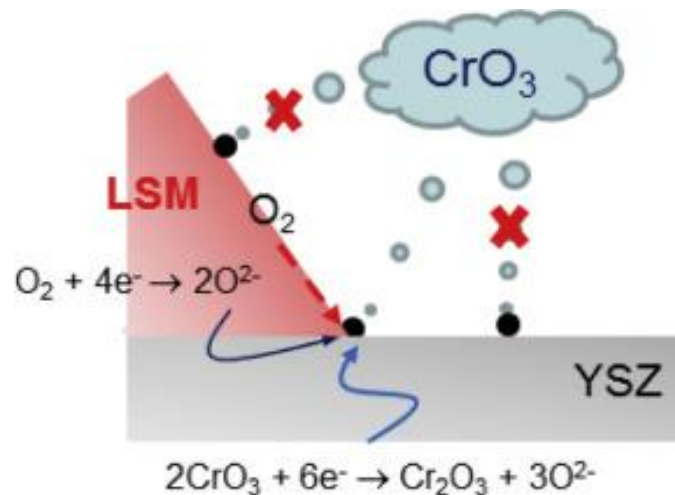


**Figure 2.21** Schematic of volatile chromium species deposition at the TPB (cathode/electrolyte interface) based on electrochemical deposition mechanism [27].

A number of studies have demonstrated that the volatile chromium species from uncoated chromium-containing alloys can lead to serious degradation in the electrocatalytic activity of LSM electrodes for the oxygen reduction reaction. Early research from Taniguchi et al. [164] demonstrated the interrelation between the polarisation losses and the accumulation of chromium-containing species at the LSM/YSZ interface of SOFC cathodes. They found an increase in the cathode polarisation by the discharge current due to the pore blockage by chromium-containing species, indicating that the accumulation of chromium reduced the

amount of cathode reaction sites and impeded the supply of oxygen. Zhen et al. [166] conducted impedance spectroscopy studies on the oxygen reduction reaction in the presence and absence of a Fe-Cr alloy. The study revealed that the electrode processes at high and low frequencies are dramatically affected by the alloy. Figure 2.22 shows the activation energy graphs of the electrode conductivity of high- and low- frequency arcs for the LSM electrode in the presence and absence of an Fe-Cr alloy in air. The activation energy of the low-frequency arc in the presence of the Fe-Cr alloy ( $153 \text{ kJ mol}^{-1}$ ) was close to that in the absence of Fe-Cr alloys ( $142 \text{ kJ mol}^{-1}$ ). However, a significant difference was observed for the activation energy between the presence of the Fe-Cr alloy ( $167 \text{ kJ mol}^{-1}$ ) and its absence ( $95 \text{ kJ mol}^{-1}$ ) at the high-frequency arc. The authors stated that the chromium species deposited on the YSZ electrode surface physically inhibited the migration of oxygen ions from the LSM electrode to the YSZ electrolyte lattice, which led to a relatively slow oxygen reduction reaction at high frequency. This was attributed to the detrimental effect of chromium vapour, decreasing the number of active sites on the LSM electrode surface available for the surface exchange reaction.

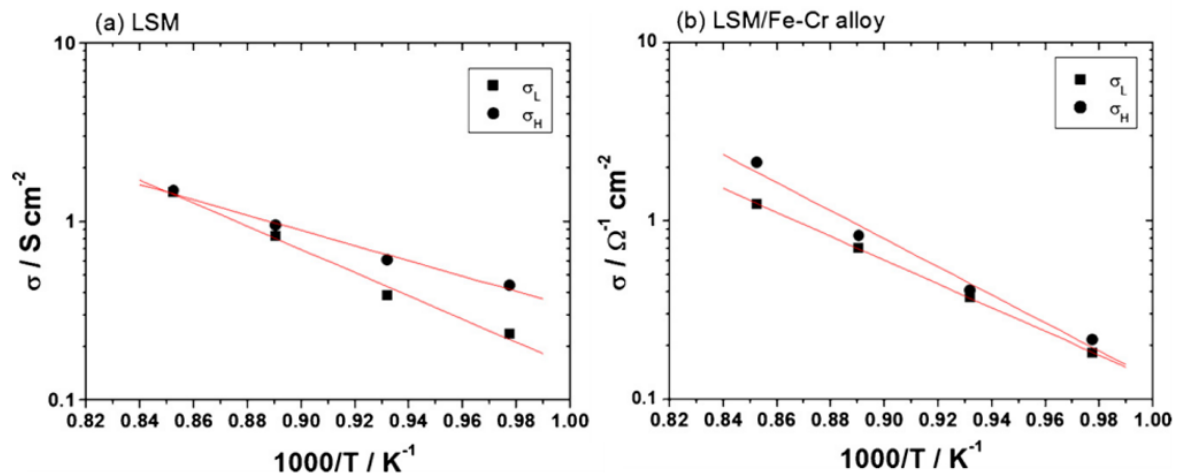


**Figure 2.22** Activation energy graphs of electrode conductivity of high- and low- frequency arcs for oxygen reduction on LSM electrodes in the presence and absence of chromium-containing alloy in air [166].

### 2.4.3 Determination of chromium evaporation

Many types of alloys and protective coatings have been developed to reduce the volatilisation of chromium species [30,37,41,116,119,167,168]. It is necessary to quantitatively measure the volatile chromium species released from high-chromium steels for SOFC applications in order to evaluate the effect of a steel or coating on the chromium retention. Figure 2.23 demonstrates a simplified schematic of the experimental setup used for collection of volatile Cr species [168]. The metallic samples in the furnace are heated to the target temperature. The reactant gas flows into the furnace allowing chemical reaction to take place at the gas/alloy interface. The vaporised Cr species are transported downstream with the carrier gas and accumulated in the collector for further quantitative analysis. A number of experimental techniques based on the schematic in Figure 2.23 have been developed to quantify chromium evaporation such as mass measurement [169], the transpiration technique [26,45,80,160,161,170], the denuder technique [94], the ionic conductivity method [171], a silicon wafer collector [172], a ceramic plate collector [173] and a quartz wool collector. Table 2.1 summarised by Key et al. [168] shows the collection efficiency and analytical precision for each technique mentioned above.

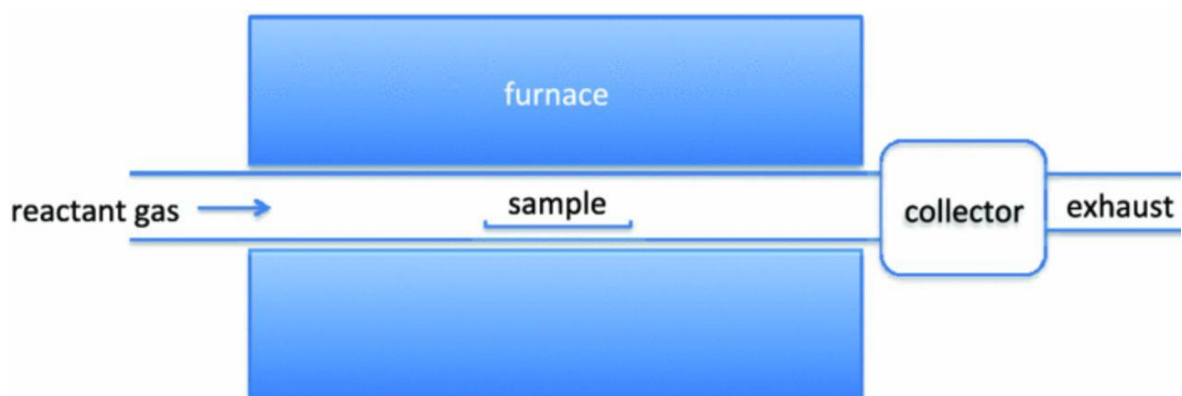


**Figure 2.23** Schematic of an experimental apparatus of transpiration method [168].

**Table 2.1** A summary of different analytic techniques employed to quantify chromium vapours [168].

Techniques	Efficiency	Disadvantages	Analysis Method	Detection Limit	Available Information
Transpiration	Assumes 100%	<ul style="list-style-type: none"> <li>Complexity of equipment.</li> <li>Formation of Cr<sub>2</sub>O<sub>3</sub> on tube wall.</li> <li>Highly concentrated acid for dissolving Cr<sub>2</sub>O<sub>3</sub>.</li> </ul>	ICP-MS	1-0.01 ppb	Total Cr and other elements
			ICP-AES	3 ppb	Total Cr and other elements
Denuder	95±5%	<ul style="list-style-type: none"> <li>Incomplete reaction between CrO<sub>2</sub>(OH)<sub>2</sub> and Na<sub>2</sub>CO<sub>3</sub>.</li> <li>CrO<sub>3</sub> is not collected.</li> </ul>	Photo spectrometry	1 ppm	Total Cr
Ionic conductivity method	100%	<ul style="list-style-type: none"> <li>Influence of conductivity by other dissolved ions.</li> </ul>	Conductivity Probe	10 ppm	Total Cr
Silicon wafer Collector	10%	<ul style="list-style-type: none"> <li>Several variables affect the collection efficiency.</li> <li>Low collection efficiency.</li> <li>RBS requires access to a particles accelerator for analysis.</li> </ul>	RBS	1 ppm	Relative Cr and other element
Ceramic plate collector	NA	<ul style="list-style-type: none"> <li>Incomplete quantitative analysis of Cr containing species.</li> </ul>	EDS	100 ppm	Relative Cr and other element
Quartz Wool Collector	80%	<ul style="list-style-type: none"> <li>Formation of Cr<sub>2</sub>O<sub>3</sub> on tube wall.</li> <li>Highly concentrated acid for dissolving Cr<sub>2</sub>O<sub>3</sub>.</li> </ul>	ICP-MS	1-0.01 ppb	Total Cr and other elements

The transpiration technique has been widely used by a number of research groups to quantify the chromium evaporation from coated alloys, chromium-containing alloys and pure Cr<sub>2</sub>O<sub>3</sub> samples. The transpiration technique works by condensing chromium vapour in a quartz condensation cell or in a fused quartz tube as it exits the furnace. Accurate collection of volatile chromium species from the transpiration technique requires the use of highly concentrated acid (hydrofluoric acid) to dissolve the condensed chromium species from the surface of the quartz tube. Two kinds of analytical instruments, namely inductively coupled plasma-atomic emission spectrometry (ICP-AES) [45,80] and inductively coupled plasma-mass spectrometry (ICP-MS) [48], have been applied to quantify the total amount of evaporated chromium species collected by the traditional condensation-based technique. Opila et al. [80] confirmed the deposition of brown chromic acid (below 600°C) and green

chromia in solid form (between 700 and 900°C) on the tube wall by the transpiration method. The denuder technique uses a quartz tube coated with Na<sub>2</sub>CO<sub>3</sub> on the inner wall to collect the evaporated CrO<sub>2</sub>(OH)<sub>2</sub> [94]. The denuder technique with a chromium collection efficiency of 95±5% has been employed in the current research for the quantification of volatile Cr species. The denuder technique has an accuracy comparable to the mostly used transpiration method, and avoids the requirement to collect Cr with highly concentrated acid. In addition, Cr evaporation can be measured without disturbing the experiment allowing for time dependent evaporation rate measurements. Froitzheim et al. [93] confirmed the protective effect of a 640 nm cobalt coating on a Sanergy HT steel surface with the denuder technique, by measuring a decrease of one order of magnitude in the chromium evaporation rate from the sample with cobalt coating.

#### **2.4.4 Chromium evaporation from alloys**

Most of the leading candidate alloys for use as BOPs in SOFCs form Cr<sub>2</sub>O<sub>3</sub> scales during oxidation. As discussed above, the evaporated Cr(VI) can cause rapid performance degradation of SOFC cathode materials for oxygen reduction. Thus, a material transformation from chromia-forming alloys for CAPH to alumina-forming alloys has been recognised as a promising solution to reduce the Cr evaporation. The Cr evaporation from chromia-forming alloys has been extensively studied and great deal of information is available. However, in literature, little research is available on the quantitative analysis of chromium evaporation from alumina-forming alloys for the Balance of Plant (BOP) application in SOFC. Konysheva et al. [174] employed the transpiration method to measure the chromium evaporation of Crofer 22 APU and Cr<sub>5</sub>Fe<sub>1</sub>Y<sub>2</sub>O<sub>5</sub> alloys and discovered that the total chromium evaporation of Cr<sub>5</sub>Fe<sub>1</sub>Y<sub>2</sub>O<sub>5</sub> alloy was three times higher than that of Crofer 22 APU. The lower amount of chromium evaporation of Crofer 22 APU derived from the

formation of a spinel layer  $(\text{Cr, Mn})_3\text{O}_4$  on the outer surface of the steel, in comparison with the  $\text{Cr}_5\text{Fe}_1\text{Y}_2\text{O}_5$  alloy forming a  $\text{Cr}_2\text{O}_3$  scale on the surface. Sachitanand et al. [99] measured the chromium evaporation behaviour of five commercial ferritic stainless steels: Sanergy HT, ZMG232, E-brite, Crofer 22 APU and Crofer 22 H at  $850^\circ\text{C}$  in a simulated SOFC cathode conditions (6.0 L/min air + 3 vol%  $\text{H}_2\text{O}$ ) with the denuder technique. They found that the accumulated chromium evaporation values after 500 hours of exposure corresponded to the Mn concentration in the alloys, as follows: E-brite with 0.08 wt% Mn ( $0.39 \text{ mg/cm}^2$ ) > ZMG232 with 0.28 wt% Mn ( $0.17 \text{ mg/cm}^2$ ) > Sanergy HT with 0.3 wt% Mn ( $0.14 \text{ mg/cm}^2$ ) > Crofer 22 H with 0.42% Mn ( $0.12 \text{ mg/cm}^2$ ) > Crofer 22 APU with 0.48 wt% Mn ( $0.078 \text{ mg/cm}^2$ ), as shown in Figure 2.24. They stated that a high Mn concentration in the alloy resulted in a low Cr evaporation rate due to the formation of a compact and thick spinel layer  $(\text{Cr, Mn})_3\text{O}_4$ , which further confirmed Konyshева et al.'s findings. The influence of temperature on the chromium evaporation of Sanergy HT was investigated by Falk-Windisch et al. [163] by the denuder technique in a 3%  $\text{H}_2\text{O}$  environment with a flow rate of 6.0 L/min. They reported that the accumulated mass of evaporated chromium over 500 hours decreased from  $0.16 \text{ mg/cm}^2$  to  $0.04 \text{ mg/cm}^2$  with the temperature decrease from  $850^\circ\text{C}$  to  $650^\circ\text{C}$ . It was suggested that the Cr-riched oxide scale formed on the surface of Sanergy HT at  $650^\circ\text{C}$  was much thinner than that formed at  $850^\circ\text{C}$ , leading to high chromium evaporation at higher temperature. Grolig et al. [175] tested the chromium evaporation of stainless steel 441 with the denuder technique in a simulated cathode environment of air with 3%  $\text{H}_2\text{O}$  at  $850^\circ\text{C}$ . The uncoated stainless steel 441 showed a total mass of evaporated chromium around  $0.14 \text{ mg/cm}^2$  after 526 hours of exposure. The high quantity of chromium leakage from stainless steel 441 was attributed to the unstable structure of the oxide scale, leading to massive spallation. Stanislawski et al. [48] studied the chromium evaporation of different Ni-based, Cr-based, and Co-based alloys, chromina austenitic and ferritic steels, and alumina-forming

steels with the transpiration technique in humidified air at 800°C. The total mass of evaporated chromium was reported as follows: Ducrolloy > Nicrofer 45 TM > Ferrotherm 4828 > Nicrofer 7520 > Nicrofer 6025 HT > IT 10 > IT 14 > IT 11 > Conicro 5010 W > AluChrom YHf, as shown in Figure 2.25. The chromium retention ability of a Cr-Mn spinel outer layer with a chromia sublayer was approximately 60 to 70% in comparison with pure chromina-forming alloys. Co-based alloys showed a decrease of chromium leakage of about 90% due to the formation of a  $\text{Co}_3\text{O}_4$  outer layer. It was obvious that AluChrom YHf showed the lowest amount of chromium evaporation over 500 hours among all the steels. The excellent chromium retention capability of AluChrom YHf was attributed to the formation of a highly stable alumina outer layer. This research suggests the alumina-forming alloys as promising materials for BOP application in terms of chromium retention ability.

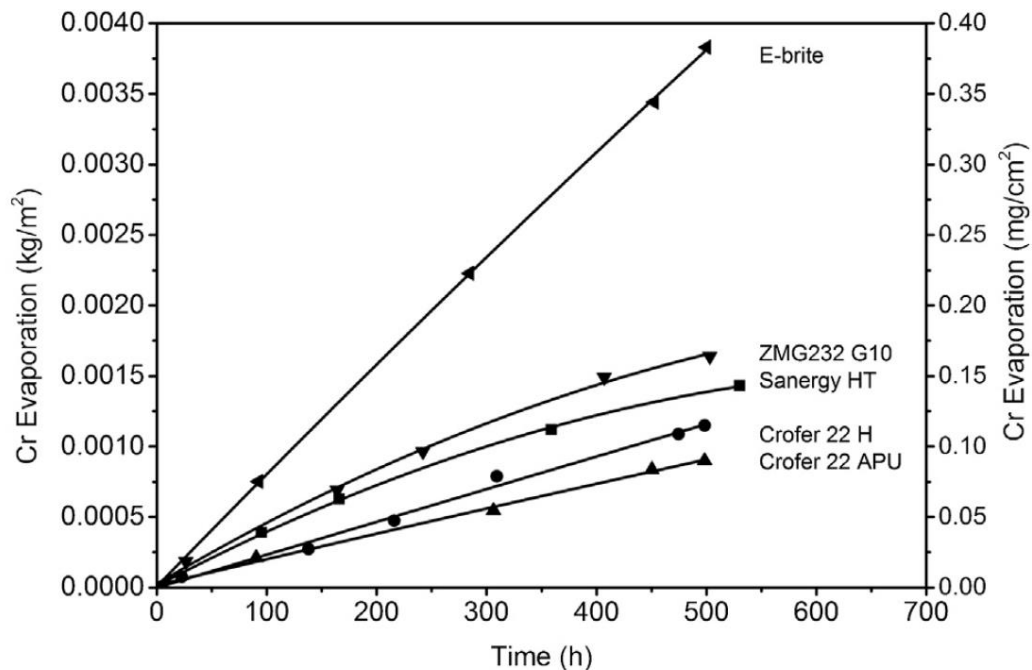


**Figure 2.24** The mass of evaporated chromium per area as a function of time for selective alloys at 850°C in air + 3%  $\text{H}_2\text{O}$  [99].

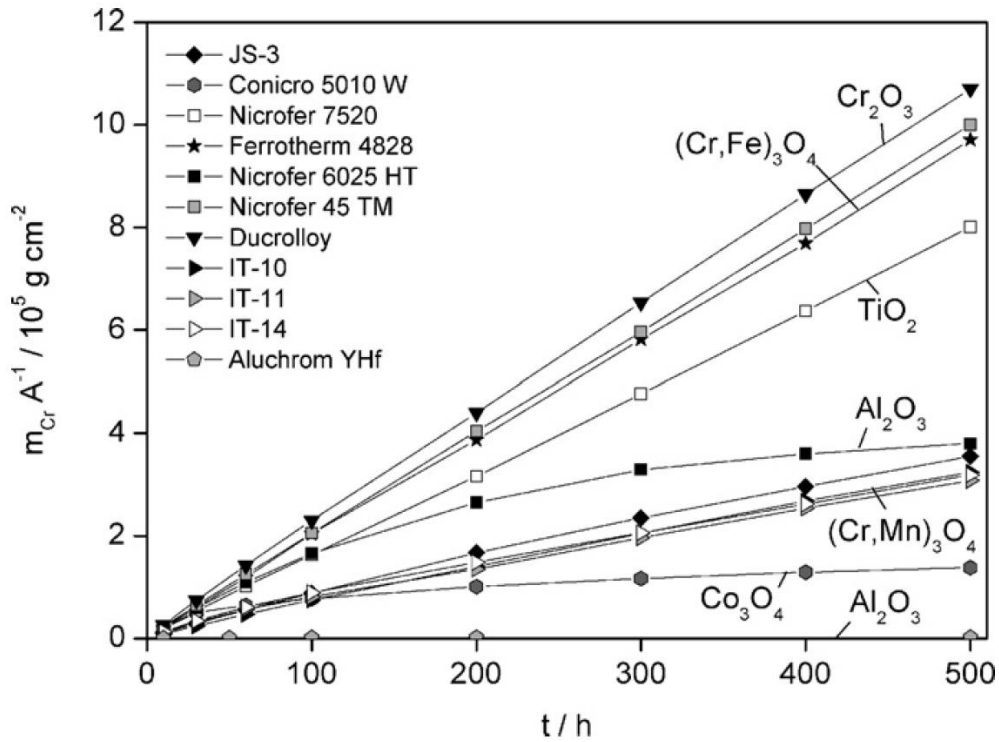


**Figure 2.25** The mass of evaporated chromium per unit area as a function of time for different alloys at 800°C in air with  $p(\text{H}_2\text{O})=1.88 \times 10^{-3}$  pa [48].

Jönsson and Westerlund [176] compared the oxidation behaviour of commercial chromia- and alumina-forming alloys by placing the test coupons in highly sintered alumina crucibles which were exposed in air at 1100 and 1200°C over 1000 hours. Based on the visual inspection of the colour of the crucible inner wall, Haynes 230 showed significantly higher emission of chromium-containing species compared to Kanthal AMP and Kanthal AMPT after long-term exposure at both 1100 and 1200°C. In Figure 2.26, the green colour depth on the inner wall was used to indicate the level of chromium leakage. Gerdes and Johnson [29] exposed materials of representative SOFC BOP component alloys to both humidified and dry air at various temperatures of 600°C, 700°C and 800°C, respectively. They predicted the deactivated SOFC area caused by Cr<sub>2</sub>O<sub>3</sub> deposition by thermodynamic calculation of chromium vapour composition estimated by SEM/EDS and XRD for each alloy. They found that the degradation of SOFC was negligible for alloys exposed to dry air even at 800°C, while the alloys caused various degrees of deactivation on the SOFC cathode in the presence

of water depending on the composition of their oxide scales, as follows: SS316 > AL453 > SS446 > HR 160 > Haynes 214 (4.5% Al). This study determined the superior resistance of the alumina layer formed on Haynes 214 against surface chromium evolution through restraining the ionic mobility of chromium and oxygen throughout the alumina scale. Ge et al. [117] quantitatively measured the chromium evaporation rate of pure chromia, AISI 310S, Nicrofer 6025 (1.8-2.4 wt% Al) and AluChrom YHf (5.5-6 wt% Al) by the transpiration technique in humidified air (3 and 12 pct H<sub>2</sub>O) at temperatures ranging from 800 to 900°C. The measured chromium vaporisation rate for the test samples decreased in the order of pure Cr<sub>2</sub>O<sub>3</sub> > Fe-Cr alloy, AISI 310S > chromia-alumina transition alloy, Nicrofer 6025 HT > alumina-forming alloy, AluChrom YHf. Similar to Stanislawski et al.'s study, the lowest chromium evaporation rate of AluChrom YHf came from the formation of a dense and continuous alumina scale. However, for Nicrofer 6025 HT, the formation rate of the aluminium oxide sublayer was relatively slow, thereby leading to significant chromium leakage.

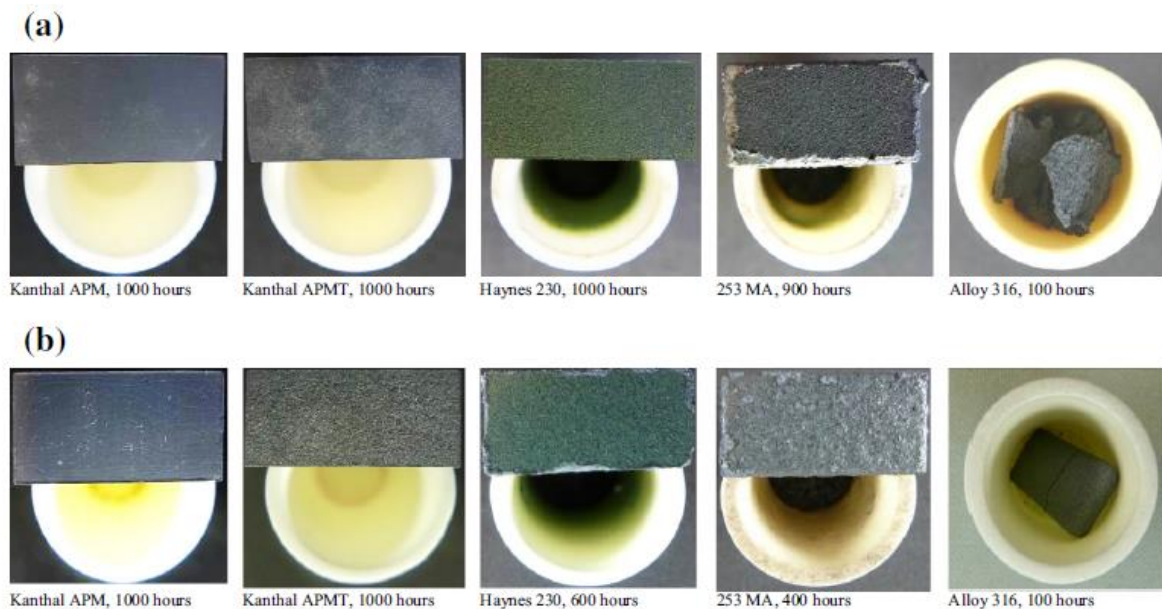


**Figure 2.26** Visual appearance of crucible and alloys after high temperature treatment at (a) 1100°C and (b) 1200°C for 1000 hours [176].

## 2.5 Summary

With the steady decrease in the operating temperature of SOFCs to 500 to 700°C, the heat-resistant alloys have attracted more attention for SOFC CAPH application due to their low material and manufacturing costs compared to the ceramic counterparts. The alloys of interest must contain sufficient Cr and/or Al to protect against corrosion and/or oxidation, and accordingly, can be divided into chromia and alumina-forming alloys. However, the high temperature alloys designed to form pure Cr<sub>2</sub>O<sub>3</sub> as protective layer may not be suitable for the CAPH application as they may be restricted by their thermodynamic instability with respect to evaporation of Cr(VI) species. It appears that the chromia-forming alloys with added Mn element provide enhanced Cr retention capability due to the lowered Cr partial pressure on the (Cr,Mn)<sub>3</sub>O<sub>4</sub> spinel scale. However, it has been verified that the amount of volatile Cr(VI) species from (Cr,Mn)<sub>3</sub>O<sub>4</sub> spinel scale still remains at an unacceptable level relative to the alumina-forming alloys. The alumina-forming alloys have been studied in lower numbers and thus lack literature on application as CAPH in SOFCs. Nevertheless, the limited studies have confirmed the excellent Cr retention capability of alumina-forming alloys used for BOP components in SOFCs. In spite of this, the alumina-forming alloys still face some challenges such as the formation of metastable alumina with lower protection relative to the  $\alpha$ -Al<sub>2</sub>O<sub>3</sub>. Furthermore, the critical amount of Al added to the alumina-forming has to be in a proper range (3 to 5 wt.%) since a high Al content (> 5 wt.%) decreases its creep strength. Thus, there is a need to develop an alloy which can combine the creep strength of a chromia-forming alloy and the Cr retention capability of an alumina-forming alloy such as surface aluminising on chromia-forming alloys. Meanwhile, the optimisation of alumina-forming alloys can be carried out by pre-oxidising the alumina-forming alloys at temperatures which only  $\alpha$ -Al<sub>2</sub>O<sub>3</sub> forms in order to avoid the formation of metastable alumina.

## **Chapter 3 – Experimental**

This chapter will detail the steel substrates investigated in this study. High temperature exposure tests are divided into two parts: chromium evaporation test and long-term oxidation test. Thus, in this chapter, the denuder technique adopted for the quantification of volatile Cr(VI) species and the long-term oxidation test used to determine the oxidation rate in this study are explained. The evaluation of the performance of the alloys is assessed based on both high-temperature exposure tests and characterisation techniques developed for surface analysis. Furthermore, the techniques used in characterising the alloys before and after the high temperature exposure tests are discussed.

### 3.1 Materials

Three commercial high-Cr stainless steels were selected for this research. The samples were cut into coupons of the dimensions 15×15×0.3 mm<sup>3</sup>. The alloy composition for these materials in wt.% is shown in Table 3.1. Additionally, SS309 was also aluminised on both sides in order to compare the high temperature corrosion behaviour with uncoated SS309. A 1 µm thick aluminium layer was applied by Teer Coating Ltd. using a proprietary physical vapour deposition (PVD) process. All samples were tested in as-received condition after having been cleaned in acetone and ethanol using an ultrasonic bath.

**Table 3.1** The chemical compositions of the stainless steel materials investigated in this study.

(wt.%)	Fe	Cr	Mn	Al	Ni	Si	Nb	W	Co	others
Inconel 625	5.0	20-23	0.5	0.4	Bal.	0.5	4.15	-	1.0	Ti: 0.4; Mo: 8-10 P 0.015; S: 0.015
AluChrom 318	Bal.	18.8	0.21	3.58	0.2	0.32	0.73	2.02	--	Hf: 0.06; Y: 0.07 Zr: 0.03; Cu: 0.03 C: 0.01; N: 0.01
SS309	Bal.	22-24	2.0	--	12-15	0.75	--	--	--	C: 0.2; P: 0.045 S: 0.03; N: 0.11

### 3.2 Pre-heat treatment on AluChrom 318

The effect of pre-heat treatment on the AluChrom 318 was investigated with regards to two variables: temperature and dwelling time. All the pre-heat treatments were conducted in a tubular furnace (Vecstar HZ ST 1100) with the samples standing vertically on an alumina plate in air atmosphere (no flow). The samples were heated to the target temperature with a heating rate of 10°C/min, held at the target temperature for the programmed duration, and subsequently cooled down to room temperature inside the furnace. The matrix of pre-treatment conditions is shown in Table 3.2.

**Table 3.2** The matrix for pre-heat treatment conditions of AluChrom 318.

Temperature	Dwelling time		
800°C	1 h	2 h	4 h
900°C	1 h	2 h	4 h
1000°C	1 h	2 h	4 h
1100°C	30 min	1 h	2 h

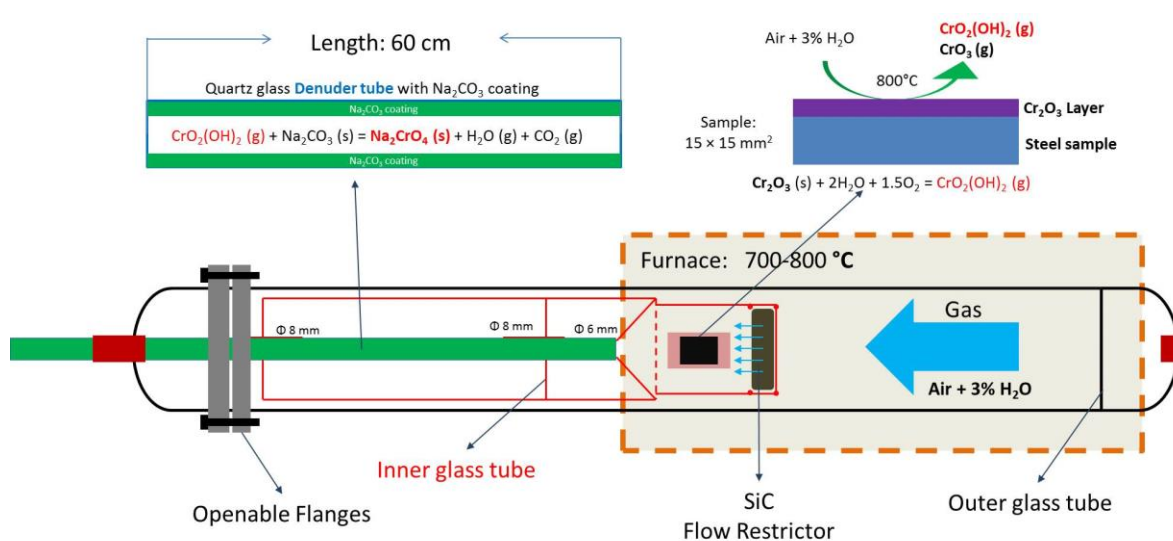


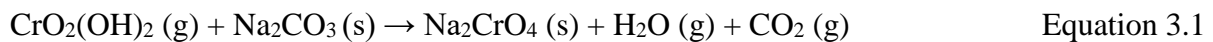
**Figure 3.1** The schematic diagram of denuder technique.

### 3.3 Exposure tests

#### 3.3.1 Cr<sub>2</sub>O<sub>3</sub> evaporation tests

For the Cr<sub>2</sub>O<sub>3</sub> evaporation test, the amount of volatile Cr species was measured by isothermally exposing three identical samples of the stainless steels and employing the denuder technique developed at Chalmers University of Technology [94]. Figure 3.1 illustrates a schematic of the denuder technique for quantitative analysis of Cr volatility. Denuders are usually made of quartz glass tubes. The denuder glassware used in this study was manufactured by Multi-Lab Ltd, UK, based on the design from the High Temperature

Corrosion Centre, Chalmers University of Technology. In a denuder setup, the outer quartz glass tube (black line in Figure 3.1) with an i.d. of 44 mm allowed the gas to pass through, and was sealed with openable flanges to ensure gas tightness. The inner glass tube (red line in Figure 3.1) served as sample holder and support for the denuder tube. The stainless steel samples which had been cut into small metal coupons were placed over the inner glass tube and exposed to high temperature in the furnace. Directly upstream of the samples, a flow restrictor consisting of porous SiC was placed to minimise natural convection and to obtain a more uniform flow pattern. Downstream of the samples, the gas stream was fed through the quartz glass denuder tube (inner diameter: 6 mm and length 700 mm) which was inserted into the inner glass tube. The inner wall of the denuder tube was coated with Na<sub>2</sub>CO<sub>3</sub> used for Cr(VI) collection. The Cr-containing gas (CrO<sub>2</sub>(OH)<sub>2</sub>) produced in the simulated SOFC environment reacted with the Na<sub>2</sub>CO<sub>3</sub> to produce Na<sub>2</sub>CrO<sub>4</sub> on the basis of equation 3.1 [94]:



After the Cr exposure test, the inside wall of the reacted denuder tube was subsequently washed with 10 ml DI water, and the dissolved solution was carefully collected. The new denuder tube with fresh Na<sub>2</sub>CO<sub>3</sub> coating were replaced without cooling down the furnace, allowing the uninterrupted measurement of Cr evaporation. For Inconel 625 and SS309 with high chromium volatility, UV-vis spectrophotometer analysis (Cecil 7500) was applied on the obtained solution to quantify the total amount of Cr(VI) species evaporated from each sample to be tested. For AluChrom 318 with extremely low Cr volatility, the volatile Cr(VI) species evaporated from the samples was far below the detection limit of the UV spectrophotometer (1 ppm). Therefore, the inductively coupled plasma optical emission spectrometry (ICP-OES) with lower detection limit (10 ppb) was employed to quantify the evaporated Cr(VI) species collected by the denuder technique.

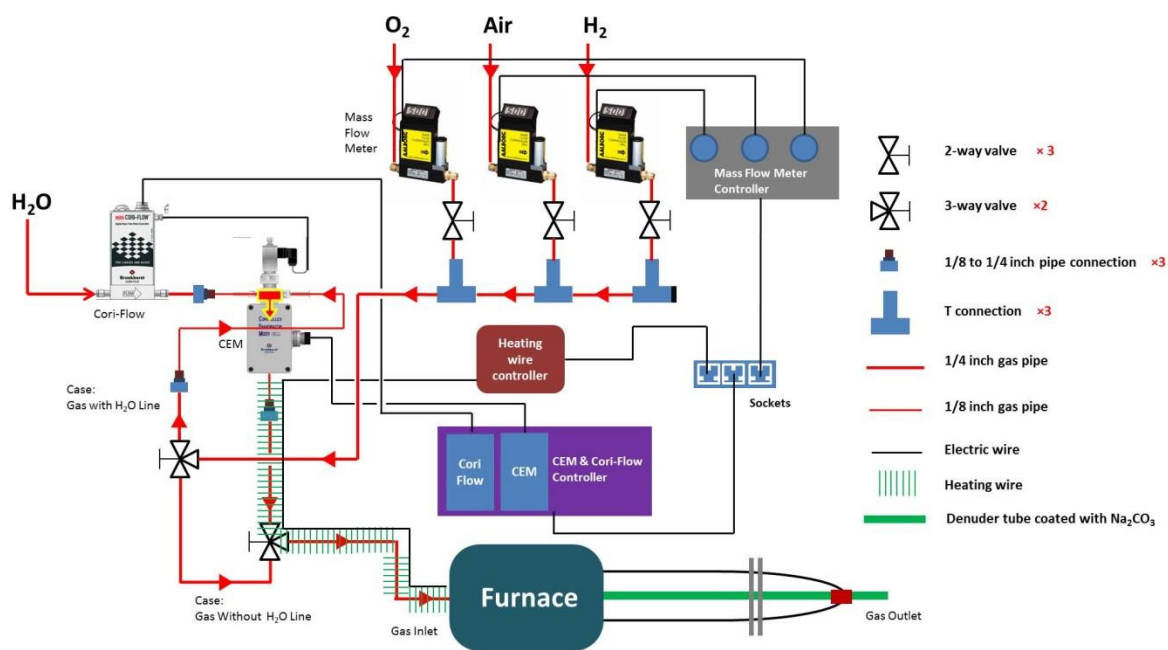


**Figure 3.2** The process flow chart for the denuder technique equipped with Bronkhorst liquid-gas delivery system.

The exposure environment used was comprised of compressed air humidified with water to simulate an SOFC cathode environment. This was prepared by a liquid-gas delivery system from Bronkhorst Ltd. The process flow chart for the denuder set-up equipped with a liquid-gas delivery system is shown in Figure 3.2. Water is injected through a Coriolis mass flow meter (Bronkhorst mini CORI-FLOW 50 g/h) and the volume of air is introduced with a GFC mass flow controller (AALBORG, GFC17, N<sub>2</sub>, 0-10 std L/min). The injected air and water were directed to the gas inlet and liquid inlet of the Controlled Evaporation and Mixture (CEM) unit (Bronkhorst W202A, maximum 10 L/min), respectively, then eventually flowed into the denuder glassware. The air flow rate was controlled to 6.0 L/min which is consistent with the Cr volatilisation test performed in High Temperature Corrosion Centre, Chalmers University of Technology. Froitzheim et al. [94] studied the influence of air flow rate (0.5 to 8 L/min) on the Cr evaporation rate of Sanergy HT at 850°C, as shown in Figure 3.3. They found that at the flow rate 6.0 L/min, which is equivalent to an average velocity of 27cm/s, the chromium evaporation rate was independent of gas flow rate and was controlled by the

material properties alone. Thus, all the exposure tests in this study were performed at 6.0 L/min of air flow to avoid any influence of gas flow rate on the amount of chromium collected. This also allowed to easily compare the Cr evaporation data with the results from Chalmers University [93,94,99,163,177–180]. The humidified air environment was applied after the samples were heated up to 850°C in stagnant air in the furnace.

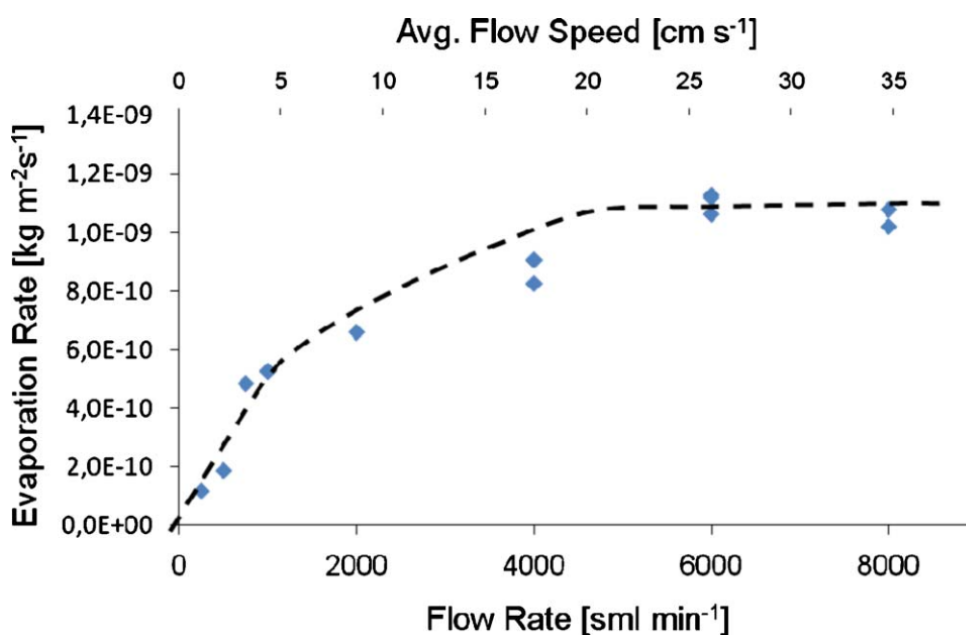


**Figure 3.3** The effect of air flow rate on the Cr evaporation rate of uncoated Sanergy HT. Each test lasted 72 hours [94].

As mentioned above, the  $\text{Na}_2\text{CO}_3$  coating with collected Cr species in the denuder tube was washed off with DI water and then quantified using a UV spectrophotometer. However, the chromium concentration in the solution obtained from the denuder coating was unknown. In order to find out the concentration of the collected chromium, commercial sodium chromate from Sigma-Aldrich was prepared into standard solutions with different concentrations, ranging from 0.05 mM to 0.5 mM. The standard solutions were prepared by diluting the mother solution with  $\text{Na}_2\text{CO}_3$  background solutions to ensure high pH of the solutions and the same background as future samples. The  $\text{Na}_2\text{CO}_3$  background solutions were prepared by leaching the coated denuder tubes (chromium free) with 10 ml DI water after the original

NaOH coating in the denuder tube was converted to Na<sub>2</sub>CO<sub>3</sub> coating by feeding CO<sub>2</sub>. UV-vis spectrophotometer (Cecil 7500) was conducted on these standard solutions and their corresponding spectra are shown in Figure 3.4a. The intensity of the peaks increased with the increase of chromium concentration. The peak values of the second peak around 370 nm were extracted and plotted into a separate graph (Figure 3.4b). Obviously, there is a relatively strong linear relation between the peak intensity and the solution concentration which is in good agreement with the Lambert Beer's law, and can be described as in equation 3.2:

$$A = \varepsilon * l * c \quad \text{Equation 3.2}$$

Where  $A$  is the absorbance,  $\varepsilon$  is the molar absorption coefficient in M<sup>-1</sup>cm<sup>-1</sup>,  $c$  is concentration of the attenuating species in M, and  $l$  is optical path length in cm.

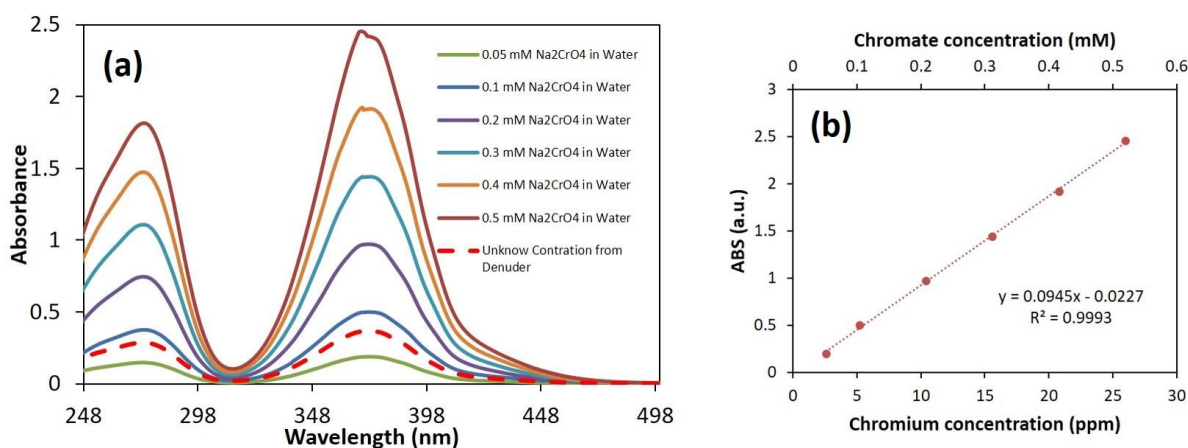


**Figure 3.4** The UV-vis spectra of sodium chromate solution with different concentrations; (b) Extraction and analysis of the peak values of UV-vis spectra.

The UV-vis spectra for the chromium solution with unknown concentration (red dashed line) collected from a pure Cr<sub>2</sub>O<sub>3</sub> pellet by the denuder technique is also shown in Figure 3.4a. The Cr concentration can be calculated from the calibration function (Figure 3.4b) with the peak intensity of the unknown solution. Thus, the Cr concentration was calculated as about 0.088 mM for the unknown solution collected from the denuder tube. The measured Cr concentrations were then converted to the actual mass of Cr<sub>2</sub>O<sub>3</sub> to compare with the mass

change of the  $\text{Cr}_2\text{O}_3$  pellet. The actual weight loss of the  $\text{Cr}_2\text{O}_3$  pellet was measured by weighing the pellet before and after  $\text{Cr}_2\text{O}_3$  evaporation test with a Cubis Micro Balance. The efficiency of the denuder setup for Cr volatiles collection was confirmed to be  $95\pm 5\%$  which is consistent with Froitzheim et al.'s study [94]. This high efficiency indicated that the denuder technique was applicable for the quantitative analysis of Cr(VI) species evaporated from stainless steels. In this study, all the Cr concentrations measured by the UV-vis spectrophotometer and ICP-OES were converted to the mass of  $\text{Cr}_2\text{O}_3$ . Thus, all the accumulated mass loss by Cr evaporation were calculated as the mass loss of  $\text{Cr}_2\text{O}_3$  evaporation and plotted as function of time.

In this study, the  $\text{Cr}_2\text{O}_3$  volatilisation of uncoated Inconel 625, SS309 and AluChrom 318 was investigated regarding the effect of temperature and water content. For the effect of temperature, the three uncoated samples were exposed isothermally for 168 hours at 650, 750 and 850°C in air humidified with 3%  $\text{H}_2\text{O}$  with a total flow rate of 6.0 L/min. For the effect of water content, the three uncoated samples were exposed isothermally for 168 hours at 850°C in air (6.0 L/min) humidified with 1%, 3% and 9% of  $\text{H}_2\text{O}$ . The  $\text{Cr}_2\text{O}_3$  volatilisation of aluminised SS309 was only tested at 850°C in 6.0 L/min air + 3%  $\text{H}_2\text{O}$  to compare the Cr retention capability with uncoated SS309 and AluChrom 318 exposed at the same conditions. The  $\text{Cr}_2\text{O}_3$  evaporation tests for Inconel 625, SS309, aluminised SS309 and AluChrom 318 at 850°C in 6.0 L/min air + 3%  $\text{H}_2\text{O}$  were repeated thrice with good repeatability, which means that the results obtained by the denuder technique are reliable. For the pre-treated AluChrom 318,  $\text{Cr}_2\text{O}_3$  evaporation tests were carried out at 850°C in air (6.0 L/min) with 3%  $\text{H}_2\text{O}$  to investigate the effect of pre-treatment on Cr retention capability of AluChrom 318. For all the  $\text{Cr}_2\text{O}_3$  evaporation tests above, three identical samples of one type were placed in the inner glass of the denuder set-up by standing on an alumina plate to expose two sides. The

humidified air environment was applied after the samples were heated up to the programmed temperature in the furnace. The exposed samples were removed from the denuder glass after 168 hours for gravimetric measurement and characterisations by naturally cooling down the furnace to room temperature.

### 3.3.2 Long-term oxidation tests

A high temperature oxidation test was additionally carried out by exposing different types of materials simultaneously in a tubular glass reactor with an inner diameter of 44 mm to investigate the oxidation behaviour of the exposed samples at long-term. All long-term exposure tests in this study were performed at 850°C with 3% water and 6.0 L/min air flow to simulate the SOFC cathode atmosphere. The humidified air environment was applied after the samples were heated up to 850°C in stagnant air in the furnace. The same Bronkhorst liquid-gas delivery system used in the denuder set-up was also employed in the long-term oxidation set-up to obtain the humidified air environment.

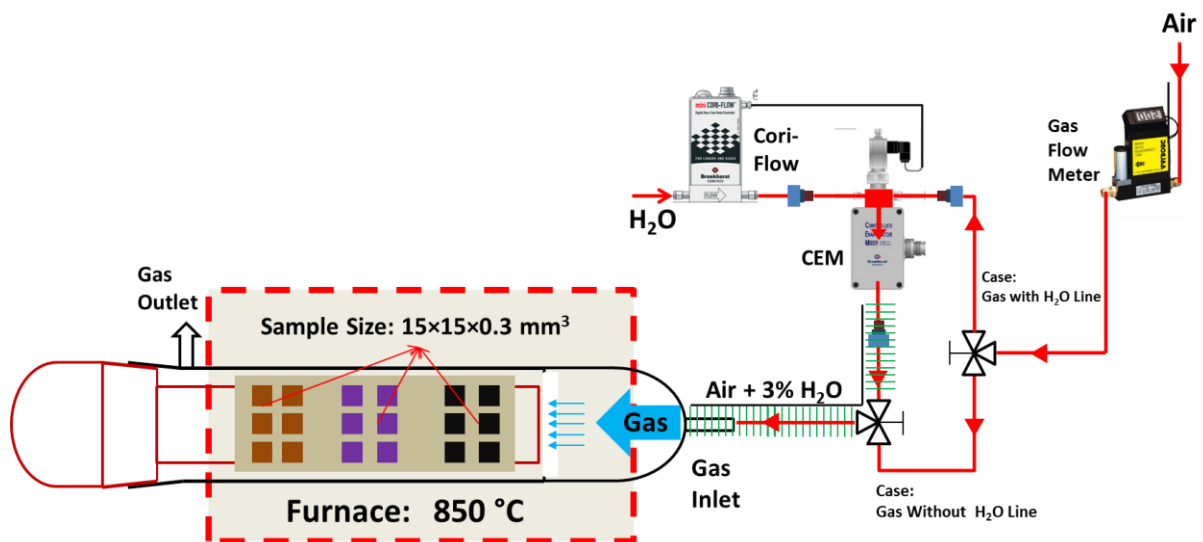


**Figure 3.5** The process flow chart for the long-term exposure set-up equipped with Bronkhorst liquid-gas delivery system.

The process flow chart for the long-term exposure test set-up equipped with a liquid-gas delivery system is shown in Figure 3.5. Six identical samples of each type were placed in the glass reactor by standing on alumina plates to expose two sides. Only two different types of samples were exposed in the furnace during one long-term oxidation test due to the limited length of the hot zone of the furnace. The exposed samples were removed from the glass reactor at regular time intervals for gravimetric measurement and characterisation by naturally cooling down the furnace to room temperature.

### 3.4 Physical characterisation

#### 3.4.1 Mass measurements

The easiest way to quantify the oxidation rate and predict the lifetime of an alloy is mass measurement. For long-term oxidation tests, gravimetric measurements on the exposed samples were conducted as a function of time after each isothermal exposure test by evaluating the mass change of the coupons exposed simultaneously using a high resolution balance capable of measuring six decimal places (Cubis Micro Balance, MSA2.7S0TRDM). For the Cr evaporation tests, the mass change of the exposed coupons was only measured when the 168 hours of Cr evaporation test finished. The mass gain of the coupons after each isothermal exposure were calculated using equation 3.3:

$$\Delta m = \frac{m_{after} - m_{before}}{A} \quad \text{Equation 3.3}$$

Where,  $\Delta m$  is the mass change after each exposure test in mg/cm<sup>2</sup>,  $m_{before}$  is the mass of the coupon before exposure in mg,  $m_{after}$  is the mass of the coupon after each exposure test in mg,  $A$  is the area of the coupon in cm<sup>2</sup>.

However, the oxidation behaviour of alloys in wet air is completely different from that in dry air. The measured mass gain is generally lower than the theoretical value due to the Cr evaporation causing mass loss. With the available Cr evaporation data, the net mass gain of the samples after 168 hours of Cr evaporation test can be corrected by adding the mass of evaporated Cr<sub>2</sub>O<sub>3</sub> to the mass measured by the balance.

### **3.4.2 Scanning electron microscope (SEM)**

In this study, the surface microstructure of non-exposed and exposed samples was studied by scanning electron microscope/energy dispersive X-ray spectrometer (SEM/EDX) (Tabletop Microscope TM3030, Hitachi-Hitec) which can support SE, BSE and mixed imaging programmes. For cross-sectional analysis, the selected coupons were mounted in epoxy by mixing EpoThin™ 2 hardener and resin, subsequently allowing the mounted sample to dry at room temperature over night. The mounted samples were mechanically polished down to 1 µm to obtain cross-sectional analysis with the same SEM/EDX technique. All images were taken at 15kV on backscattering electron mode. Surface SEM images were taken to characterise the morphology and structure of the oxides formed on the alloy surface. Cross-sectional SEM images were taken to study the thickness and layered structure of the oxide scale formed on the alloy surface.

### **3.4.3 Focused ion beam-scanning electron microscope (FIB-SEM)**

A focused ion beam/scanning electron microscope (FIB/SEM) (FIB-SEM, FEI Quanta 3D dual beam) was used to prepare in-situ lift-out TEM specimens for selected AluChrom 318 samples. A rectangle Pt strip with size of 4 × 20 × 4 µm was deposited on the area of interesting on the sample surface by two steps. In the first step, an extremely thin (around 10 nm) Pt layer was coated on the area to be analysed by electron beam in order to avoid damage

of the oxide scale from the second step deposition process which is ion beam deposition. Then a 4  $\mu\text{m}$  Pt layer was deposited on the area of interest by ions in the second step. The process of preparing an in-situ lift-out TEM specimen is outlined as follow:

1. Milling and polishing: use ion beams to mill two deep trenches with size about  $6 \times 20 \times 10 \mu\text{m}$  on both sides of the area of interest. Polish the two sides of the cross-section with ion beams to make the side walls smooth.
2. U-shape cut: use ion beams to mill through the cross-section between the trenches (remaining material section) with a square shape but leave one side of the square not fully milled to keep the sample standing.
3. Attaching the sample to the omniprobe: insert the omniprobe and adjust its position until the probe touches the top of the Pt coating previously deposited on the sample. The probe and sample are welded together by depositing Pt on the joint point. Finally, use Si to cut off the remaining connection on the square cross-section to detach the sample from the base material.
4. Move the omniprobe away from the sample stage and lift out the freed material section. Find the copper grid and place the sample on an appropriate position on the TEM grid. Then weld the sample on the copper grid by depositing Pt and cut joint between the omniprobe and the sample.
5. Finally, thin a part of the sample down to 100-200 nm by polishing with ion beams.

#### **3.4.4 X-ray diffraction (XRD)**

The crystalline structure of the oxide scales formed on the steel surfaces was analysed by X-ray diffraction (XRD) (D2 PHASER 2<sup>nd</sup> generation, Bruker) with Co- $K_{\alpha}$  radiation ( $\lambda=0.179026$ ). The XRD patterns for all the analysed samples were calculated in a  $2\theta$  range

from 20° to 90°. The obtained XRD patterns were analysed using DIFFRAC.EVA 5.1 software for peak identification.

### **3.4.5 TEM and Scanning transmission electron microscopy (STEM)**

The alumina phase could not be detected on the XRD patterns for AluChrom 318 obtained by XRD. Thus, convergent beam electron diffraction (CBED) was carried out on the alumina scale formed on the AluChrom 318 for phase identification. In this study, high resolution imaging was done on a JEOL 2100 LaB6 TEM operated at 200 kV. The TEM is equipped with STEM facilities. This technique was used for imaging the bulk structure, allowing better observations of the crystalline structure of the oxide scale formed on the AluChrom 318 alloy. In addition, CBED was used to identify the phase composition of the oxide scale formed on AluChrom 318. Nevertheless, this instrument was not able to perform elemental mapping and compositional analysis of the analysed specimen using EDX. A FEI Philips TECNAI F20 equipped with an Oxford Instruments ISIS EDS was used to produce STEM images, EDX linescans, EDX maps and EDX spot analyses for the cross-sectional microstructure of the oxide scale grown on the AluChrom 318 sample.

## **Chapter 4 – Effect of Temperature and Water Content on the Oxidation Behaviour and Cr Evaporation of High-Cr Steels for SOFC Cathode Air Preheater\***

Chromium vaporisation and oxide scale growth are probably the two most important degradation mechanisms associated with the cathode air pre-heater (CAPH) made of high Cr-containing alloys in Solid Oxide Fuel Cells (SOFC) systems. The oxide scale growth on a high Cr-containing alloy is also closely interrelated to the  $\text{Cr}_2\text{O}_3$  evaporation. However, both degradation mechanisms of different high Cr-containing alloys strongly depend on the temperature and humidity level the CAPH is subjected to. A high operating temperature applied to the CAPH is known to have a significant effect on the oxide growth and  $\text{Cr}_2\text{O}_3$  evaporation rates. Furthermore, the humidity level of the exhaust gas and ambient air applied to the CAPH cause an increase in the  $\text{Cr}_2\text{O}_3$  evaporation rate. This chapter examines the effect of exposure temperature and water content on both mechanisms for Inconel 625, SS309 and AluChrom 318. For the influence of water content, the Inconel 625, SS309 and AluChrom 318 were isothermally exposed at 850°C in dry air and air containing 1%, 3% and 9% of  $\text{H}_2\text{O}$  at a high flow rate for 168 hours. For the influence of temperature, the Inconel 625, SS309 and AluChrom 318 were isothermally exposed at 650°C, 750°C and 850°C in a 6.0 L/min air stream containing 3%  $\text{H}_2\text{O}$  for 168 hours.

---

\* This work was published in Corrosion Science <K. Zhang, A. El-kharouf, and R. Steinberger-Wilckens. *Corros. Sci.*, Manuscript submitted>.

## 4.1 Results

### 4.1.1 Gravimetric measurements

Figure 4.1a-c shows the effect of exposure temperature on the mass change of Inconel 625, SS309 and AluChrom 318 in air with 3% H<sub>2</sub>O over 168 hours. Under the same water content (3%), the mass change of Inconel 625 decreased with the increase of exposure temperature from 650 to 850°C. The measured mass gains were 9.1  $\mu\text{g}/\text{cm}^2$  and 6.4  $\mu\text{g}/\text{cm}^2$  for Inconel 625 exposed at 650 and 750°C, respectively. However, the Inconel 625 exhibited a mass loss of -0.0159  $\text{mg}/\text{cm}^2$  after exposure at 850°C for 168 hours. In contrast, both SS309 and AluChrom 318 presented an exponential increase of mass gain with the increase of temperature under the same humidity. The observed mass gains for SS309 were 0.0106  $\text{mg}/\text{cm}^2$  at 650°C, 0.0145  $\text{mg}/\text{cm}^2$  at 750°C, and 0.0703  $\text{mg}/\text{cm}^2$  at 850°C over 168 hours. The AluChrom 318 recorded mass gains of 8.9  $\mu\text{g}/\text{cm}^2$ , 0.0191  $\text{mg}/\text{cm}^2$  and 0.122  $\text{mg}/\text{cm}^2$  after exposure for 168 hours at 650, 750 and 850°C, respectively.

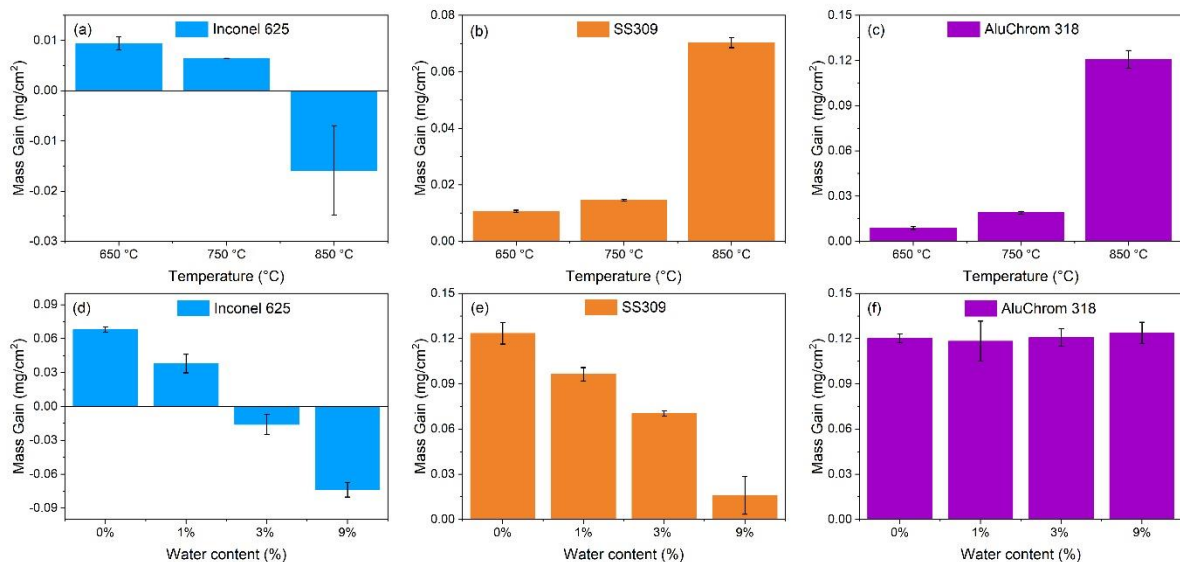


**Figure 4.1** Mass gain of (a) Inconel 625, (b) SS309 and (c) AluChrom 318 isothermally exposed at 650, 750 and 850°C in air with 3% H<sub>2</sub>O for 168 hours; Mass gain of (d) Inconel 625, (e) SS309 and (f) AluChrom 318 isothermally exposed at 850°C in dry air and air containing 1%, 3% and 9% H<sub>2</sub>O for 168 hours.

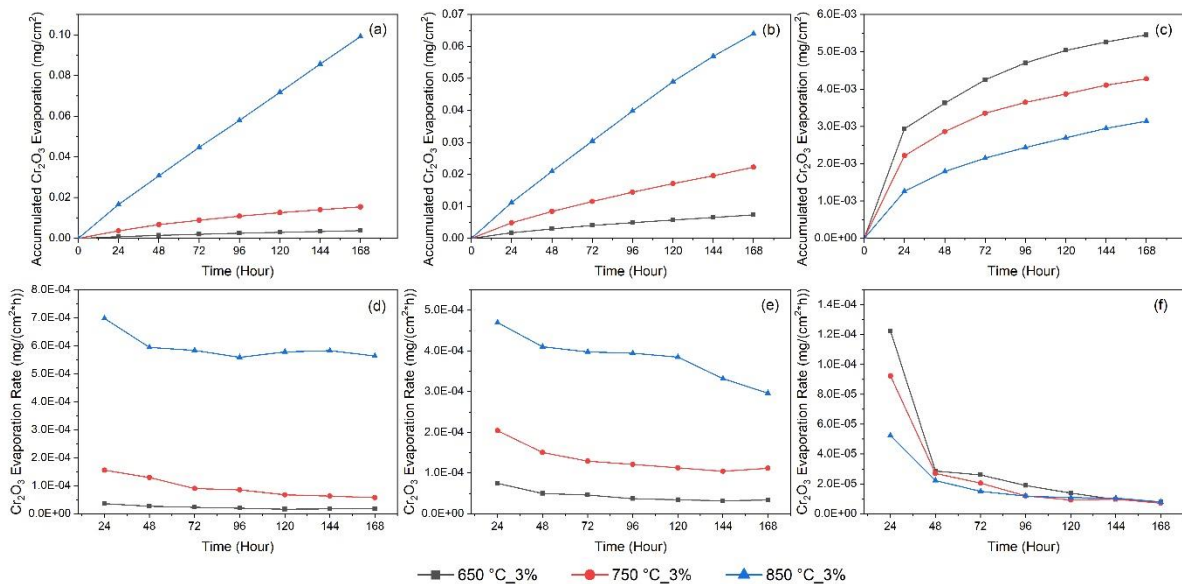
The influence of water content on the mass gain of Inconel 625, SS309 and AluChrom 318 exposed at 850°C for 168 hours is shown in Figure 4.1d-f. At 850°C, the Inconel 625 showed a decreasing trend of mass gain with the increase of water content from 0 to 9%. A mass gain of 0.0379 mg/cm<sup>2</sup> was recorded for Inconel 625 exposed in 1% H<sub>2</sub>O atmosphere for 168 hours, while a mass loss of -0.0737 mg/cm<sup>2</sup> was observed for Inconel 625 exposed in 9% H<sub>2</sub>O atmosphere compared to the samples exposed in 3% H<sub>2</sub>O (-0.0159 mg/cm<sup>2</sup>). The mass gain of SS309 seemed to follow a trend similar to the Inconel 625 but no mass loss was observed. The measured mass gains were 0.0964 mg/cm<sup>2</sup>, 0.0703 mg/cm<sup>2</sup> and 0.0161 mg/cm<sup>2</sup> for SS309 after exposure at 850°C in 1%, 3% and 9% H<sub>2</sub>O, respectively. However, the mass gains remained constant for AluChrom 318 exposed in different water contents at 850°C. The observed mass gains for AluChrom 318 exposed at 850°C were 0.120 mg/cm<sup>2</sup> in 1% H<sub>2</sub>O environment, 0.122 mg/cm<sup>2</sup> in 3% H<sub>2</sub>O environment and 0.126 mg/cm<sup>2</sup> in 9% H<sub>2</sub>O environment.

## 4.1.2 Cr<sub>2</sub>O<sub>3</sub> evaporation measurements

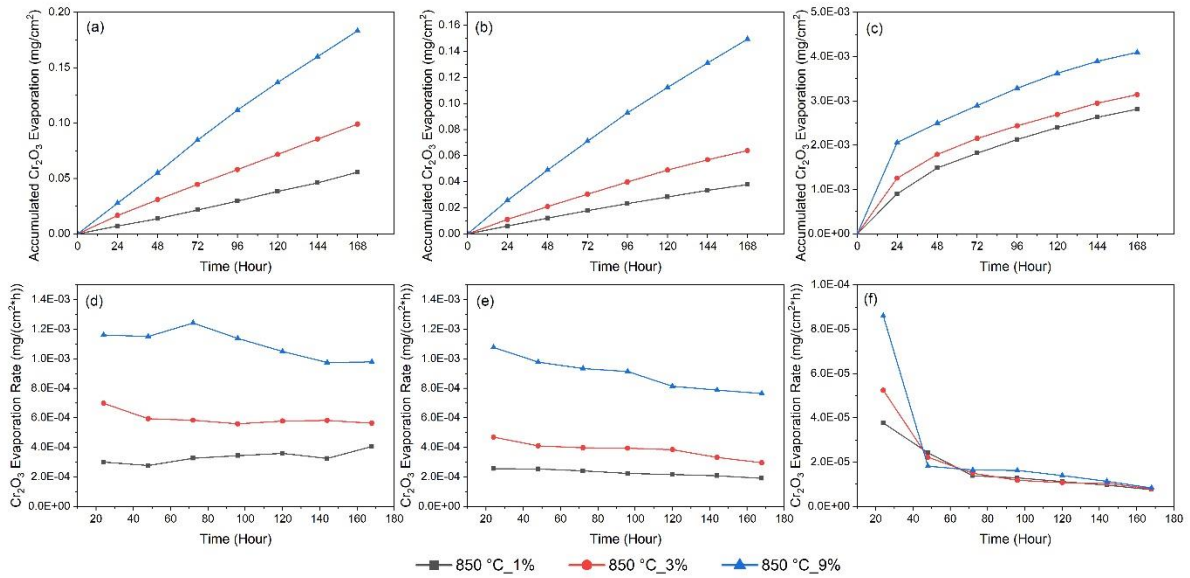
### 4.1.2.1 Influence of temperature

Figure 4.2a-c presents results from denuder technique measurements of Cr<sub>2</sub>O<sub>3</sub> evaporation. They show the influence of temperature on the amount of Cr<sub>2</sub>O<sub>3</sub> evaporation for Inconel 625, SS309 and AluChrom 318 after exposure in 3% H<sub>2</sub>O containing air for a total of 168 hours. Figure 4.2d-f illustrate the rates of Cr<sub>2</sub>O<sub>3</sub> evaporation as a function of time for Inconel 625, SS309 and AluChrom 318 based on the data presented in Figure 4.2a-c. Both Inconel 625 and SS309 showed similar Cr<sub>2</sub>O<sub>3</sub> evaporation behaviour where the total amount and rate of Cr<sub>2</sub>O<sub>3</sub> evaporation decreased with decreasing temperatures. For a total exposure time of 168 hours the quantity of Cr<sub>2</sub>O<sub>3</sub> evaporated from Inconel 625 exposed at 850°C (0.0991 mg/cm<sup>2</sup>) was higher than that from SS309 (0.0640 mg/cm<sup>2</sup>). However, it is interesting to notice that

the Inconel 625 displayed a lower amount of  $\text{Cr}_2\text{O}_3$  evaporation when exposed at  $650^\circ\text{C}$  ( $3.8 \mu\text{g}/\text{cm}^2$ ) and  $750^\circ\text{C}$  ( $0.0155 \text{ mg}/\text{cm}^2$ ) compared to SS309 exposed at  $650^\circ\text{C}$  ( $7.3 \mu\text{g}/\text{cm}^2$ ) and  $750^\circ\text{C}$  ( $0.0223 \text{ mg}/\text{cm}^2$ ), respectively. Correspondingly, Inconel 625 exhibited a higher  $\text{Cr}_2\text{O}_3$  evaporation rate than SS309 when exposed at  $850^\circ\text{C}$  while it had lower  $\text{Cr}_2\text{O}_3$  evaporation rates than SS309 when exposed at  $650$  and  $750^\circ\text{C}$  over 168 hours. However, the AluChrom 318 demonstrated a reverse trend to temperature dependence for  $\text{Cr}_2\text{O}_3$  evaporation compared to Inconel 625 and SS309. For a total exposure time of 168 hours the amount of  $\text{Cr}_2\text{O}_3$  evaporation of AluChrom 318 was measured as follows:  $5.5 \mu\text{g}/\text{cm}^2$  at  $650^\circ\text{C}$   $>$   $4.3 \mu\text{g}/\text{cm}^2$  at  $750^\circ\text{C}$   $>$   $3.1 \mu\text{g}/\text{cm}^2$  at  $850^\circ\text{C}$ .



**Figure 4.2** Accumulated  $\text{Cr}_2\text{O}_3$  evaporation as a function of time for (a) Inconel 625, (b) SS309 and (c) AluChrom 318 isothermally exposed at 650, 750 and  $850^\circ\text{C}$  in air with 3%  $\text{H}_2\text{O}$  for 168 hours; Rate of  $\text{Cr}_2\text{O}_3$  evaporation as a function of time for (d) Inconel 625, (e) SS309 and (f) AluChrom 318 isothermally exposed at 650, 750 and  $850^\circ\text{C}$  in air with 3%  $\text{H}_2\text{O}$  for 168 hours.



**Figure 4.3** Accumulated  $\text{Cr}_2\text{O}_3$  evaporation as a function of time for (a) Inconel 625, (b) SS309 and (c) AluChrom 318 isothermally exposed at  $850^\circ\text{C}$  in air containing 1%, 3% and 9%  $\text{H}_2\text{O}$  for 168 hours; Rate of  $\text{Cr}_2\text{O}_3$  evaporation as a function of time for (d) Inconel 625, (e) SS309 and (f) AluChrom 318 isothermally exposed at  $850^\circ\text{C}$  in air containing 1%, 3% and 9%  $\text{H}_2\text{O}$  for 168 hours.

#### 4.1.2.2 Influence of water content

The influence of water content (1%, 3% and 9%) on the  $\text{Cr}_2\text{O}_3$  evaporation of Inconel 625, SS309 and AluChrom 318 exposed at  $850^\circ\text{C}$  for 168 hours is shown in Figure 4.3a-c. Figure 4.3d-f illustrates the rates of  $\text{Cr}_2\text{O}_3$  evaporation as a function of time for Inconel 625, SS309 and AluChrom 318 based on the data presented in Figure 4.3a-c. All three tested materials showed identical dependence of  $\text{Cr}_2\text{O}_3$  evaporation on the water content. The amount of  $\text{Cr}_2\text{O}_3$  evaporated measured over 168 hours increased with increasing water content at  $850^\circ\text{C}$ . Furthermore, Inconel 625 showed the highest amount of  $\text{Cr}_2\text{O}_3$  evaporation at each water content condition with a total  $\text{Cr}_2\text{O}_3$  evaporation of  $0.0558 \text{ mg/cm}^2$  in 1%  $\text{H}_2\text{O}$ ,  $0.0992 \text{ mg/cm}^2$  in 3%  $\text{H}_2\text{O}$  and  $0.1834 \text{ mg/cm}^2$  in 9%  $\text{H}_2\text{O}$ . The  $\text{Cr}_2\text{O}_3$  evaporation for SS309 exposed in each water content condition was lower than for Inconel 625 under the same conditions. The measured total  $\text{Cr}_2\text{O}_3$  evaporated from SS309 when exposed at  $850^\circ\text{C}$  was

0.0380 mg/cm<sup>2</sup> in 1% H<sub>2</sub>O, 0.0640 mg/cm<sup>2</sup> in 3% H<sub>2</sub>O, and 0.1494 mg/cm<sup>2</sup> in 9% H<sub>2</sub>O over 168 hours. Moreover, as shown in Figure 4.3d&e, SS309 exhibited a tendency for a more rapid decrease in Cr<sub>2</sub>O<sub>3</sub> evaporation rate than Inconel 625 at each water content condition. Obviously, AluChrom 318 always exhibited the lowest amount of Cr<sub>2</sub>O<sub>3</sub> evaporation among the materials tested in each water content environment. The total Cr<sub>2</sub>O<sub>3</sub> evaporation of 2.8 μg/cm<sup>2</sup>, 3.1 μg/cm<sup>2</sup>, and 4.1 μg/cm<sup>2</sup> was recorded for AluChrom 318 exposed at 850°C in 1%, 3% and 9% H<sub>2</sub>O content, respectively. The Cr<sub>2</sub>O<sub>3</sub> evaporation rates of AluChrom 318 exposed to each water content level were all significantly higher in the first 24 hours followed by a rapid decrease to a low value with a slowly further decreasing rate.

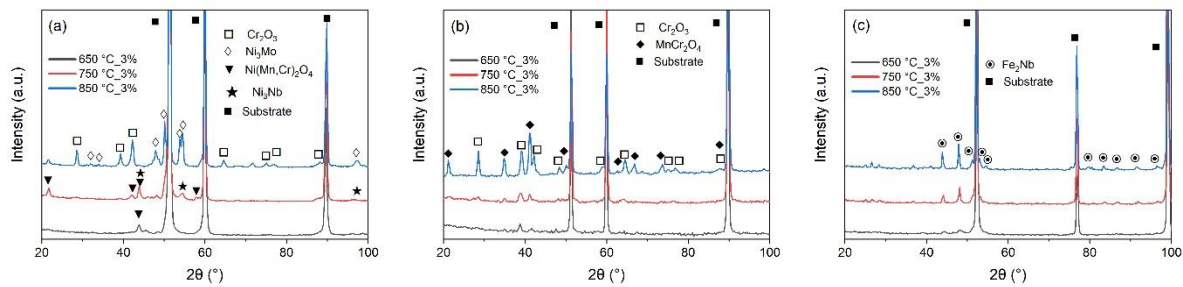


**Figure 4.4** XRD patterns for (a) Inconel 625, (b) SS309 and (c) AluChrom 318 isothermally exposed at 650, 750 and 850°C in air containing 3% H<sub>2</sub>O for 168 hours.

**Table 4.1** Type of the outer oxide scales formed on Inconel 625, SS309 and AluChrom 318 at respective temperatures in air containing 3% H<sub>2</sub>O for 168 hours.

	650°C	750°C	850°C
Inconel 625	External (Mn,Ni)Cr <sub>2</sub> O <sub>4</sub>	External Cr <sub>2</sub> O <sub>3</sub> /(Mn,Ni)Cr <sub>2</sub> O <sub>4</sub>	Mainly external Cr <sub>2</sub> O <sub>3</sub>
SS309	Cr <sub>2</sub> O <sub>3</sub> nuclei doped with Mn	Outer MnCr <sub>2</sub> O <sub>4</sub> nuclei with some Cr <sub>2</sub> O <sub>3</sub>	External MnCr <sub>2</sub> O <sub>4</sub> with internal Cr <sub>2</sub> O <sub>3</sub> and SiO <sub>2</sub>
AluChrom 318	Outer Fe <sub>2</sub> O <sub>3</sub> , Cr <sub>2</sub> O <sub>3</sub> and Al <sub>2</sub> O <sub>3</sub> nuclei	Outer Al <sub>2</sub> O <sub>3</sub> layer with some Fe <sub>2</sub> O <sub>3</sub> and Cr <sub>2</sub> O <sub>3</sub>	Double-layered Al <sub>2</sub> O <sub>3</sub> with Cr <sub>2</sub> O <sub>3</sub> middle layer

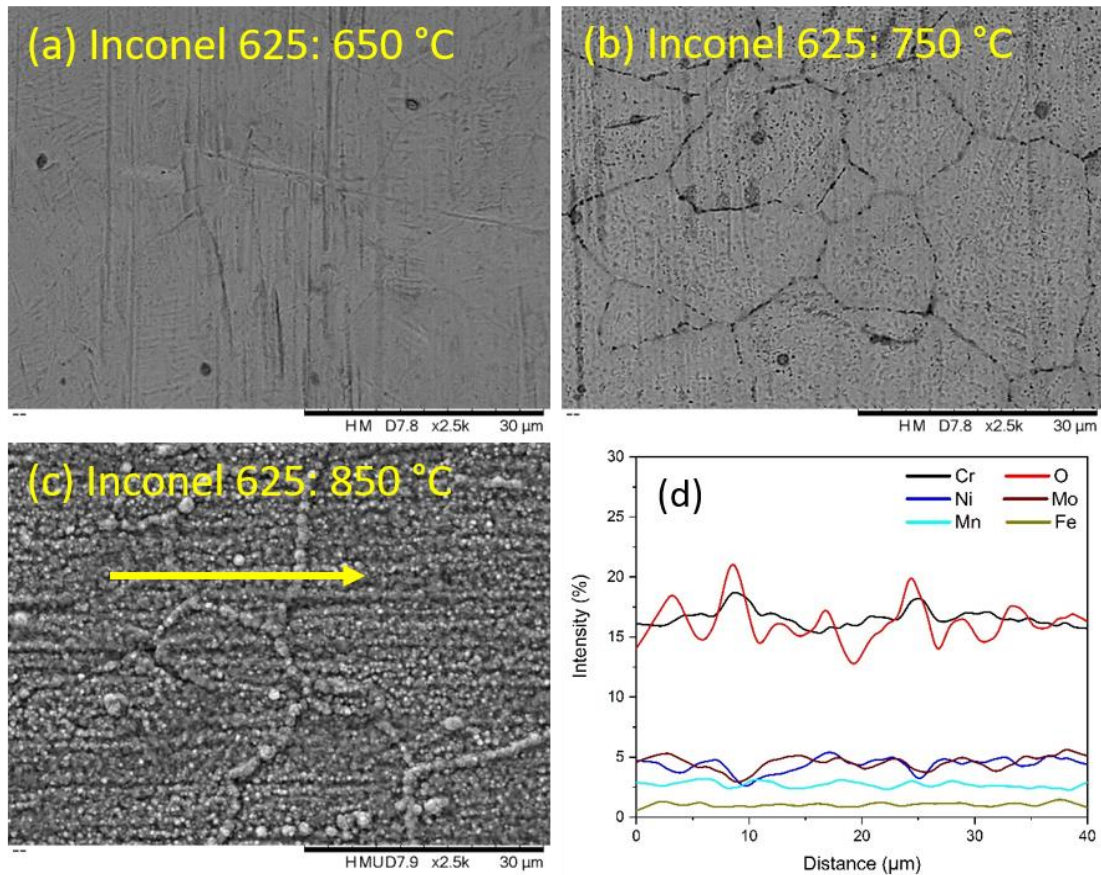


**Figure 4.5** Surface SEM images of Inconel 625 exposed in air with 3% H<sub>2</sub>O for 168 hours at (a) 650°C, (b) 750°C and (c) 850°C; EDX line scan along the line in indicated Figure 4.5c.

### 4.1.3 Microstructural analysis

#### 4.1.3.1 Influence of temperature

The XRD spectrum of Inconel 625, SS309 and AluChrom 318 exposed at 650, 750 and 850°C in air + 3% H<sub>2</sub>O for 168 hours are shown in Figure 4.4a-c. Figures 4.5 to 4.7 demonstrate the surface microstructure of the samples of Inconel 625, SS309 and AluChrom 318 exposed at 650, 750 and 850°C for 168 hours. Table 4.1 shows the type of oxide scales formed on the surface of Inconel 625, SS309 and AluChrom 318 at 650, 750 and 850°C, respectively. The surface of Inconel 625 retained the scratches originating from the steel manufacturing process even after 168 hours exposure at 650°C. For Inconel 625 exposed at 750°C, early nucleation of sub-micron sized oxides started to be visible on the steel surface,

accompanied by even faster nucleation of  $\text{Cr}_2\text{O}_3$  over the alloy grain boundaries. XRD confirmed the presence of  $(\text{Ni,Mn})\text{Cr}_2\text{O}_4$  [89] and  $\text{Ni}_3\text{Nb}$  [181] phases on the surface Inconel 625 exposed at  $750^\circ\text{C}$  for 168 hours. After 168 hours of oxidation at  $850^\circ\text{C}$ , the surface was mostly covered by a porous oxide scale. Moreover, some large oxide nodules were observed along the grain boundaries which might have been produced from the voids detected on the alloy surface exposed at  $750^\circ\text{C}$ . The EDX linescans (Figure 4.5d) show that the surface contained extremely high concentration of Cr and O. The EDX results combined with the XRD analysis indicated the formation of  $\text{Cr}_2\text{O}_3$  scale on the steel surface.

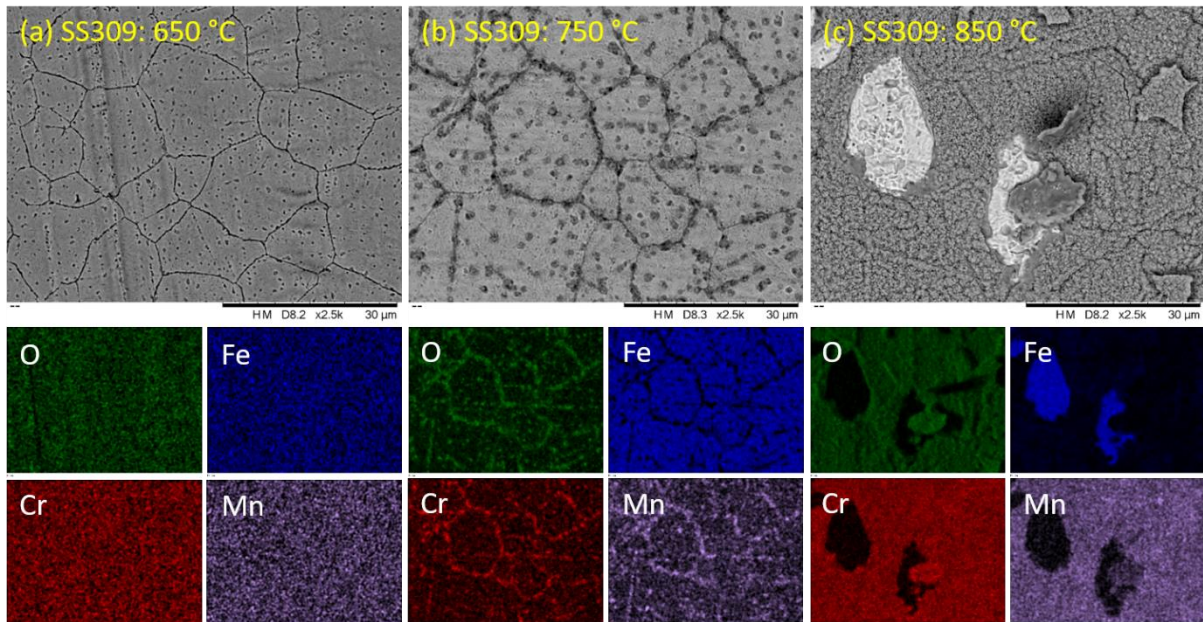


**Figure 4.6** Surface SEM images and EDX element maps of SS309 exposed in air + 3%  $\text{H}_2\text{O}$  for 168 hours at (a)  $650^\circ\text{C}$ , (b)  $750^\circ\text{C}$  and (c)  $850^\circ\text{C}$ .

For SS309, early stage nucleation of a large amount of oxides started to be visible on the steel surface after 168 hours of exposure at  $650^\circ\text{C}$ . These oxide nuclei observed on the surface and grain boundaries had grown much larger after exposure at  $750^\circ\text{C}$  for 168 hours. EDX maps confirmed that these oxide nodules were enriched with Cr, Mn and O. Similar to the SS309 exposed at  $850^\circ\text{C}$  for 100 hours in Chapter 5, a porous oxide scale with severe spallation formed on the SS309 surface after exposure at  $850^\circ\text{C}$  for 168 hours. The formed oxide scale

contained significant amounts of Cr, Mn and O according to EDX analysis. In addition, the edges of the spalled areas below the porous top scale contained exclusively Cr and O. In combination with the XRD patterns shown in Figure 4.4b, it can be concluded that the outer layer was a  $(\text{Cr, Mn})_3\text{O}_4$  spinel-type oxide and the inner layer was  $\text{Cr}_2\text{O}_3$ . The EDX also detected the formation of a  $\text{SiO}_2$  sub-layer (not shown here) on the rear side of the spalled  $(\text{Cr, Mn})_3\text{O}_4$  spinel scale for the SS309 exposed at  $850^\circ\text{C}$ , which was also observed in Chapter 5.

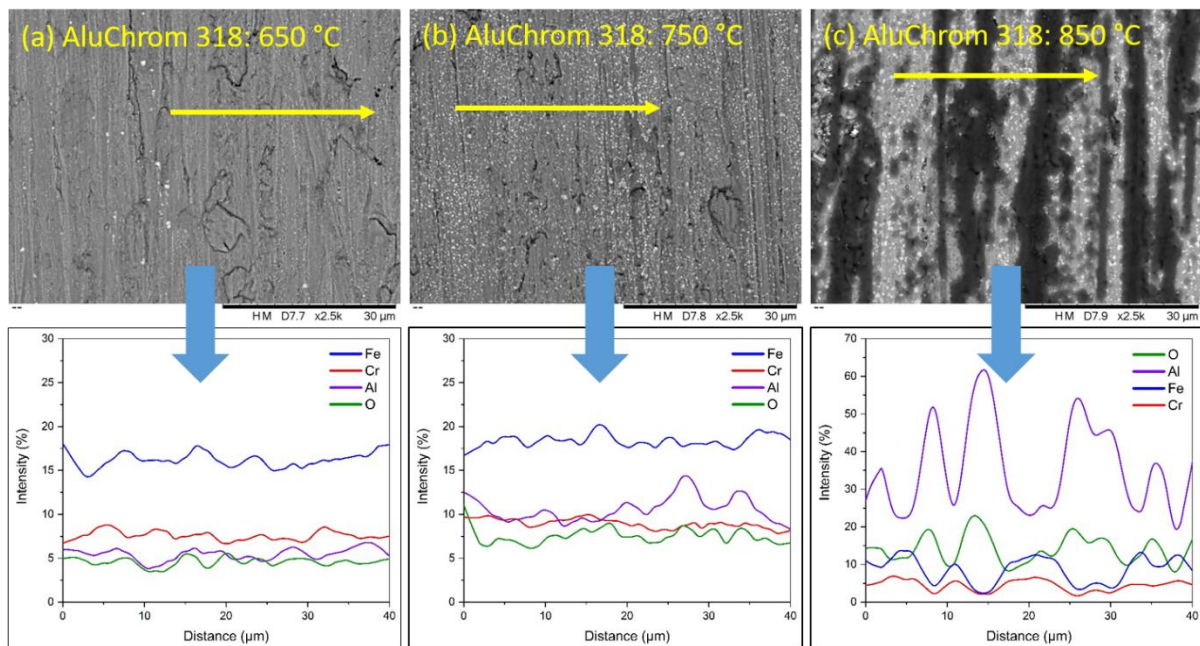


**Figure 4.7** Surface SEM images of AluChrom 318 exposed in air with 3%  $\text{H}_2\text{O}$  for 168 hours at (a)  $650^\circ\text{C}$ , (b)  $750^\circ\text{C}$  and (c)  $850^\circ\text{C}$  with corresponded EDX line scan analysis.

The surface morphologies of the AluChrom 318 exposed at  $650^\circ\text{C}$  and  $750^\circ\text{C}$  for 168 hours were quite similar. At both temperatures, AluChrom 318 formed a thin alumina layer with a number of white spots randomly distributed on the alloy surface. XRD confirmed the white spots present on the surface are  $\text{Fe}_2\text{Nb}$  Laves phases. EDX linescans (Figure 4.7) indicated that Fe was still the dominant element on the alloy surface after exposure at  $650^\circ\text{C}$  and  $750^\circ\text{C}$ . The surface morphology of AluChrom 318 exposure at  $850^\circ\text{C}$  was characterised by oxide ridges which corresponded to high thickness alumina. The plane region between the oxide ridges corresponded to low thickness alumina. However, the phase of the alumina formed on

the AluChrom 318 at 850°C was not possible to be detected by XRD (Figure 4.4c). The reasons for the undetectable alumina phase will be explained in Chapter 5.

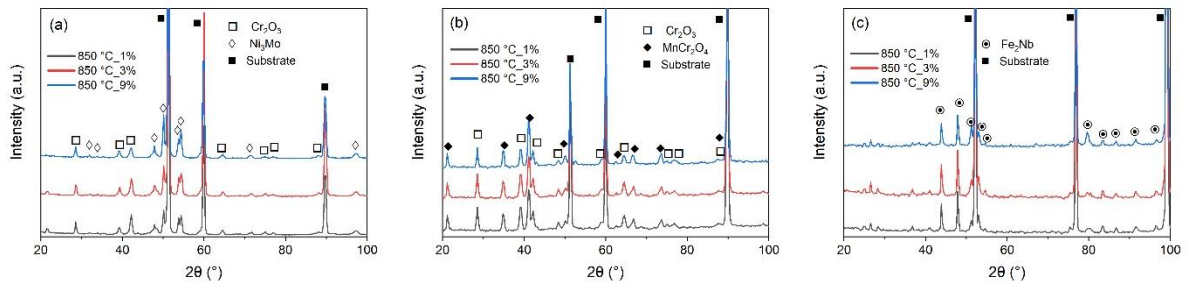


**Figure 4.8** XRD patterns for (a) Inconel 625, (b) SS309 and (c) AluChrom 318 isothermally exposed at 850°C in air containing 1%, 3% and 9% H<sub>2</sub>O for 168 hours.

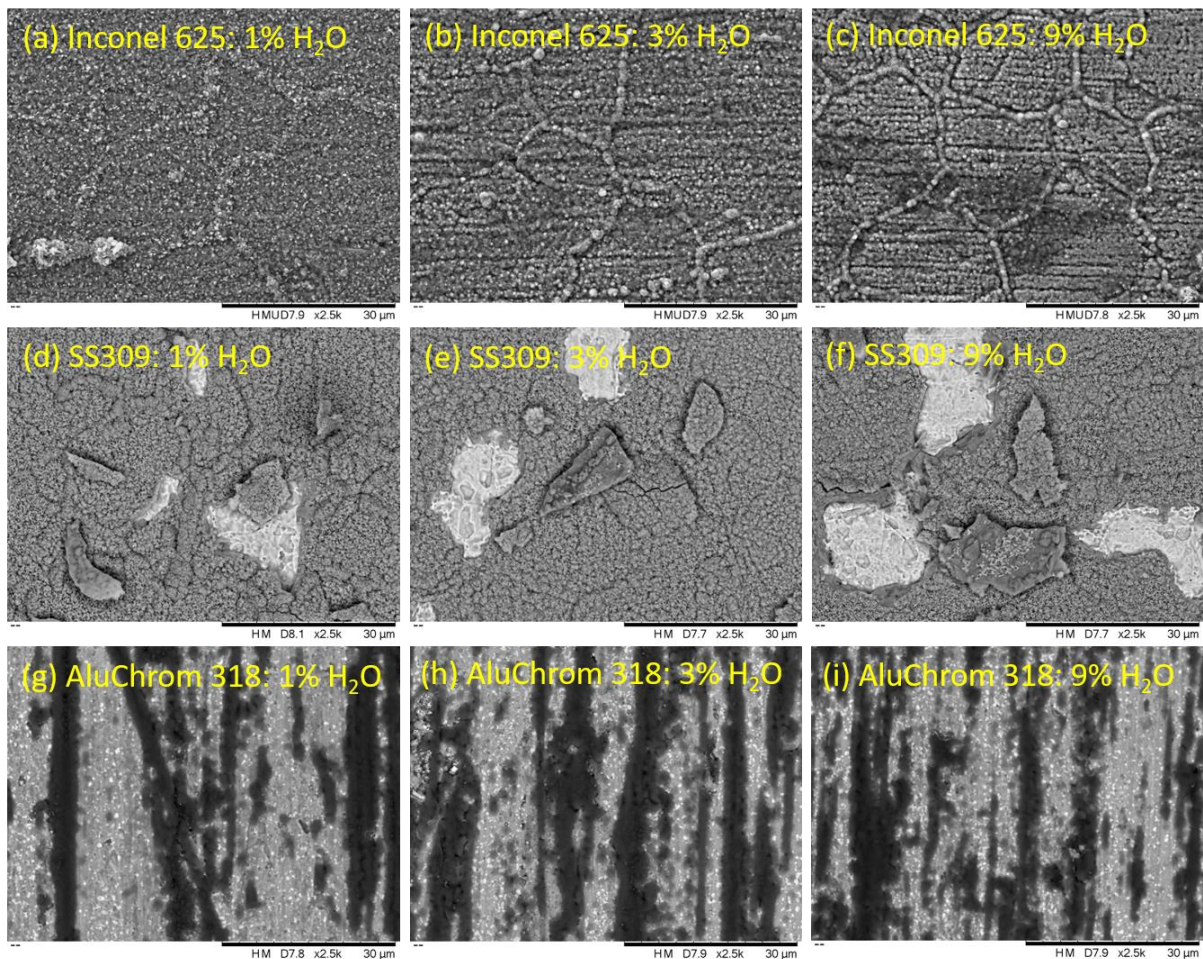


**Figure 4.9** Surface SEM images of Inconel 625 exposed at 850°C in air with (a) 1% H<sub>2</sub>O, (b) 3% H<sub>2</sub>O and (c) 9% H<sub>2</sub>O for 168 hours, SS309 exposed at 850°C in air with (d) 1% H<sub>2</sub>O, (e) 3% H<sub>2</sub>O and (f) 9% H<sub>2</sub>O for 168 hours, and AluChrom 318 exposed at 850°C in air with (g) 1% H<sub>2</sub>O, (h) 3% H<sub>2</sub>O and (i) 9% H<sub>2</sub>O for 168 hours.

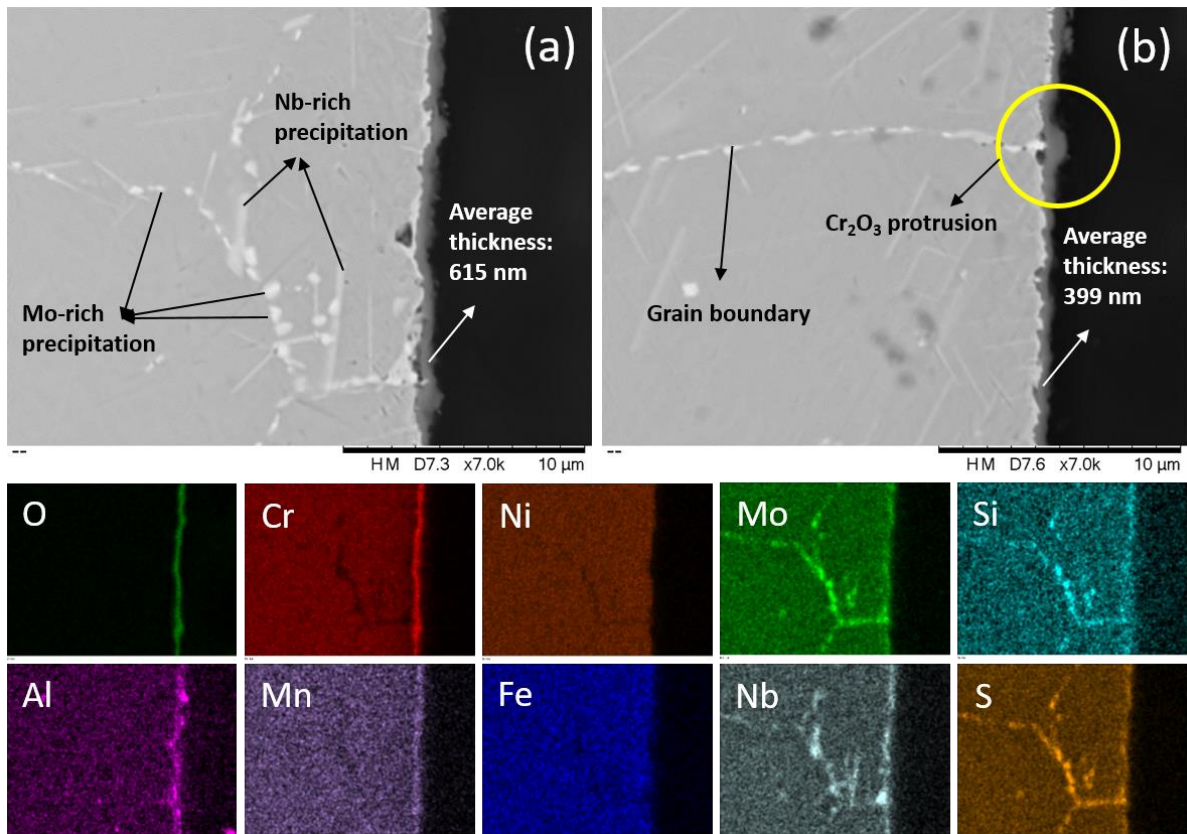


**Figure 4.10** Cross-sectional SEM of Inconel 625 exposed in (a) 1% and (b) 9% H<sub>2</sub>O at 850°C for 168 hours; EDX maps of Inconel 625 exposed in 1% at 850°C for 168 hours.

#### 4.1.3.2 Influence of water content

Figure 4.8a-c shows the XRD spectrum of Inconel 625, SS309 and AluChrom 318 exposed at 850°C in air with 1%, 3% and 9% H<sub>2</sub>O for 168 hours. Figure 4.9 demonstrates the surface microstructure of Inconel 625, SS309 and AluChrom 318 exposed at 850°C in air with 1%, 3% and 9% H<sub>2</sub>O for 168 hours. The surface of Inconel 625 exposed in 1% H<sub>2</sub>O seemed to be filled with chromia scale after 168 hours of oxidation at 850°C. However, the Cr<sub>2</sub>O<sub>3</sub> scale became thinner after exposure in 9% water containing air due to the more pronounced Cr<sub>2</sub>O<sub>3</sub> evaporation with high water content. Cross-sectional SEM images including an EDX map of Inconel 625 exposed at 850°C in 1% and 9% H<sub>2</sub>O are shown in Figure 4.10. From the cross-sectional elemental maps, it can be seen that the oxide scale was mainly made of Cr and O together with a small amount of Al and Mn. The thickness of the chromia scale formed on the

Inconel 625 exposed in 1% H<sub>2</sub>O was around 615 nm while that formed on the Inconel 625 exposed in 9% H<sub>2</sub>O was only 399 nm. The scale layer was also enriched by Nb and Mo near the scale/alloy interface, which is consistent with other studies and suggests the formation of Nb- and Mo-rich precipitates [182]. XRD confirmed the existence of Ni<sub>3</sub>Mo (Figure 4.8a). The Cr<sub>2</sub>O<sub>3</sub> protrusion circled in Figure 4.10b corresponds to the oxide nodules grown from the grain boundary which were detected on the surface SEM (Figure 4.9c).

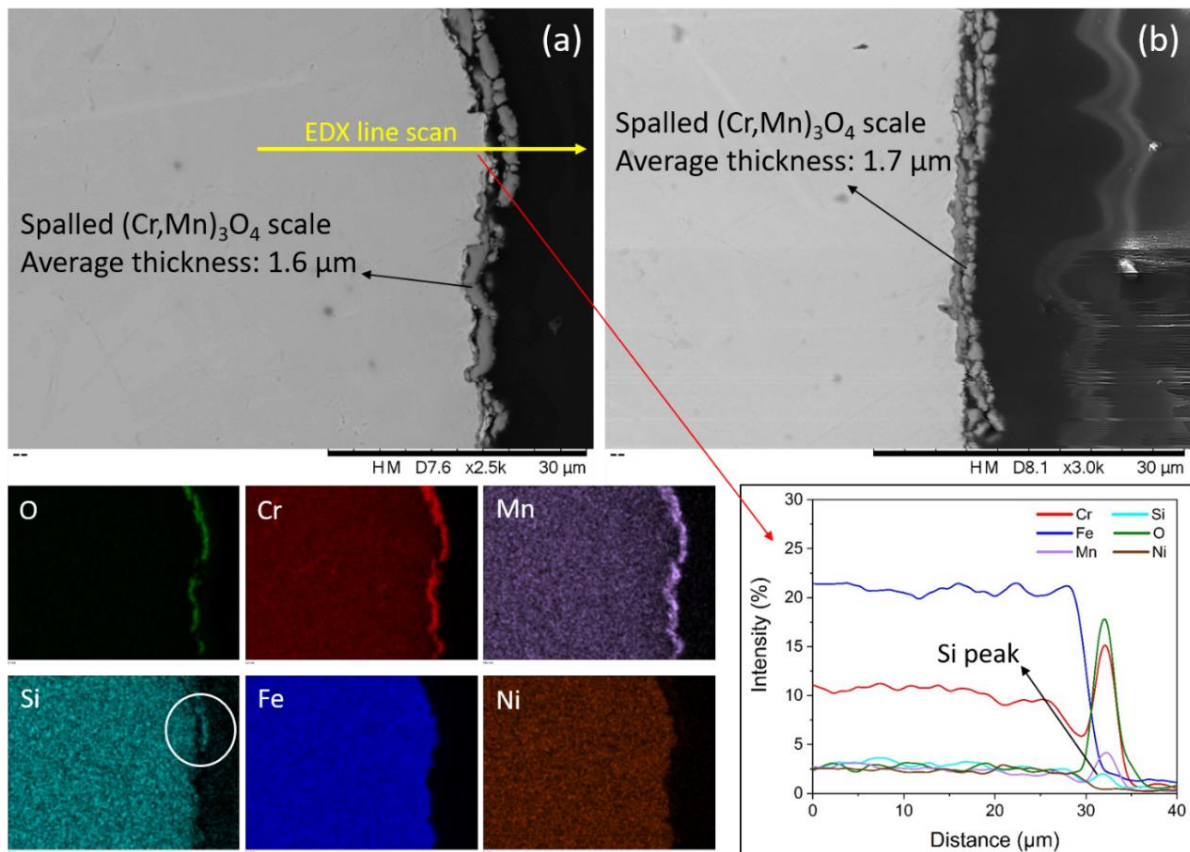


**Figure 4.11** Cross-sectional SEM of SS309 exposed in (a) 1% and (b) 9% H<sub>2</sub>O at 850°C for 168 hours; EDX maps and linescans of SS309 exposed in 1% at 850°C for 168 hours.

SS309 exposed in different water content at 850°C exhibited a similar surface morphology with the spallation of (Cr,Mn)<sub>3</sub>O<sub>4</sub> spinel observed to randomly occur on the surfaces. Figure 4.11 displays the cross-sectional SEM images of SS309 exposed in 1% and 9% H<sub>2</sub>O at 850°C and EDX elemental maps and line scans of the SS309 exposed in 1% H<sub>2</sub>O. The first to be observed from Figure 4.11 is that a serious crack was formed in the oxide scale of the SS309

exposed in both 1% and 9% H<sub>2</sub>O-containing environments. The EDX analysis showed that the cracked scale comprised mainly of Cr, Mn and O, consistent with the (Cr,Mn)<sub>3</sub>O<sub>4</sub> spinel layer. However, it is difficult to distinguish the Cr<sub>2</sub>O<sub>3</sub> from the (Cr,Mn)<sub>3</sub>O<sub>4</sub> layer but XRD confirmed the presence of MnCr<sub>2</sub>O<sub>4</sub> phase and Cr<sub>2</sub>O<sub>3</sub> phase. The inner Cr<sub>2</sub>O<sub>3</sub> layer might be polished off by mechanical polishing during sample preparation for cross-section analysis. Si was detected on the delaminated area of the scale. The cross-sectional microstructure image revealed a similar oxide scale thickness for SS309 exposed in 1% and 9% for 168 hours. By comparing the surface morphologies of AluChrom 318 exposed in different water content, it was easily seen that the water vapour had no obvious influence on the oxide scale growth on the AluChrom 318 surface, which also corresponded with the mass gains measured for the AluChrom 318 oxidised in different water content.

## 4.2 Discussion

### 4.2.1 Cr<sub>2</sub>O<sub>3</sub> evaporation corrected mass gain

The mass gains in Figure 4.1 cannot directly represent the oxidation rate of the high-Cr alloys exposed in the high temperature oxidising environment containing water vapour due to the unavoidable factors such as oxide scale spallation and Cr<sub>2</sub>O<sub>3</sub> evaporation. In order to quantitatively compare the oxidation rate of the alloys exposed under different temperatures and water contents, it is necessary to calculate the gross mass gain by compensating for the material loss caused by Cr<sub>2</sub>O<sub>3</sub> evaporation [99,163]. The gross mass gains were obtained by adding the mass of the evaporated Cr<sub>2</sub>O<sub>3</sub> in Figure 4.2 and 4.3 to the gravimetrically measured net mass gains in Figure 4.1. Subsequently, Figure 4.12 compares the net mass gain and the gross mass gain for Inconel 625, SS309 and AluChrom 318 exposed under different temperatures and water contents for 168 hours. Theoretically, the actual gross mass gains of SS309 exposed at 850°C should be higher than the values presented in Figure 4.12e. Since

the SS309 exposed at 850°C suffered severe scale spallation which is not accounted for, the material loss during sample transfer was inevitable and unpredictable. In Figure 4.12, the difference between the gross mass gain and net mass gain indicates the total loss of Cr<sub>2</sub>O<sub>3</sub> by evaporation over the testing period. Obviously, the AluChrom 318 exposure under different temperatures and water contents showed the smallest difference between the gross mass gain and net mass gain owing to the excellent Cr retention capability of the alumina scale. In the case of Inconel 625 exposed at different temperatures (Figure 4.12a), it was observed that the oxidation rate (gross mass gain) increased when the exposure temperature increased from 650 to 850°C, which marked a complete reversal of the net mass gain. Moreover, the gross mass gains of Inconel 625 and SS309 were also found to increase with higher water content used in the oxidising atmosphere. Othman et al. reported that the growth rate of Cr<sub>2</sub>O<sub>3</sub> on Fe-17Cr and Fe-25Cr alloys in wet oxygen was faster than in dry oxygen [183]. This can be explained by the inward diffusion of OH<sup>-</sup> and H<sub>2</sub>O in the presence of water vapour since the ionic radius of OH<sup>-</sup> is smaller than O<sup>2-</sup>, thereby resulting in a faster effective diffusion of oxygen through the chromia scale [184–186].

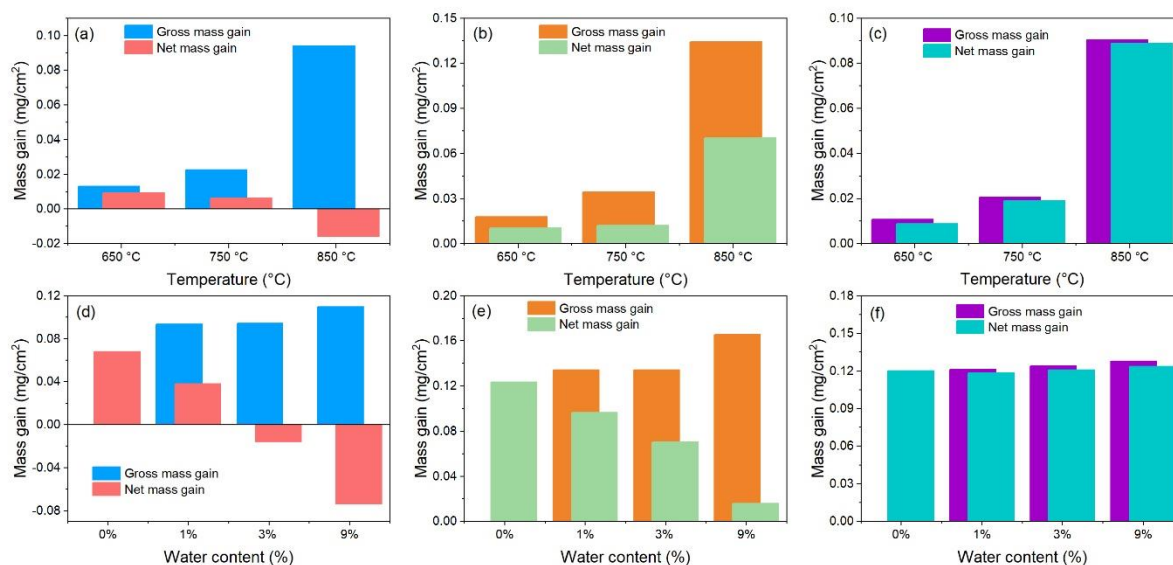


**Figure 4.12** Gross mass gain and net mass gain for (a) Inconel 625, (b) SS309 and (c) AluChrom 318 isothermally exposed at 650, 750 and 850 °C in air + 3% H<sub>2</sub>O for 168 hours; Gross mass gain and net mass gain for (d) Inconel 625, (e) SS309 and (f) AluChrom 318 isothermally exposed at 850 °C in air containing 1%, 3% and 9% H<sub>2</sub>O for 168 hours.

#### 4.2.2 Influence of temperature

The negative mass gain of Inconel 625 exposed at 850 °C can be directly related to the large amount of Cr<sub>2</sub>O<sub>3</sub> loss due to evaporation as volatile Cr (VI) species. As mentioned before, SS309 showed a lower amount of Cr<sub>2</sub>O<sub>3</sub> evaporation than Inconel 625 exposed at 850 °C for the exposure time of 168 hours. At a given temperature, the rate of the evaporation reaction (Equation 2.12) remains constant for all the different alloys when the exposure atmosphere is the same (6.0 L/min air + 3% H<sub>2</sub>O in this work). Stanislawski et al. mentioned that the kinetics of Cr<sub>2</sub>O<sub>3</sub> evaporation were controlled by the evaporation reaction at the oxide scale surface [48]. Therefore, the amount of Cr<sub>2</sub>O<sub>3</sub> evaporated from an alloy solely depends on the partial pressure of Cr present on the oxide surface. The lower amount of Cr<sub>2</sub>O<sub>3</sub> evaporation from (Cr,Mn)<sub>3</sub>O<sub>4</sub> spinel layer is owed to the lower partial pressure of Cr over (Cr,Mn)<sub>3</sub>O<sub>4</sub> compared to pure Cr<sub>2</sub>O<sub>3</sub> scale [163]. The formation and growth of an outer (Cr,Mn)<sub>3</sub>O<sub>4</sub> spinel top layer is dependent on the outward flux of Mn, and, consequently, it can be inferred that

the lower Cr evaporation rate of SS309 is related to the alloying element of Mn. It is well-known that the rate of Mn ion outward diffusion is orders of magnitude faster than that of Cr ions in  $\text{Cr}_2\text{O}_3$  [92,187]. The faster  $\text{Mn}^{2+}$  diffusion through the inner  $\text{Cr}_2\text{O}_3$  layer on the SS309 surface resulted in the rapid growth of a coarse  $(\text{Cr,Mn})_3\text{O}_4$  spinel layer with high defect concentration. Hua et al. [100] found that the oxidation rate of the Fe-Cr alloys strongly depends on the content of Mn in the alloy, suggesting that the fast outward diffusion of  $\text{Mn}^{2+}$  in the Mn-containing alloys results in a much higher oxidation rate compared to the Mn-free Fe-Cr alloys. In the present case, Figure 4.12 shows that the  $\text{Cr}_2\text{O}_3$  evaporation corrected mass gain of SS309 is higher than Inconel 625 exposed at  $850^\circ\text{C}$  for 168 hours, which indicates a higher oxidation rate for SS309 than Inconel 625 exposed at  $850^\circ\text{C} + 3\% \text{H}_2\text{O}$ . It can also be seen in Figure 4.2e that the  $\text{Cr}_2\text{O}_3$  evaporation rate of SS309 exposed at  $850^\circ\text{C}$  in  $3\% \text{H}_2\text{O}$  has a decreasing trend with time, suggesting that the continuous growth of the  $(\text{Cr,Mn})_3\text{O}_4$  spinel layer results in a decreased Cr diffusion rate through the oxide scale with time. Thus, this led to the hypothesis that the positive net mass gain detected for SS309 exposed at  $850^\circ\text{C}$  was due to a faster scale growth rate than the  $\text{Cr}_2\text{O}_3$  evaporation rate. The relatively lower oxidation rate of Inconel 625 might relate to the incorporation of Al in the  $\text{Cr}_2\text{O}_3$  scale. Both Liu et al. and Hou et al. reported that the addition of a low amount of Al (< 1 wt.%) dramatically improved the oxidation resistance of chromia-forming alloys with the formation of an alumina sublayer [124,188]. In addition, the  $\text{Cr}_2\text{O}_3$  evaporation rate of Inconel 625 exposed at  $850^\circ\text{C}$  showed an almost flat trend without decreasing over 168 hours, meaning the termination of  $\text{Cr}_2\text{O}_3$  scale thickening. The rate of  $\text{Cr}_2\text{O}_3$  evaporation was much faster than the scale growth rate of  $\text{Cr}_2\text{O}_3$ , thereby leading to a negative mass gain of the Inconel 625 exposed at  $850^\circ\text{C}$  in air +  $3\% \text{H}_2\text{O}$ .

For Inconel 625 and SS309, the Cr evaporation was dramatically decreased by lowering the exposure temperature from 850 to 750°C and from 750 to 650°C (Figure 4.2a&b). To further investigate the influence of temperature on the Cr evaporation behaviour, the activation energy for the Cr evaporation reaction was calculated using the Arrhenius equation, showing below:

$$\ln(k) = \frac{-E_a}{RT} + \ln(A) \quad \text{Equation 4.1}$$

Where  $k$  is the rate constant of a  $\text{Cr}_2\text{O}_3$  evaporation reaction,  $E_a$  is the activation energy,  $R$  is the universal gas constant,  $T$  is the absolute temperature and  $A$  is the pre-exponential factor. Figure 4.13 exhibits the Arrhenius plot based on the Cr evaporation data from the non-isothermally exposed samples (Figure 4.2). The calculated activation energy of the  $\text{Cr}_2\text{O}_3$  evaporation reaction was 96 kJ/mol for SS309. This value is in good agreement with the 91 and 92 kJ/mol reported by Falk-Windisch et al. for  $\text{Cr}_2\text{O}_3$  evaporation on Sanergy HT and Crofer 22 H, respectively [163]. However, the calculated activation energy of  $\text{Cr}_2\text{O}_3$  evaporation reaction was 177 kJ/mol for Inconel 625. The Arrhenius plot confirmed that the effect of temperature on Cr evaporation was more pronounced in the case of Inconel 625, in comparison with SS309. Falk-Windisch et al. [163] reported the influence of temperatures (650, 750 and 850°C) on Cr evaporation for Crofer 22 H and Sanergy HT which formed  $(\text{Cr,Mn})_3\text{O}_4$  spinel as protective layer for both alloys. They discovered that the amount of evaporated  $\text{Cr}_2\text{O}_3$  was reduced by a factor of 2 to 3 by decreasing the exposure temperature by 100°C, which is in good agreement with the  $\text{Cr}_2\text{O}_3$  evaporation data obtained for SS309 in this work. A reduction of total evaporated  $\text{Cr}_2\text{O}_3$  by a factor of 2.8 was obtained for SS309 when the temperature decreased from 850 to 750°C. A factor of 3 decrease was observed when the temperature decreased from 750 to 650°C. For Inconel 625, by reducing the temperature from 850 to 750°C, the total  $\text{Cr}_2\text{O}_3$  loss by evaporation decreased by a factor of 6,

while the vaporised  $\text{Cr}_2\text{O}_3$  reduced by a factor of 4 with the temperature decreasing from 750 to 650°C.

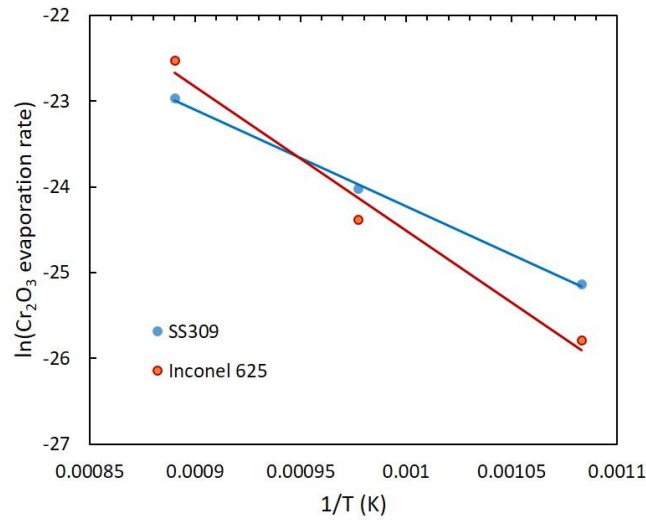


**Figure 4.13** Arrhenius plot showing the influence of temperature on the  $\text{Cr}_2\text{O}_3$  evaporation rate from Figure 4.2 for SS309 and Inconel 625 in 6.0 L/min air with 3%  $\text{H}_2\text{O}$ .

The above discussion also revealed a faster  $\text{Cr}_2\text{O}_3$  evaporation rate for SS309 than Inconel 625 at both 650 and 750°C, which was opposite to the  $\text{Cr}_2\text{O}_3$  evaporation behaviour observed at 850°C. Both Inconel 625 and SS309 exhibited a reduced  $\text{Cr}_2\text{O}_3$  evaporation rate with time at 750°C due to the continuous growth of oxide scales on both materials. As shown in Figure 4.12, by compensating for  $\text{Cr}_2\text{O}_3$  evaporation a higher gross mass gain was observed for SS309 exposed at 650 and 750°C, respectively, compared to Inconel 625, indicating a faster oxidation rate of SS309 than Inconel 625 at both temperatures. However, as the oxide layer formed on the Inconel 625 was mostly confirmed as a  $(\text{Ni},\text{Mn})\text{Cr}_2\text{O}_4$  phase by XRD at 750°C, it can be inferred that the consumption of Cr by evaporation may exceed the resupply from the alloy base. This would cause the amount of the chromia retained on the Inconel 625 surface to drop below the detection limit of the XRD. For SS309, the consumption of Cr by evaporation was fast for SS309 but the evaporated Cr could be rapidly compensated for by diffusion due to the inherent fast formation of the  $(\text{Cr},\text{Mn})_3\text{O}_4$  spinel. This led to a higher Cr

partial pressure on SS309 exposed at 750°C than Inconel 625. The formation of both chromia and spinel phases on the SS309 surface at 750°C was confirmed by XRD as at 850°C. Furthermore, the top view EDX indicated that the surface on SS309 was covered by a large amount of crystallites enriched with Mn and Cr along the alloy grain boundaries and on the sub-micron pores. Thus, the lower partial pressure of Cr on the Inconel 625 surface resulted in higher reduction of Cr<sub>2</sub>O<sub>3</sub> evaporation when the exposed temperature decreased from 850 to 750°C, in comparison with SS309.

As temperature decreased to 650°C, the ion diffusion became significantly slower, which possibly explains the lowest gross mass gain for both materials exposed at 650°C compared to 750 and 850°C. However, unlike SS309, Inconel 625 exposed at 650°C obtained a much higher net mass gain than that exposed at 750°C. The high net mass gain was mainly due to the higher growth rate of the oxide scale compared to the Cr<sub>2</sub>O<sub>3</sub> evaporation rate. However, the XRD pattern of Inconel 625 exposed at 650°C only showed one peak for the (Ni,Mn)Cr<sub>2</sub>O<sub>4</sub> phase without any signal from Cr<sub>2</sub>O<sub>3</sub>. Furthermore, XRD analysis confirmed the presence of chromia and spinel on the SS309 exposed at 650°C but the intensity was much lower compared to 750°C. Moreover, the Cr evaporation rate data indicated that the Cr evaporation rate of Inconel 625 and SS309 exposed at 650°C levelled off at 1.7E-5 and 3.3E-5 mg/(cm<sup>2</sup>\*h) after the first 24 hours, respectively. The constant Cr<sub>2</sub>O<sub>3</sub> evaporation rates imply that the solid state diffusion throughout the thin scale formed at 650°C was unlikely to be the rate limiting step for both alloys. It was pointed out by Neil [61] and Yong [189] that the diffusion through the thin oxide scale developed in the initial stage of oxidation can be very fast and that it does not contribute to rate control, whereas a planar phase boundary process, which is chemisorption of oxygen for oxide formation, might be turned into the rate-determining step for the Cr<sub>2</sub>O<sub>3</sub> evaporation at 650°C [61,189]. The oxide growth pattern on

the SS309 exposed at 750°C (Figure 4.6b) confirmed that the appearance of numerous nucleation sites on the surface and grain boundaries of SS309 exposed at 650°C (Figure 4.6a) facilitated the fast formation of (Cr,Mn)<sub>3</sub>O<sub>4</sub> spinel to contribute to Cr evaporation. However, the Inconel 625 exposed at 650°C lacked these nucleation sites for fast formation of Cr<sub>2</sub>O<sub>3</sub> on alloy surface. In addition, the simultaneously oxidised elements such as Ni, Mn and Mo could result in a low partial pressure of chromia on the alloy surface, thereby suppressing Cr evaporation of Inconel 625 exposed at 650°C.

In contrast to SS309 and Inconel 625, AluChrom 318 exhibited a decreased trend of total amount of Cr evaporation with increasing temperature. However, the Cr evaporation rate of AluChrom 318 only showed a remarkable difference in the first 24 hours as shown in Figure 4.2f. When AluChrom 318 was exposed to high temperature oxidising environment, not only Al oxidised, but Cr and Fe oxidised simultaneously. For AluChrom 318 exposed at 650°C, the alumina scale formed during the first 24 hours could be a non-continuous layer which exposed the simultaneously formed Cr<sub>2</sub>O<sub>3</sub> and Fe<sub>2</sub>O<sub>3</sub> to the oxidising environment. As the temperature increased to 850°C, Al preferentially oxidised over Cr and Fe due to the higher affinity between Al and O [76,79]. Therefore, the Cr<sub>2</sub>O<sub>3</sub> and Fe<sub>2</sub>O<sub>3</sub> formed on the surface during the furnace heating-up stage were covered by the alumina layer. As shown by the TEM study in Chapter 5, the alumina scale formed on the AluChrom 318 at 850°C consisted of an inner  $\alpha$ -Al<sub>2</sub>O<sub>3</sub> layer and an outer metastable alumina layer. A Cr-rich band and Fe-rich band were observed at the interface between the inner and outer alumina layers. In this case, the concentration of Cr retained on the oxide surface of AluChrom 318 exposed at 850°C would be expected to be extremely low.

The kinetics of Cr<sub>2</sub>O<sub>3</sub> evaporation is controlled by the activity of Cr<sub>2</sub>O<sub>3</sub> (evaporation reaction) on the surface in the first 24 hours [48]. Subsequently, the Cr evaporation rate rapidly

decreased to a similar level for AluChrom 318 exposed at the three different temperatures. The dramatic decrease of Cr evaporation rate of AluChrom 318 at all temperatures after 24 hours implied the change of Cr evaporation kinetics. For AluChrom 318 exposed at 850°C, the Cr diffusion through the oxide scale became the rate-determining step for the Cr evaporation once the partial pressure of Cr became low at the surface. The oxide scale on AluChrom 318 formed at 650°C was formed with a low thickness but the rates of Cr<sub>2</sub>O<sub>3</sub> evaporation and oxide formation reactions were also significantly low at that temperature. Although the rate of evaporation reaction at 850°C was much faster than that at 650°C, Cr diffusion through the thick alumina scale formed on the AluChrom 318 at 850°C was extremely low. It has been reported that the solubility of Cr in  $\alpha$ -Al<sub>2</sub>O<sub>3</sub> is only a few percentages at 900°C [136]. In the present case, the exposure temperature (850°C) was lower and the solubility of Cr<sup>3+</sup> in the bottom  $\alpha$ -Al<sub>2</sub>O<sub>3</sub> scale was expected to be lower than that reported at 900°C. It is, therefore, reasonable to see the Cr<sub>2</sub>O<sub>3</sub> evaporation rate of AluChrom 318 exposed to the three different temperatures decreased to a similar level after 24 hours.

#### **4.2.3 Influence of water content**

The Cr evaporation data in Figure 4.3d-e exhibits a direct relation between the water content in the exposure atmosphere and the amount of Cr<sub>2</sub>O<sub>3</sub> evaporated from the alloys; higher water content was seen to result in a higher amount of Cr<sub>2</sub>O<sub>3</sub> evaporation for the alloys exposed at the same temperature. One should bear in mind that the humidified air used in this work was applied when the tested samples inside the furnace reached the programmed temperature (850°C in this study). The same activity of Cr was obtained on the surface of one type of alloy before the different water-containing environments were applied. The Cr<sub>2</sub>O<sub>3</sub> evaporation rate of the alloys exposed at constant temperature would solely depend on the partial pressure of water when the partial pressures of Cr<sub>2</sub>O<sub>3</sub> and O<sub>2</sub> were fixed. Likewise, it

is reasonable to assume that if the amount of  $\text{Cr}_2\text{O}_3$  present on the oxide surface is high enough, the amount of evaporated  $\text{Cr}_2\text{O}_3$  would increase with increasing water content in the exposure environment. This assumption was strongly supported by mass change and  $\text{Cr}_2\text{O}_3$  evaporation data of Inconel 625 and SS309 with both materials found to have an increased  $\text{Cr}_2\text{O}_3$  evaporation with the water content increased from 1% to 9%, which gave rise to a declining trend of mass change for both materials.

By compensating for  $\text{Cr}_2\text{O}_3$  evaporation, the growth rate of  $(\text{Cr,Mn})_3\text{O}_4$  spinel on SS309 was higher than the pure  $\text{Cr}_2\text{O}_3$  on Inconel 625 at different water contents in the present study. Moreover, as was expected, the  $\text{Cr}_2\text{O}_3$  evaporation rate of Inconel 625 was observed to be higher than that of SS309 exposed in 1%, 3% and 9%  $\text{H}_2\text{O}$ , respectively, due to the partial pressure of Cr presented on the pure  $\text{Cr}_2\text{O}_3$  surface being higher than that on the  $(\text{Cr,Mn})_3\text{O}_4$  spinel [48]. After 168 hours, Inconel 625 only showed positive net mass gain when it was exposed to a 1%  $\text{H}_2\text{O}$ -containing environment, suggesting a higher scale thickening rate than the  $\text{Cr}_2\text{O}_3$  evaporation rate. In contrast, a much higher mass loss was obtained for Inconel 625 exposed in 9%  $\text{H}_2\text{O}$  compared to that exposed in 3%  $\text{H}_2\text{O}$ , owing to a much higher  $\text{Cr}_2\text{O}_3$  evaporation rate than the growth rate of the oxide scale under this condition. It has been shown that the chromia scale grown in 9%  $\text{H}_2\text{O}$ -containing atmosphere was much thinner than that formed in 1%  $\text{H}_2\text{O}$ -containing atmosphere (Figure 4.10). Thus, it can be inferred that the water vapour present in the oxidising environment contributed much more to  $\text{Cr}_2\text{O}_3$  evaporation and less to oxide growth. Compared to Inconel 625, the growth of  $(\text{Cr,Mn})_3\text{O}_4$  spinel on SS309 was much less affected by  $\text{Cr}_2\text{O}_3$  evaporation, thereby resulting in a positive mass gain of SS309 even under the severest condition of 9%  $\text{H}_2\text{O}$ . In addition, the thickness of the  $(\text{Cr,Mn})_3\text{O}_4$  spinel formed on the SS309 exposed in 9%  $\text{H}_2\text{O}$ -containing atmosphere was found to be comparable to that established in 1%  $\text{H}_2\text{O}$ -containing atmosphere. This is

because the large loss of  $\text{Cr}_2\text{O}_3$  by evaporation was quickly compensated for by outwards diffusion of Cr to maintain the stoichiometric structure of  $(\text{Cr,Mn})_3\text{O}_4$  spinel over the tested period [48]. It can be proven by XRD analysis that no peak for  $\text{MnO}_x$  or  $\text{Fe}_{1-x}\text{Mn}_x\text{O}_3$  phases was detected in the XRD spectrum of SS309 exposed in 9%  $\text{H}_2\text{O}$  after 168 hours.

The increased amount of  $\text{Cr}_2\text{O}_3$  evaporation with water content was also detected for AluChrom 318 exposed at  $850^\circ\text{C}$ . However, similar to the  $\text{Cr}_2\text{O}_3$  evaporation rate investigated under different temperatures, the  $\text{Cr}_2\text{O}_3$  evaporation rate of AluChrom 318 exposed in different water content also only exhibited a remarkable difference in the first 24 hours. As stated above, the Cr partial pressure on the AluChrom 318 surface would be at the same level when samples in the furnace just reached the target temperature before applying the humidified air to the environment. The  $\text{Cr}_2\text{O}_3$  evaporation rate during the first 24 hours was controlled by the partial pressure of water vapour in the applied atmosphere. Thus, the AluChrom 318 exposed in higher water vapour containing environment promoted higher  $\text{Cr}_2\text{O}_3$  evaporation during the first 24 hours. Moreover, the AluChrom 318 exposed in 9%  $\text{H}_2\text{O}$  seemed to take less time to reduce the rate of  $\text{Cr}_2\text{O}_3$  evaporation to a stable state than those exposed in 1% and 3%  $\text{H}_2\text{O}$  at  $850^\circ\text{C}$ . Once the  $\text{Cr}_2\text{O}_3$  evaporation rate was stabilised, the evaporation of  $\text{Cr}_2\text{O}_3$  from AluChrom 318 started to be controlled by the rate of Cr diffusion through the alumina scale due to the fast growth rate of alumina scale at  $850^\circ\text{C}$ . Liu et al. [136] reported the nucleation of the inner  $\alpha\text{-Al}_2\text{O}_3$  on the isostructural  $\text{Cr}_2\text{O}_3$  and the formation of the outer  $\gamma\text{-Al}_2\text{O}_3$  on Kanthal AF exposed in dry and wet  $\text{O}_2$  at  $900^\circ\text{C}$  for 24 hours. As detected in Figure 4.12f, the net mass gains of the AluChrom 318 exposed under different water content were similar to one another, indicating that water vapour presented in the exposure environment had no effect on the oxidation behaviour of AluChrom 318 exposed at  $850^\circ\text{C}$ . Thus, it is possible to see that the  $\text{Cr}_2\text{O}_3$  evaporation rate of the AluChrom

318 exposed at different water content levelled off at a similar level after 168 hours when the Cr diffusion through the oxide scale became the rate-determining step for  $\text{Cr}_2\text{O}_3$  evaporation. The additional work performed on the AluChrom 318 exposed in dry atmosphere (6.0 L/min air only) revealed a net mass gain of  $0.120 \text{ mg/cm}^2$  after 168 hours, which was very close to the gross mass gains of the AluChrom 318 exposed in 1%, 3% and 9%  $\text{H}_2\text{O}$ -containing environments. However, several studies have confirmed that the oxidation of alumina-forming alloys shows higher mass gain and more formation of metastable alumina in wet atmosphere compared to dry atmosphere [125,135,136,152,153,155,158,190,191]. Engkvist et al. [158] investigated the corrosion behaviour of Kanthal APMT in dry  $\text{O}_2$  and  $\text{O}_2 + 40\%$   $\text{H}_2\text{O}$  for 72 hours at 900, 1000 and 1100°C. Gotlind et al. [152] measured the mass gain of Kanthal AF after exposure in both dry  $\text{O}_2$  and  $\text{O}_2 + 40\%$   $\text{H}_2\text{O}$  at 900°C for 168 hours.

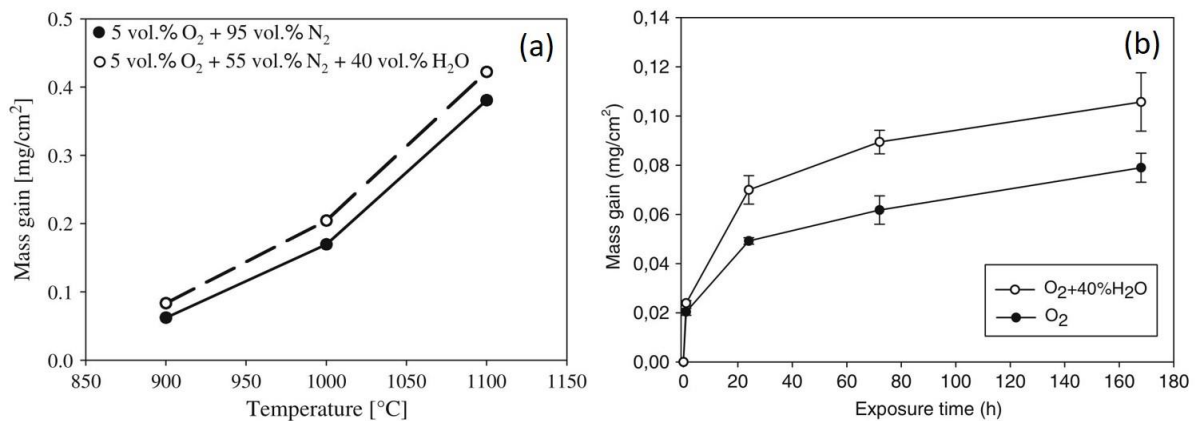


**Figure 4.14** Mass gain curves of (a) Kanthal APMT exposed in 5%  $\text{O}_2 + 95\%$   $\text{N}_2$  and 5%  $\text{O}_2 + 55\%$   $\text{N}_2 + 40\%$   $\text{H}_2\text{O}$  at 900-1100°C for 72 hours [158] and (b) Kanthal AF oxidised in  $\text{O}_2$  and  $\text{O}_2 + 40\%$   $\text{H}_2\text{O}$  at 900°C for 168 hours [152].

The gravimetrically measured mass gains from Engkvist et al. and Gotlind et al.'s studies are presented in Figure 4.14. It is worth noting that even when 40%  $\text{H}_2\text{O}$  was applied in the oxidising environment in their studies, the excess mass gain caused by water vapour was still extremely small. In the present case, the amount of water vapour applied in the atmosphere was much lower and so the influence of the water vapour on the oxidation behaviour was,

thus, expected to be negligible. Kvernes et al. [125] reported that the oxidation of Fe-13Cr-4.4Al alloys was not significantly dependent on the humidity level in the air once the continuous Al<sub>2</sub>O<sub>3</sub> scale was formed at 680, 820 and 920°C. This reveals that the water vapour might have had a more significant effect on the initial stages of oxidation and influence the stability of the metastable alumina rather than the transport process in the protective  $\alpha$ -Al<sub>2</sub>O<sub>3</sub> scale once it was developed [190]. In this study, the prior formed alumina scale during the furnace heating process to 850°C might have also prohibited the observation of the effect of water vapour on the growth of the alumina scale on the AluChrom 318 surface.

### 4.3 Conclusions

This work focused on the effect of the exposure temperature and water content on the oxidation behaviour and Cr<sub>2</sub>O<sub>3</sub> evaporation of Inconel 625, SS309 and AluChrom 318. Inconel 625 showed higher Cr evaporation than SS309 exposed at 850°C in 3% H<sub>2</sub>O due to the higher partial pressure of Cr presented on the pure Cr<sub>2</sub>O<sub>3</sub> than the (Cr,Mn)<sub>3</sub>O<sub>4</sub> spinel. The Cr<sub>2</sub>O<sub>3</sub> evaporation was dramatically reduced with lower temperatures for Inconel 625 and SS309. However, by lowering the temperature by 100°C, a more pronounced reduction in Cr<sub>2</sub>O<sub>3</sub> evaporation was detected for Inconel 625 than for SS309. SS309 was found to demonstrate a higher oxidation rate than Inconel 625 at both 650 and 750°C, which resulted in a higher Cr partial pressure on the SS309 surface. The AluChrom 318 showed the lowest Cr<sub>2</sub>O<sub>3</sub> evaporation level at all the investigated temperatures among the three tested materials. However, a higher Cr<sub>2</sub>O<sub>3</sub> evaporation was observed for AluChrom 318 when it was exposed at lower temperature. The highest Cr<sub>2</sub>O<sub>3</sub> evaporation of AluChrom 318 exposed at 650°C occurred because the alumina scale formed at low temperature could not cover the simultaneously formed Cr<sub>2</sub>O<sub>3</sub>.

The major effect of water vapour on the three tested materials was the enhanced evaporation of  $\text{Cr}_2\text{O}_3$  with higher water content applied in the oxidising atmosphere. At  $850^\circ\text{C}$ , the amount of evaporated  $\text{Cr}_2\text{O}_3$  from the alloys exposed in the same humidity level corresponded to the Cr partial pressure on the surface, as follows:  $\text{Cr}_2\text{O}_3$  (Inconel 625) >  $(\text{Cr,Mn})_3\text{O}_4$  spinel (SS309) >  $\text{Al}_2\text{O}_3$  (AluChrom 318). When the net mass gains were compensated for the Cr evaporation, it was observed that the water vapour slightly increased the growth rate of the  $\text{Cr}_2\text{O}_3$  and  $(\text{Cr,Mn})_3\text{O}_4$  spinel formed on the Inconel 625 and SS309. However, no evidence was observed that the growth rate of the protective alumina was influenced by the presence of water vapour in the oxidising atmosphere for the tested period in this study.

## **Chapter 5 – The effect of aluminium addition on the high temperature oxidation behaviour and Cr evaporation of aluminised and alumina-forming alloys for SOFC cathode air pre-heaters\***

The previous chapter confirmed that the AluChrom 318 showed the best anti-corrosion performance and Cr retention ability under different temperatures and water content due to the formation of an alumina scale as protective layer. For material optimisation, a protective alumina layer was applied on the SS309 surface by coating the alloy surface with pure aluminium and subsequently oxidising. This research was conducted to investigate whether the corrosion resistance and Cr<sub>2</sub>O<sub>3</sub> evaporation performance of SS309 can be improved by surface aluminising. Thus, the purpose of this chapter is to quantitatively measure the Cr(VI) species evaporated from uncoated SS309, aluminised SS309 and AluChrom 318 by means of the denuder technique at the temperature of 850°C. In addition, the suitability of aluminised and alumina-forming high-Cr alloys for CAPH application concerning the reduction of Cr<sub>2</sub>O<sub>3</sub> evaporation will be discussed.

---

\* This work was published in ECS Transactions <K. Zhang, J.E. Hong and R. Steinberger-Wilckens. *ECS Trans.*, 78 (2017) 1641-1651> and Corrosion Science <K. Zhang, A. El-kharouf, J.E. Hong and R. Steinberger-Wilckens. *Corros. Sci.*, 169 (2020) 108612>.

## 5.1 Results

### 5.1.1 Mass measurements

The isothermal oxidation kinetics, represented by the mass gain as a function of time for SS309, aluminised SS309 and AluChrom 318 exposed at 850°C with a flow of 6.0 L/min air (3% H<sub>2</sub>O) for 2500 hours are presented in Figure 5.1a. Figure 5.1b shows the plot of mass gain rate as a function of time. Up to 500 hours, the SS309 showed a roughly parabolic oxidation behaviour with a mass gain of 0.079 mg/cm<sup>2</sup>. However, the sample revealed an abrupt mass loss up to 2500 hours. The aluminised SS309 showed a rapid mass gain of 0.160 mg/cm<sup>2</sup> up to 1000 hours, displaying a much higher mass gain rate than that of uncoated SS309 due to the fast and direct reaction between Al and O during the initial oxidation. However, the aluminised SS309 started to suffer a mass loss after 1000 hours exposure mainly because of the exfoliation of the formed alumina scale. The AluChrom 318 with 3.58 wt.% of Al content exhibited a continuous mass increase over 2500 hours with an ultimate mass gain of 0.202 mg/cm<sup>2</sup>, with oxidation kinetics following a parabolic law. No mass loss was observed, implying a continuous growth of alumina scale on the alloy surface.

### 5.1.2 Cr<sub>2</sub>O<sub>3</sub> evaporation

The results of the time resolved Cr<sub>2</sub>O<sub>3</sub> evaporation tests are presented in Figure 5.1c. Figure 5.1d shows the plot of Cr<sub>2</sub>O<sub>3</sub> evaporation rate as a function of time. A total value of 0.0078 mg/cm<sup>2</sup> evaporated Cr<sub>2</sub>O<sub>3</sub> was recorded for aluminised SS309 after 168 hours exposure, 0.0028 mg/cm<sup>2</sup> was obtained for the AluChrom 318, whereas the bare SS309 had a total value of evaporated Cr<sub>2</sub>O<sub>3</sub> of 0.064 mg/cm<sup>2</sup> after the same oxidation time. The aluminised SS309 showed a slight increase in the rate of Cr<sub>2</sub>O<sub>3</sub> evaporation with time. This phenomenon was caused by spallation of the formed alumina scale which will be discussed later in the section

of microstructure analysis. However, the  $\text{Cr}_2\text{O}_3$  evaporation rate of AluChrom 318 decreased with time because of the increase of alumina scale coverage on the alloy surface.

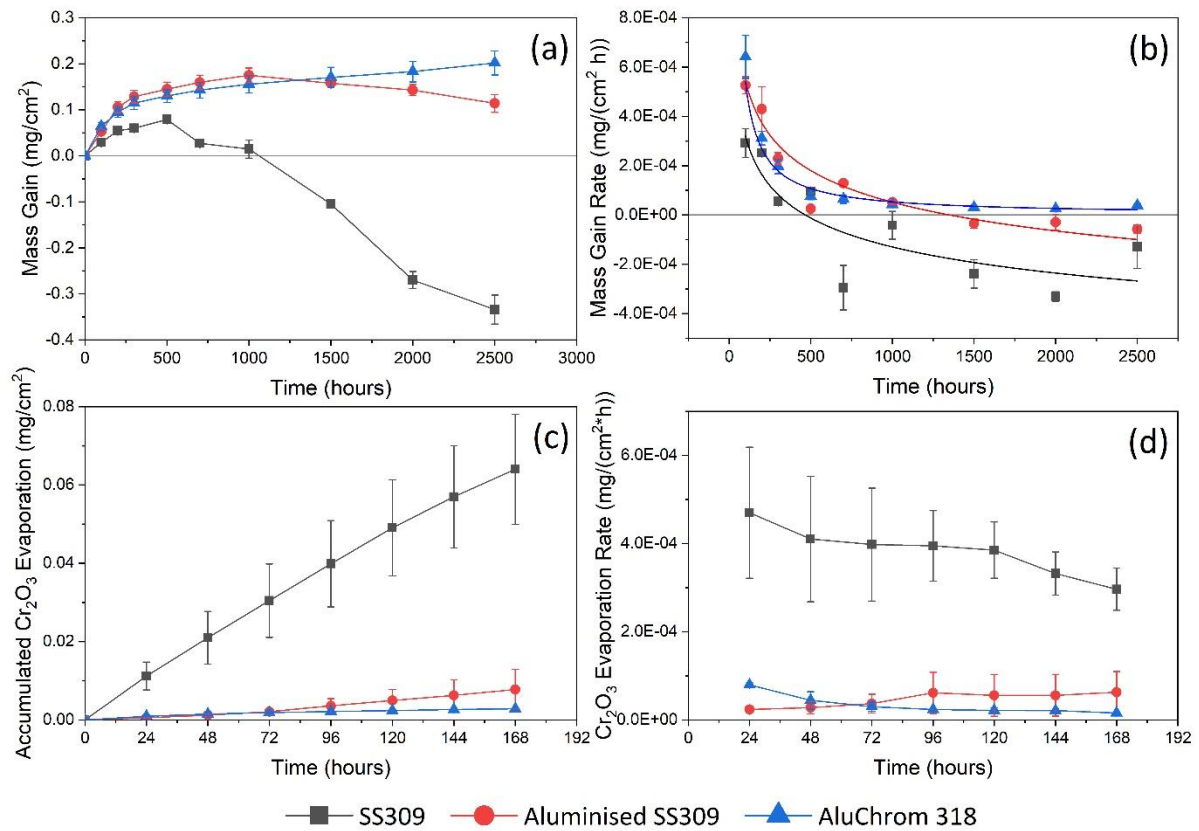


**Figure 5.1** (a) Discontinuous mass measurements and (b) mass gain rates as a function of time for SS309, aluminised SS309 and AluChrom 318 in 3%  $\text{H}_2\text{O}$  humidified air at  $850^\circ\text{C}$  for 2500 hours; (c) Accumulated  $\text{Cr}_2\text{O}_3$  evaporation and (d)  $\text{Cr}_2\text{O}_3$  evaporation rates as a function of time for SS309, aluminised SS309 and AluChrom 318 exposed to 3%  $\text{H}_2\text{O}$  humidified air at  $850^\circ\text{C}$  for 168 hours.

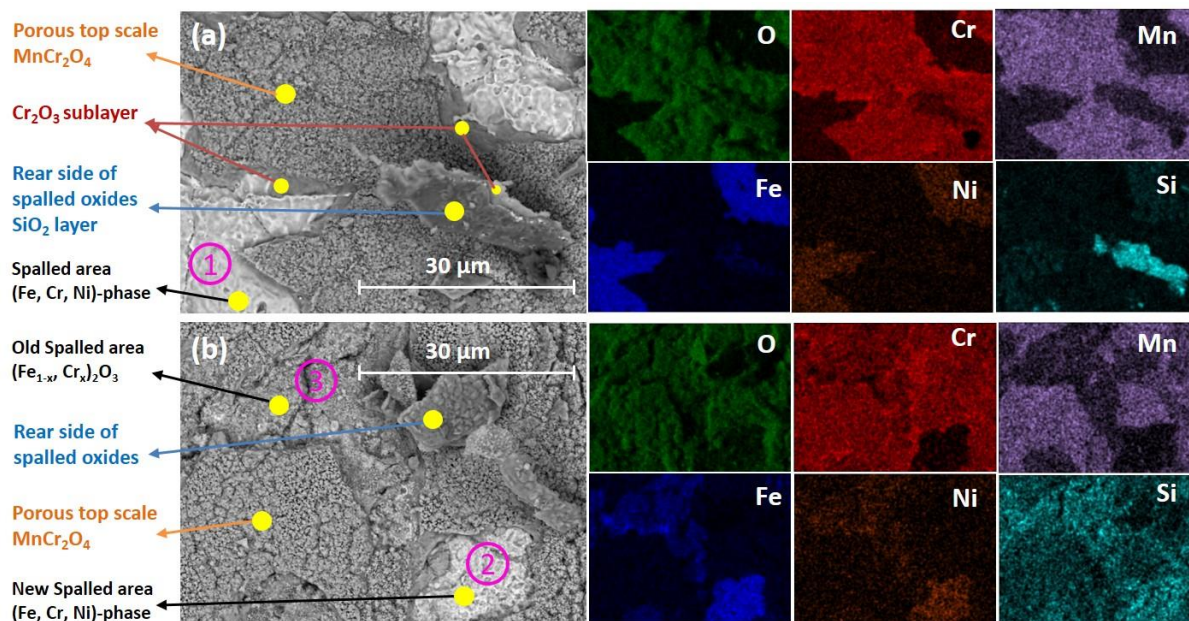


**Figure 5.2** SEM top view and EDX mapping of SS309 exposed at 850°C in air + 3% H<sub>2</sub>O for (a) 100 and (b) 1000 hours.

### 5.1.3 Microstructural investigation

#### 5.1.3.1 SS309

Figure 5.2 shows the results of microstructure evolution on SS309 oxidised for 100 and 1000 hours at 850°C in air with 3% H<sub>2</sub>O. EDX mapping analyses were conducted on both 100 and 1000 hour exposed samples. XRD patterns of SS309 oxidised for 0, 100, 500, 1000 and 2000 hours at 850°C in air with 3% H<sub>2</sub>O are displayed in Figure 5.3. Oxide scale spallation was already observed on SS309 after 100 hours of oxidation (Figure 5.2a). EDX mapping of SS309 after 100 hours of oxidation revealed that the cracked surface oxides were composed of a high concentration of Cr, Mn and O with traces of Fe. The edges of the spalled areas, which were located below the porous top scale, contained exclusively Cr and O. In Figure 5.3, the formation of a MnCr<sub>2</sub>O<sub>4</sub> spinel top scale and Cr<sub>2</sub>O<sub>3</sub> sublayer was confirmed by XRD after 100 hours exposure. The top scale of MnCr<sub>2</sub>O<sub>4</sub> spinel showed a very porous structure, while the Cr<sub>2</sub>O<sub>3</sub> sublayer appeared to be relatively dense. An enrichment of Si was observed on the rear side of the exfoliated scale (metal/oxide interface). An EDX study (Table 5.1) pointed

out that the spalled area beneath the oxide scale contained very high amounts of Fe, Cr and Ni, which can be generally described as (Ni, Fe, Cr)-phase. However, the formula of the (Ni, Fe, Cr)-phase cannot be identified by XRD measurement due to insufficient surface coverage. EDX maps on the front and rear sides of the spalled oxides in Figure 5.2a showed a layered structure from the alloy/oxide interface to the outer oxide surface: Steel/SiO<sub>2</sub>/Cr<sub>2</sub>O<sub>3</sub>/MnCr<sub>2</sub>O<sub>4</sub>. With the oxidation progressing to 1000 hours, more oxides spalled off and the underlying (Ni, Fe, Cr)-phase region considerably increased in size compared to the 100 hours sample, as can be seen from Figure 5.2b. Point EDX analysis performed on the old spalled area (Table 5.1) revealed that the (Ni, Fe, Cr)-phase was gradually replaced with (Fe, Cr)-rich oxide with high oxygen intensity. XRD analysis conducted on the sample exposed for 2000 hours confirmed the presence of Cr<sub>1.3</sub>Fe<sub>0.7</sub>O<sub>3</sub>.

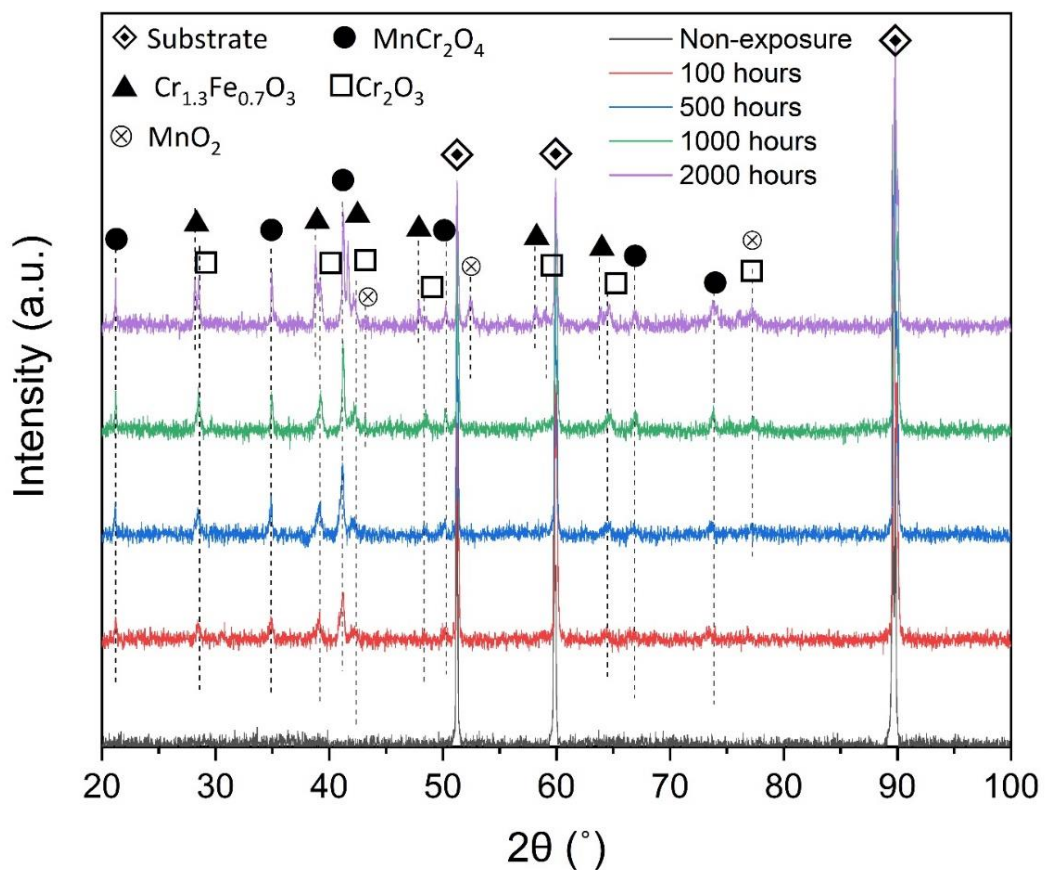


**Figure 5.3** XRD patterns of SS309 after oxidation at 850°C in air with 3% H<sub>2</sub>O (6.0 L/min) for 0, 100, 500, 1000 and 2000 hours.

**Table 5.1** EDX point analysis on the indicated spots in Figure 5.2.

at.%	O	Fe	Cr	Ni	Mn	C	Si	S	P
1	16.03	48.63	14.62	6.99	1.73	9.44	2.36	0.13	0.07
2	39.07	32.54	13.79	4.35	1.46	6.6	2.1	0.09	0
3	57.14	12.19	19.37	1.22	3.59	4.05	1.29	0.08	0

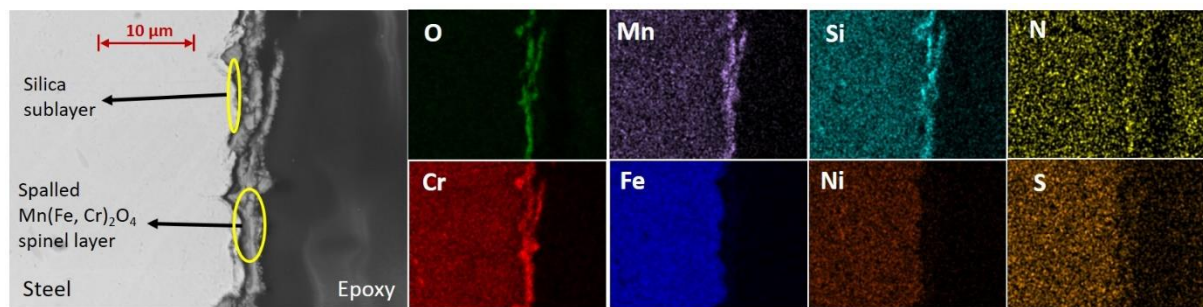


**Figure 5.4** SEM cross-sectional images of SS309 after exposure to humidified air at 850°C for 1000 hours with the corresponded EDX maps.

Figure 5.4 shows the SEM/EDX maps on the cross-section of the bare SS309 exposed to humidified air at 850°C for 1000 hours. It suggests that, compared to the steel base, there were higher concentrations of Cr, Mn and O in the oxide scale, suggesting that the oxide scale mainly consisted of MnCr<sub>2</sub>O<sub>4</sub> spinel phase. Si was found to be accumulated at the alloy and oxide interface, but the silica layer was discontinuous and porous. However, it is difficult to distinguish the Cr<sub>2</sub>O<sub>3</sub> from the (Cr,Mn)<sub>3</sub>O<sub>4</sub> layer but XRD confirmed the presence of MnCr<sub>2</sub>O<sub>4</sub> phase and Cr<sub>2</sub>O<sub>3</sub> phase. The inner Cr<sub>2</sub>O<sub>3</sub> layer might be polished off during the sample preparation for cross-section analysis. It was easily seen that the oxide layer formed on the bare SS309 surface was poorly adherent and discontinuous, which meant that the microstructure analysis on the cross-section was difficult using the mechanically polished specimen [99]. Thus, the cross-sectional structure of the oxide scale on SS309 was

benchmarked against the layered structure found on the spalled oxides on the surface micrograph (Figure 5.2).

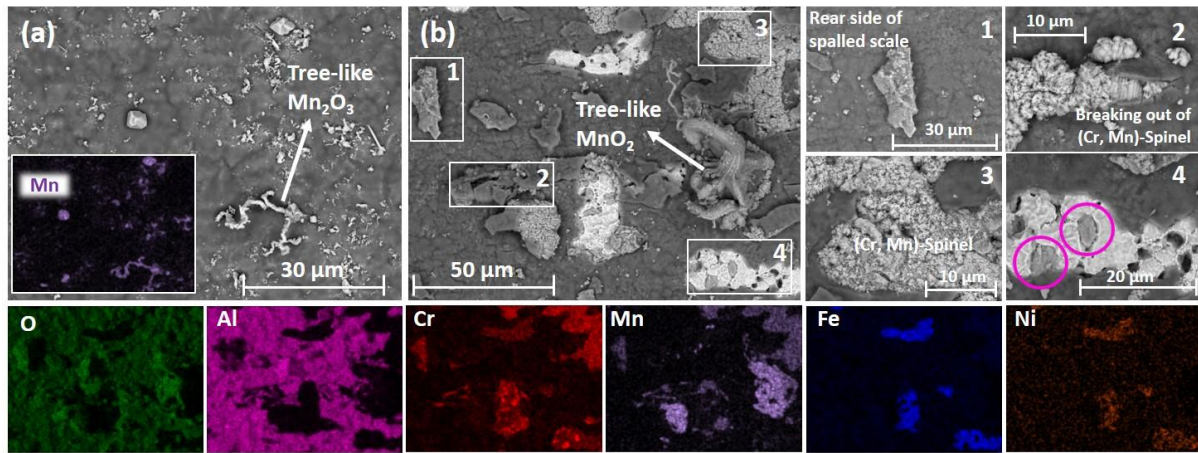


**Figure 5.5** SEM top view of aluminised SS309 exposed at 850°C in air + 3% H<sub>2</sub>O for (a) 100 and (b) 1000 hours. EDX mapping showing the element distribution on Figure 5.5b.

### 5.1.3.2 Aluminised SS309

The SEM micrographs of the aluminised SS309 exposed at 850°C in air with 3% H<sub>2</sub>O for 100 and 1000 hours are shown in Figure 5.5. EDX maps in Figure 5.5 show the element distribution on the micrograph of the aluminised SS309 oxidised for 1000 hours. Figure 5.6 displays the XRD patterns of SS309 oxidised in air with 3% H<sub>2</sub>O for 100, 500, 1000 and 2000 hours. For aluminised SS309, after 100 hours of oxidation, the sample surface appeared to be completely covered by a wrinkled alumina scale with ramiform and polygonal MnO<sub>2</sub> crystals randomly distributed along the scale wrinkles (Figure 5.5a), as confirmed by EDX analysis. Heating up in air prompts the aluminium coating to react with oxygen, leading to formation of an alumina scale on the alloy surface. Significant scale spallation was visible in the aluminised SS309 when the oxidation time increased to 1000 hours. There are two types of spalled areas observed in Figure 5.5b. One was a (Ni, Fe, Cr)-phase with a number of large pores, and some of the large pores were about to be filled with (Cr, Mn)-spinel oxides as confirmed by EDX in Figure 5.5b-4. Another type of the spalled area (Figure 5.5b-3) showed

a strong intensity of Cr and Mn in EDX maps, which coupled with XRD results in Figure 5.6, illustrating the internal growth of a foam-like (Cr, Mn)-spinel phase which broke out through the alumina scale. Moreover, the EDX maps also disclosed that the residual (Cr, Mn)-spinel oxide was stuck to the rear side of the spalled alumina scale (Figure 5.5b-1). Despite this, a substantial amount of Mn migrated to the alloy surface throughout the alumina scale, resulting in a further growth of tree-like MnO<sub>2</sub>. According to the XRD analysis in Figure 5.6, the diffraction peaks for spinel oxides and MnO<sub>2</sub> can be easily detected on the spectrum of 2000 hours. This can be explained by the severe delamination of the alumina layer on the aluminised SS309 surface. However, XRD could not identify any alumina phase on aluminised SS309 at different exposure time. This is due to the high intensity alumina peaks overlapping with peaks from  $\sigma$ -FeCr phase, and the low intensity alumina peaks merging with the background of the XRD patterns. However, both surface and cross-sectional EDX element maps confirmed the formation of an alumina scale on the SS309 surface.

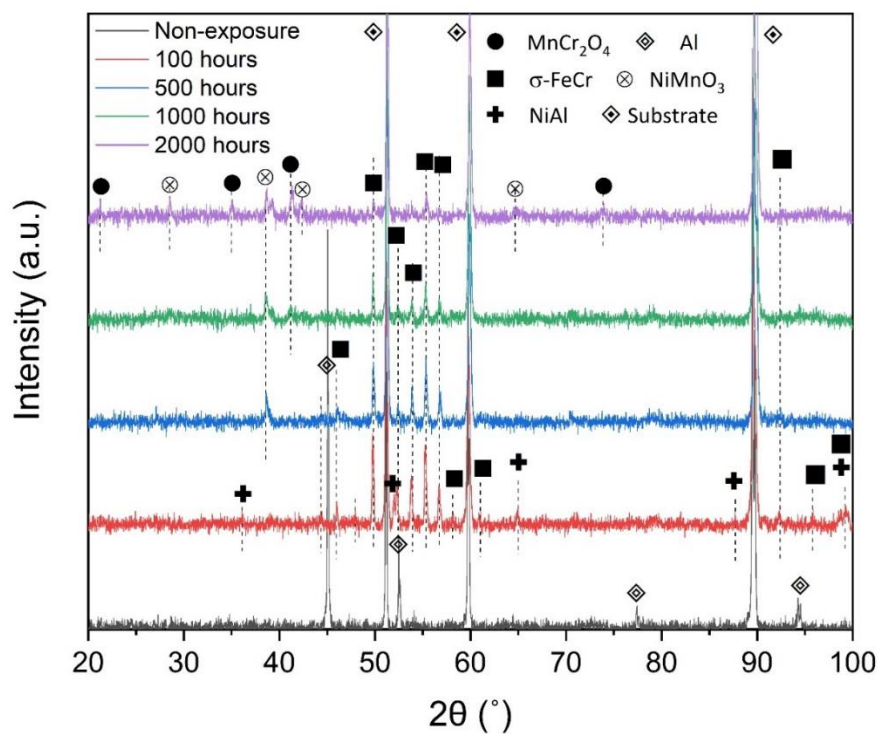


**Figure 5.6** XRD patterns of aluminised SS309 after oxidation at 850°C in air with 3% H<sub>2</sub>O (6.0 L/min) for 0, 100, 500, 1000 and 2000 hours.

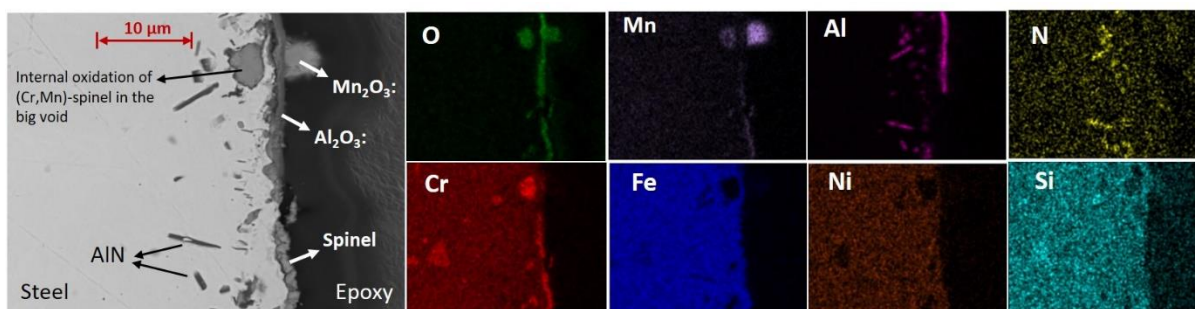


**Figure 5.7** SEM cross-sectional images and EDX mapping of aluminised SS309 after exposure to humidified air at 850°C for 1000 hours.

The cross-sectional image of aluminised SS309 presented in Figure 5.7 was selected at the location where all the features present on the surface can be seen in the SEM image (Figure 5.5b). On the top half part of the cross-sectional image, the discontinuous scale containing Al and O after 1000 hours exposure is shown, confirming the presence of the alumina scale. Large Mn-rich oxide grains were present in the external part of the alumina scale, corresponding to a fast outward growth of the tree-like  $MnO_2$  in Figure 5.5b. The fast Mn outward diffusion resulted in a void formation underneath the alumina scale. The underlying voids connected to each other, leading to the formation of a gap between the base alloy and the alumina scale. Additionally, the void was found to be filled with (Cr, Mn)-rich spinel oxides right below the external tree-like  $MnO_2$ . In the middle part, the oxide scale had a duplex structure with an outer alumina scale and an inner (Cr, Mn)-spinel scale, indicating the internal growth of (Cr, Mn)-spinel via oxygen inward diffusion. The bottom half of the scale which corresponded to alumina scale exfoliation was occupied by a Cr and Mn enriched spinel layer, as indicated by EDX mapping. Additionally, the aluminised SS309 showed the formation of polygonal precipitates beneath the oxide scale with a relatively higher concentration of Al and N (Figure 5.7), indicating that the precipitation of AlN occurred during the high temperature oxidation. In Figure 5.8, the cross-sectional SEM of aluminised SS309 exhibited numerous diamond-shaped features enriched with Ni and Al after 100 hours exposure. Combined with the XRD spectrum for aluminised SS309 after 100 hours exposure,

the results suggest that the NiAl precipitates had formed close to the metal and oxide interface after 100 hours of oxidation [192].

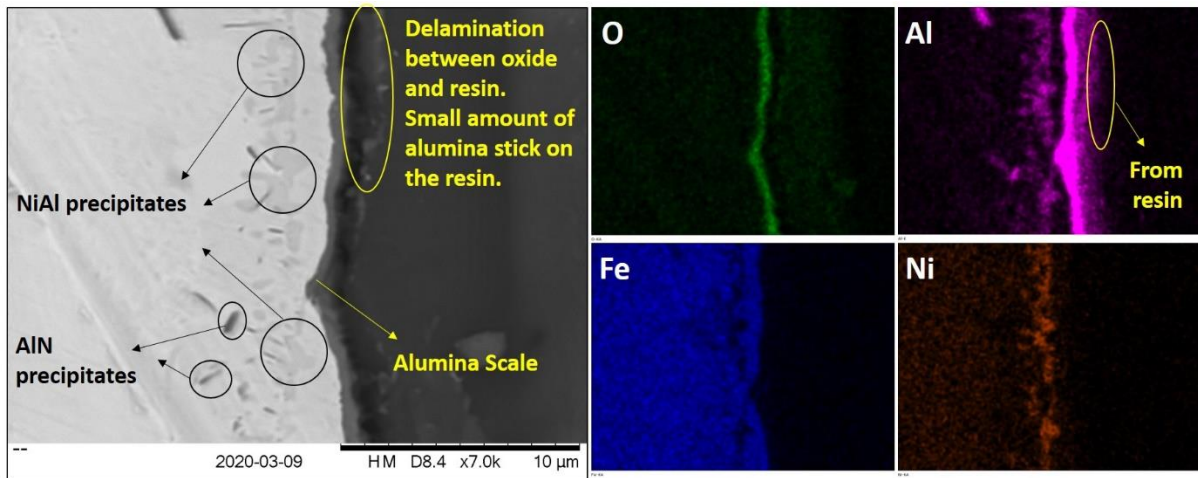


**Figure 5.8** Cross-sectional SEM image and EDX mapping of aluminised SS309 after 100 hours exposure at 850°C in air with 3% H<sub>2</sub>O environment.

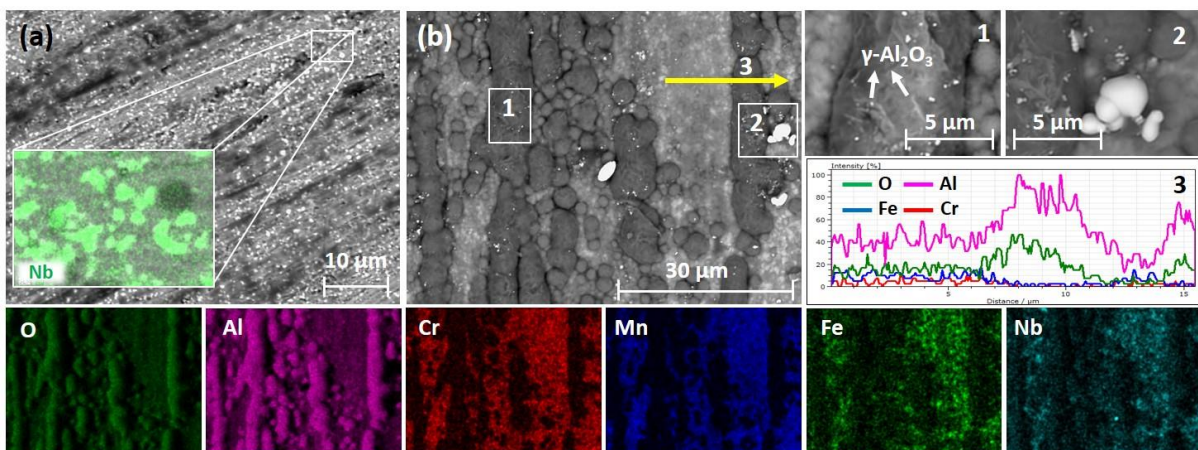
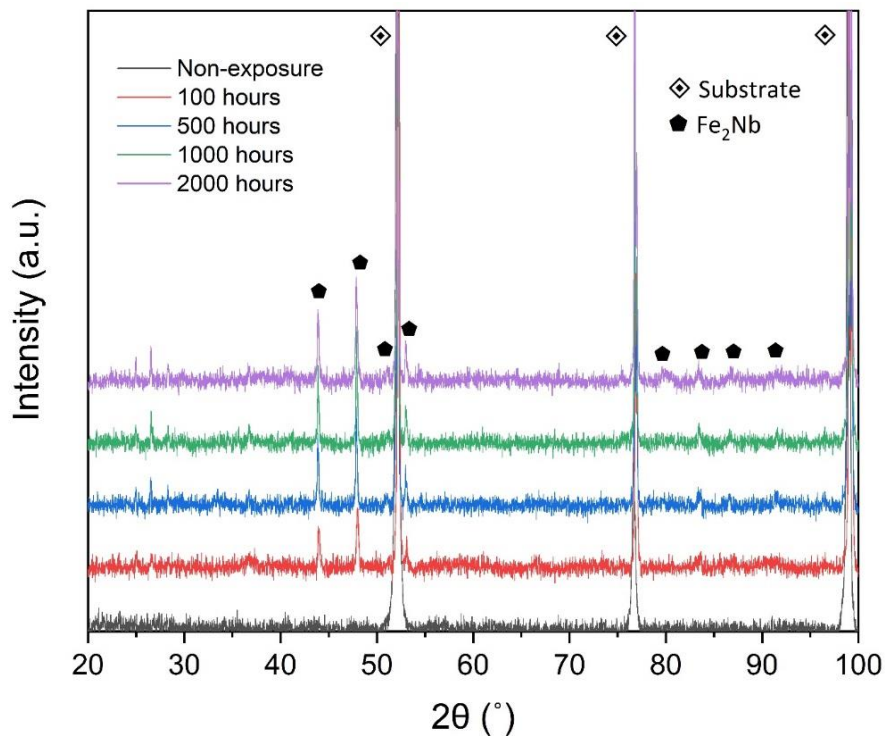


**Figure 5.9** SEM top view of AluChrom 318 exposed at 850°C in air + 3% H<sub>2</sub>O for (a) 100 and (b) 1000 hours. EDX linescan along the line indicated in Figure 5.9b. EDX mapping showing element distribution on Figure 5.9b.

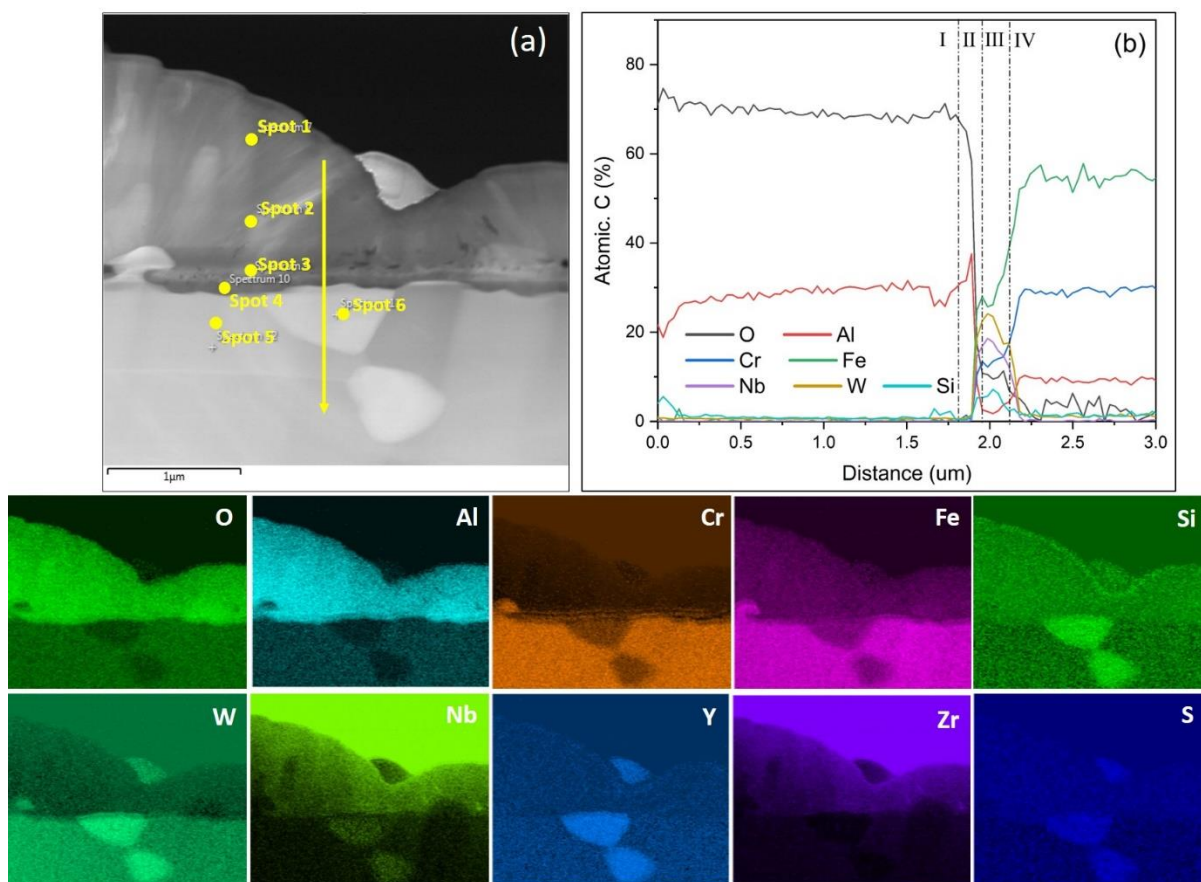
### 5.1.3.3 AluChrom 318

Figure 5.9 demonstrates the surface microstructure of the AluChrom 318 exposed at 850°C in air with 3% H<sub>2</sub>O for 100 and 1000 hours. The XRD spectrums for AluChrom 318 exposed at 850°C for 100, 500, 1000 and 2000 hours are shown in Figure 5.10. It can be seen that a relatively thin oxide film was observed containing numerous white spots randomly

distributed on the surface of AluChrom 318 after 100 hours exposure (Figure 5.9a). The surface of AluChrom 318 with the exposure time of 1000 hours revealed two distinct alumina zones in Figure 5.9b, chequered with globular and long-ridged alumina with dark grey colour and plane (flat) alumina with light grey colour, while a small amount of the fine-size white particles were still found to penetrate the oxide scale and mostly were distributed on the top of the ridged alumina scale. EDX line scanning (Figure 5.9b-3) showed that the ridged oxides contained extremely high concentration of Al and O, indicating that a dense surface scale of  $\text{Al}_2\text{O}_3$  was formed. The concentration of Al and O in the plane region was found to be lower than that in the ridged region but still with higher concentration than all other elements, which means that the plane region was covered with a relatively thinner alumina scale. Unexpectedly, the alumina phase could not be detected on the XRD spectrums for AluChrom 318 obtained by either XRD (Figure 5.10) or GI-XRD (not shown). The presence of a  $\text{Fe}_2\text{Nb}$  Laves phase in the steel was confirmed by XRD.



**Figure 5.10** XRD patterns of AluChrom 318 after oxidation at 850°C in air with 3%  $\text{H}_2\text{O}$  (6.0 L/min) for 0, 100, 500, 1000 and 2000 hours.



**Figure 5.11** (a) STEM cross-sectional image and EDX mapping of AluChrom 318 exposed at 850°C in air + 3% H<sub>2</sub>O for 1000 hours; (b) EDX linescan along the line indicated in Figure 5.11a.

Figure 5.11 shows the STEM and EDX results measured on the cross-section of AluChrom 318 oxidised for 1000 hours at 850°C in humidified air, which was prepared using a FIB in-situ lift-out technique [151]. The oxide scale formed on AluChrom 318 had a duplex structure with aluminium as dominant cation in both layers, and the outer scale made up about 90% of the total thickness. Moreover, the thick outer layer with a semi-circular shape corresponded to the ridged alumina detected on the surface SEM images (Figure 5.9b). The EDX mapping showed a narrow and straight Cr-rich band in the inner oxide layer, just below the interface to the bottom oxide. Apart from Cr, this band was also enriched with Fe. Quantitative STEM/EDX linescans obtained from the oxide scale are shown in Figure 5.11b. EDX point analysis on the indicated spots in Figure 5.11a is shown in Table 5.2. The linescan result

exhibits four different regions in the scanned area. Region I was situated close to the gas/scale interface and contained a high level of Al (37.98 wt.%) and O (58.85 wt.%) (Spot 1). Region II had relatively higher in Cr (3.42 wt.%) and Al (40.79 wt.%) levels which corresponded to the Cr-rich band (Spot 3) and inner alumina scale (Spot 4), respectively. Region III was located at the Laves phase and contained a high level of W (47.47 wt%) and Nb (18.65 wt.%), with some Fe (22.62 wt.%) and Cr (8.21 wt.%) (Spot 6).

**Table 5.2** EDX point analysis on the indicated spots Figure 5.11a.

at.%	1	2	3	4	5	6
O	70.93	69.07	68.31	68.45	-	-
Al	27.25	26.11	24.86	29.52	9.57	1.64
Si	1.44	4.57	6.65	1.86	2.00	7.79
Cr	-	-	0.07	0.06	29.32	14.01
Fe	0.38	0.25	0.12	0.11	59.10	35.83
Nb	-	-	-	-	-	17.79
W	-	-	-	-	-	22.93
Total	100	100	100	100	100	100

The cross-section TEM bright field image of AluChrom 318 is displayed in Figure 5.12. Again, two distinctive alumina scales can be observed. The Fe<sub>2</sub>Nb particles were found to penetrate the inner alumina scale and move up to the gas/oxide interface. In order to determine the phase composition of both layers, which consisted of oxide grains on the nanometre scale, convergent beam electron diffraction (CBED) was carried out on both oxide scales. Unfortunately, neither CBED could confirm the phase composition of the alumina scales formed on AluChrom 318. The undetectable diffraction phase of both inner and outer alumina scales could be potentially caused by two reasons: 1) the oxide grains in both inner and outer scales are amorphous; 2) the oxide grains in both inner and outer scales have an

extremely small size. The research carried out by the Swedish High Temperature Corrosion Centre (HTC) reported the effect of water on the oxidation status of the FeCrAl alloy Kanthal AF [136,151,152]. Kanthal AF was exposed at 900°C for 1, 24, 72 and 168 hours in both dry O<sub>2</sub> and O<sub>2</sub> + 40% H<sub>2</sub>O. The TEM CBED results obtained indicated that the oxide scales showed a double-layered structure including an inward-growing bottom layer of  $\alpha$ -Al<sub>2</sub>O<sub>3</sub> and an outward-growing upper layer of  $\gamma$ -Al<sub>2</sub>O<sub>3</sub> with Cr-rich band in the middle, indicating the original metal/gas interface. The well-developed two-layered scale structure observed after 1000 hours exposure in the research reported here was quite comparable to the multi-layered oxides obtained by researchers from HTC. Therefore, in the current work, it is assumed that the outer and inner oxide layers formed on AluChrom 318 surface are  $\gamma$ -Al<sub>2</sub>O<sub>3</sub> and  $\alpha$ -Al<sub>2</sub>O<sub>3</sub>, respectively.

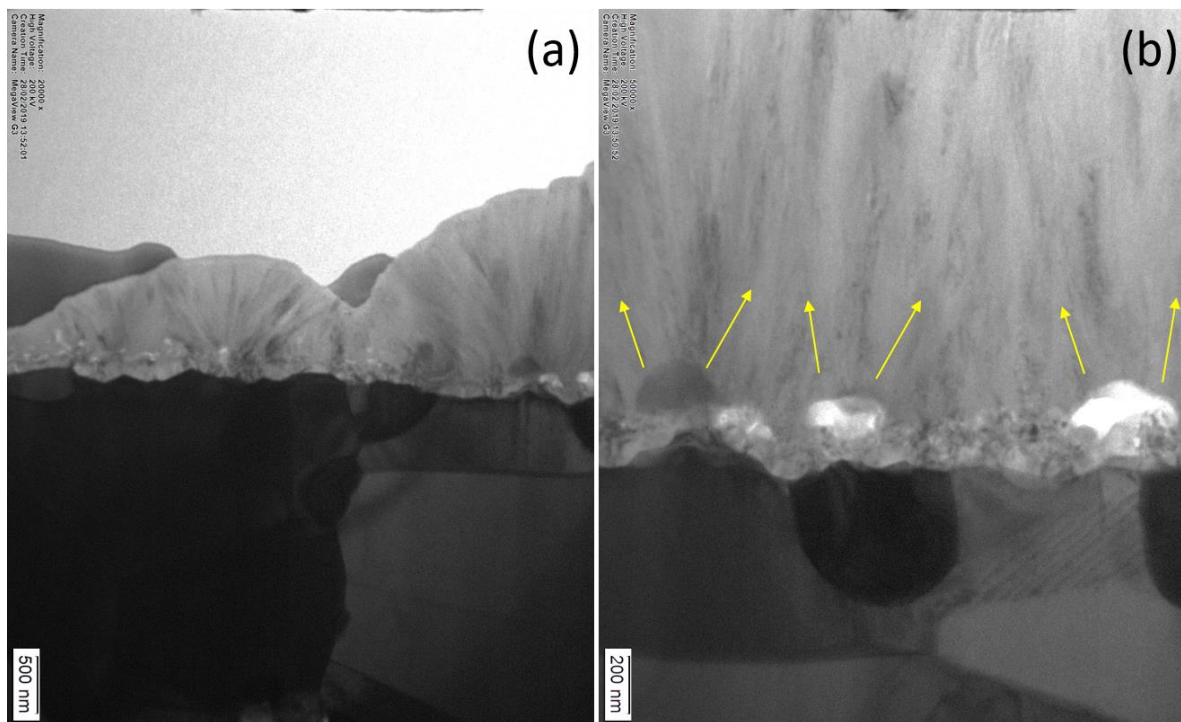


**Figure 5.12** TEM bright field cross-sectional images of the duplex alumina scales on the AluChrom 318 exposed at 850°C in air + 3% H<sub>2</sub>O for 1000 hours.

## 5.2. Discussion

### 5.2.1 Corrosion and Cr<sub>2</sub>O<sub>3</sub> evaporation of SS309

In this study, the corrosion behaviour of SS309 in oxidising environment with the presence of water vapour can be directly correlated to the Cr<sub>2</sub>O<sub>3</sub> evaporation and scale spallation. The relatively low parabolic mass gain of bare SS309 up to 500 hours, in comparison to all the investigated materials can be accredited to Cr<sub>2</sub>O<sub>3</sub> loss because of the steam induced Cr<sub>2</sub>O<sub>3</sub> volatilisation in the form of CrO<sub>2</sub>(OH)<sub>2</sub>. The parabolic trend before 500 hours corresponded to a higher oxidation rate than the Cr<sub>2</sub>O<sub>3</sub> evaporation rate. The mass loss by Cr<sub>2</sub>O<sub>3</sub> volatilisation can be rapidly compensated by the oxidation of a larger amount of Cr diffused outwards from the alloy, resulting in a balance of mass gain. The large amount of continuous chromium loss by evaporation could be a possible reason for the formation of a porous MnCr<sub>2</sub>O<sub>4</sub> top layer on the SS309 surface. However, Sachitanand et al. [99] reported that a higher concentration of the alloying element Mn in the alloy resulted in a lower Cr evaporation rate due to the formation of a compact and thick spinel layer of MnCr<sub>2</sub>O<sub>4</sub>. By comparing the obtained data with the aforementioned work [99], the SS309 in this research exhibited a Cr evaporation level which was comparable to the E-brite steel with 0.08 wt.% Mn (the lowest Mn content of the investigated alloys in their work) which had the highest Cr leakage under the exactly same exposure conditions. Thus, it can be inferred that stainless steels containing Mn in a critical range of 0.3 to 0.5 wt.% develop a well adhering MnCr<sub>2</sub>O<sub>4</sub> spinel top layer above the Cr<sub>2</sub>O<sub>3</sub> layer at 800 and 850°C, and that the rate of Cr vaporisation for those alloys is 2 to 3 times lower than for alloys that form a non-continuous MnCr<sub>2</sub>O<sub>4</sub> top layer. In this research work, the transportation of chromium through the porous MnCr<sub>2</sub>O<sub>4</sub> spinel scale with high defect concentration [193] formed on the SS309 surface was fast, meaning that the vaporised Cr could be rapidly replaced by the quick grain boundary

diffusion of Cr from the substrate [194,195], leaving plenty of cation vacancies in the alloy grain boundaries [48]. During further oxidation, the vacancies within the grain boundaries in the steel base connected with each other to form cracks and even big gaps among alloy grains. Eventually the oxide scale detached and this resulted in the cracked surface. The serious mass loss noted for uncoated SS309 after 500 hours was due to a combined action of scale spallation and Cr vaporisation. The main reason for the poor adhesion of the oxide scale can be accredited to the formation of a silica sublayer beneath the  $\text{Cr}_2\text{O}_3/\text{MnCr}_2\text{O}_4$ . EDX maps of the reverse side of the spalled scale (Figure 5.2a) show a high intensity of Si at the metal/oxide interface, indicating the internal precipitation and oxidation of Si. Silica has a much lower TEC than  $\text{Cr}_2\text{O}_3$  and steel, which is recognised as detrimental for scale adhesion. A poor adherent  $(\text{Cr},\text{Mn})_3\text{O}_4$  spinel scale was also detected on AISI 441 in Grolig et al.'s study due to the insufficient amount of Nb-enriched Laves phases to bind silica [175]. Spallation of oxide scales allows air (oxygen) access to the underlying Ni-enriched and Cr-depleted alloy. In the spalled region, internal oxidation of Ni-containing (Fe, Cr, Ni)-spinel oxides was evidenced by EDX (Figure 5.2a). With the oxidation continuing, the fast-outward Fe and inward O diffusion led to the transformation from the non-protective (Fe, Cr, Ni)-spinel oxides to the stronger Fe-enriched  $\text{Cr}_{1.3}\text{Fe}_{0.7}\text{O}_4$  as healing layer. This was detected in the EDX maps (Figure 5.2b) and XRD (Figure 5.3).

## **5.2.2 Corrosion and $\text{Cr}_2\text{O}_3$ evaporation of alumina formers**

### *5.2.2.1 Alumina formation*

As mentioned before, the oxidation of AluChrom 318 leads to the formation of an oxide that consists of two subscales with a Cr-band which separates the top and bottom parts of the scale. The high mass gain rate in the initial stage corresponds to the rapid growth of the top metastable alumina by Al outward diffusion during the furnace heat-up process. Meanwhile,

this initial oxidation is accompanied by decomposition of the hydroxylated air-formed oxide film to form the mixture of chromium oxide and iron oxides which indicates the original steel surface [136,152]. The formation of the bottom  $\alpha$ -Al<sub>2</sub>O<sub>3</sub> layer in AluChrom 318 seems to have been favoured by the isostructural corundum-type oxides (Cr<sub>2</sub>O<sub>3</sub> and Fe<sub>2</sub>O<sub>3</sub>) produced in the metal/oxide interface by acting as nucleation sites where Al can incorporate [136]. During this oxidation period, Al diffuses outwards, nucleates on the isostructural corundum oxides, and then rapidly turns into the dominant cation to form a continuous alumina layer (stable stages) on the surface [152]. The position of the Cr-rich band in the outer part of the lower oxide suggests that the  $\alpha$ -Al<sub>2</sub>O<sub>3</sub> grains have nucleated close to the original sample surface and have grown predominantly inwards. When a dense layer of  $\alpha$ -Al<sub>2</sub>O<sub>3</sub> is formed, the outward growth rate of the outer  $\gamma$ -Al<sub>2</sub>O<sub>3</sub> is expected to dramatically slow down since the outward diffusion rate of aluminium cation decreases [196]. This oxide growth pattern of AluChrom 318 is also in agreement with the parabolic relation found for the gravimetric analysis. As mentioned earlier, the Fe<sub>2</sub>Nb particles were found to penetrate the inner  $\alpha$ -Al<sub>2</sub>O<sub>3</sub> scale and stay on the top of the ridged alumina. Meanwhile, this barrier penetration process of Fe<sub>2</sub>Nb particles may generate pores in the inner  $\alpha$ -Al<sub>2</sub>O<sub>3</sub> scale. Hence, the aluminium from the steel base was found to erupt from the pores to the scale/gas interface in all the directions to react with oxygen and build the thick outer alumina scale. The eruption path for aluminium outward diffusion is still clearly visible over the Fe<sub>2</sub>Nb particles that already broke through the inner alumina scale in Figure 5.12. This volcanic eruption growth pattern results in the formation of alumina in globular shape. Subsequently, the adjacent globular alumina scale grew larger and joined together to form the long ridged alumina, as detected in Figure 5.9b. As discussed above, the  $\gamma$ -Al<sub>2</sub>O<sub>3</sub> in the outer oxide layer is assumed to be metastable and is thus expected to transform to  $\alpha$ -Al<sub>2</sub>O<sub>3</sub> with time when exposed to oxygen. However, the presence of water vapour was found to stabilise the  $\gamma$ -Al<sub>2</sub>O<sub>3</sub> phase, thereby inhibiting its

phase transformation to the stable  $\alpha$ -Al<sub>2</sub>O<sub>3</sub> and, resulting in the formation of a duplex structure of a thick  $\gamma$ -Al<sub>2</sub>O<sub>3</sub> scale over an extremely thin  $\alpha$ -Al<sub>2</sub>O<sub>3</sub> scale [136,152].

However, the third element effect of chromium oxide for  $\alpha$ -Al<sub>2</sub>O<sub>3</sub> nucleation on aluminised SS309 is not yet clear. The growth mechanism of the alumina scale on aluminised SS309 clearly differs from the observed duplex alumina scales formed on AluChrom 318. During exposure, the aluminium coating on the alloy surface evolved in the following processes: (1) quick reaction with oxygen to form a continuous alumina layer accompanied with Al inward diffusion to the inner substrate and (2) Al outward diffusion to form and/or re-heal the alumina scale. For the former case, the fast oxidation of Al in the initial stage of exposure with a relatively fast parabolic rate corresponded to the rapid growth of a metastable alumina scale to produce a continuous layer due to the low temperature requirement for growth [197]. The inward diffusion of Al into the substrate combined with Ni, thereby promoting the formation of the intermetallic compound NiAl. The formation of NiAl can be accredited to the low diffusivity of Al in the alloy, confirming the typical reservoir behaviour for maintaining the supply of Al for the further growth of the alumina layer [192]. For the latter case, the further thickening of the outer alumina scale took place at the expense of the NiAl precipitates close to the alloy/oxide interface [198]. The decrease in the oxidation rate during further oxidation was probably associated with the prolonged diffusion path for the dominant Al outward transport to the gas/scale interface due to the continuous alumina scale thickening. However, Figure 5.7 shows that the NiAl denuded zone beneath the scale layer was no longer detectable after 1000 hours oxidation, compared to a large amount of NiAl denuded zones detected after 100 hours oxidation in Figure 5.8. This confirms that the NiAl precipitates underlying the denuded zone were not able to maintain the supply of Al to the oxidation front, resulting in the termination of the alumina scale thickening after 1000 hours exposure. In

addition, comparing the cross-section for the 100 hours (Figure 5.8) and 1000 hours (Figure 5.7) exposure, shows that the AlN precipitates had grown remarkably in size with the increase of exposure time. Therefore, it can be suggested that the aluminium in the NiAl denuded zone which were supposed to contribute to the growth of the outer alumina scale had been preferentially captured by the nitrogen impurity (0.11 wt.%) to form AlN in the inner zone of the alloy.

#### *5.2.2.2 Cr<sub>2</sub>O<sub>3</sub> evaporation*

The AluChrom 318 and aluminised SS309 showed 95% and 88% reduction in Cr<sub>2</sub>O<sub>3</sub> evaporation compared to the bare SS309, respectively. This confirmed the excellent Cr retention ability of the formed alumina scale acting as an effective Cr barrier. The alumina scale restrained the surface chromium evolution through restraining the ionic mobility of chromium and oxygen through the alumina grain boundaries [29], thus causing a significant reduction in Cr<sub>2</sub>O<sub>3</sub> evaporation. In the first 24 hours of Cr leakage detection, AluChrom 318 showed a higher Cr<sub>2</sub>O<sub>3</sub> evaporation rate than the aluminised SS309. For AluChrom 318, the high Cr<sub>2</sub>O<sub>3</sub> evaporation rate in the first 24 hours was derived from the transient Cr<sub>2</sub>O<sub>3</sub> formed in the initial stage at the gas/metal interface, leading to the slightly higher Cr<sub>2</sub>O<sub>3</sub> evaporation before the eventual development of the continuous alumina layer [117]. The rapid formation of the alumina scale on the aluminised SS309 by direct reaction between the aluminium coating and oxygen accompanied by the inward diffusion of aluminium into the alloy matrix resulted in a lack of exposure of Cr<sub>2</sub>O<sub>3</sub> crystals, thereby leading to low Cr<sub>2</sub>O<sub>3</sub> evaporation in the initial stage. However, the denuder technique revealed that the alumina scale formed on AluChrom 318 possessed a better Cr retention ability compared to that formed on the aluminised SS309. Fe<sup>3+</sup> and Cr<sup>3+</sup> are not expected to diffuse into the oxide scale after the formation of a continuous Al<sub>2</sub>O<sub>3</sub> scale. The solubility of Fe<sup>3+</sup> and Cr<sup>3+</sup> in  $\alpha$ -Al<sub>2</sub>O<sub>3</sub> is

considered to be extremely low at temperatures below 1000 °C [199]. The STEM/EDX results for AluChrom 318 showed that no chromium was detected on spot 1 and 2 in Figure 5.11. However, the relatively higher concentration of Fe in the outer  $\gamma$ -Al<sub>2</sub>O<sub>3</sub> can be accredited to its presence in the divalent state [136]. Meanwhile, the alumina scale on the aluminised SS309 surface grew with pores and cracks along the wrinkles due to the thermal stress which caused scale volume change. Thus, it can be deducted that Cr transport through the wrinkled alumina scale with accelerated speed led to the increased trend of the Cr<sub>2</sub>O<sub>3</sub> evaporation rate, as can be seen in Figure 5.1d. Furthermore, the serious scale spallation with the depletion of the NiAl reservoir which occurred on aluminised SS309 will definitely provoke the Cr<sub>2</sub>O<sub>3</sub> evaporation rate to an exponential growth during extended exposure. Meanwhile, the Cr<sub>2</sub>O<sub>3</sub> evaporation rate of AluChrom 318 in Figure 5.1d decreased with time. This can be explained by the slightly higher surface Cr<sub>2</sub>O<sub>3</sub> concentration on the thin alumina region which contributed to the initial evaporation process, whereas after the ridged alumina had formed, the Cr<sub>2</sub>O<sub>3</sub> vaporisation process in the ridged alumina oxide was governed by the Cr diffusion via alumina grain boundaries. Once the dense and ridged oxides expanded over the entire surface the Cr<sub>2</sub>O<sub>3</sub> evaporation rate stayed approximately constant.

### 5.3 Conclusions

The oxidation and Cr<sub>2</sub>O<sub>3</sub> evaporation behaviour of SS309, aluminised SS309 and AluChrom 318 were investigated at 850°C in a flow of 6.0 L/min of air with 3% H<sub>2</sub>O. The bare SS309 did not satisfy the requirements for a successful application as CAPH material due to the formation of a porous multi-layered SiO<sub>2</sub>/Cr<sub>2</sub>O<sub>3</sub>/(Cr,Mn)<sub>3</sub>O<sub>4</sub> scale giving rise to serious scale spallation and substantial Cr<sub>2</sub>O<sub>3</sub> evaporation. The Cr evaporation measurements showed that the Cr<sub>2</sub>O<sub>3</sub> evaporation rate of aluminised SS309 was one order of magnitude lower than that of SS309, indicating that surface aluminising is an efficient way to minimise the Cr<sub>2</sub>O<sub>3</sub>

evaporation. Furthermore, the aluminised SS309 exhibited a comparable  $\text{Cr}_2\text{O}_3$  evaporation level as AluChrom 318 which exhibited the best Cr retention ability over 168 hours. However, the alumina scale formed on aluminised SS309 suffered spallation during oxidation. It was observed that a high Mn outward flux and O inward diffusion throughout the alumina scale led to the breaking out of the internally formed (Cr,Mn)-spinel oxides. The difference in the  $\text{Cr}_2\text{O}_3$  evaporation kinetics between both alumina formers was due to a different oxide formation mechanism. The AluChrom 318 formed a  $\gamma\text{-Al}_2\text{O}_3/\alpha\text{-Al}_2\text{O}_3$  layered scale with the aid of the isostructural  $\text{Cr}_2\text{O}_3$ , and the inner  $\alpha\text{-Al}_2\text{O}_3$  could effectively prevent the  $\text{Cr}^{3+}$  from outward diffusion at  $850^\circ\text{C}$ . In contrast, the aluminised SS309 formed an alumina scale with a large amount of cracks and voids formation which led to an accelerated  $\text{Cr}_2\text{O}_3$  evaporation rate. Thus, the AluChrom 318 demonstrated an outstanding Cr retention ability and the alloys formed will be useful for overcoming the  $\text{Cr}_2\text{O}_3$  evaporation in SOFC balance of plant components, in the case inspected here specifically the cathode air pre-heater.

## **Chapter 6 – Microstructural analysis of an AluChrom 318 Cathode Air Pre-heater for an SOFC system\***

Within the HEATSTACK project, an advanced CAPH fabricated out of AluChrom 318 for micro-CHP was developed by Senior Flexonics Ltd. A long term corrosion test of the CAPH stack will require the CAPHs to be installed into a micro-CAPH system and put through rigorous testing under various operating conditions, which will give confidence in the overall lifetime and robustness of the AluChrom 318 CAPH stack. The field test of the integration of AluChrom 318 CAPHs and fuel cell stacks was carried out by Vaillant GmbH. The customised micro-CHP system with an AluChrom 318 CAPH was installed on 19<sup>th</sup> Nov 2014 within a field test at a customer site and accumulated a hot-operation time of 25,000 hours in total before its decommissioning on 19<sup>th</sup> Nov 2017. The role of University of Birmingham in the HEATSTACK project was to carry out extensive material testing on this AluChrom 318 CAPH in order to get a better understanding of its corrosion behaviour. Therefore, the focus of this chapter is on characterising the AluChrom 318 CAPH operated for 25,000 hours by Vaillant GmbH, and offering improvement suggestions to Senior Flexonics to optimise the AluChrom 318 used for CAPH applications.

---

\* This work was partly published in ECS Transactions <K. Zhang, A. El-kharouf, and R. Steinberger-Wilckens. *ECS Trans.*, 91 (2019) 2253-2260> and ACS Applied Materials & Interfaces <K. Zhang, A. El-kharouf, and R. Steinberger-Wilckens. *ACS. Appl. Mater. Interfaces*. Manuscript submitted>.

## 6.1 Results

### 6.1.1 AluChrom 318 CAPH stack

The results in Chapter 5 proved that AluChrom 318 formed an alumina layer on its surface which acted as a protective scale and reduced the  $\text{Cr}_2\text{O}_3$  evaporation rate to an order of magnitude lower than the chromia-forming alloys studied. However, the performance of heat exchanger stacks made of AluChrom 318 and operated under the practical operating conditions of a residential system showed that the issue was far more complicated compared to what was observed in the small coupons exposed under isothermal conditions. Figure 6.1 shows the CAPH prototype made of AluChrom 318 and developed by Senior Flexonics. This 50-cell heat exchanger stack was operated under simulated SOFC environment for 25,000 hours by Vaillant GmbH. Each single cell was fabricated by welding two single heat exchanger plates together by a laser welding technique to form a closed ‘cassette’ (cell). The gas-to-gas heat exchanger presented in this study is a counter flow design. As shown in Figure 6.1c, the fresh air from the blower enters the channel fabricated in each single cell (cassette). The high-temperature exhaust gas from the afterburner goes the opposite direction along the outer surface of each cassette. The thermal specifications of the AluChrom 318 CAPH during operation are shown in Table 6.1. It is common knowledge that the convective flow of the high-temperature exhaust gas and the low-temperature air will cause a temperature gradient across the entire heat exchanger stack, as shown in Figure 6.2a. The oxidation stage of the CAPH cell under the different temperature regimes is evident by the different colours shown in Figure 6.2b. The most obvious difference is that the outer surface of the cells which was exposed to the highest temperature (hot zone) exhibited a brown colour, while that exposed to the lowest temperature showed a dark green colour. As indicated in Figure 6.2b, coupons were cut from both hot zone (location 1) and cold zone

(location 2) and used to analyse the microstructure evolution of both inner and outer surfaces of the AluChrom 318 plate exposed to the two extreme conditions.

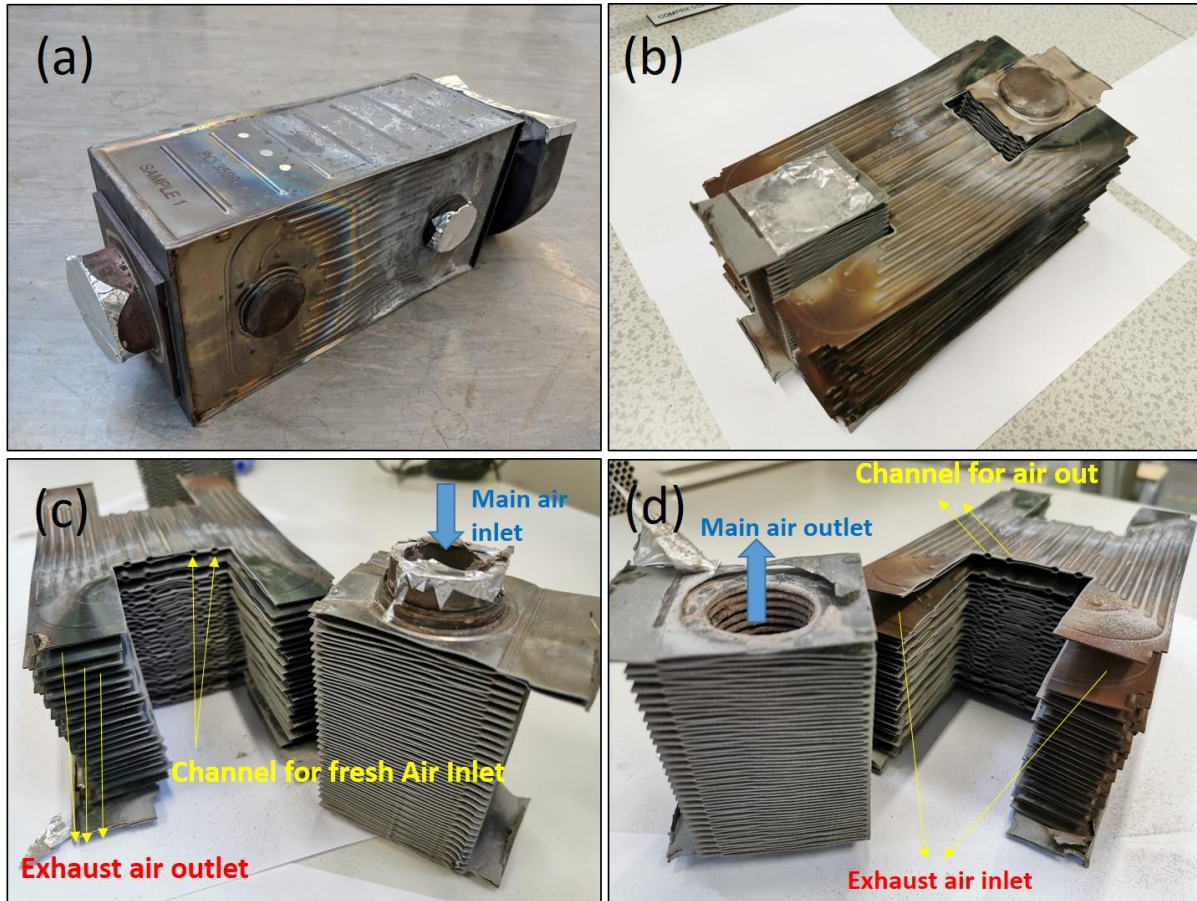


**Figure 6.1** (a-b) Picture of CAPH stack made of AluChrom 318 developed at Senior Flexonics Ltd.; (c-d) picture of CAPH stack made of multiple cells, showing the inlet and outlet for exhaust gas and fresh air.

**Table 6.1** Thermal specifications of the AluChrom 318 made CAPH during operation. Data supplied by Vaillant GmbH.

Exhaust gas in	910°C	Air in	50°C
Exhaust gas out	324°C	Air out	830°C
Total efficiency		90.8%	

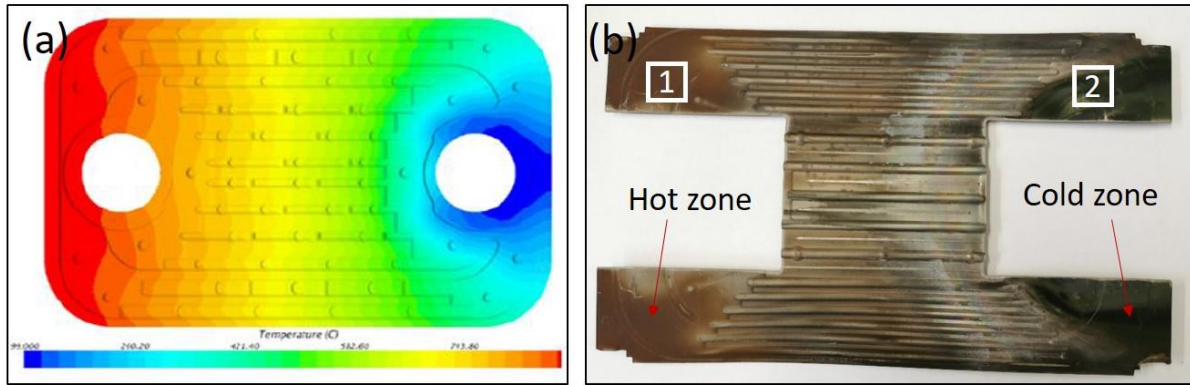


**Figure 6.2** (a) Schematic of heat distribution on a single CAPH cell during operation; (b) photograph of a single CAPH cell, showing different oxidation states in different temperature regions.

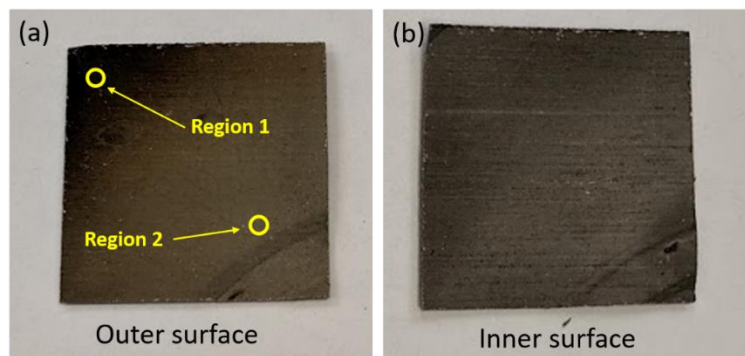
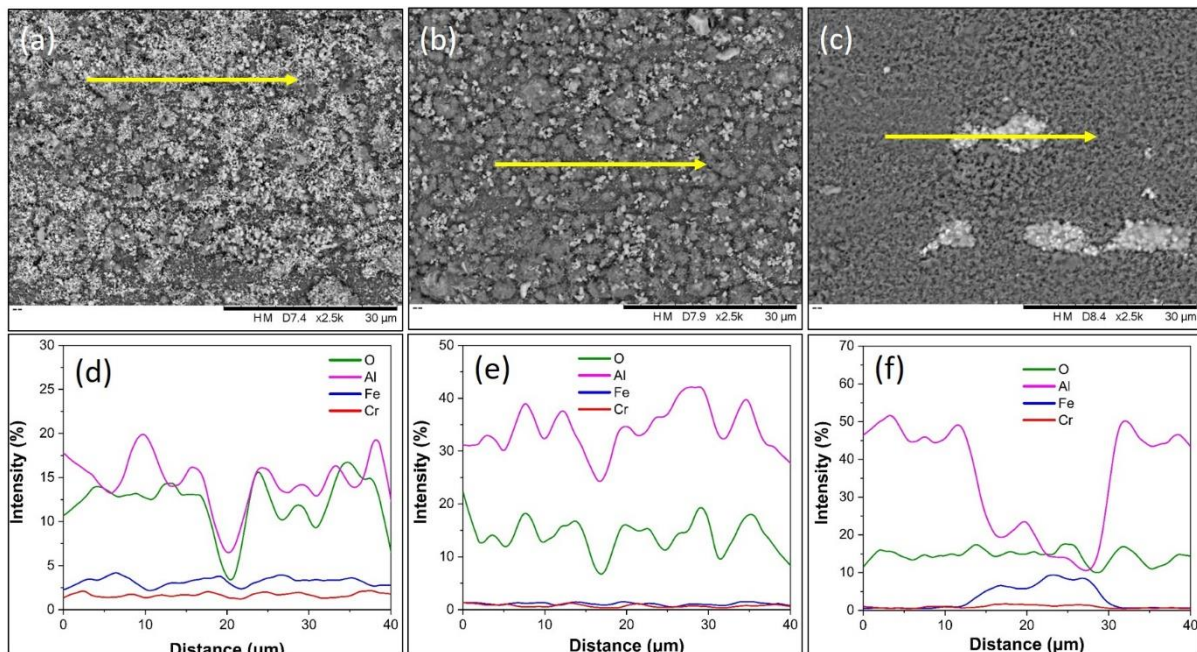


**Figure 6.3** Photos of the outer (a) and inner (b) surfaces of a single CAPH cell exposed to the hot zone. The sample was selected at location 1 in Figure 6.2b.

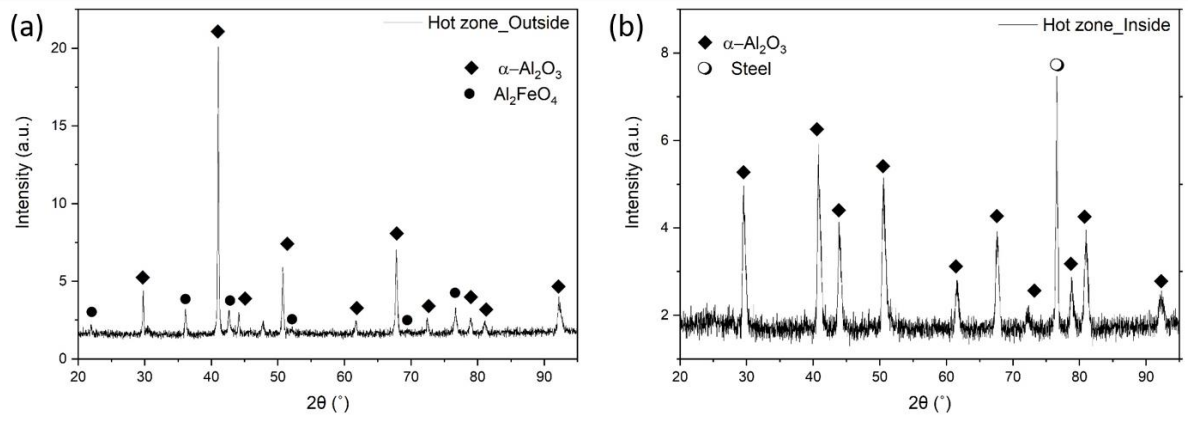
### 6.1.2 Hot zone

Figure 6.3 compares the appearance of the outer (front side) and inner (rear side) surface of the single cell exposed to the hot zone. As can be seen in Figure 6.3a, two different regions of different colour were observed on the outer surface of the cell. Region 1 which was located at the edge of the exhaust gas inlet, showed a dark brown colour. While region 2 situated close to the air outlet had a grey colour. However, the inner surface of the cassette which was exposed to an air atmosphere in the hot zone only showed a dark grey colour. Figure 6.4 shows the surface microstructure of the outer surface of the cell with region 1 and region 2 and the inner surface of the cell exposed to the hot zone. The surface oxide layers formed on

the outer surface were continuous for both region 1 and region 2 and no sign of spallation could be detected. EDX line scans revealed that both the inner and outer surface of the cell exposed in the hot zone contained a significantly high amount of Al and O. In region 1 of the outer surface, Ni and Fe also showed strong intensity in the spectrum. Figure 6.5 displays the XRD patterns of the inner and outer surface of the cell exposed in the hot zone. XRD analysis indicated that the oxide scales formed on both the inner and outer surface were mainly  $\alpha$ -Al<sub>2</sub>O<sub>3</sub>. However, an Al<sub>2</sub>FeO<sub>4</sub> phase was detected on the outer surface of the cell, which was consistent with the EDX line scan for the outer surface. Cross-sectional SEM of both the inner and outer surfaces of the cell including EDX linescans are shown in Figure 6.6. It can be seen that both the inner and the outer surface formed a continuous alumina scale since the EDX elemental maps and line scans showed a high intensity of Al in the oxide. However, the alumina scale was found to be thicker on the outer surface (4.17  $\mu$ m) than on the inner surface (3.41  $\mu$ m).



**Figure 6.4** Top view SEM images of (a) region 1 on outer surface, (b) region 2 on outer surface and (c) inner surface of the single cell exposed to the hot zone with corresponding EDX line scan analysis.



**Figure 6.5** XRD patterns of the outer (a) and inner (b) surfaces of a single CAPH cell exposed in the hot zone.

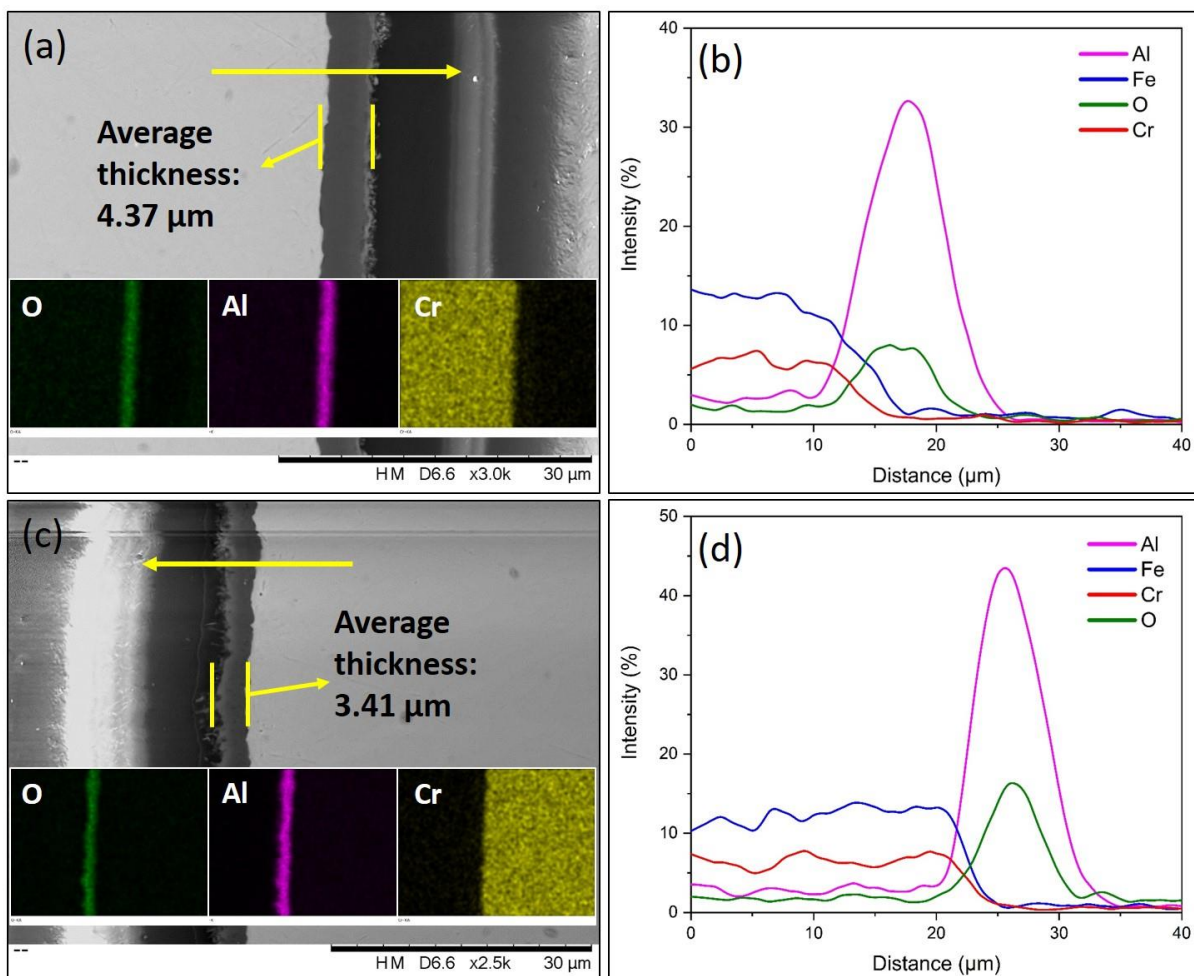


**Figure 6.6** Cross-sectional SEM images of the outer (a) and inner (c) surfaces of a single CAPH cell exposed in the hot zone. EDX linescan profiles across the oxide film on the outer (b) and inner (d) surface of a single CAPH cell exposed in the hot zone.

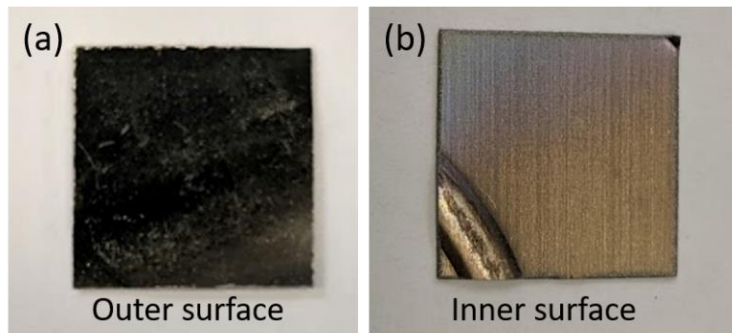
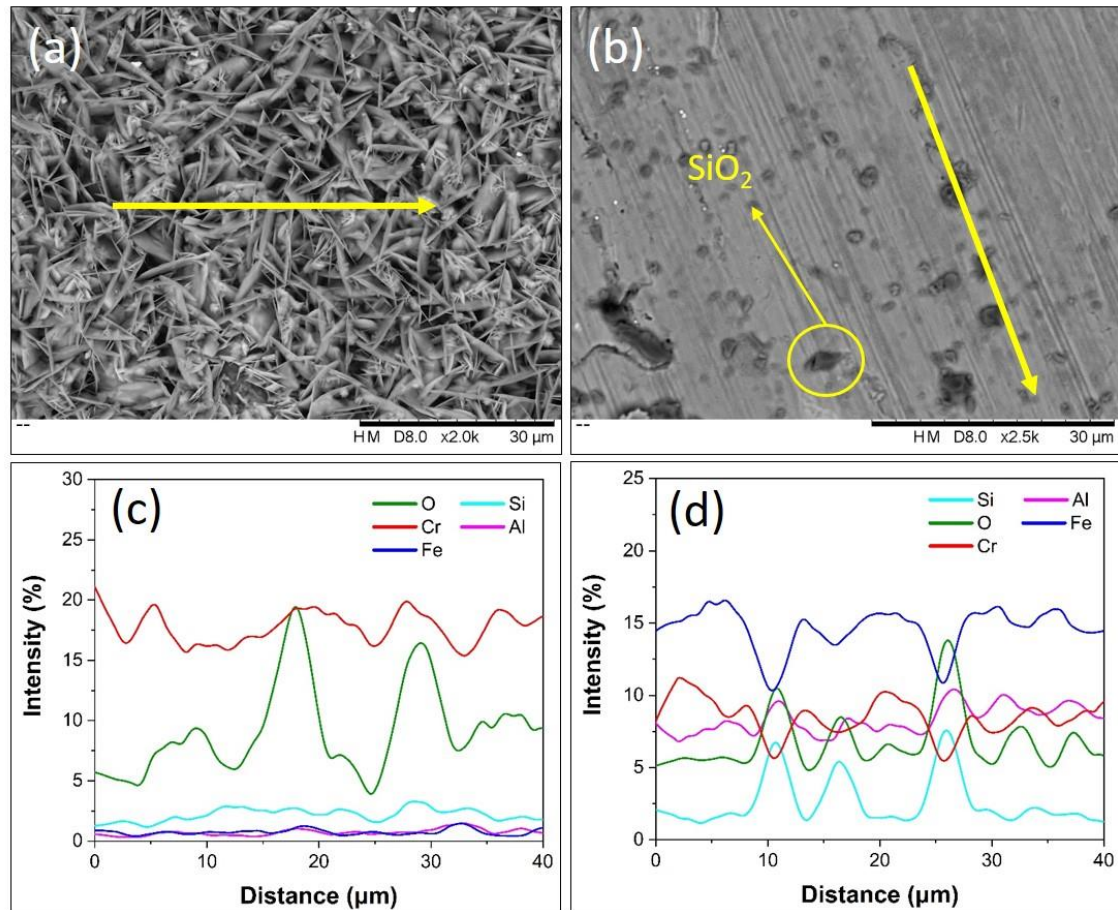


**Figure 6.7** Pictures of the outer (a) and inner (b) surfaces of a single CAPH cell exposed in the cold zone. The sample was selected at location 2 in Figure 6.2b.

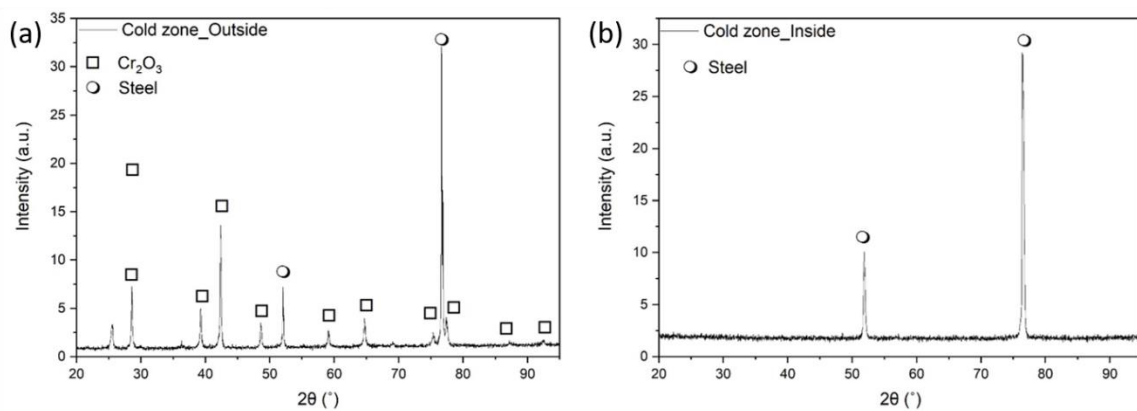
### 6.1.3 Cold zone

Figure 6.7 compares the outer and inner appearance of the single cell exposed to the cold zone for 25,000 hours. Figure 6.8 shows the surface SEM of both inner and outer surfaces of the cell exposed to the cold zone and the corresponding EDX linescans. In Figure 6.7a, the dark green film on the outer surface corresponds to the platelet-like crystals observed in the SEM (Figure 6.8a). The EDX linescan through the surface revealed that the platelet-like crystals were enriched with Cr and O. With the aid of XRD analysis (Figure 6.9a), the formation of  $\text{Cr}_2\text{O}_3$  on the outer surface was identified. Zhang et al. [200] reported that the formation of platelet-like  $\text{Cr}_2\text{O}_3$  was due to the diffusion of Cr along the tunnel within the oxides instead of grain boundaries. Cross-sectional EDX (Figure 6.10b) confirmed the finding of the XRD analysis that the oxide scale contained exclusively Cr and O, again suggesting  $\text{Cr}_2\text{O}_3$ . It can be seen that the  $\text{Cr}_2\text{O}_3$  layer was continuous and the thickness was approximately  $2.15\ \mu\text{m}$ . Visual inspection of Figure 6.7b showed that the inner surface of the cell exposed to the cold zone still remained metallic even after 25,000 hours of operation. Based on EDX analysis, the inner surface of the cell exposed in the cold zone was still dominated by Fe. The XRD pattern of the inner surface of the cell exposed in the cold zone (Figure 6.9b) showed exclusively two background peaks from the alloy base. The cross-

sectional analysis in Figure 6.10c-d further proved that the surface of the cell exposed in the cold zone still retained the extremely thin passivation layer formed at room temperature.



**Figure 6.8** Top view SEM images and EDX linescan profiles of (a,c) outer and (b,d) inner surfaces of a single cell exposed in the cold zone for 25,000 hours.



**Figure 6.9** XRD patterns of outer (a) and inner (b) surface of a single CAPH cell exposed in the cold zone for 25,000 hours.

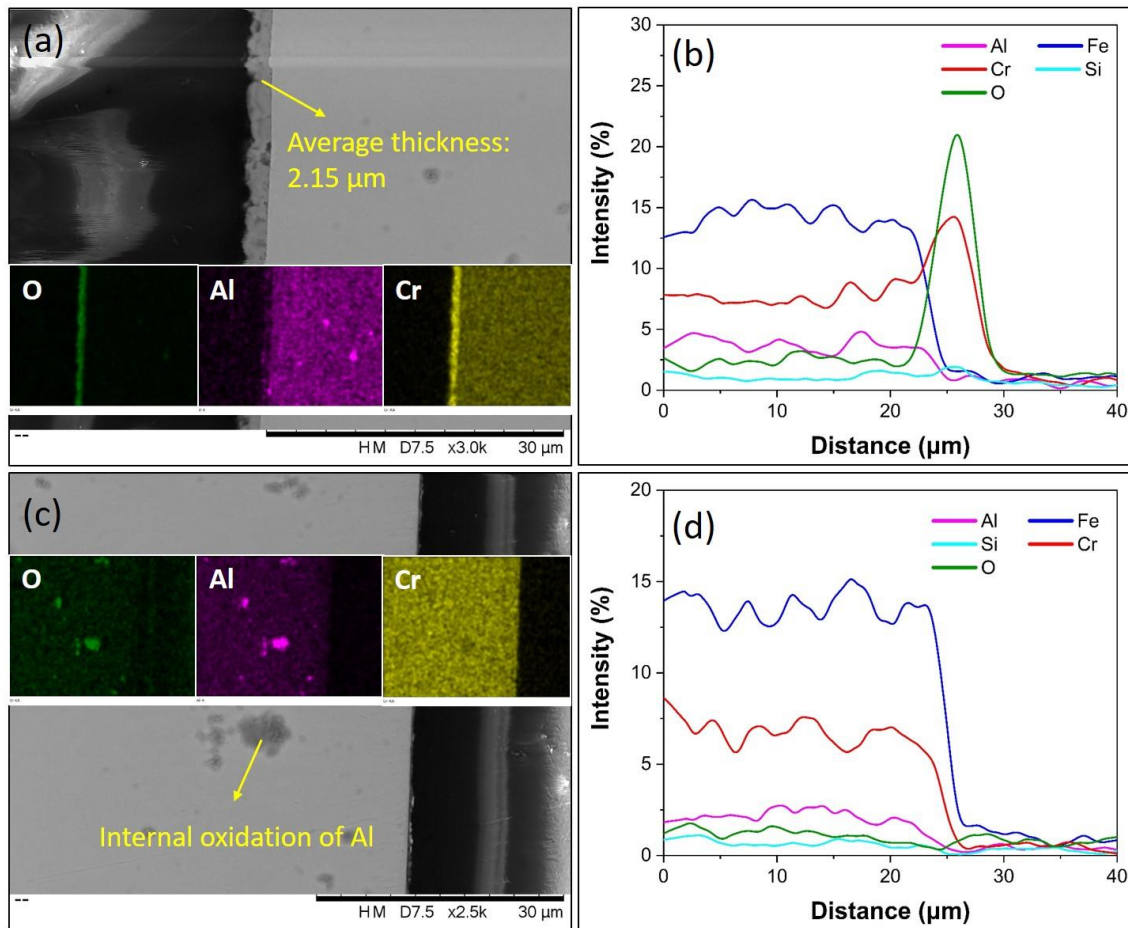


**Figure 6.10** Cross sectional images of outer (a) and inner (c) surface of a single CAPH cell exposed in the cold zone. EDX line scan profiles across the oxide film on the outer (b) and inner (d) surface of a single CAPH cell exposed in the cold zone.

## 6.2 Discussion

### 6.2.1 Hot zone

It should be noted that the analysed coupons from the hot zone were selected around the exhaust gas inlet which had direct contact with the afterburner exhaust. The temperature of the exhaust gas from the afterburner was around 910°C based on the technical data supplied by Vaillant GmbH. However, the temperature at the inner surface (air outlet) had to be lower than that of the outer surface (exhaust inlet) as the efficiency of the heat transfer cannot be 100%. This illustrates that the oxidation rate of Al was faster on the outer surface compared to the inner surface in the hot zone as the cross-sectional images showed that the alumina

scale formed on the outer surface was thicker than that on the inner surface. In addition to the effect of temperature, the composition of the exhaust gas might also have had an effect on the oxidation rate of the outer surface of the cell exposed to the hot zone. A simulation study of SOFC-CHP performed by Park et al. [201] indicated that the composition of exhaust gas from the afterburner was almost identical to the ambient air but with a higher amount of steam (around 10%). It was reported by a number of researchers that the water vapour added to the high temperature oxidising atmosphere increased the oxidation rate of alumina-forming alloys [146,153,155]. In addition, that alumina scale established in the wet atmosphere contained a higher concentration of Fe and Cr compared to that developed in dry atmosphere. This was consistent with results detected in this study, where a thicker oxide scale mixed with  $\alpha$ -Al<sub>2</sub>O<sub>3</sub> and Al<sub>2</sub>FeO<sub>4</sub> phase was formed on the outer surface of the cell exposed to the exhaust gas. This was, however, contrary to observations discussed in Chapter 4. Saunders et al. [190] pointed out that the major effect of water vapour was in the initial stage of oxidation and influenced the stability of transition alumina rather than the diffusion process in the protective  $\alpha$ -Al<sub>2</sub>O<sub>3</sub> scale once it was established. In Chapter 4, the humidified air was applied on the samples when the tested samples inside the furnace reached the programmed temperature (850°C in this study). Thus, the formation of an alumina scale during the furnace heating process to 850°C might have prohibited the observation of the effect of water vapour on the growth of the alumina scale on the AluChrom 318 surface. However, during the practical operation of the AluChrom 318 CAPH, the exhaust from the afterburner had direct contact with the heat exchanger plates without the pre-heating stage. The effect of water vapour on the initial stage oxidation of the AluChrom 318 CAPH was thus more obvious.

The corrosion resistance of the heat exchanger cells exposed in the hot zone was provided by the formation and growth of an alumina scale on both inner and outer surfaces, which also

concurrently consumed the Al reservoir in the alloy. The fast growth rate of alumina on the outer surface of the hot zone would eventually cause the exhaustion of the Al reservoir in the bulk if the growth of the alumina scale could not be sustained by the supply of Al from the underlying metal, or the content of Al was below the critical value required for the formation of alumina as outermost scale [139]. This can cause breakaway oxidation resulting in further oxidation of alloy metals and the formation of a poorly protective iron oxide. It is worth noting that both the inner and the outer surface of the CAPH cell were simultaneously exposed to air and exhaust gas, respectively. If the concentration of Al in the bulk was too low to maintain the continuous growth of alumina on the outer surface, there would not be enough Al to re-heal the scale spallation observed on the inner surface of the cell. The underlying metal (spalled area) exposed to the oxidising environment would lead to an exponential increase in Cr<sub>2</sub>O<sub>3</sub> evaporation from the CAPH cells exposed in the hot zone. Thus, a pre-formed alumina scale on the AluChrom 318 CAPH will be beneficial in preventing the deleterious effect of steam in the atmosphere. This will be further discussed in chapter 7.

### 6.2.2 Cold zone

The anti-corrosion protection of the CAPH exposed in the hot zone was provided by the formation of an  $\alpha$ -Al<sub>2</sub>O<sub>3</sub> scale under high temperature conditions. However, due to its extremely low growth rates at low and intermediate temperatures, the  $\alpha$ -Al<sub>2</sub>O<sub>3</sub> scale offers less protection at these temperatures. It has been reported that the alumina-forming alloys that are designed for very high temperatures also contain sufficient chromium to produce a Cr<sub>2</sub>O<sub>3</sub> scale at intermediate temperatures [202]. Terrani et al. [203] reported the formation of a Cr<sub>2</sub>O<sub>3</sub> outer layer on the FeCrAl alloy exposed to pure water + 2 ppm O<sub>2</sub> at 288°C for 1 year. Therefore, the protection against oxidation of the outer surface in the cold zone (low temperature region) relied on the formation of the Cr<sub>2</sub>O<sub>3</sub> scale. The SEM/EDX and XRD

results suggested that no protective layer was formed on the inner surface of the cell exposed to the cold zone due to the extremely low temperature (50°C) of the inlet air which was not high enough to trigger the oxidation of Cr and Al. Therefore, it can be inferred that the formed Cr<sub>2</sub>O<sub>3</sub> layer on the outer surface and the uncovered inner surface in the cold zone were vulnerable to migration/evaporation of Cr(VI) species from the CAPH into the environment and the fuel cell system. For the same principle, a pre-formed alumina scale on the AluChrom 318 CAPH will be able to prevent the formation of the Cr<sub>2</sub>O<sub>3</sub> layer on the outer surface and give protection for the inner surface in the cold zone.

### 6.3 Conclusions

This chapter mainly focused on the characterisation of an AluChrom 318 CAPH after its practical operation in simulated SOFC environment for 25,000 hours. Due to the convective flow between the hot exhaust gas and the incoming cold air, the temperature gradient across the heat exchanger plate caused different oxidation states from high to low temperature regions. In the high temperature area, both inner and outer surfaces of the single CAPH cells were protected by the formed  $\alpha$ -Al<sub>2</sub>O<sub>3</sub> scale. However, the detection of an Al<sub>2</sub>FeO<sub>4</sub> compound on the outer surface indicated an accelerated oxidation rate of the outer surface exposed in high temperature exhaust with high humidity. In the low temperature area, a thick Cr<sub>2</sub>O<sub>3</sub> layer formed on the outer surface of the single CAPH cell, owing to the extremely low growth rate of Al<sub>2</sub>O<sub>3</sub> at low temperatures. Besides, no oxide layer was formed on the inner surface of the cell exposed to the cold zone due to the extremely low temperature of the inlet air. A pre-treatment was suggested to enable the heat exchanger plate to form an alumina scale prior to the application in the SOFC system. The pre-treatment was expected to produce an  $\alpha$ -Al<sub>2</sub>O<sub>3</sub> scale on the entire heat exchanger surface that would reduce the growth rate of alumina scale in the hot zone and eliminate the formation of a Cr<sub>2</sub>O<sub>3</sub> scale in the cold zone.

## Chapter 7 – The Effect of Pre-treatment of AluChrom 318 on the Corrosion Behaviour and Cr Evaporation in SOFC Cathode Air Pre-heaters\*

As discussed in chapter 6, longer-term operation of the AluChrom 318 heat exchanger plates in SOFC cathode environment showed a large amount of  $\text{Cr}_2\text{O}_3$  formation around the exhaust outlet (cold zone) and a fast Al oxidation rate around the exhaust inlet (hot zone). For material optimisation, a pre-heat treatment was therefore proposed to allow sufficient formation of an alumina scale on the AluChrom 318 CAPH prior to the application in SOFC environments. Studies on the effects of pre-treatment on alumina-forming alloys have been reported in the literature [43,127], showing the corrosion resistance to be hugely improved. Stanislawski et al. [43] found an improvement in the corrosion resistance and Cr retention ability of alumina formers such as AluChrom YHf, AluChrom YB, Kanthal AF and PM 2000 after a pre-oxidation at  $1200^\circ\text{C}$  in air for 24 hours. However, the pre-treatments were mostly performed at extremely high temperature ( $1200^\circ\text{C}$ ) with a long dwelling time (24 hours) which would considerably increase the cost of production, if employed in CAPH manufacturing. Thus, in the current work, the pre-treatment of the AluChrom 318 was suggested to be performed directly in air atmosphere with relatively low temperatures ( $800$  to  $1100^\circ\text{C}$ ) and short dwelling time (0.5 to 4 hours) to form the most stable alumina phase ( $\alpha\text{-Al}_2\text{O}_3$ ) on both inner and outer surfaces of the single CAPH cell, which would make the pre-treatment process cost-effective and suitable for industrialisation. The aim of this chapter is to study the effect of pre-treatment temperature and time on the phase formation of alumina scale and measure the Cr(VI) species released from the AluChrom 318 pre-treated at different

---

\* This work was published in ECS Transactions <K. Zhang, A. El-kharouf, and R. Steinberger-Wilckens. *ECS Trans.*, 91 (2017) 2253-2260> and ACS Applied Materials & Interfaces <K. Zhang, A. El-kharouf, and R. Steinberger-Wilckens. *ACS Appl. Mater. Interfaces*. Manuscript submitted>.

conditions by means of a denuder technique. The suitability of pre-treatment for AluChrom 318 for SOFC CAPH application concerning the Cr retention capability will be discussed.

## 7.1 Results

### 7.1.1 Pre-Treatment

#### 7.1.1.1 Mass measurement

Figure 7.1 shows the effect of pre-treatment temperature and dwelling time on the oxidation behaviour of AluChrom 318. The mass increase obtained from pre-treatment corresponds to the reaction between oxygen and alloy elements which is mainly the establishment of an alumina layer in the case of an alumina-forming alloy. It can be seen that the mass gain values increased with the pre-treatment temperature and time. The mass gain showed a linear relationship with pre-treatment dwelling time (Figure 7.1a) while it had an exponential relation to pre-heating temperature (Figure 7.1b). Moreover, depending on the pre-treatment temperature, the slope of each linear relationship increased with the temperature as shown in Figure 7.1a.

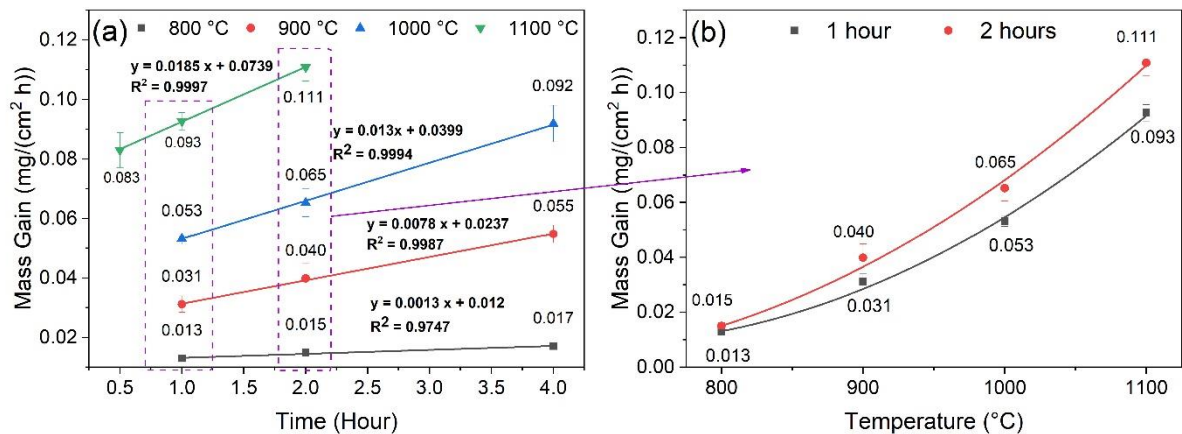


**Figure 7.1** (a) Mass gain of AluChrom 318 pre-treated at 800°C for 1, 2 and 4 hours, 900°C for 1, 2 and 4 hours, 1000°C for 1, 2 and 4 hours and 1100°C for 0.5, 1 and 2 hours; (b) Mass gain of the AluChrom pre-treated at 800°C, 900°C, 1000°C and 1100°C for 1 and 2 hours.

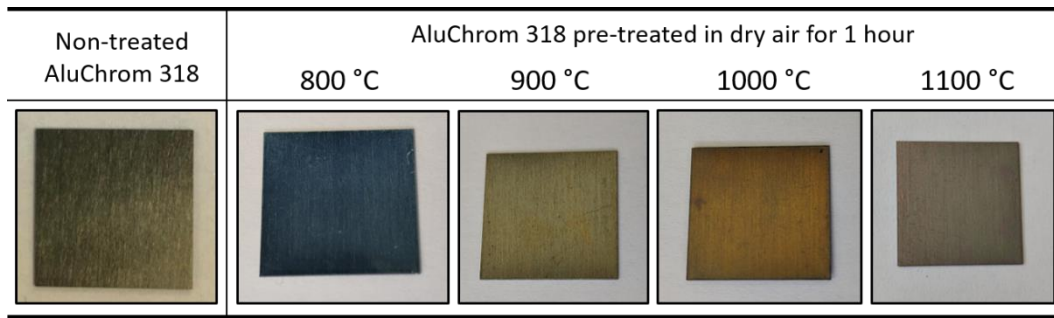


**Figure 7.2** Photographs of the non-treated AluChrom 318 and the AluChrom 318 pre-treated at 800, 900, 1000 and 1100°C in dry air for 1 hour.

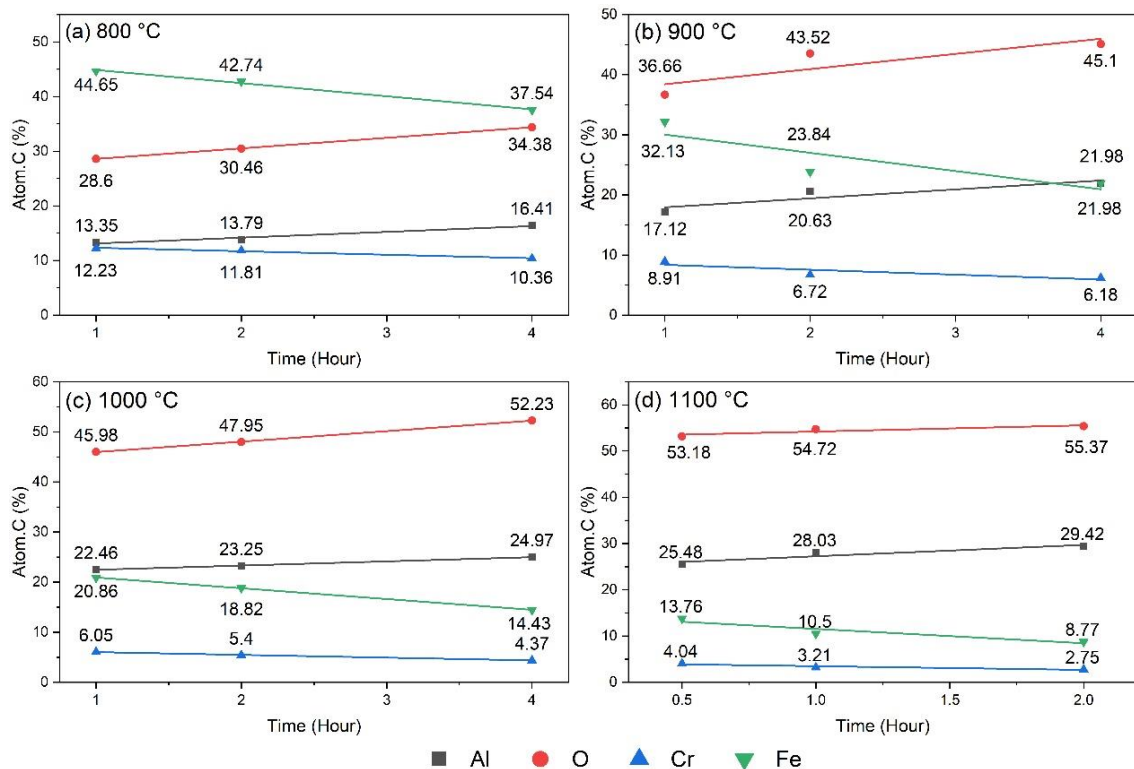
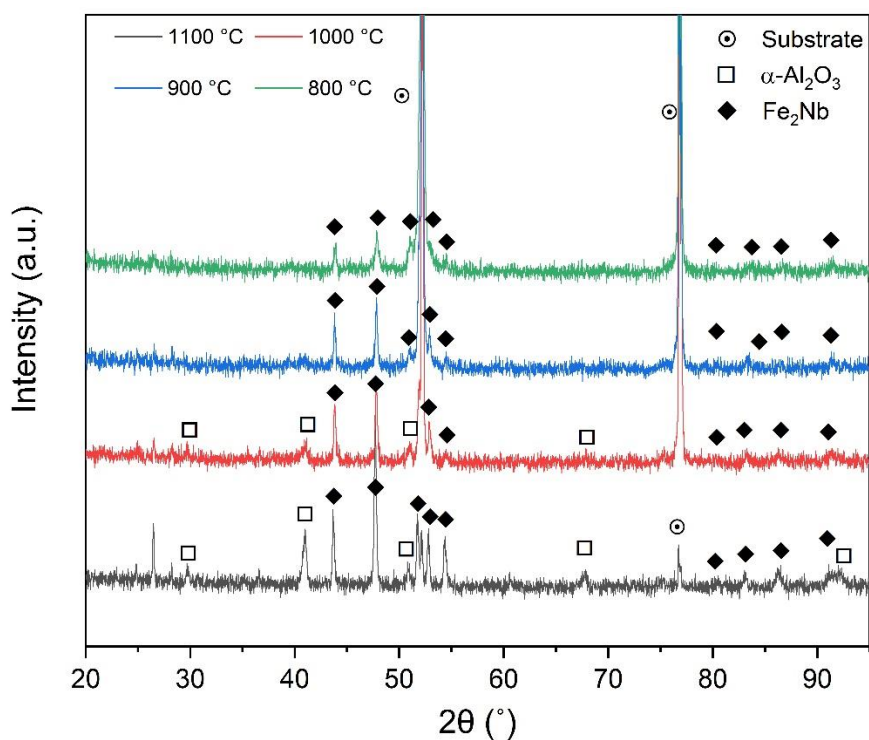


**Figure 7.3** EDX elemental concentration of AluChrom 318 surface pre-heated at (a) 800°C for 1, 2 and 4 hours, (b) 900°C for 1, 2 and 4 hours, (c) 1000°C for 1, 2 and 4 hours and (d) 1100°C for 0.5, 1 and 2 hours.

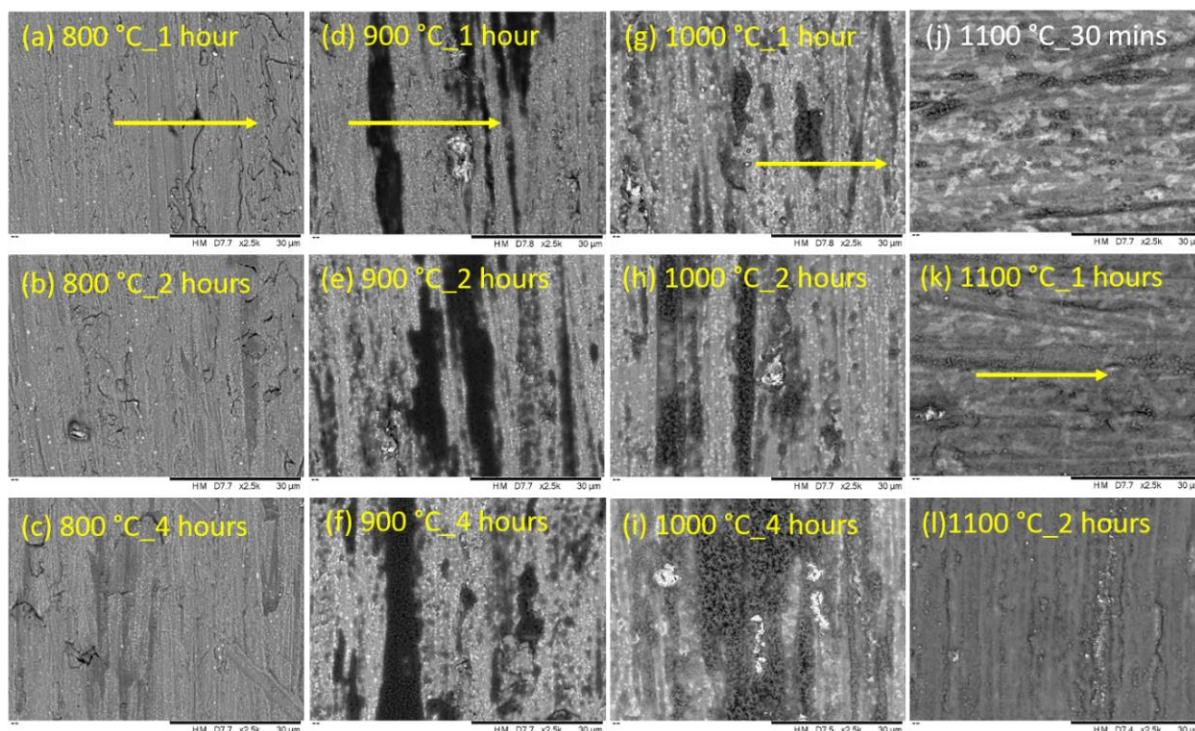
### 7.1.1.2 Surface characterisation

Figure 7.2 exhibits the photographs of the non-treated AluChrom 318 and the AluChrom 318 pre-treated at 800, 900, 1000 and 1100°C in dry air for 1 hour. The non-treated AluChrom 318 showed a shiny metallic surface. The samples pre-treated at 800, 900, 1000 and 1100°C exhibited dark blue, green, gold and grey colours, respectively. The different colours

presented by the alloy surfaces might indicate the oxidation degree of the AluChrom 318 pre-treated at different temperatures. Figure 7.3 shows the EDX elemental concentration of four critical elements (O, Al, Cr and Fe) present on the alloy surface after being pre-treated at different temperatures from 800 to 1100°C. For all the four pre-treatment temperatures, the concentrations of Al and O increased with the ascending dwelling time which corresponded to the continuous growth of alumina scale on the alloy surface. The decreased concentration of Fe and Cr could be attributed to the increased coverage by alumina scale on the alloy surface, since aluminium will preferentially oxidise prior to Cr and Fe when the concentration of Al is higher than 3 wt.% in the alumina-forming alloy [37]. The sample pre-treated at 800°C showed the highest surface concentration of Cr (12 at.%), in comparison with the lowest Cr surface concentration of 2.75 at.% for the sample pre-treated at 1100°C for 2 hours. It is also interesting to note that the surface concentration of the four elements on the sample pre-treated at 800°C for 4 hours was comparable to that on the sample pre-treated at 900°C for 1 hour. In addition, the samples pre-treated at 900°C for 4 hours and 1000°C for 1 hour demonstrated quite similar levels of surface concentration of O, Al, Cr and Fe. The surface element concentrations of the sample pre-treated at 1000°C for 4 hours was also found to be close to that of the sample pre-treated at 1100°C for 30 minutes. The AluChrom 318 pre-treated at 800, 900, 1000 and 1100°C for 1 hour were characterised by XRD to examine the effect of temperature on the alumina crystalline structure, and the obtained diffractograms are displayed in Figure 7.4. Peak pattern matching of the XRD patterns showed the presence of Fe<sub>2</sub>Nb for the samples pre-treated at all four temperatures. For the samples pre-treated at 1000 and 1100°C, XRD confirmed the formation of an  $\alpha$ -Al<sub>2</sub>O<sub>3</sub> phase on the alloy surface. However, it is worth noting that the phase of alumina formed on the samples after being pre-treated at 800 and 900°C could not be detected by XRD because the oxides are extremely thin, resulting in a very low intensity of the diffraction peaks [152,204].



**Figure 7.4** XRD patterns of the AluChrom 318 pre-treated at 800, 900, 1000 and 1100°C for 1 hour.



**Figure 7.5** Backscattered electron images of the oxide scale formed after being pre-treated at 800°C for 1 (a), 2 (b) and 4 (c) hours, at 900°C for 1 (d) , 2 (e) and 4 (f) hours, at 1000°C for 1 (g), 2 (h) and 4 (i) hours and at 1100°C for 0.5 (j), 1 (k) and 2 (l) hours.

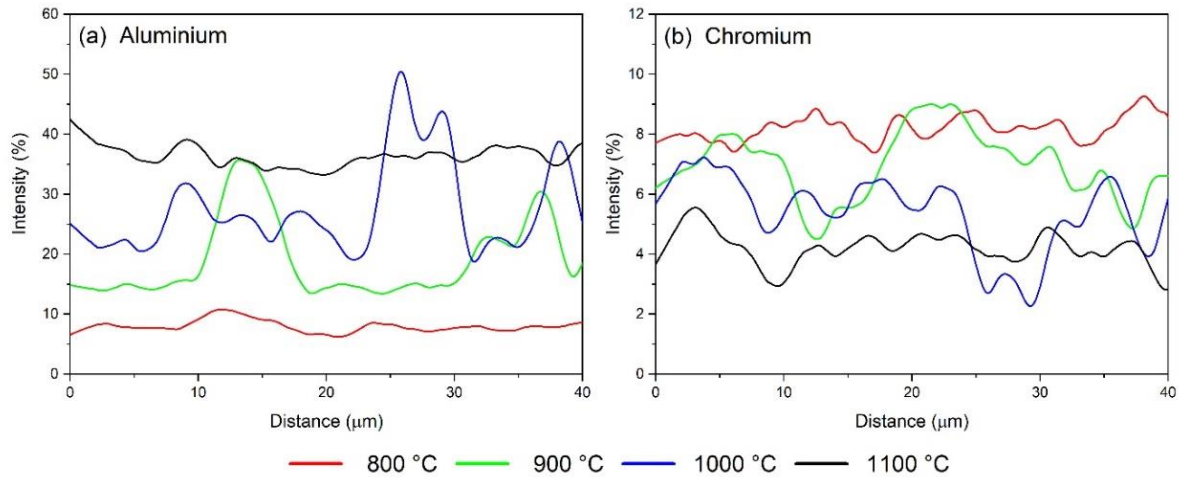


**Figure 7.6** EDX line scan of Al (a) and Cr (b) for the AluChrom 318 pre-heated at 800, 900, 1000 and 1100°C for 1 hour along the line indicated in Figure 7.5.

The SEM micrographs of all pre-treated samples are displayed in Figure 7.5. Figure 7.6 compares the EDX line scan intensity of Al and Cr along the indicated lines from the samples pre-treated for 1 hour at the four different temperatures. After pre-treatment at 800°C for 1, 2 and 4 hours, the surfaces still looked metallic, and the original scratches left from manufacturing were still visible on the surface. As indicated by the EDX line scan, the surface of the AluChrom 318 after being treated at 800°C for 1 hour exhibited the lowest intensity of Al and the highest intensity of Cr among all the 1-hour pre-treated samples. The samples pre-treated at 900°C had built more alumina on the alloy surface in comparison. However, the distribution of alumina on the surface was considered to be nonhomogeneous. As indicated by the EDX linescan for the sample pre-treated at 900°C for 1 hour, the dark region showed extremely high intensity of Al and low intensity of Cr corresponding to areas covered with a thick alumina scale. Furthermore, more areas on the surface were observed to be covered with a thick alumina scale with the pre-treatment dwelling time increased to 4 hours at 900°C. In contrast, the grey region with lower intensity of Al and slightly higher intensity of Cr corresponded to the formation of a thinner alumina scale on the alloy surface. The alumina scale developed on the samples after being pre-treated at 1000°C also had a

nonhomogeneous thickness. However, the partially covered thick alumina formed on the samples pre-treated at 1000°C exhibited a platelet-like structure which was completely different from that formed on the samples pre-treated at 900°C. The EDX line scan confirmed that the platelet-like alumina showed the highest intensity of Al and the lowest intensity of Cr. With the increase of dwelling time, the platelet-like alumina considerably expanded in size. However, the thin alumina area in the sample pre-treated at 1000°C for 1 hour still showed a lower Al intensity and higher intensity of Cr in comparison with the sample pre-heated at 1100°C for 1 hour. Unlike the samples pre-heated at 900 and 1000°C, the distribution of alumina scale on the samples pre-treated at 1100°C was much more homogeneous with the highest intensity of Al and the lowest intensity of Cr. It is noted that the platelet-like alumina formed on the AluChrom 318 pre-treated at 1100°C was much less compared to that formed at 1000°C. Furthermore, when the dwelling time increased to 2 hours at 1100°C, the platelet-like alumina almost disappeared and only a dense oxide layer was observed. The TEM samples for samples pre-treated at 900 and 1100°C for 1 hour were prepared from the region covered by both dense oxide layer and the platelet-like alumina.

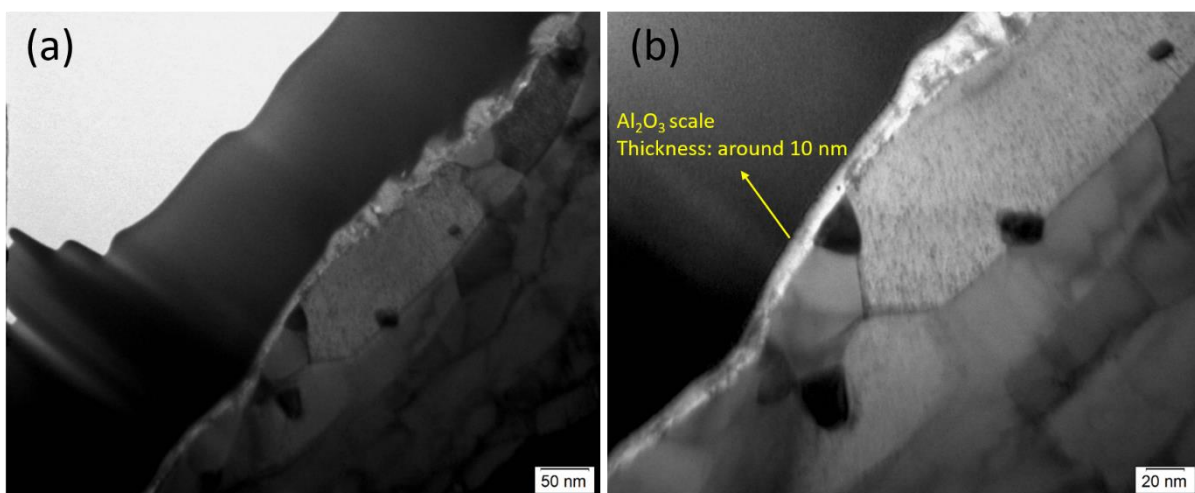


**Figure 7.7** (a) TEM bright field cross-sectional images of the oxide scale formed on the AluChrom 318 pre-treated at 900°C for 1 hour; (b) Magnified TEM image of Figure (a), showing a two-layered structure.

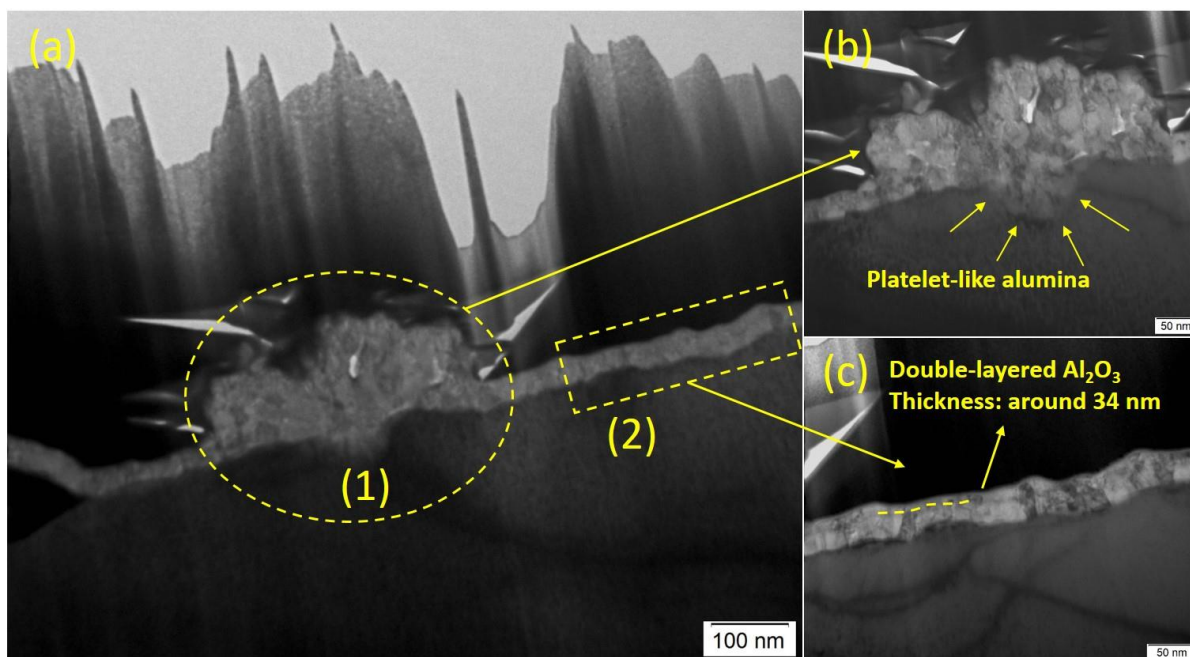


**Figure 7.8** (a) TEM bright field cross-sectional images of the oxide scale formed on the AluChrom 318 pre-treated at 900°C for 1 hour; (b) Magnification of location 1 in Figure 7.8a, showing the platelet-like alumina grown above a pit; (c) Magnification of location 2 in Figure 7.8a, showing a two-layered structure.

### 7.1.1.3 Cross-section analysis

The TEM images in Figure 7.7 show a cross-section through the oxide scale formed after 1 hour exposure in dry air at 900°C. It can be seen that the oxide scale was extremely thin and had a thickness around 10 nm. Both Liu et al. [136] and Gotlind et al. [152] reported the formation of a double-layered alumina scale with 100 nm thickness on Kanthal AF (Al 5.1 wt.%) after exposure in dry O<sub>2</sub> at 900°C for 1 hours. However, the duplex structure of the scale formed on the AluChrom 318 after 1 hour pre-treatment at 900°C was difficult to distinguish even in a TEM micrograph at high magnification due to the extremely thin layer. This may also be the reason for the failure of XRD to detect the alumina phase for samples pre-treated at 800 and 900°C, where the amount of alumina formed was too low and below the detection limit of the XRD technique. The TEM images in Figure 7.8 display a cross-section through the oxide scale formed on the AluChrom 318 after 1 hour pre-treatment in air

at 1100°C. Figure 7.8b shows the growth of the platelet-like alumina above a pit. Figure 7.8c shows that the oxide scale was around 34 nm thick and had a double-layered structure with an outer and inner layer, the inner layer making up approximately two thirds of the total thickness. As can be seen, this oxide thickness was about three times higher than that formed at 900°C. This was consistent with the mass measurements. The mass gain of the AluChrom 318 pre-treated at 1100°C for 1 hour was three times higher than that pre-treated at 900°C (Figure 7.1a). A STEM cross-sectional image of the oxide scale formed on the AluChrom 318 pre-treated at 1100°C for 1 hour is exhibited in Figure 7.9a, accompanied by EDX elemental maps. The Cr map detected a narrow Cr-rich band located at the interface between outer and inner alumina layers. In the Fe map, the distribution of Fe in the oxide scale only showed a very weak signal in the outer layer. EDX linescans (Figure 7.9b) were performed in order to further analyse the elemental distribution in the oxide scale. As can be seen, the compositional profiles of the oxide scale exhibited three different regions. Region I was the inner  $\alpha$ -Al<sub>2</sub>O<sub>3</sub> layer and contained the highest level of Al, with no Cr and Fe. Region II had a high concentration of Cr, indicating the Cr-rich band detected in the Cr map. Region III was the outer alumina layer and had a lower Al concentration compared to region I. In addition, a small amount of Fe and Cr was also observed in region III.

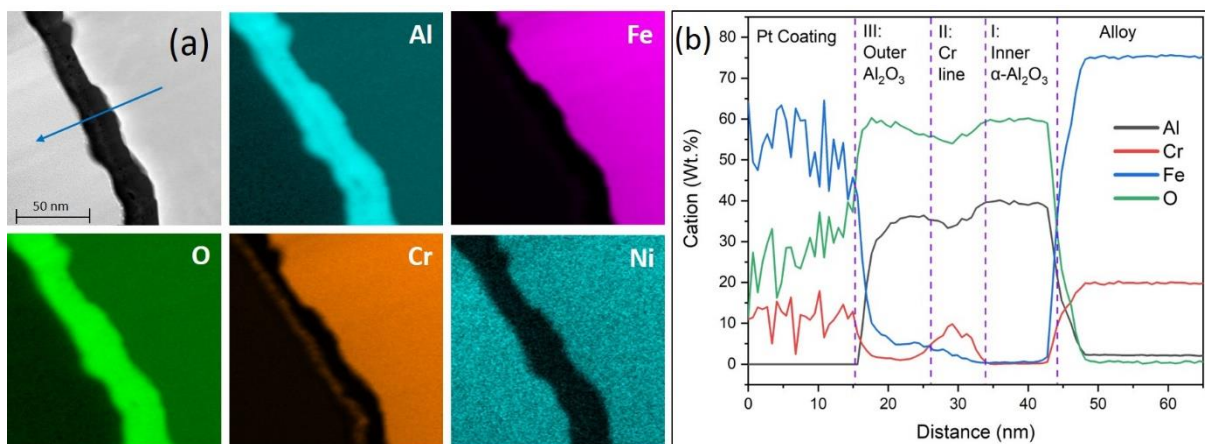


**Figure 7.9** STEM bright field image and EDX maps of the AluChrom 318 pre-treated at 1100°C for 1 hour; (b) EDX linescan along the line indicated in Figure 7.9a.

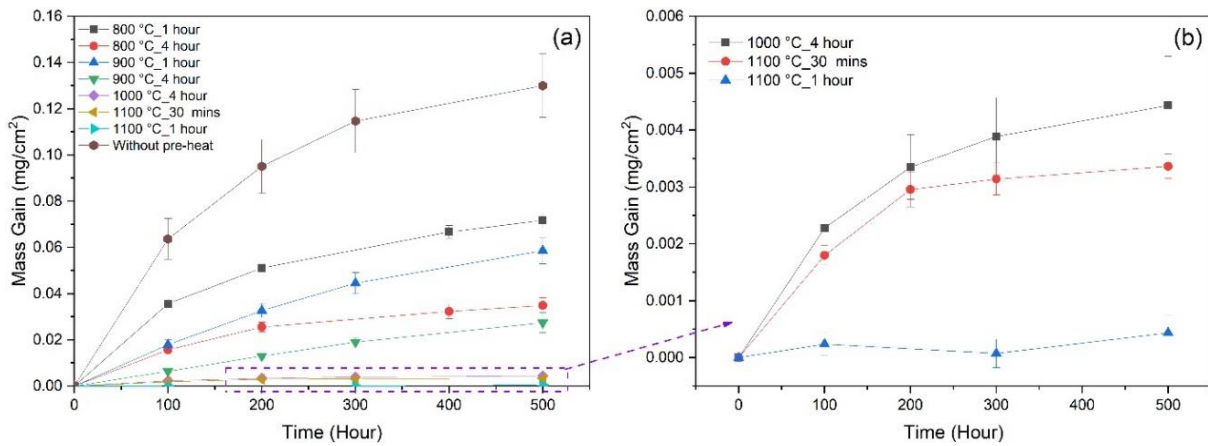


**Figure 7.10** Discontinuous mass measurements of the non-treated and pre-treated AluChrom 318 exposed to 3% humidified air (6.0 L/min) at 850°C for 500 hours.

## 7.1.2 Exposure Test

### 7.1.2.1 Mass measurements

The mass gain of the pre-treated samples after 500 hours exposure at 850°C in 3% humidified air (6.0 L/min) compared with the non-treated sample is plotted in Figure 7.10. It can be seen that all the pre-treated samples showed a lower mass gain compared to the non-treated sample (0.130 mg/cm<sup>2</sup>) over the 500 hours exposure test. In this study, a low mass gain corresponded to a low oxidation rate for the pre-treated samples exposed to the simulated SOFC cathode conditions. The samples pre-treated at 800°C for 1 hour showed the highest mass gain (0.072 mg/cm<sup>2</sup>) among all the pre-treated samples after 500 hours exposure while the mass gain was found to be dramatically decreased with the pre-treated samples when the dwelling time increased to 4 hours (0.035 mg/cm<sup>2</sup>) at the same pre-treatment temperature. By comparing the same dwelling time and varying the temperature, the samples pre-treated at 900°C for 1 hour (0.059 mg/cm<sup>2</sup>) showed a lower mass gain than the samples treated at 800°C for 1 hour, and the samples pre-treated at 900°C for 4 hours (0.027 mg/cm<sup>2</sup>) showed a lower mass gain than the samples pre-treated at 800°C for 4 hour after the exposure tests. The overall mass gain of the samples pre-treated at 1100°C for 30 minutes ( $3.36 \times 10^{-3}$  mg/cm<sup>2</sup>) was slightly

lower than the samples pre-treated at 1000°C for 4 hours ( $4.44 \times 10^{-3}$  mg/cm<sup>2</sup>) after 500 hours exposure. The best corrosion resistance was observed for the samples pre-heated at 1100°C for 1 hour ( $4.37 \times 10^{-4}$  mg/cm<sup>2</sup>) with a 98% reduction of oxidation rate compared to the non-treated AluChrom 318 due to the formation of an  $\alpha$ -Al<sub>2</sub>O<sub>3</sub> layer.

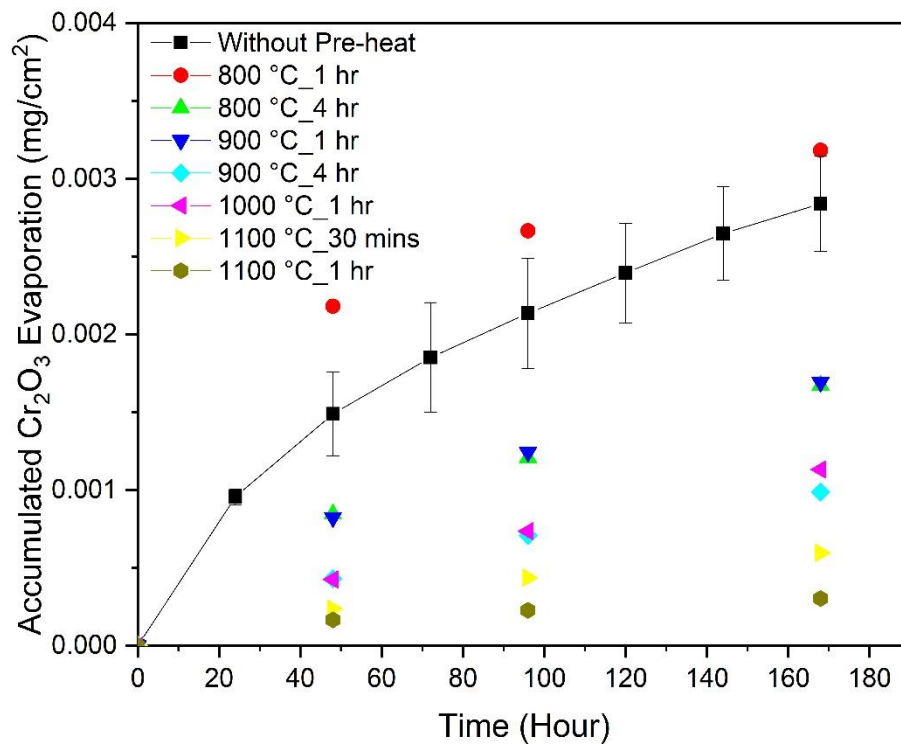


**Figure 7.11** Accumulated Cr<sub>2</sub>O<sub>3</sub> evaporation as function of time for the non-treated and pre-heated AluChrom 318 exposed at 850°C in 3% humidified air for 168 hours.

### 7.1.2.2 Cr evaporation

The evaporation of Cr<sub>2</sub>O<sub>3</sub> from the treated and non-treated AluChrom 318 is plotted in Figure 7.11. It is interesting to note that the samples pre-treated at 800°C for 1 hour showed the highest amount of Cr<sub>2</sub>O<sub>3</sub> evaporation ( $3.18 \times 10^{-3}$  mg/cm<sup>2</sup>). In contrast, the amount of Cr<sub>2</sub>O<sub>3</sub> evaporated from the samples pre-treated at 800°C for 4 hours ( $1.67 \times 10^{-3}$  mg/cm<sup>2</sup>) was lower than the non-treated samples ( $2.84 \times 10^{-3}$  mg/cm<sup>2</sup>). The samples pre-heated at 900°C for 1 hour had a similar level of Cr<sub>2</sub>O<sub>3</sub> evaporation ( $1.69 \times 10^{-3}$  mg/cm<sup>2</sup>) as those pre-heated at 800°C for 4 hours. Whereas, with pre-treatment time increasing to 4 hours at 900°C, the

amount of  $\text{Cr}_2\text{O}_3$  evaporated from the alloys had decreased to  $9.88 \times 10^{-4} \text{ mg/cm}^2$  which is 35% of that from non-treated samples. The samples pre-treated at  $1000^\circ\text{C}$  for 1 hour showed an amount of  $\text{Cr}_2\text{O}_3$  vaporisation of  $1.13 \times 10^{-3} \text{ mg/cm}^2$  which was comparable to that from the samples pre-treated at  $900^\circ\text{C}$  for 4 hours. It is worth noting that the samples pre-heated at  $1100^\circ\text{C}$  displayed the lowest level of  $\text{Cr}_2\text{O}_3$  evaporation among all the pre-treatment temperatures investigated in this research. The quantity of  $\text{Cr}_2\text{O}_3$  evaporated from the non-treated sample ( $2.84 \times 10^{-3} \text{ mg/cm}^2$ ) was 5 times higher than that from the sample pre-treated at  $1100^\circ\text{C}$  for 30 minutes ( $5.97 \times 10^{-4} \text{ mg/cm}^2$ ) and 10 times higher than that from the sample pre-treated at  $1100^\circ\text{C}$  for 1 hour ( $3.03 \times 10^{-4} \text{ mg/cm}^2$ ) over the 168 hours of collection.

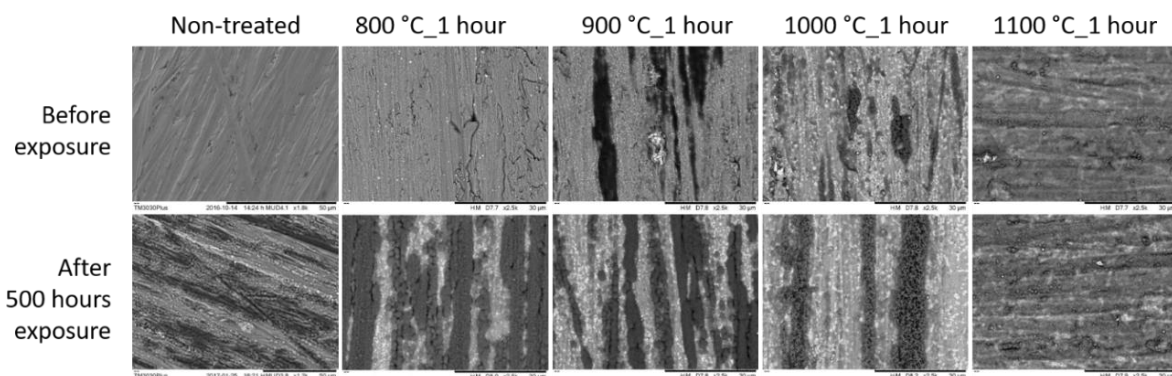


**Figure 7.12** Surface SEM images of the non-treated AluChrom 318 and the AluChrom 318 pre-treated for 1 hour at 800, 900, 1000 and  $1100^\circ\text{C}$  before and after being exposed at  $850^\circ\text{C}$  in 3% humidified air for 500 hours.

### 7.1.2.3 Surface analysis

Figure 7.12 compares the surface morphology of non-treated AluChrom 318 and pre-treated AluChrom 318 for 1 hour at 800, 900, 1000 and  $1100^\circ\text{C}$  before and after the 500 hours exposure at  $850^\circ\text{C}$  in 3% humidified air. The surface of non-treated AluChrom 318 with the exposure time of 500 hours produced two distinct alumina zones, chequered with globular and long ridged alumina with dark grey colour and plane (flat) alumina with light grey colour. The formation mechanism of the long ridged alumina on AluChrom 318 surface had been

elaborated in chapter 5. However, this surface morphology was more noticeable in the SEM images of samples pre-treated at 800 and 900°C than the non-treated one after 500 hours exposure. For the samples pre-treated at 1000°C for 1 hour, the partially covered platelet-like alumina had grown larger after 500 hours exposure. It is worth noting that the morphology of alumina scale formed on the samples pre-treated at 1100°C did not show any change before and after 500 hours of exposure in simulated SOFC atmosphere.

## 7.2 Discussion

### 7.2.1 Pre-heat Treatment

Of the pre-treated samples in Figure 7.1, the mass gain showed a linear increase with dwelling time and an exponential growth with temperature. For samples pre-treated at the same temperature, the Al diffusion rate from the alloy base was constant for short-term pre-treatment, which resulted in the growth of the alumina scale at a constant rate. Whereas, for the samples pre-treated for the same dwelling time but with different temperatures, the exponentially increased Al diffusion rate at elevated temperatures led to much more rapid growth of alumina on the surface. This is further confirmed in the EDX analysis in Figure 7.3. The surface concentration of Al for the samples pre-treated for the longest dwelling time was nearly equivalent to that pre-treated for the shortest dwelling time with a 100°C increase in temperature. These findings confirmed the high effectiveness of the pre-treatment process with high temperature and short dwelling time compared to that with low temperature and long dwelling time.

As indicated by XRD, the oxide scales formed at 1000 and 1100°C consisted exclusively of  $\alpha$ -Al<sub>2</sub>O<sub>3</sub>. Since the alumina-forming alloys generally developed multi-layered oxide scales

with different crystalline structures, it is impossible to identify the phase composition of each oxide layer with XRD. The work performed by the Swedish High Temperature Corrosion Centre employed convergent beam electron diffraction (CBED) to determine the phase composition of the top and bottom alumina scales formed on Kanthal AF exposed at 900°C for 1 hour [136,152,157,158]. In their studies, the CBED patterns obtained from both the inner and outer alumina scales indicated that the double-layered alumina formed on Kanthal AF consisted of a bottom layer of  $\alpha$ -Al<sub>2</sub>O<sub>3</sub> and an upper layer of  $\gamma$ -Al<sub>2</sub>O<sub>3</sub> after 1 hour exposure at 900°C in dry oxygen. CBED analysis was also conducted on the double-layered oxide scales formed on the AluChrom 318 pre-treated at 900 and 1100°C in order to identify the phase composition of both inner and outer alumina scales. However, in this study, the CBED technique failed to identify the phase composition of both inner and outer alumina on the AluChrom 318 pre-treated at 900 and 1100°C due to the extremely thin oxide scale and small oxide grains.

Most workers in this field agree that the outer alumina scale grows by Al outward diffusion while the inner  $\alpha$ -Al<sub>2</sub>O<sub>3</sub> grows mainly by oxygen inward diffusion [205–207]. The Cr-rich oxide band is suggested to have been produced during the initial stage of oxidation to provide corrosion protection prior to the formation of an alumina scale, indicating the original metal/gas interface [152]. In addition, several researchers also reported the coexistence of  $\gamma$ -Al<sub>2</sub>O<sub>3</sub> and  $\alpha$ -Al<sub>2</sub>O<sub>3</sub> on FeCrAl alloy oxidised at low temperatures (650 to 700°C) [197,208]. Therefore, both  $\gamma$ -Al<sub>2</sub>O<sub>3</sub> and  $\alpha$ -Al<sub>2</sub>O<sub>3</sub> are expected to form simultaneously on the surface of the AluChrom 318 pre-treated at all the four temperatures in dry air environment in this study. It has been widely reported that the initially formed corundum-type oxides ( $\alpha$ -Cr<sub>2</sub>O<sub>3</sub> and  $\alpha$ -Fe<sub>2</sub>O<sub>3</sub>), which are isostructural with  $\alpha$ -Al<sub>2</sub>O<sub>3</sub>, act as crystallographic template for the nucleation and growth of  $\alpha$ -Al<sub>2</sub>O<sub>3</sub>, facilitating the easy formation of  $\alpha$ -Al<sub>2</sub>O<sub>3</sub> in the beginning

of oxidation [114,123,149]. The location of the Cr-rich band suggests that the inner  $\alpha$ -Al<sub>2</sub>O<sub>3</sub> scale nucleated near the original alloy surface and grew primarily inwards [152]. For the AluChrom 318 pre-treated at 1100°C, the presence of the  $\alpha$ -Al<sub>2</sub>O<sub>3</sub> phase confirmed by XRD must indicate the inner scale detected below the Cr-rich band.

Both Liu et al. [136] and Gotlind et al. [152] found that the thickness of the outer alumina layer (80 nm) was much higher than that of the inner layer (20 nm) on Kanthal AF exposed at 900°C in dry O<sub>2</sub> for 1 hour. In contrast, the AluChrom 318 pre-treated at 1100°C for 1 hour developed a thicker inner alumina scale than the outer alumina. This means that the outer alumina scale did not have significant growth during pre-treatment at 1100°C. Thus, the oxidation of the AluChrom 318 pre-treated at 1100°C was mainly proceeded by oxygen inward diffusion for the growth of the inner alumina layer. Liu et al. [136] also found that the outer  $\gamma$ -Al<sub>2</sub>O<sub>3</sub> on Kanthal AF transformed to  $\alpha$ -Al<sub>2</sub>O<sub>3</sub> with exposure time extended from 1 hour to 24 hours at 900°C in dry O<sub>2</sub>. Rybicki and Smialek [142] reported that the rate of the phase transformation from metastable alumina to  $\alpha$ -Al<sub>2</sub>O<sub>3</sub> was faster at higher temperatures. Thus, the outer oxide layer on the AluChrom 318 formed at 1100°C was assumed to be two different cases: 1) mixture of metastable alumina and  $\alpha$ -Al<sub>2</sub>O<sub>3</sub>; 2) pure  $\alpha$ -Al<sub>2</sub>O<sub>3</sub> formed by phase transformation from the metastable alumina at 1100°C [136,158]. As shown in Figure 7.9b, both Cr and Fe show higher concentration in the outer layer than in the inner layer. The concentration of Fe was found to be higher than that of Cr in the outer layer. Engkvist et al. [158] stated that the higher mobility of Fe in the outer Al<sub>2</sub>O<sub>3</sub> was attributed to it being in the divalent state (Fe<sup>2+</sup>). Furthermore, the growth of the outer alumina scale provided an outwards transport path for divalent cations, causing higher concentration of Fe in the outer alumina scale [152].

For the AluChrom 318 pre-treated at 1000°C, the surface SEM images revealed a different alumina phase composition which was confirmed by XRD analysis. It should be noticed that the platelet-like alumina (Figure 7.5g,h,i) had a similar morphology to the  $\gamma$ -Al<sub>2</sub>O<sub>3</sub> discovered by Kadiri et al. [135]. Moreover, the amount of the platelet-like alumina on the AluChrom 318 pre-treated at 1000°C remarkably increased as the dwelling time increased from 1 to 4 hours. In addition, the pre-treatment temperature of 1000°C was not high enough to support the complete phase transformation to the stable  $\alpha$ -Al<sub>2</sub>O<sub>3</sub> [134], thereby leaving the platelet-like metastable alumina on the surface. Therefore, we can infer the scale growth on the AluChrom 318 pre-treated at 1000°C mainly occurred in the outer alumina layer by cation outward diffusion. However, for the samples pre-treated at 1100°C, the very small amount of platelet-like alumina formed during the temperature ramping stage had dramatically decreased as the pre-treatment dwelling time increased from 30 minutes to 1 hour. In addition, with the pre-treatment time increasing to 2 hours, the surface had been completely covered with a relatively dense and even  $\alpha$ -Al<sub>2</sub>O<sub>3</sub> layer with no visible platelet-like alumina. This can be explained by the fact that the 1100°C used for pre-treatment promoted faster phase transformation of metastable alumina formed during the temperature ramping stage to the stable  $\alpha$ -Al<sub>2</sub>O<sub>3</sub> phase compared to the other lower temperatures used [142]. It can be inferred that there must be a transition temperature between 1000 and 1100°C in which only  $\alpha$ -Al<sub>2</sub>O<sub>3</sub> is formed [191]. Thus, the samples pre-treated at 1100°C for 30 minutes and 1 hour are considered to constitute promising pre-treatment conditions for industrial application in cost-effective processing.

### 7.2.2 Exposure Test

The relatively low mass gain and Cr<sub>2</sub>O<sub>3</sub> evaporation of the pre-treated samples compared to the non-treated was due to the alumina scales established on the alloy surface during pre-

treatment effectively slowing down the outward diffusion of cations ( $\text{Al}^{3+}$  and  $\text{Cr}^{3+}$ ) in the exposure tests. In addition, the corrosion behaviour and Cr retention ability of the pre-heated samples under simulated SOFC atmosphere were found to strongly depend on the pre-treatment time and temperature which can be explained by the influence of different types of alumina phases formed at different pre-treatment conditions. However, the higher  $\text{Cr}_2\text{O}_3$  evaporation of the samples pre-treated at  $800^\circ\text{C}$  for 1 hour compared to the non-treated samples was due to the fact that the  $\text{Cr}_2\text{O}_3$  formed in the initial stage of pre-treatment could not be completely covered by the simultaneously formed alumina scale under low pre-treatment temperature and short dwelling time conditions. The average thickness of the alumina scale developed on the AluChrom 318 pre-treated at  $900^\circ\text{C}$  for 1 hour was about 10 nm. A drop of the temperature by  $100^\circ\text{C}$  reduced the scale thickness of the AluChrom 318 pre-treated at  $800^\circ\text{C}$  since a reduction of temperature dramatically reduces the diffusion rates [191]. Therefore, a large amount of  $\text{Cr}_2\text{O}_3$  evaporation from the already built  $\text{Cr}_2\text{O}_3$  was observed for the samples pre-treated at  $800^\circ\text{C}$  for 1 hour. However, with the dwelling time being extended to 4 hours at  $800^\circ\text{C}$ , a decreased  $\text{Cr}_2\text{O}_3$  evaporation was detected due to the increased surface coverage by alumina scale. The higher mass gain for the samples pre-treated at 800 and  $900^\circ\text{C}$  corresponded to a faster Al outward diffusion rate for the development of an alumina scale on the outer surface, in comparison with the samples pre-treated at 1000 and  $1100^\circ\text{C}$ . It should be noted that a high Al consumption rate will cause the exhaustion of the Al reservoir in the alloy base which will eventually result in material failure at an accelerated rate [139]. In this research, one of the main objectives to carry out the pre-treatment for the AluChrom 318 was to decrease the Al oxidation rate and make the Al reservoir last longer in the CAPH application. The gross mass gain of the sample pre-treated at  $1100^\circ\text{C}$  for 1 hour can be calculated by adding the mass gain from the pre-treatment and the mass of evaporated  $\text{Cr}_2\text{O}_3$  to the mass gain obtained from the 500 hours exposure test. It

was found that the calculated gross mass gain of the sample pre-treated at 1100°C for 1 hour is 0.094 mg/cm<sup>2</sup> which is much smaller compared to gross mass gain of 0.133 mg/cm<sup>2</sup> for non-treated sample after 500 hours exposure test in simulated SOFC cathode environment. It indicates that the total Al diffused from the alloy base to the scale/gas interface for alumina formation is less for the sample pre-treated at 1100°C for 1 hour (0.094 mg/cm<sup>2</sup>) compared to the non-treated sample (0.133 mg/cm<sup>2</sup>) because the extremely low diffusivity of Al through the  $\alpha$ -Al<sub>2</sub>O<sub>3</sub> built on the sample pre-treated at 1100°C for 1 hour. Therefore, the sample pre-treated at 1100°C for 1 hour with the lowest oxidation rate amongst all the tested pre-treated samples could potentially extend material lifetime much longer for the CAPH application.

The lowest mass gain and Cr<sub>2</sub>O<sub>3</sub> evaporation of the sample pre-treated at 1100°C for 1 hour was due to the double-layered alumina scale with a thick inner  $\alpha$ -Al<sub>2</sub>O<sub>3</sub> which had a more compact lattice structure, as compared to the metastable alumina phase developed on the samples pre-treated at lower temperatures [44]. Metastable aluminas are cation-deficient and are therefore considered to possess a lower Cr retention capability than  $\alpha$ -Al<sub>2</sub>O<sub>3</sub> [43]. Furthermore, the extremely low amount of Cr<sub>2</sub>O<sub>3</sub> evaporation from the sample pre-treated at 1100°C was considered to be the Cr outward diffusion from the Cr-rich band between the upper and bottom oxide scale [152], instead of from the alloy base. The observation that no other cations were detected in the inner  $\alpha$ -Al<sub>2</sub>O<sub>3</sub>, is suggested to reflect the excellent barrier effect of  $\alpha$ -Al<sub>2</sub>O<sub>3</sub> for Cr retention.

The measured oxidation rates of the samples pre-treated at different temperatures were also consistent with the morphology change detected by surface SEM analysis. As shown in Figure 7.12, the expansion of the size and area of the long ridged alumina before and after the 500 hours exposure was detected as follows: 800°C\_1 hour > 900°C\_1 hour > 1000°C\_1 hour. However, it is worth noting that no significant change of surface morphology could be

detected for the sample pre-treated at 1100°C for 1 hour even after the 500 hours exposure test. It has been confirmed by several studies that  $\gamma$ -Al<sub>2</sub>O<sub>3</sub> does not transform to  $\alpha$ -Al<sub>2</sub>O<sub>3</sub> in humid environment during high temperature exposure since water vapour stabilises  $\gamma$ -Al<sub>2</sub>O<sub>3</sub> by hydroxylation of the surface [136,152,157,158]. The metastable alumina is known to be prevalent at low temperature, due to its easier nucleation than  $\alpha$ -Al<sub>2</sub>O<sub>3</sub> [158]. Therefore, in the current research, the growth of alumina scale on the pre-treated samples under these exposure conditions (850°C, 6.0 L/min air and 3% water) was dominated by the Al outward diffusion for the outward growth of metastable alumina, rather than the oxygen inward diffusion for the growth of an inner  $\alpha$ -Al<sub>2</sub>O<sub>3</sub> layer. As mentioned before, the difference in the alumina growth rate for the samples pre-treated at the four temperatures during the exposure tests was caused by the difference of the Al outward diffusion rate throughout the alumina scale developed during the pre-treatment. The alumina scale established at low pre-treatment temperatures had a low thickness and was dominated by alumina in the metastable phase. However, the pre-treatment for AluChrom 318 conducted at high temperatures facilitated the growth of a compact  $\alpha$ -Al<sub>2</sub>O<sub>3</sub> scale with high thickness. Therefore, the fastest Al outward diffusion rate via the thin metastable alumina scale developed at 800°C for 1 hour led to the formation of the largest amount of long-ridged alumina on the surface. On the contrary, the  $\alpha$ -Al<sub>2</sub>O<sub>3</sub> formed a dense and continuous layer on the samples pre-treated at 1100°C for 1 hour, restricting the supply of cations for the growth of the outer  $\gamma$ -Al<sub>2</sub>O<sub>3</sub> layer during the exposure test. This resulted in a much slower oxidation rate in the SOFC cathode environment.

### 7.3 Conclusions

The oxidation rate and Cr<sub>2</sub>O<sub>3</sub> evaporation of the AluChrom 318 at 850°C in humidified air was shown to be dramatically decreased by pre-treatment. It can be assumed that the kinetics of oxidation rate and Cr(VI) release for the pre-treated AluChrom 318 is governed by the

phase formation of alumina on the alloy surface during pre-treatment. Pre-treatment at 800 and 900°C resulted in less improvement in the oxidation resistance and Cr retention capability than at 1000 and 1100°C due to the metastable alumina scale formed which allows relatively faster Al and Cr outward diffusion. The best corrosion resistance was observed for the samples pre-treated at 1100°C for 1 hour with a 98% reduction of oxidation rate and 90% reduction of Cr<sub>2</sub>O<sub>3</sub> evaporation compared to the non-treated AluChrom 318 due to the formation of a compact and homogenous  $\alpha$ -Al<sub>2</sub>O<sub>3</sub> scale which effectively prevented the Al and Cr from outward diffusion in the simulated SOFC environment. For the application in SOFC CAPHs, the  $\alpha$ -Al<sub>2</sub>O<sub>3</sub> scale developed on the AluChrom 318 during pre-heat treatment at 1100°C for 1 hour will decrease the outward diffusion rate of Al on both inner and outer surface of the CAPH cells exposed to hot zone during operation, which extends the lifetime of the AluChrom 318 CAPH. Furthermore, the pre-formed  $\alpha$ -Al<sub>2</sub>O<sub>3</sub> scale also stops the formation of Cr<sub>2</sub>O<sub>3</sub> on the AluChrom 318 CAPH exposed to cold zone owing to the extremely low solubility of Cr<sup>3+</sup> in the  $\alpha$ -Al<sub>2</sub>O<sub>3</sub> scale.

## Chapter 8 – Summary

### 8.1 Conclusions

Developing low-cost CAPH materials with good oxidation resistance and Cr retention capability is a key technical challenge in commercialising SOFC micro-CHPs and was the focus of the HEATSTACK project. This thesis evaluated the corrosion behaviour and  $\text{Cr}_2\text{O}_3$  evaporation of different types of high temperature alloys, as well as their suitability for use in CAPH.

In this work, the high temperature oxidation test and the  $\text{Cr}_2\text{O}_3$  evaporation test conducted in a simulated SOFC environment were the main methods used to evaluate the corrosion performance of stainless steels. The oxidation rate and  $\text{Cr}_2\text{O}_3$  evaporation rate were related to the morphology and composition of the oxide scale developed at different humidity levels and temperatures. The conclusions made for each chapter are shown as following:

Chapter 4 presented the influence of temperature and water content on the oxidation behaviour and  $\text{Cr}_2\text{O}_3$  evaporation of various high-temperature alloys with the formation of three typical oxide scales, namely  $\text{Cr}_2\text{O}_3$  on Inconel 625,  $(\text{Cr,Mn})_3\text{O}_4$  spinel on SS309, and  $\text{Al}_2\text{O}_3$  on AluChrom 318. It was found that, at the same temperature and humidity, the amount of  $\text{Cr}_2\text{O}_3$  evaporated from different high-temperature alloys depended on the partial pressure of Cr present on the oxide surface. The main effect of temperature on the alumina forming alloy was that the oxidation rate increased with temperature. However, the  $\text{Cr}_2\text{O}_3$  evaporation rate of the alumina forming alloy was less affected by temperature. For alloys with  $\text{Cr}_2\text{O}_3$  and  $(\text{Cr,Mn})_3\text{O}_4$  spinel as protective layer, the major effect of temperature was that both oxidation rate and  $\text{Cr}_2\text{O}_3$  evaporation rate were dramatically reduced at lower temperatures. It was found that a  $100^\circ\text{C}$  decrease in temperature showed more reduction on

the  $\text{Cr}_2\text{O}_3$  evaporation rate than on the oxidation rate for Inconel 625 with  $\text{Cr}_2\text{O}_3$  as protective layer. In contrast, the effect of temperature on the oxidation rate was greater than the  $\text{Cr}_2\text{O}_3$  evaporation rate at 100°C lower temperature for the  $(\text{Cr,Mn})_3\text{O}_4$  spinel layer formed on SS309. By increasing the water content in the exposed atmosphere the amount of Cr(VI) species evaporated from the high-temperature alloys was increased. Furthermore, the water vapour enhanced the oxidation rate for the alloys that formed a  $\text{Cr}_2\text{O}_3$  or  $(\text{Cr,Mn})_3\text{O}_4$  spinel scale compared to those exposed in dry atmosphere. In contrast, the water vapour effect on the oxidation rate for the alumina forming alloy was insignificant.

Chapter 5 confirmed the importance of alumina as protective layer in enhancing the corrosion resistance and Cr retention capability of the high-Cr alloys used in SOFC system components which do not have a current-conducting function. It was found that the formed alumina scale restrained the surface chromium evolution through restraining the ionic mobility of chromium and oxygen throughout the alumina grain boundaries. The  $(\text{Cr,Mn})_3\text{O}_4$  spinel layer formed on SS309 may reduce  $\text{Cr}_2\text{O}_3$  evaporation but did not form a true barrier layer since Cr(VI) species still evaporated at an unacceptable level. Surface aluminising is an interesting approach to reduce  $\text{Cr}_2\text{O}_3$  evaporation from high-temperature steels. However, in this study, the aluminised SS309 failed the application as CAPH material owing to the breakaway oxidation induced by alumina scale spallation. The alumina-former AluChrom 318 which formed a double-layered scale demonstrated outstanding Cr retention ability and oxidation resistance.

In Chapter 6, a microstructural analysis on the AluChrom 318 CAPH was conducted after exposing it to an SOFC operational environment for 25,000 hours. It was found that the oxide scale formed on the AluChrom 318 CAPH was related to the temperature of the exposure environment. Besides, the source of volatile Cr(VI) species was also identified. From the

inner surface of the single CAPH cell, the spalled alumina scale in the hot zone and the uncovered surface in the cold zone were believed to contaminate the SOFC system with volatile Cr(VI) species. From the outer surface of the single CAPH cell, the fast alumina growth with depleted Al reservoir in the hot zone and the large amount of Cr<sub>2</sub>O<sub>3</sub> formed in the cold zone would have contributed to a large amount of Cr<sub>2</sub>O<sub>3</sub> evaporation to the environment.

In chapter 7, a pre-treatment was applied to the AluChrom 318 in order to achieve a protective alumina scale prior to SOFC application. It was found that the kinetics of oxidation rate and Cr<sub>2</sub>O<sub>3</sub> evaporation for the pre-treated AluChrom 318 were governed by the phase formation of alumina on the alloy surface during pre-treatment. The AluChrom 318 pre-treated at 1100°C for 1 hour showed the best corrosion resistance and Cr retention capability due to the formation of a homogenous and compact  $\alpha$ -Al<sub>2</sub>O<sub>3</sub> scale. Furthermore, the  $\alpha$ -Al<sub>2</sub>O<sub>3</sub> scale formed on the surface of the AluChrom 318 CAPH surface during the pre-heat treatment was also believed to slow down the Al oxidation rate in the hot zone and stop the formation of Cr<sub>2</sub>O<sub>3</sub> in the cold zone. These results were of great benefit to the HEATSTACK project as they can improved the performance of the AluChrom 318 CAPH based on the pre-treatment results obtained from this work.

## 8.2 Future work

As shown in this work, the corrosion performance of aluminised SS309 is not ideal due to the severe spallation of alumina scale. However, surface aluminising is still an interesting method to reduce Cr evaporation from chromia-forming alloys. Thus, future work is required to improve the performance of aluminised SS309. For example, it is necessary to increase the thickness of the aluminium coating to make the Al reservoir last longer. In addition, pre-

treatment of the aluminised SS309 in inert gas (Ar) or air at high temperature might offer a possibility to improve scale adhesion and corrosion resistance. Alternative coating techniques to the PVD coatings used here might give better results.

In this experimental study, the AluChrom 318 coupons pre-treated at 1100°C for 1 hour showed excellent corrosion resistance and Cr retention ability. However, the corrosion behaviour of the pre-treated AluChrom 318 coupon exposed in isothermal condition will be totally different from that of the CAPH stack exposed under the counter flow of exhaust gas and air. Thus, a long-term exposure test on the CAPH stack made of pre-treated AluChrom 318 under SOFC system operation environment is still required to confirm the promising effect of the proposed pre-treatment.

## References

- [1] Clean Growth - Transforming Heating - Overview of Current Evidence, 2018. <https://www.gov.uk/government/publications/heat-decarbonisation-overview-of-current-evidence-base> (accessed November 17, 2019).
- [2] I. Staffell, Zero carbon infinite COP heat from fuel cell CHP, *Appl. Energy*. 147 (2015) 373–385. <https://doi.org/10.1016/j.apenergy.2015.02.089>.
- [3] A. Sorrentino, A.M. Pantaleo, C.N. Markides, G. Braccio, E. Fanelli, S.M. Camporeale, Energy performance and profitability of biomass boilers in commercial sector: The case study of Sainsbury's stores in the UK, *Energy Procedia*. 148 (2018) 639–646. <https://doi.org/10.1016/j.egypro.2018.08.152>.
- [4] A. Holey, Will gas be gone in the United Kingdom (UK) by 2050? An impact assessment of urban heat decarbonisation and low emission vehicle uptake on future UK energy system scenarios, *Renew. Energy*. 142 (2019) 695–705. <https://doi.org/10.1016/j.renene.2019.04.052>.
- [5] A. Arsalis, A comprehensive review of fuel cell-based micro-combined-heat-and-power systems, *Renew. Sustain. Energy Rev.* 105 (2019) 391–414. <https://doi.org/10.1016/j.rser.2019.02.013>.
- [6] Carbon Trust, Introducing combined heat and power, 2010. <https://www.carbontrust.com/home/> (accessed November 16, 2019).
- [7] A. Adam, E.S. Fraga, D.J.L. Brett, Modelling and optimisation in terms of CO<sub>2</sub>

- emissions of a solid oxide fuel cell based micro-CHP system in a four bedroom house in London, in: *Energy Procedia*, Elsevier Ltd, 2013: pp. 201–209. <https://doi.org/10.1016/j.egypro.2013.11.020>.
- [8] A. Hawkes, I. Staffell, D. Brett, N. Brandon, Fuel cells for micro-combined heat and power generation, *Energy Environ. Sci.* 2 (2009) 729–744. <https://doi.org/10.1039/b902222h>.
- [9] G. Bidini, U. Desideri, S. Saetta, P.P. Bocchini, Internal combustion engine combined heat and power plants: Case study of the university of perugia power plant, *Appl. Therm. Eng.* 18 (1998) 401–412. [https://doi.org/10.1016/S1359-4311\(97\)00051-3](https://doi.org/10.1016/S1359-4311(97)00051-3).
- [10] J. Harrison, E. On, Stirling engine systems for small and micro combined heat and power (CHP) applications, in: *Small Micro Comb. Heat Power Syst.*, 2011: pp. 179–205. <https://doi.org/10.1533/9780857092755.2.179>.
- [11] A. Arsalis, M.P. Nielsen, S.K. Kær, Application of an improved operational strategy on a PBI fuel cell-based residential system for Danish single-family households, *Appl. Therm. Eng.* 50 (2013) 704–713. <https://doi.org/10.1016/j.applthermaleng.2012.07.025>.
- [12] G. Di Marcoberardino, G. Manzolini, Investigation of a 5 kW micro-CHP PEM fuel cell based system integrated with membrane reactor under diverse EU natural gas quality, *Int. J. Hydrogen Energy.* 42 (2017) 13988–14002. <https://doi.org/10.1016/j.ijhydene.2017.02.016>.
- [13] A.D. Hawkes, P. Aguiar, B. Croxford, M.A. Leach, C.S. Adjiman, N.P. Brandon, Solid oxide fuel cell micro combined heat and power system operating strategy:

- Options for provision of residential space and water heating, *J. Power Sources*. 164 (2007) 260–271. <https://doi.org/10.1016/j.jpowsour.2006.10.083>.
- [14] R. Napoli, M. Gandiglio, A. Lanzini, M. Santarelli, Techno-economic analysis of PEMFC and SOFC micro-CHP fuel cell systems for the residential sector, *Energy Build.* 103 (2015) 131–146. <https://doi.org/10.1016/j.enbuild.2015.06.052>.
- [15] P. Kazempoor, V. Dorer, A. Weber, Modelling and evaluation of building integrated SOFC systems, *Int. J. Hydrogen Energy*. 36 (2011) 13241–13249. <https://doi.org/10.1016/j.ijhydene.2010.11.003>.
- [16] D. Carter, *Fuel Cell Residential Micro-CHP Developments in Japan*, 2013. [www.fuelcelltoday.com](http://www.fuelcelltoday.com) (accessed November 13, 2019).
- [17] Callux project, (n.d.). <http://enefield.eu/related-projects/callux-project/> (accessed November 28, 2019).
- [18] F.C. Today, *The Fuel Cell Industry Review*, 2013.
- [19] ene.field, (n.d.). <http://enefield.eu/> (accessed November 28, 2019).
- [20] E. Jannelli, M. Minutillo, A. Perna, Analyzing microcogeneration systems based on LT-PEMFC and HT-PEMFC by energy balances, *Appl. Energy*. 108 (2013) 82–91. <https://doi.org/10.1016/j.apenergy.2013.02.067>.
- [21] M. Gandiglio, A. Lanzini, M. Santarelli, P. Leone, Design and optimization of a proton exchange membrane fuel cell CHP system for residential use, *Energy Build.* 69 (2014)

- 381–393. <https://doi.org/10.1016/j.enbuild.2013.11.022>.
- [22] J. Kupecki, Off-design analysis of a micro-CHP unit with solid oxide fuel cells fed by DME, *Int. J. Hydrogen Energy*. 40 (2015) 12009–12022. <https://doi.org/10.1016/j.ijhydene.2015.06.031>.
- [23] D.J.L. Brett, A. Atkinson, N.P. Brandon, S.J. Skinner, Intermediate temperature solid oxide fuel cells, *Chem. Soc. Rev.* 37 (2008) 1568–1578. <https://doi.org/10.1039/b612060c>.
- [24] T. Elmer, M. Worall, S. Wu, S.B. Riffat, Emission and economic performance assessment of a solid oxide fuel cell micro-combined heat and power system in a domestic building, *Appl. Therm. Eng.* 90 (2015) 1082–1089. <https://doi.org/10.1016/j.applthermaleng.2015.03.078>.
- [25] F. Arpino, M. Dell’Isola, D. Maugeri, N. Massarotti, A. Mauro, A new model for the analysis of operating conditions of micro-cogenerative SOFC units, *Int. J. Hydrogen Energy*. 38 (2013) 336–344. <https://doi.org/10.1016/j.ijhydene.2012.10.003>.
- [26] K. Hilpert, Chromium Vapor Species over Solid Oxide Fuel Cell Interconnect Materials and Their Potential for Degradation Processes, *J. Electrochem. Soc.* 143 (2006) 3642–3647. <https://doi.org/10.1149/1.1837264>.
- [27] S.P. Jiang, X. Chen, Chromium deposition and poisoning of cathodes of solid oxide fuel cells - A review, *Int. J. Hydrogen Energy*. 39 (2014) 505–531. <https://doi.org/10.1016/j.ijhydene.2013.10.042>.

- [28] J.L. Córdova, H. Heshmat, Development of a ceramic heat exchanger for application as solid oxide fuel cell cathode air preheater, in: Am. Soc. Mech. Eng. Power Div. POWER, American Society of Mechanical Engineers (ASME), 2016. <https://doi.org/10.1115/POWER2016-59333>.
- [29] K. Gerdes, C. Johnson, Surface Scale Formation on Solid Oxide Fuel Cell Proximal Balance of Plant Components, J. Fuel Cell Sci. Technol. 6 (2008) 011018 1–5. <https://doi.org/10.1115/1.2971195>.
- [30] N. Shaigan, W. Qu, D.G. Ivey, W. Chen, A review of recent progress in coatings, surface modifications and alloy developments for solid oxide fuel cell ferritic stainless steel interconnects, J. Power Sources. 195 (2010) 1529–1542. <https://doi.org/10.1016/J.JPOWSOUR.2009.09.069>.
- [31] A. Sommers, Q. Wang, X. Han, C. T’Joen, Y. Park, A. Jacobi, Ceramics and ceramic matrix composites for heat exchangers in advanced thermal systems-A review, Appl. Therm. Eng. 30 (2010) 1277–1291. <https://doi.org/10.1016/j.applthermaleng.2010.02.018>.
- [32] L.C. De Jonghe, C.P. Jacobson, S.J. Visco, SUPPORTED ELECTROLYTE THIN FILM SYNTHESIS OF SOLID OXIDE FUEL CELLS \*, Annu. Rev. Mater. Res. 33 (2003) 169–82. <https://doi.org/10.1146/annurev.matsci.33.041202.103842>.
- [33] S.P. Jiang, Nanoscale and nano-structured electrodes of solid oxide fuel cells by infiltration: Advances and challenges, Int. J. Hydrogen Energy. 37 (2012) 449–470. <https://doi.org/10.1016/j.ijhydene.2011.09.067>.

- [34] Y.J. Leng, S.H. Chan, S.P. Jiang, K.A. Khor, Low-temperature SOFC with thin film GDC electrolyte prepared in situ by solid-state reaction, *Solid State Ionics*. 170 (2004) 9–15. <https://doi.org/10.1016/j.ssi.2004.02.026>.
- [35] E. Perry Murray, T. Tsai, S.A. Barnett, A direct-methane fuel cell with a ceria-based anode, *Nature*. 400 (1999) 649–651. <https://doi.org/10.1038/23220>.
- [36] E.D. Wachsman, K.T. Lee, Lowering the temperature of solid oxide fuel cells, *Science* (80-. ). 334 (2011) 935–939. <https://doi.org/10.1126/science.1204090>.
- [37] Z. Yang, K.S. Weil, D.M. Paxton, J.W. Stevenson, Selection and Evaluation of Heat-Resistant Alloys for SOFC Interconnect Applications, *J. Electrochem. Soc.* 150 (2003) A1188–A1201. <https://doi.org/10.1149/1.1595659>.
- [38] S. Geng, J. Zhu, M.P. Brady, H.U. Anderson, X.-D. Zhou, Z. Yang, A low-Cr metallic interconnect for intermediate-temperature solid oxide fuel cells, *J. Power Sources*. 172 (2007) 775–781. <https://doi.org/10.1016/j.jpowsour.2007.05.022>.
- [39] X. Chen, C. Jin, L. Zhao, L. Zhang, C. Guan, L. Wang, Y.F. Song, C.C. Wang, J.Q. Wang, S.P. Jiang, Study on the Cr deposition and poisoning phenomenon at  $(\text{La}_{0.6}\text{Sr}_{0.4})(\text{Co}_{0.2}\text{Fe}_{0.8})\text{O}_{3-\delta}$  electrode of solid oxide fuel cells by transmission X-ray microscopy, *Int. J. Hydrogen Energy*. 39 (2014) 15728–15734. <https://doi.org/10.1016/j.ijhydene.2014.07.112>.
- [40] B. Hua, J. Pu, F. Lu, J. Zhang, B. Chi, L. Jian, Development of a Fe–Cr alloy for interconnect application in intermediate temperature solid oxide fuel cells, *J. Power Sources*. 195 (2010) 2782–2788. <https://doi.org/10.1016/J.JPOWSOUR.2009.08.077>.

- [41] J.W. Fergus, Metallic interconnects for solid oxide fuel cells, *Mater. Sci. Eng. A*. 397 (2005) 271–283. <https://doi.org/10.1016/j.msea.2005.02.047>.
- [42] D.J. Young, Oxidation of Alloys I: Single Phase Scales, in: *High Temp. Oxid. Corros. Met.*, 2016: pp. 193–206. <https://doi.org/10.1016/B978-0-08-100101-1.00005-4>.
- [43] M. Stanislawski, E. Wessel, T. Markus, L. Singheiser, W.J. Quadackers, Chromium vaporization from alumina-forming and aluminized alloys, *Solid State Ionics*. 179 (2008) 2406–2415. <https://doi.org/10.1016/J.SSI.2008.09.015>.
- [44] D.J. Young, Alloy Oxidation III: Multiphase Scales, in: *High Temp. Oxid. Corros. Met.*, 2016: pp. 335–392. <https://doi.org/10.1016/b978-0-08-100101-1.00007-8>.
- [45] E.J. Opila, N.S. Jacobson, D.L. Myers, E.H. Copland, Predicting oxide stability in high-temperature water vapor, *J. Miner. Met. Mater. Soc.* 58 (2006) 22–28. <https://doi.org/10.1007/s11837-006-0063-3>.
- [46] R. Trebbels, T. Markus, L. Singheiser, Investigation of Chromium Vaporization from Interconnector Steels with Spinel Coatings, *J. Electrochem. Soc.* 157 (2010) B490–B495. <https://doi.org/10.1149/1.3298434>.
- [47] X. Sun, W.N. Liu, E. Stephens, M.A. Khaleel, Determination of interfacial adhesion strength between oxide scale and substrate for metallic SOFC interconnects, *J. Power Sources*. 176 (2008) 167–174. <https://doi.org/10.1016/j.jpowsour.2007.10.027>.
- [48] M. Stanislawski, J. Froitzheim, L. Niewolak, W.J. Quadackers, K. Hilpert, T. Markus, L. Singheiser, Reduction of chromium vaporization from SOFC interconnectors by

- highly effective coatings, *J. Power Sources*. 164 (2007) 578–589.  
<https://doi.org/10.1016/J.JPOWSOUR.2006.08.013>.
- [49] W.N. Liu, X. Sun, M.A. Khaleel, Effect of creep of ferritic interconnect on long-term performance of solid oxide fuel cell stacks, *Fuel Cells*. 10 (2010) 703–717.  
<https://doi.org/10.1002/fuce.200900075>.
- [50] V. Miguel-Pérez, A. Martínez-Amesti, M.L. Nó, A. Larrañaga, M.I. Arriortua, Oxide scale formation on different metallic interconnects for solid oxide fuel cells, *Corros. Sci.* 60 (2012) 38–49. <https://doi.org/10.1016/j.corsci.2012.04.014>.
- [51] T. Brylewski, M. Nanko, T. Maruyama, K. Przybylski, Application of Fe–16Cr ferritic alloy to interconnector for a solid oxide fuel cell, *Solid State Ionics*. 143 (2001) 131–150. [https://doi.org/10.1016/S0167-2738\(01\)00863-3](https://doi.org/10.1016/S0167-2738(01)00863-3).
- [52] T. Horita, Y. Xiong, K. Yamaji, N. Sakai, H. Yokokawa, Evaluation of Fe-Cr alloys as interconnects for reduced operation temperature SOFCs, *J. Electrochem. Soc.* 150 (2003) A243–A248. <https://doi.org/10.1149/1.1539498>.
- [53] S. Linderoth, P. V. Hendriksen, M. Mogensen, N. Langvad, Investigations of metallic alloys for use as interconnects in solid oxide fuel cell stacks, *J. Mater. Sci.* 31 (1996) 5077–5082. <https://doi.org/10.1007/BF00355908>.
- [54] P.D. Jablonski, C.J. Cowen, J.S. Sears, Exploration of alloy 441 chemistry for solid oxide fuel cell interconnect application, *J. Power Sources*. 195 (2010) 813–820.  
<https://doi.org/10.1016/j.jpowsour.2009.08.023>.

- [55] HEATSTACK, (n.d.). <http://www.heatstack.eu/>.
- [56] D.J. Young, Corrosion by Carbon, in: *High Temp. Oxid. Corros. Met.*, 2016: pp. 431–493. <https://doi.org/10.1016/b978-0-08-100101-1.00009-1>.
- [57] D.J. Young, Corrosion in Complex Environments, in: *High Temp. Oxid. Corros. Met.*, 2016: pp. 603–645. <https://doi.org/10.1016/b978-0-08-100101-1.00012-1>.
- [58] D.J. Young, Corrosion by Sulphur, in: *High Temp. Oxid. Corros. Met.*, 2016: pp. 393–430. <https://doi.org/10.1016/b978-0-08-100101-1.00008-x>.
- [59] D.J. Young, Mixed Gas Corrosion of Pure Metals, in: *High Temp. Oxid. Corros. Met.*, 2016: pp. 145–191. <https://doi.org/10.1016/b978-0-08-100101-1.00004-2>.
- [60] D.J. Young, Oxidation of Pure Metals, in: *High Temp. Oxid. Corros. Met.*, Elsevier, 2016: pp. 85–144. <https://doi.org/10.1016/B978-0-08-100101-1.00003-0>.
- [61] N. Birks, G.H. Meier, F.S. Pettit, Mechanisms of oxidation, in: *Introd. to High-Temperature Oxid. Met.*, Cambridge University Press, Cambridge, 2006: pp. 39–74. <https://doi.org/10.1017/CBO9781139163903.005>.
- [62] D.J. Young, Enabling Theory, in: *High Temp. Oxid. Corros. Met.*, 2016: pp. 31–84. <https://doi.org/10.1016/b978-0-08-100101-1.00002-9>.
- [63] A.S. Khanna, *High-Temperature Oxidation*, (2018). <https://doi.org/10.1016/B978-0-323-52472-8.00006-X>.

- [64] S.R.J. SAUNDERS, J.R. NICHOLLS, *Oxidation, Hot Corrosion and Protection of Metallic Materials*, 1996. <https://doi.org/10.1016/b978-044489875-3/50019-3>.
- [65] H.J.T. Ellingham, Reducibility of oxides and sulphides in metallurgical process, *J. Soc. Chem. Ind.* 63 (1944) 125–160. <https://doi.org/10.1002/jctb.5000630501>.
- [66] University of Cambridge, The Ellingham diagram, (n.d). [https://www.doitpoms.ac.uk/tlplib/ellingham\\_diagrams/ellingham.php](https://www.doitpoms.ac.uk/tlplib/ellingham_diagrams/ellingham.php) (accessed October 24, 2020).
- [67] N. Birks, G.H. Meier, F.S. Pettit, N. Birks, G.H. Meier, F.S. Pettit, Oxidation of pure metals, *Introd. to High-Temperature Oxid. Met.* 1 (2012) 75–100. <https://doi.org/10.1017/cbo9781139163903.006>.
- [68] P. Alnegren, Oxidation behavior of selected FeCr alloys in environments relevant for solid oxide electrolysis applications Master thesis performed at Chalmers High Temperature Corrosion Center, 2012. <https://odr.chalmers.se/handle/20.500.12380/171854> (accessed October 19, 2020).
- [69] R. Haugsrud, On the high-temperature oxidation of nickel, *Corros. Sci.* 45 (2003) 211–235. [https://doi.org/10.1016/S0010-938X\(02\)00085-9](https://doi.org/10.1016/S0010-938X(02)00085-9).
- [70] A. Atkinson, R.I. Taylor, A.E. Hughes, A quantitative demonstration of the grain boundary diffusion mechanism for the oxidation of metals, *Philos. Mag. A.* 45 (1982) 823–833. <https://doi.org/10.1080/01418618208239905>.
- [71] R.J. Hussey, M.J. Graham, The influence of reactive-element coatings on the high-

- temperature oxidation of pure-Cr and high-Cr-content alloys, *Oxid. Met.* 45 (1996) 349–374. <https://doi.org/10.1007/BF01046989>.
- [72] N. Birks, G.H. Meier, F.S. Pettit, Oxidation of alloys, in: *Introd. to High-Temperature Oxid. Met.*, Cambridge University Press, Cambridge, 2006: pp. 101–162. <https://doi.org/10.1017/CBO9781139163903.007>.
- [73] A.H. Heuer, Oxygen and aluminum diffusion in  $\alpha$ -Al<sub>2</sub>O<sub>3</sub>: How much do we really understand?, *J. Eur. Ceram. Soc.* 28 (2008) 1495–1507. <https://doi.org/10.1016/j.jeurceramsoc.2007.12.020>.
- [74] A.H. Heuer, T. Nakagawa, M.Z. Azar, D.B. Hovis, J.L. Smialek, B. Gleeson, N.D.M. Hine, H. Guhl, H.S. Lee, P. Tangney, W.M.C. Foulkes, M.W. Finnis, On the growth of Al<sub>2</sub>O<sub>3</sub> scales, *Acta Mater.* 61 (2013) 6670–6683. <https://doi.org/10.1016/j.actamat.2013.07.024>.
- [75] P. Sarrazin, A. Galerie, J. Fouletier, Kinetic Approach to High Temperature Corrosion: Growth of A Compact Scale, in: *Mech. High Temp. Corros. - A Kinet. Approach*, 2008: pp. 117–192.
- [76] Y. Behnamian, A. Mostafaei, A. Kohandehghan, B.S. Amirkhiz, D. Serate, Y. Sun, S. Liu, E. Aghaie, Y. Zeng, M. Chmielus, W. Zheng, D. Guzonas, W. Chen, J.L. Luo, A comparative study of oxide scales grown on stainless steel and nickel-based superalloys in ultra-high temperature supercritical water at 800 °C, *Corros. Sci.* 106 (2016) 188–207. <https://doi.org/10.1016/J.CORSCI.2016.02.004>.
- [77] J.G. Goedjen, D.A. Shores, The effect of alloy grain size on the transient oxidation

- behavior of an alumina-forming alloy, *Oxid. Met.* 37 (1992) 125–142.  
<https://doi.org/10.1007/BF00665186>.
- [78] D.J. Young, Alloy Oxidation II: Internal Oxidation, in: *High Temp. Oxid. Corros. Met.*, 2016: pp. 261–333. <https://doi.org/10.1016/B978-0-08-100101-1.00006-6>.
- [79] D. Zou, Y. Zhou, X. Zhang, W. Zhang, Y. Han, High temperature oxidation behavior of a high Al-containing ferritic heat-resistant stainless steel, *Mater. Charact.* 136 (2018) 435–443. <https://doi.org/10.1016/j.matchar.2017.11.038>.
- [80] E.J. Opila, D.L. Myers, N.S. Jacobson, I.M.B. Nielsen, D.F. Johnson, J.K. Olminky, M.D. Allendorf, Theoretical and Experimental Investigation of the Thermochemistry of  $\text{CrO}_2(\text{OH})_2(\text{g})$ , *J. Phys. Chem. A.* 111 (2007) 1971–1980. <https://doi.org/10.1021/jp0647380>.
- [81] D. Mortimer, W.B.A. Sharp, Oxidation of Fe—Cr Binary Alloys, *Br. Corros. J.* 3 (1968) 61–67. <https://doi.org/10.1179/000705968798326424>.
- [82] Z. Yang, G.-G. Xia, J.W. Stevenson, Evaluation of Ni—Cr-base alloys for SOFC interconnect applications, *J. Power Sources.* 160 (2006) 1104–1110. <https://doi.org/10.1016/J.JPOWSOUR.2006.02.099>.
- [83] Y. Liu, J. Zhu, Stability of Haynes 242 as metallic interconnects of solid oxide fuel cells (SOFCs), *Int. J. Hydrogen Energy.* 35 (2010) 7936–7944. <https://doi.org/10.1016/J.IJHYDENE.2010.05.053>.
- [84] J.H. Zhu, S.J. Geng, D.A. Ballard, Evaluation of several low thermal expansion Fe—

- Co–Ni alloys as interconnect for reduced-temperature solid oxide fuel cell, *Int. J. Hydrogen Energy*. 32 (2007) 3682–3688.  
<https://doi.org/10.1016/J.IJHYDENE.2006.08.026>.
- [85] X. Cheng, Z. Jiang, B.J. Monaghan, D. Wei, R.J. Longbottom, J. Zhao, J. Peng, M. Luo, L. Ma, S. Luo, L. Jiang, Breakaway oxidation behaviour of ferritic stainless steels at 1150 °C in humid air, *Corros. Sci.* 2016 (2016) 11–22.  
<https://doi.org/10.1016/j.corsci.2016.02.042>.
- [86] Z. Yu, M. Chen, C. Shen, S. Zhu, F. Wang, Oxidation of an austenitic stainless steel with or without alloyed aluminum in O<sub>2</sub> + 10% H<sub>2</sub>O environment at 800 °C, *Corros. Sci.* 121 (2017) 105–115. <https://doi.org/10.1016/j.corsci.2017.03.015>.
- [87] J. Zhang, X. Peng, D.J. Young, F. Wang, Nano-crystalline coating to improve cyclic oxidation resistance of 304 stainless steel, *Surf. Coatings Technol.* 217 (2013) 162–171. <https://doi.org/10.1016/j.surfcoat.2012.12.007>.
- [88] J. Yuan, X. Wu, W. Wang, S. Zhu, F. Wang, Investigation on the enhanced oxidation of ferritic/martensitic steel P92 in pure steam, *Materials (Basel)*. 7 (2014) 2772–2783.  
<https://doi.org/10.3390/ma7042772>.
- [89] I.G. Wright, R.B. Dooley, A review of the oxidation behaviour of structural alloys in steam, *Int. Mater. Rev.* 55 (2010) 129–167.  
<https://doi.org/10.1179/095066010x12646898728165>.
- [90] P.J. Ennis, W.J. Quadackers, Implications of steam oxidation for the service life of high-strength martensitic steel components in high-temperature plant, *Int. J. Press.*

- Vessel. Pip. 84 (2007) 82–87. <https://doi.org/10.1016/j.ijpvp.2006.09.008>.
- [91] A. Naoumidis, H.A. Schulze, W. Jungen, P. Lersch, Phase studies in the chromium-manganese-titanium oxide system at different oxygen partial pressures, *J. Eur. Ceram. Soc.* 7 (1991) 55–63. [https://doi.org/10.1016/0955-2219\(91\)90054-4](https://doi.org/10.1016/0955-2219(91)90054-4).
- [92] M.G.C. Cox, B. McEnaney, V.D. Scott, A chemical diffusion model for partitioning of transition elements in oxide scales on alloys, *Philos. Mag.* 26 (1972) 839–851. <https://doi.org/10.1080/14786437208226960>.
- [93] J. Froitzheim, S. Canovic, M. Nikumaa, R. Sachitanand, L.G. Johansson, J.E. Svensson, Long term study of Cr evaporation and high temperature corrosion behaviour of Co coated ferritic steel for solid oxide fuel cell interconnects, *J. Power Sources.* 220 (2012) 217–227. <https://doi.org/10.1016/j.jpowsour.2012.06.092>.
- [94] J. Froitzheim, H. Ravash, E. Larsson, L.G. Johansson, J.E. Svensson, Investigation of Chromium Volatilization from FeCr Interconnects by a Denuder Technique, *J. Electrochem. Soc.* 157 (2010) B1295–B1300. <https://doi.org/10.1149/1.3462987>.
- [95] K. Fujita, K. Ogasawara, Y. Matsuzaki, T. Sakurai, Prevention of SOFC cathode degradation in contact with Cr-containing alloy, *J. Power Sources.* 131 (2004) 261–269. <https://doi.org/10.1016/j.jpowsour.2003.12.051>.
- [96] Z. Yang, J.S. Hardy, M.S. Walker, G. Xia, S.P. Simner, J.W. Stevenson, Structure and Conductivity of Thermally Grown Scales on Ferritic Fe-Cr-Mn Steel for SOFC Interconnect Applications, *J. Electrochem. Soc.* 151 (2004) A1825. <https://doi.org/10.1149/1.1797031>.

- [97] D.M. England, Oxidation Kinetics of Some Nickel-Based Superalloy Foils and Electronic Resistance of the Oxide Scale Formed in Air Part I, *J. Electrochem. Soc.* 146 (1999) 3196–3202. <https://doi.org/10.1149/1.1392454>.
- [98] D.M. England, A. V. Virkar, Oxidation Kinetics of Some Nickel-Based Superalloy Foils in Humidified Hydrogen and Electronic Resistance of the Oxide Scale Formed Part II, *J. Electrochem. Soc.* 148 (2002) A330–A338. <https://doi.org/10.1149/1.1354611>.
- [99] R. Sachitanand, M. Sattari, J.-E.E. Svensson, J. Froitzheim, Evaluation of the oxidation and Cr evaporation properties of selected FeCr alloys used as SOFC interconnects, *Int. J. Hydrogen Energy.* 38 (2013) 15328–15334. <https://doi.org/10.1016/j.ijhydene.2013.09.044>.
- [100] B. Hua, Y. Kong, W. Zhang, J. Pu, B. Chi, L. Jian, The effect of Mn on the oxidation behavior and electrical conductivity of Fe–17Cr alloys in solid oxide fuel cell cathode atmosphere, *J. Power Sources.* 196 (2011) 7627–7638. <https://doi.org/10.1016/J.JPOWSOUR.2011.05.007>.
- [101] F.H. Stott, F.I. Wei, C.A. Enahoro, The influence of manganese on the High-temperature oxidation of iron-chromium alloys, *Mater. Corros.* 40 (1989) 198–205. <https://doi.org/10.1002/maco.19890400403>.
- [102] A.L. Marasco, D.J. Young, The oxidation of Iron-Chromium-Manganese alloys at 900°C, *Oxid. Met.* 36 (1991) 157–174. <https://doi.org/10.1007/BF00938460>.
- [103] H.X. Chen, X.H. Ma, S.S. Bo, J.B. Chen, Preparation of Fe/Cr doped SiO<sub>2</sub> thin film

- on 304 stainless steel substrate originated from corrosion, *Corros. Eng. Sci. Technol.* 45 (2010) 475–479. <https://doi.org/10.1179/174327809X409196>.
- [104] B. Li, B. Gleeson, Effects of silicon on the oxidation behavior of Ni-base chromia-forming alloys, *Oxid. Met.* 65 (2006) 101–122. <https://doi.org/10.1007/s11085-006-9003-4>.
- [105] H. Buscail, S. El Messki, F. Riffard, S. Perrier, R. Cueff, E. Caudron, C. Issartel, Characterization of the oxides formed at 1000 °C on the AISI 316L stainless steel—Role of molybdenum, *Mater. Chem. Phys.* 111 (2008) 491–496. <https://doi.org/10.1016/J.MATCHEMPHYS.2008.04.054>.
- [106] R. Pettersson, L. Liu, J. Sund, Cyclic oxidation performance of silicon-alloyed stainless steels in dry and moist air, *Corros. Eng. Sci. Technol.* 40 (2005) 211–216. <https://doi.org/10.1179/174327805x66254>.
- [107] J.S. Dunning, D.E. Alman, J.C. Rawers, Influence of silicon and aluminum additions on the oxidation resistance of a lean-chromium stainless steel, *Oxid. Met.* 57 (2002) 409–425. <https://doi.org/10.1023/A:1015344220073>.
- [108] S. Mahboubi, H.S. Zurob, G.A. Botton, J.R. Kish, Effect of water vapour partial pressure on the chromia (Cr<sub>2</sub>O<sub>3</sub>)-based scale stability, *Can. Metall. Q.* 57 (2018) 89–98. <https://doi.org/10.1080/00084433.2017.1373968>.
- [109] G. Bamba, Y. Wouters, A. Galerie, F. Charlot, A. Dellali, Thermal oxidation kinetics and oxide scale adhesion of Fe–15Cr alloys as a function of their silicon content, *Acta Mater.* 54 (2006) 3917–3922. <https://doi.org/10.1016/J.ACTAMAT.2006.04.023>.

- [110] S. Mahboubi, H.S. Zurob, G.A. Botton, J.R. Kish, Silicon effects on the wet oxidation of type 310 stainless steel, *Corros. Sci.* 143 (2018) 376–389. <https://doi.org/10.1016/J.CORSCI.2018.08.011>.
- [111] X.-W. Cheng, Z.-Y. Jiang, B.J. Monaghan, R.J. Longbottom, D.-B. Wei, A.C. Hee, L.-Z. Jiang, Degradation of ferritic stainless steels at 1200 °C in air, *Mater. Corros.* 69 (2018) 63–75. <https://doi.org/10.1002/maco.201709577>.
- [112] V. Badin, E. Diamanti, P. Forêt, E. Darque-Ceretti, Water Vapor Oxidation of Ferritic 441 and Austenitic 316L Stainless Steels at 1100 °C for Short Duration, *Procedia Mater. Sci.* 9 (2015) 48–53. <https://doi.org/10.1016/J.MSPRO.2015.04.006>.
- [113] T. Ohashi, T. Harada, High-temperature oxidation of Fe-Cr-Al-Si alloys extruded into honeycomb structures, *Oxid. Met.* 46 (1996) 235–254. <https://doi.org/10.1007/BF01050798>.
- [114] T. Liu, C. Wang, H. Shen, W. Chou, N.Y. Iwata, A. Kimura, The effects of Cr and Al concentrations on the oxidation behavior of oxide dispersion strengthened ferritic alloys, *Corros. Sci.* 76 (2013) 310–316. <https://doi.org/10.1016/j.corsci.2013.07.004>.
- [115] P.T. Moseley, K.R. Hyde, B.A. Bellamy, G. Tappin, The microstructure of the scale formed during the high temperature oxidation of a ferralloy steel, *Corros. Sci.* 24 (1984) 547–565. [https://doi.org/10.1016/0010-938X\(84\)90036-2](https://doi.org/10.1016/0010-938X(84)90036-2).
- [116] J.C.W. Mah, A. Muchtar, M.R. Somalu, M.J. Ghazali, Metallic interconnects for solid oxide fuel cell: A review on protective coating and deposition techniques, *Int. J. Hydrogen Energy.* 42 (2017) 9219–9229.

<https://doi.org/10.1016/j.ijhydene.2016.03.195>.

- [117] L. Ge, A. Verma, R. Goettler, D. Lovett, R.K.S. Raman, P. Singh, Oxide Scale Morphology and Chromium Evaporation Characteristics of Alloys for Balance of Plant Applications in Solid Oxide Fuel Cells, *Metall. Mater. Trans. A.* 44 (2013) 193–206. <https://doi.org/10.1007/s11661-012-1492-y>.
- [118] F. Tietz, Thermal expansion of SOFC materials, *Ionics (Kiel)*. 5 (1999) 129–139. <https://doi.org/10.1007/BF02375916>.
- [119] O. Thomann, M.H. Pihlatie, J.A. Schuler, O. Himanen, J. Kiviaho, Method for Measuring Chromium Evaporation from SOFC Balance-of-Plant Components, *ECS Trans.* 35 (2011) 2609–2616. <https://doi.org/10.1149/1.3570260>.
- [120] B. Jönsson, Q. Lu, D. Chandrasekaran, R. Berglund, F. Rave, Oxidation and creep limited lifetime of kanthal APMT®, a dispersion strengthened FeCrAlMo alloy designed for strength and oxidation resistance at high temperatures, *Oxid. Met.* 79 (2013) 29–39. <https://doi.org/10.1007/s11085-012-9324-4>.
- [121] P. Tomaszewicz, G.R. Wallwork, The oxidation of high-purity iron-chromium-aluminum alloys at 800°C, *Oxid. Met.* 20 (1983) 75–109. <https://doi.org/10.1007/BF00662042>.
- [122] M. Turker, H. Cama, T.A. Hughes, The performance of ferritic ODS alloys at high temperatures in nitrogen-containing environments, *Corros. Sci.* 37 (1995) 413–428. [https://doi.org/10.1016/0010-938X\(94\)00138-V](https://doi.org/10.1016/0010-938X(94)00138-V).

- [123] J. Engkvist, U. Bexell, M. Grehk, M. Olsson, High temperature oxidation of FeCrAl-alloys - Influence of Al-concentration on oxide layer characteristics, *Mater. Corros.* 60 (2009) 876–881. <https://doi.org/10.1002/maco.200805186>.
- [124] T. Liu, L. Wang, C. Wang, H. Shen, Effect of Al content on the oxidation behavior of Y<sub>2</sub>Ti<sub>2</sub>O<sub>7</sub>-dispersed Fe-14Cr ferritic alloys, *Corros. Sci.* 104 (2016) 17–25. <https://doi.org/10.1016/J.CORSCI.2015.11.025>.
- [125] I. Kvernes, M. Oliveira, P. Kofstad, High temperature oxidation of Fe-13Cr-xAl alloys in air/H<sub>2</sub>O vapour mixtures, *Corros. Sci.* 17 (1977) 237–252. [https://doi.org/10.1016/0010-938X\(77\)90049-X](https://doi.org/10.1016/0010-938X(77)90049-X).
- [126] M. Turker, T.A. Hughes, Oxidation behavior of three commercial ODS alloys at 1200°C, *Oxid. Met.* 44 (1995) 505–525. <https://doi.org/10.1007/BF01051041>.
- [127] J.C. Gomez-Vidal, A.G. Fernandez, R. Tirawat, C. Turchi, W. Huddleston, Corrosion resistance of alumina-forming alloys against molten chlorides for energy production. I: Pre-oxidation treatment and isothermal corrosion tests, *Sol. Energy Mater. Sol. Cells.* 166 (2017) 222–233. <https://doi.org/10.1016/j.solmat.2017.02.019>.
- [128] A. Kimura, R. Kasada, N. Iwata, H. Kishimoto, C.H. Zhang, J. Isselin, P. Dou, J.H. Lee, N. Muthukumar, T. Okuda, M. Inoue, S. Ukai, S. Ohnuki, T. Fujisawa, T.F. Abe, Development of Al added high-Cr ODS steels for fuel cladding of next generation nuclear systems, *J. Nucl. Mater.* 417 (2011) 176–179. <https://doi.org/10.1016/J.JNUCMAT.2010.12.300>.
- [129] M.P. Brady, Y. Yamamoto, M.L. Santella, B.A. Pint, Effects of minor alloy additions

- and oxidation temperature on protective alumina scale formation in creep-resistant austenitic stainless steels, *Scr. Mater.* 57 (2007) 1117–1120. <https://doi.org/10.1016/J.SCRIPTAMAT.2007.08.032>.
- [130] Y. Yamamoto, M.P. Brady, Z.P. Lu, P.J. Maziasz, C.T. Liu, B.A. Pint, K.L. More, H.M. Meyer, E.A. Payzant, Creep-resistant, Al<sub>2</sub>O<sub>3</sub>-forming austenitic stainless steels., *Science*. 316 (2007) 433–436. <https://doi.org/10.1126/science.1137711>.
- [131] Y. Yamamoto, G. Muralidharan, M.P. Brady, Development of L12-ordered Ni<sub>3</sub>(Al,Ti)-strengthened alumina-forming austenitic stainless steel alloys, *Scr. Mater.* 69 (2013) 816–819. <https://doi.org/10.1016/j.scriptamat.2013.09.005>.
- [132] R. Prescott, D.F. Mitchell, M.J. Graham, J. Doychak, Oxidation mechanisms of  $\beta$ -NiAl + Zr determined by SIMS, *Corros. Sci.* 37 (1995) 1341–1364. [https://doi.org/10.1016/0010-938X\(95\)00034-H](https://doi.org/10.1016/0010-938X(95)00034-H).
- [133] W.J. Quadakkers, A. Elschner, W. Speier, H. Nickel, Composition and growth mechanisms of alumina scales on FeCrAl-based alloys determined by SNMS, *Appl. Surf. Sci.* 52 (1991) 271–287. [https://doi.org/10.1016/0169-4332\(91\)90069-V](https://doi.org/10.1016/0169-4332(91)90069-V).
- [134] R. Prescott, M.J. Graham, The formation of aluminum oxide scales on high-temperature alloys, *Oxid. Met.* 38 (1992) 233–254. <https://doi.org/10.1007/BF00666913>.
- [135] H. El Kadiri, R. Molins, Y. Bienvenu, M.F. Horstemeyer, Abnormal high growth rates of metastable aluminas on FeCrAl alloys, *Oxid. Met.* 64 (2005) 63–97. <https://doi.org/10.1007/s11085-005-5715-0>.

- [136] F. Liu, H. Götlind, J.-E.E. Svensson, L.-G.G. Johansson, M. Halvarsson, Early stages of the oxidation of a FeCrAlRE alloy (Kanthal AF) at 900 °C: A detailed microstructural investigation, *Corros. Sci.* 50 (2008) 2272–2281. <https://doi.org/10.1016/J.CORSCI.2008.05.019>.
- [137] S. Kitaoka, T. Kuroyama, M. Matsumoto, R. Kitazawa, Y. Kagawa, Control of polymorphism in Al<sub>2</sub>O<sub>3</sub> scale formed by oxidation of alumina-forming alloys, *Corros. Sci.* 52 (2010) 429–434. <https://doi.org/10.1016/j.corsci.2009.09.031>.
- [138] T. Sudiro, T. Sano, S. Kyo, O. Ishibashi, M. Nakamori, K. Kurokawa, A comparative study of high temperature corrosion of Al<sub>2</sub>O<sub>3</sub>, SiO<sub>2</sub> and Al<sub>2</sub>O<sub>3</sub>-SiO<sub>2</sub> Forming Alloys in a Na<sub>2</sub>SO<sub>4</sub>-NaCl atmosphere, *Oxid. Met.* 80 (2013) 589–597. <https://doi.org/10.1007/s11085-013-9398-7>.
- [139] J.R. Nicholls, M.J. Bennett, R. Newton, A life prediction model for the chemical failure of FeCrAlRE alloys: preliminary assessment of model extension to lower temperatures, *Mater. High Temp.* 20 (2003) 429–438. <https://doi.org/10.1179/mht.2003.050>.
- [140] M.J. Bennett, R. Newton, J.R. Nicholls, H. Al-Badairy, G.J. Tatlock, The Oxidation Behaviour of the Commercial FeCrAlRE Alloys Aluchrom YHf and Kanthal AF Foils in Air at 800-950°C, *Mater. Sci. Forum.* 461–464 (2009) 463–472. <https://doi.org/10.4028/www.scientific.net/MSF.461-464.463>.
- [141] W. Gitzen, *Alumina as a ceramic material*, Wiley, 1970.
- [142] G.C. Rybicki, J.L. Smialek, Effect of the  $\theta$ - $\alpha$ -Al<sub>2</sub>O<sub>3</sub> transformation on the oxidation

- behavior of  $\beta$ -NiAl+Zr, *Oxid. Met.* 31 (1989) 275–304.  
<https://doi.org/10.1007/BF00846690>.
- [143] M.W. Brumm, H.J. Grabke, The oxidation behaviour of NiAl-I. Phase transformations in the alumina scale during oxidation of NiAl and NiAl-Cr alloys, *Corros. Sci.* 33 (1992) 1677–1690. [https://doi.org/10.1016/0010-938X\(92\)90002-K](https://doi.org/10.1016/0010-938X(92)90002-K).
- [144] B.A. Pint, L.W. Hobbs, The formation of  $\alpha$ -Al<sub>2</sub>O<sub>3</sub> scales at 1500°C, *Oxid. Met.* 41 (1994) 203–233. <https://doi.org/10.1007/BF01080781>.
- [145] T. Nakayma, K. Kaneko, Selective Oxide Films of a 5% Aluminum-Iron Alloy in a Low Oxygen Potential Atmosphere, *CORROSION.* 26 (1970) 287–288.  
<https://doi.org/10.5006/0010-9312-26.7.287>.
- [146] W.E. Boggs, The Oxidation of Iron-Aluminum Alloys from 450° to 900°C, *J. Electrochem. Soc.* 118 (1971) 906–913. <https://doi.org/10.1149/1.2408222>.
- [147] T.A. Ramanarayanan, M. Raghavan, R. Petkovic-Luton, Al<sub>2</sub>O<sub>3</sub> scales on ODS alloys (oxide dispersion strengthened), *Japan Inst. Met. Trans.* 24 (1983) 199–206.
- [148] J. Peters, H.J. Grabke, Formation of alumina layers on iron-base alloys, *Werkst. Korros.* 35 (1984) 385–394. <https://doi.org/osti.gov/etdeweb/biblio/6105668>.
- [149] H. Josefsson, F. Liu, J.E. Svensson, M. Halvarsson, L.G. Johansson, Oxidation of FeCrAl alloys at 500-900°C in dry O<sub>2</sub>, *Mater. Corros.* 56 (2005) 801–805.  
<https://doi.org/10.1002/maco.200503882>.

- [150] H. Chen, S.H. Kim, C. Long, C. Kim, C. Jang, Oxidation behavior of high-strength FeCrAl alloys in a high-temperature supercritical carbon dioxide environment, *Prog. Nat. Sci. Mater. Int.* 28 (2018) 731–739. <https://doi.org/10.1016/J.PNSC.2018.11.004>.
- [151] F. Liu, H. Josefsson, J.E. Svensson, L.G. Johansson, M. Halvarsson, TEM investigation of the oxide scales formed on a FeCrAlRE alloy (Kanthal AF) at 900°C in dry O<sub>2</sub> and O<sub>2</sub> with 40% H<sub>2</sub>O, *Mater. High Temp.* 22 (2005) 521–526. <https://doi.org/10.1179/mht.2005.062>.
- [152] H. Götlind, A.F. Liu, J.-E. Svensson, A.M. Halvarsson, L.-G. Johansson, F. Liu, Á.M. Halvarsson, The Effect of Water Vapor on the Initial Stages of Oxidation of the FeCrAl Alloy Kanthal AF at 900 °C, *Oxid Met.* 67 (2007) 251–266. <https://doi.org/10.1007/s11085-007-9055-0>.
- [153] H. Buscail, S. Heinze, P. Dufour, J.P. Larpin, Water-vapor-effect on the oxidation of Fe-21.5 wt.%Cr-5.6 wt.%Al at 1000°C, *Oxid. Met.* 47 (1997) 445–464. <https://doi.org/10.1007/BF02134786>.
- [154] K.A. Unocic, E. Essuman, S. Dryepondt, B.A. Pint, Effect of environment on the scale formed on oxide dispersion strengthened FeCrAl at 1050°C and 1100°C, *Mater. High Temp.* 29 (2012) 171–180. <https://doi.org/10.3184/096034012X13317275660176>.
- [155] K. Onal, M.C. Maris-Sida, G.H. Meier, F.S. Pettit, Water vapor effects on the cyclic oxidation resistance of alumina forming alloys, *Mater. High Temp.* 20 (2003) 327–337. <https://doi.org/10.1179/mht.2003.039>.
- [156] J.L. Smialek, G.N. Morscher, Delayed alumina scale spallation on Rene’N5 + Y:

- Moisture effects and acoustic emission, *Mater. Sci. Eng. A.* A332 (2002) 11–24.  
[https://doi.org/10.1016/S0921-5093\(01\)01712-9](https://doi.org/10.1016/S0921-5093(01)01712-9).
- [157] K. Hellström, N. Israelsson, N. Mortazavi, S. Canovic, M. Halvarsson, J.E. Svensson, L.G. Johansson, Oxidation of a Dispersion-Strengthened Powder Metallurgical FeCrAl Alloy in the Presence of O<sub>2</sub> at 1100 °C: The Influence of Water Vapour, *Oxid. Met.* 83 (2015) 533–558. <https://doi.org/10.1007/s11085-015-9534-7>.
- [158] J. Engkvist, S. Canovic, K. Hellström, A. Järnäs, J.-E. Svensson, L.-G. Johansson, M. Olsson, M. Halvarsson, Alumina Scale Formation on a Powder Metallurgical FeCrAl Alloy (Kanthal APMT) at 900-1100 °C in Dry O<sub>2</sub> and in O<sub>2</sub>+H<sub>2</sub>O, *Oxid Met.* 73 (2010) 233–253. <https://doi.org/10.1007/s11085-009-9177-7>.
- [159] J.A. Schuler, C. Gehrig, Z. Wuillemin, A.J. Schuler, J. Wochele, C. Ludwig, A. Hessler-Wyser, J. Van Herle, Air side contamination in Solid Oxide Fuel Cell stack testing, *J. Power Sources.* 196 (2011) 7225–7231.  
<https://doi.org/10.1016/j.jpowsour.2010.10.058>.
- [160] B.B. Ebbinghaus, Thermodynamics of gas phase chromium species: The chromium oxides, the chromium oxyhydroxides, and volatility calculations in waste incineration processes, *Combust. Flame.* 93 (1993) 119–137. [https://doi.org/10.1016/0010-2180\(93\)90087-J](https://doi.org/10.1016/0010-2180(93)90087-J).
- [161] C. Gindorf, L. Singheiser, K. Hilpert, Vaporisation of chromia in humid air, *J. Phys. Chem. Solids.* 66 (2005) 384–387. <https://doi.org/10.1016/j.jpcs.2004.06.092>.
- [162] X. Chen, Y. Zhen, J. Li, S.P. Jiang, Chromium deposition and poisoning in dry and

- humidified air at  $(\text{La}_{0.8}\text{Sr}_{0.2})_{0.9}\text{MnO}_{3+\delta}$  cathodes of solid oxide fuel cells, *Int. J. Hydrogen Energy*. 35 (2010) 2477–2485. <https://doi.org/10.1016/j.ijhydene.2009.12.185>.
- [163] H. Falk-Windisch, J.E. Svensson, J. Froitzheim, The effect of temperature on chromium vaporization and oxide scale growth on interconnect steels for Solid Oxide Fuel Cells, *J. Power Sources*. 287 (2015) 25–35. <https://doi.org/10.1016/j.jpowsour.2015.04.040>.
- [164] S. Taniguchi, M. Kadowaki, H. Kawamura, T. Yasuo, Y. Akiyama, Y. Miyake, T. Saitoh, Degradation phenomena in the cathode of a solid oxide fuel cell with an alloy separator, *J. Power Sources*. 55 (1995) 73–79. [https://doi.org/10.1016/0378-7753\(94\)02172-Y](https://doi.org/10.1016/0378-7753(94)02172-Y).
- [165] S.P. Jiang, J.P. Zhang, L. Apateanu, K. Foger, Deposition of Chromium Species at Sr-Doped  $\text{LaMnO}_3$  Electrodes in Solid Oxide Fuel Cells. I. Mechanism and Kinetics, *J. Electrochem. Soc.* 147 (2000) 4013–4022. <https://doi.org/10.1149/1.1394012>.
- [166] Y.D. Zhen, J. Li, S.P. Jiang, Oxygen reduction on strontium-doped  $\text{LaMnO}_3$  cathodes in the absence and presence of an iron-chromium alloy interconnect, *J. Power Sources*. 162 (2006) 1043–1052. <https://doi.org/10.1016/j.jpowsour.2006.08.034>.
- [167] W. Junwei, L. Xingbo, Recent Development of SOFC Metallic Interconnect, *J. Mater. Sci. Technol.* 26 (2010) 293–305. [https://doi.org/10.1016/s1005-0302\(10\)60049-7](https://doi.org/10.1016/s1005-0302(10)60049-7).
- [168] C. Key, J. Eziashi, J. Froitzheim, R. Amendola, R. Smith, P. Gannon, Methods to Quantify Reactive Chromium Vaporization from Solid Oxide Fuel Cell Interconnects,

- J. Electrochem. Soc. 161 (2014) C373–C381. <https://doi.org/10.1149/2.0041409jes>.
- [169] Y.-W. Kim, G.R. Belton, The Thermodynamics of Volatilization of Chromic Oxide: Part I. The Species  $\text{CrO}_3$  and  $\text{CrO}_2\text{OH}$ , Metall. Trans. 5 (1974) 1811–1816.
- [170] C. Gindorf, L. Singheiser, K. Hilpert, Chromium vaporisation from Fe, Cr base alloys used as interconnect in fuel cells, Steel Res. 72 (2001) 528–533. <https://doi.org/10.1002/srin.200100163>.
- [171] M. Casteel, D. Lewis, P. Willson, M. Alinger, Ionic Conductivity Method for measuring vaporized chromium species from solid oxide fuel cell interconnects, Int. J. Hydrogen Energy. 37 (2012) 6818–6829. <https://doi.org/10.1016/j.ijhydene.2012.01.016>.
- [172] C. Collins, J. Lucas, T.L. Buchanan, M. Kopczyk, A. Kayani, P.E. Gannon, M.C. Deibert, R.J. Smith, D.S. Choi, V.I. Gorokhovskiy, Chromium volatility of coated and uncoated steel interconnects for SOFCs, Surf. Coatings Technol. 201 (2006) 4467–4470. <https://doi.org/10.1016/j.surfcoat.2006.08.053>.
- [173] T. Uehara, N. Yasuda, T. Ohno, A. Toji, Improvement of Oxidation Resistance of Fe-Cr Ferritic Alloy Sheets for SOFC Interconnects, Electrochemistry. 77 (2012) 131–133. <https://doi.org/10.5796/electrochemistry.77.131>.
- [174] E. Konyshcheva, H. Penkalla, E. Wessel, J. Mertens, U. Seeling, L. Singheiser, K. Hilpert, Chromium Poisoning of Perovskite Cathodes by the ODS Alloy  $\text{Cr}_5\text{Fe}_1\text{Y}_2\text{O}_3$  and the High Chromium Ferritic Steel Crofer22APU, J. Electrochem. Soc. 153 (2006) A765–A773. <https://doi.org/10.1149/1.2172563>.

- [175] J.G. Grolig, J. Froitzheim, J.E. Svensson, Coated stainless steel 441 as interconnect material for solid oxide fuel cells: Evolution of electrical properties, *J. Power Sources*. 284 (2015) 321–327. <https://doi.org/10.1016/j.jpowsour.2015.03.029>.
- [176] B. Jönsson, A. Westerlund, Oxidation Comparison of Alumina-Forming and Chromia-Forming Commercial Alloys at 1100 and 1200 °C, *Oxid. Met.* 88 (2017) 315–326. <https://doi.org/10.1007/s11085-016-9710-4>.
- [177] R. Sachitanand, J.E. Svensson, J. Froitzheim, The Influence of Cr Evaporation on Long Term Cr Depletion Rates in Ferritic Stainless Steels, *Oxid. Met.* 84 (2015) 241–257. <https://doi.org/10.1007/s11085-015-9552-5>.
- [178] R. Sachitanand, M. Sattari, J.E. Svensson, J. Froitzheim, The Oxidation of Coated SOFC Interconnects in Fuel Side Environments, *Fuel Cells*. 16 (2016) 32–38. <https://doi.org/10.1002/fuce.201500066>.
- [179] J.G. Grolig, J. Froitzheim, J.E. Svensson, Effect of Cerium on the Electrical Properties of a Cobalt Conversion Coating for Solid Oxide Fuel Cell Interconnects - A Study Using Impedance Spectroscopy, *Electrochim. Acta*. 184 (2015) 301–307. <https://doi.org/10.1016/j.electacta.2015.10.111>.
- [180] H. Falk-Windisch, M. Sattari, J.E. Svensson, J. Froitzheim, Chromium vaporization from mechanically deformed pre-coated interconnects in Solid Oxide Fuel Cells, *J. Power Sources*. 297 (2015) 217–223. <https://doi.org/10.1016/j.jpowsour.2015.07.085>.
- [181] E.A. Lass, M.R. Stoudt, M.E. Williams, M.B. Katz, L.E. Levine, T.Q. Phan, T.H. Gnaeupel-Herold, D.S. Ng, Formation of the Ni<sub>3</sub>Nb<sub>d</sub>-Phase in Stress-Relieved

- Inconel 625 Produced via Laser Powder-Bed Fusion Additive Manufacturing, (n.d).  
<https://doi.org/10.1007/s11661-017-4304-6>.
- [182] D.M. Gorman, R.L. Higginson, H. Du, G. McColvin, A.T. Fry, R.C. Thomson, Microstructural Analysis of IN617 and IN625 Oxidised in the Presence of Steam for use in Ultra-Supercritical Power Plant, *Oxid. Met.* 79 (2013) 553–566.  
<https://doi.org/10.1007/s11085-012-9342-2>.
- [183] N.K. Othman, N. Othman, J. Zhang, D.J. Young, Effects of water vapour on isothermal oxidation of chromia-forming alloys in Ar/O<sub>2</sub> and Ar/H<sub>2</sub> atmospheres, *Corros. Sci.* 51 (2009) 3039–3049. <https://doi.org/10.1016/j.corsci.2009.08.032>.
- [184] D.J. Young, Effects of water vapour on the oxidation of chromia formers, *Mater. Sci. Forum.* 595–598 (2008) 1189–1197.  
<https://doi.org/10.4028/www.scientific.net/msf.595-598.1189>.
- [185] J. Zurek, D.J. Young, E. Essuman, M. Hänsel, H.J. Penkalla, L. Niewolak, W.J. Quadackers, Growth and adherence of chromia based surface scales on Ni-base alloys in high- and low-pO<sub>2</sub> gases, *Mater. Sci. Eng. A.* 477 (2008) 259–270.  
<https://doi.org/10.1016/j.msea.2007.05.035>.
- [186] P. Alnegren, M. Sattari, J.E. Svensson, J. Froitzheim, Temperature dependence of corrosion of ferritic stainless steel in dual atmosphere at 600-800 °C, *J. Power Sources.* 392 (2018) 129–138. <https://doi.org/10.1016/j.jpowsour.2018.04.088>.
- [187] L. Jian, P. Jian, X. Jianzhong, Q. Xiaoliang, Oxidation of Haynes 230 alloy in reduced temperature solid oxide fuel cell environments, *J. Power Sources.* 139 (2005) 182–187.

<https://doi.org/10.1016/J.JPOWSOUR.2004.07.019>.

- [188] P.Y. Hou, J. Stringer, The effect of reactive element additions on the selective oxidation, growth and adhesion of chromia scales, *Mater. Sci. Eng. A.* 202 (1995) 1–10. [https://doi.org/https://doi.org/10.1016/0921-5093\(95\)09798-8](https://doi.org/https://doi.org/10.1016/0921-5093(95)09798-8).
- [189] D.J. Young, The Nature of High Temperature Oxidation, in: *High Temp. Oxid. Corros. Met.*, 2016: pp. 1–30. <https://doi.org/10.1016/b978-0-08-100101-1.00001-7>.
- [190] S.R.J. Saunders, M. Monteiro, F. Rizzo, The oxidation behaviour of metals and alloys at high temperatures in atmospheres containing water vapour: A review, *Prog. Mater. Sci.* 53 (2008) 775–837. <https://doi.org/10.1016/J.PMATSCI.2007.11.001>.
- [191] H. Al-Badairy, D. Naumenko, J. Le Coze, G.J. Tatlock, W.J. Quadackers, Materials at High Temperatures Significance of minor alloying additions and impurities on alumina scale growth and adherence in FeCrAl alloys, *Mater. High Temp.* 20 (2014) 405–412. <https://doi.org/10.1179/mht.2003.047>.
- [192] X. Xu, X. Zhang, X. Sun, Z.P. Lu, Effects of silicon additions on the oxide scale formation of an alumina-forming austenitic alloy, *Corros. Sci.* 65 (2012) 317–321. <https://doi.org/10.1016/j.corsci.2012.08.039>.
- [193] D.H. Speidel, A. Muan, The System Manganese Oxide–Cr<sub>2</sub>O<sub>3</sub> in Air, *J. Am. Ceram. Soc.* 46 (1963) 577–578. <https://doi.org/doi:10.1111/j.1151-2916.1963.tb14619.x>.
- [194] A. Col, V. Parry, C. Pascal, Oxidation of a Fe–18Cr–8Ni austenitic stainless steel at 850 °C in O<sub>2</sub>: Microstructure evolution during breakaway oxidation, *Corros. Sci.* 114

- (2017) 17–27. <https://doi.org/10.1016/J.CORSCI.2016.10.029>.
- [195] B.K. Kim, D.-I. Kim, K.-W. Yi, Suppression of Cr evaporation by Co electroplating and underlying Cr retention mechanisms for the 22wt.% Cr containing ferritic stainless steel, *Corros. Sci.* 130 (2018) 45–55. <https://doi.org/https://doi.org/10.1016/j.corsci.2017.10.019>.
- [196] J. Engkvist, S. Canovic, K. Hellström, A. Järnäs, J.E. Svensson, L.G. Johansson, M. Olsson, M. Halvarsson, Alumina Scale Formation on a Powder Metallurgical FeCrAl Alloy (Kanthal APMT) at 900–1,100 °C in Dry O<sub>2</sub> and in O<sub>2</sub> + H<sub>2</sub>O, *Oxid. Met.* 73 (2010) 233–253. <https://doi.org/10.1007/s11085-009-9177-7>.
- [197] H. Josefsson, F. Liu, J.E. Svensson, M. Halvarsson, L.G. Johansson, Oxidation of FeCrAl alloys at 500-900°C in dry O<sub>2</sub>, *Mater. Corros.* 56 (2005) 801–805. <https://doi.org/10.1002/maco.200503882>.
- [198] L.-F. He, P. Roman, B. Leng, K. Sridharan, M. Anderson, T.R. Allen, Corrosion behavior of an alumina forming austenitic steel exposed to supercritical carbon dioxide, *Corros. Sci.* 82 (2014) 67–76. <https://doi.org/https://doi.org/10.1016/j.corsci.2013.12.023>.
- [199] P.Y. Hou, X.F. Zhang, R.M. Cannon, Impurity distribution in Al<sub>2</sub>O<sub>3</sub> formed on an FeCrAl alloy, *Scr. Mater.* 50 (2004) 45–49. <https://doi.org/https://doi.org/10.1016/j.scriptamat.2003.09.044>.
- [200] W. Zhang, J. Li, J. Yang, B. Zhou, B. Chi, J. Pu, L. Jian, Characterization of a new Fe-based alloy as metallic interconnect in SOFC anode environment, *Int. J. Hydrogen*

- Energy. 41 (2016) 22246–22253. <https://doi.org/10.1016/J.IJHYDENE.2016.09.197>.
- [201] Y.J. Park, G. Min, J. Hong, Comparative study of solid oxide fuel cell-combined heat and power system designs for optimal thermal integration, *Energy Convers. Manag.* 182 (2019) 351–368. <https://doi.org/10.1016/j.enconman.2018.12.068>.
- [202] G.Y. Lai, *High-temperature corrosion and materials applications*, ASM International, 2007.
- [203] K.A. Terrani, B.A. Pint, Y.J. Kim, K.A. Unocic, Y. Yang, C.M. Silva, H.M. Meyer, R.B. Rebak, Uniform corrosion of FeCrAl alloys in LWR coolant environments, *J. Nucl. Mater.* 479 (2016) 36–47. <https://doi.org/10.1016/j.jnucmat.2016.06.047>.
- [204] K. Zhang, A. El-Kharouf, J.E. Hong, R. Steinberger-Wilckens, The effect of aluminium addition on the high-temperature oxidation behaviour and Cr evaporation of aluminised and alumina-forming alloys for SOFC cathode air pre-heaters, *Corros. Sci.* (2020) 108612. <https://doi.org/10.1016/j.corsci.2020.108612>.
- [205] B.A. Pint, A.J. Garratt-Reed, L.W. Hobbs, The reactive element effect in commercial ODS FeCrAl alloys, *Mater. High Temp.* 13 (1995) 3–16. <https://doi.org/10.1080/09603409.1995.11689496>.
- [206] W.J. Quadackers, H. Holzbrecher, K.G. Briefs, H. Beske, Differences in growth mechanisms of oxide scales formed on ODS and conventional wrought alloys, *Oxid. Met.* 32 (1989) 67–88. <https://doi.org/10.1007/BF00665269>.
- [207] B.A. Pint, J.R. Martin, L.W. Hobbs, 18O/SIMS characterization of the growth

mechanism of doped and undoped  $\alpha$ -Al<sub>2</sub>O<sub>3</sub>, *Oxid. Met.* 39 (1993) 167–195.  
<https://doi.org/10.1007/BF00665610>.

- [208] W. Chen, X. Shan, Y. Guo, J. Li, Z. Zou, F. Guo, X. Zhao, P. Xiao, The effect of reactive element species and concentrations on the isothermal oxidation of  $\beta$ -NiAl coating fabricated by spark plasma sintering, *Surf. Coatings Technol.* 357 (2019) 841–848. <https://doi.org/https://doi.org/10.1016/j.surfcoat.2018.10.071>.